

Preface

Special Issue on Up-to-Date Problems in Modern Railways

The current issue is the continuation of the Vol. 19, No. 3 issue (<http://acta.uni-obuda.hu/Issue121.htm>), published in Acta Polytechnica Hungarica, the high-rank scientific journal.

This Special Issue series aimed to provide a main international podium for a wide range of professionals to discuss and present the most recent challenges and developments in *Up-to-date problems in modern railways*. The Guest Editors' goal was to collect international papers containing the most modern results connecting the railways themselves with up-to-date methods. It means that the topics of civil engineering, electrical engineering, and mechanical engineering were highly welcome from all over the world. It can be proudly said that this proposal has been fulfilled and many papers were received.

We are very thankful to all the authors and the co-authors for their devotion during the formulation of contributions for this special issue and for sharing their results with the journal.

Last but not least, we are sincerely thankful to the editorial board of journal Acta Polytechnica Hungarica for preparing and managing this issue technically, as well as Prof. Dr. Péter Baranyi, Rector of Széchenyi István University, Győr, the organizer of this Special Issue.

The Editorial Team and the Guest Editors would like to follow this way and publish more Special Issues on this topic in Acta Polytechnica Hungarica journal. At this moment we have approximately enough submitted papers for the third one.

Dragan Marinkovic, Dmytro Kurhan, Mykola Sysyn and Szabolcs Fischer

Guest Editors

Management Schemes Incorporating all Services for Optimum Railway System Energy Utilization Based on Level Set Calculation Method

Yan Cao^{1*}, Srdjan Stojičić², Miloš Milovančević³

¹ School of Mechatronic Engineering, Xi'an Technological University, Xi'an, 710021 China, caoyan@xatu.edu.cn

² Railway College of Vocational Studies, Serbia, srdjan.stojicic@vzs.edu.rs

³ University of Niš, Faculty of Mechanical Engineering, Aleksandra Medvedeva 14, Niš, Serbia, milos.milovancevic@masfak.ni.ac.rs

Abstract: The Rail Technical Strategy aims to meet the goals that reduce carbon emissions, increase rail speed, lower rail costs and improve customer satisfaction. The reduction of fuel consumption and costs for rail travel depends on more effective maintenance and operation. In a railway system, mainly diesel energy is needed for traction followed by 30 percent energy consumption. The engine will start a reaction to extract this carbon by running the gas supplying hot and reactive. The heat released by the reaction will be adequate to support the reaction under such conditions, resulting in very high local temperatures usually as a thermal wave. Energy efficiency of rail vehicles, expressed in the reduction of the size of diesel engines and the consistent development of battery and supercapacitor systems to promote regenerative braking are in focus. For the accessibility study of these issues with regard to the implementation of the engine control approach, level set calculations approaches were used in this study.

Keywords: optimization; train diesel engine; maximizing efficiency; driving quality

1 Introduction

Steam locomotives were the dominant source of electricity for railways in worldwide between the 1830s and 1940s [1]. Steam engines were unreliable and expensive to keep and run. The first petrol engine was invented by Dr. N. A Otto in 1876 and by Gottlieb Daimler in 1884. In 1886-1890 James Ackroyd Stuart created a compression-ignition oil engine and Dr. Rudolf introduced an oil-only engine after many years of work. Theoretical tests by Diesel have shown that compression-ignition engines can attain thermal efficiencies of up to 73% compared to 6-10%

for a steam engine and 18-22% for gasoline spark-ignition engines [1]. The term Diesel is used to create the compression-ignition engine. At the time, diesel trains had many benefits relative to steam locomotives described as follows: It is known that rail operations now use energy and fuel very efficiently. Rail emissions are comparatively low and are referred to as 'green transport' compared with other transport methods (e.g. planes and trucks) [2]. The government supports the modal change from road to track; thus, rail transport development will be accelerated and rail capability pressure brought on. The energy shortage and environmental emissions will be intensified by increased capacity and the expansion of rail traction and operations. Most countries around the globe are seeking to find a way to reduce energy demand and emissions of greenhouse gas (GHG). In Britain, the report of the RSSB called 'Meeting Rail's Carbon Ambition' states that rail emissions could be reduced by 38 percent per passenger per kilometer and saves 400,000 tons/day in 5 years. The industry must meet four criteria: energy efficient driving; weight control for new trains; auto shut down of auxiliary loads and regenerative braking considering the carbon and cost saving viewpoint. The reduction of fuel consumption and costs in rail travel would rely on more efficient rolling stock production, infrastructure modernization, and operational optimization. The reduction to GHG emissions would rely both on improving the energy efficiency of diesel trains and on the electrification of railway networks to ensure that railway emissions are extremely low. Increased track capacity should be introduced with the aim of optimizing traffic flow, increasing the efficiency of railways and reducing upgrading time.

Different policies for improving Energy Efficiency (EE) include a corner stone for sustainability goals for the European Union (EU) and other countries in the world. Transportation accounts for a high percentage of the ultimate energy consumption and could have significant improvement opportunities. In last decade, sustainability is a significant issue for railway sector as the Community of European Railway and Infrastructure Companies (CER) and International Union of Railways (UIC) [3]. Following the 1990 consumption baseline, the objectives are 50% reduction in the intensity of energy use (energy per passenger and km, i.e., kWh/p km) in 2030 (0.09 kWh /pkm), and 60% in 2050. Also, a reduction in emissions of 75% in 2050 is predicted from the environmental point of view.

Various countries work in different fields to reduce the increase and domination of road transport as well as increase the market share of so-called eco-friendly means of transportation (e.g. railway and maritime), such as the model of Polish Intermodal Transport or China's One Belt One Road Initiative (OBOR) and the OBOR in particular. Around 13,000 trains have been operated in the last eight years [4]. Railway transportation has several advantages that explain its development in the last decade both in the passenger sector (for instance, the development of 25,000 km of high-speed infrastructures in China [5]), but mainly in the freight sector: Short time (one-third of shipping), no weather influence, high safety, green environmental protection, and its complementarity with shipping transportation

(and the development of new harbor infrastructures around the world [5]). For trains, one significant comment is that in some countries passenger traveling is cheap, but only on high-speed services (for example in Spain). Transport by freight generates a benefit mostly in certain countries (Canada and the US) or is conducted with high capacities (up to 90% in the North Rail Express Freight Service, in Northern Europe), in the German Bahn (DB) (the largest market for freight). For instance, by 2038-2050, the DB Cargo operator is increasing its rail transport volumes in Germany by 70% [3]. It is also understood, however, that conventional passenger and freight services depend heavily on government subsidies (e.g., China Railway Express [5]). The energy management schemes aim at optimum management within the railway system and at incorporating all energy services of the system improve this by properly utilizing of energy (an effective expense for railway operation) [6, 7]. Different organizations and operators aim to integrate the techniques and procedures that could reduce the effect of the transport industry on total energy demand in the medium and long-term.

1.1 Energy Efficiency in Railways

1.1.1 The Use of Regenerative Braking

Regenerative braking is conceptually simplistic and is a popular solution to enhance energy efficiency, but in fact entails a very complicated problem since there is no certainty that all trains have separate positions in the rail systems at the same time and location (electrically speaking) with different roles in the Rail Power System (i.e., generator vs. load). In traditional railways, this issue is much more difficult since many trains will be in the same track as catenaries. In this case, power cannot be injected into the network because the overhead line voltages are increased or reverse flows are not necessary, so due to the substation configuration, the locomotive resistive braking bank generation is consumed and dissipated [8]. It should be kept in mind that there are two reasons that increase the potential for regenerative braking. Firstly, the reduction in capital cost and the increase of energy density. Energy density and lifetime of storage systems seems now more possible than one decade before (partially driven by the deployment of Electric Vehicles and the Integration of Renewables, RES). Second, regenerative braking capacity can be increased by converters so that the same friction rate (pneumatic braking) does not need to be used in fusion mode during service breakage throughout all practical speed ranges. Pure electric frequency is referred to [9]. This increases the braking efficiency as can be seen in various statistics, but only when energy can be stored or used some way [10, 11, 12, 13, 14]. Table 1 shows the energy losses in diesel train, and Table 2 indicates the comparison of transmission systems in diesel traction.

1.2 Level Set Method

1.2.1 Basic Level Set Formulation

Interface evolution description is a key component of the flow of gas and liquid. Osher and Sethian's level set method offers an efficiently functional representation of the interface as the level set of a greater dimensional function. It has evolved from a multi-faceted and high-powered interface methodology. The major advantage of this implicit image of a driving interface is the ability to accommodate diesel engine modifications naturally. Following is the level set formulation. The level set method shows the interface (Γ) as the zero-contour of a higher dimensional function (ϕ) as level set method defined as the signed distance function to Γ :

$$|\phi(\vec{x}, t)| = |\vec{x} - \vec{x}_r| \quad (1)$$

[20]

$x \rightarrow \Gamma = \text{interface location (closest to } x \rightarrow)$

ϕ takes positive and negative values on the sides of interface. Interface curvature k and interface normal vector $n \rightarrow$ is computed as:

$$\vec{n} = \frac{\nabla\phi}{|\nabla\phi|} \text{ and } k = -\nabla \cdot \vec{n} \quad (2)$$

Regarding the velocity field $u \rightarrow = (u, v, w)$, the interface evolves based on the level set transport equation is

$$\frac{\partial\phi}{\partial t} + \vec{u} \cdot \nabla\phi = 0 \quad (3)$$

Since the Level Set function has not retained the property of its signed distance function. The re-initialization equation was proposed by Sussman *et al.* as Eq. (4) to change a level set function ϕ_0 into the signed distance function ϕ .

$$\phi_r + \text{sgn}(\phi_0)(|\nabla\phi| - 1) = 0 \quad (4)$$

$\text{sgn} = a$ smoothed-out signum function

$\tau =$ fictitious time controlling the width of band around 0 level set.

Theoretically the signed distance function is preserved without re-initialization in this extension velocity technique. However, the original extension rate is only a first-order velocity approximation close the interface and can lead to unexpected numerical items as local solutions for the flow near the interface. Similar to the extension velocity, Ovsyannikov *et al.* suggested that the distance function of the signed device is held by inserting a source term direct into the recently established level-set equation. This approach rewrites the level set equation for transport as

$$\frac{\partial\phi}{\partial t} + \vec{u} \cdot \nabla\phi = A(\vec{x}, t)\phi, \quad (5)$$

$A(x \rightarrow, t) = \text{an arbitrary regular function not based on } \phi(x \rightarrow, t)$

Through theoretical analysis, the source term could be expressed as

$$A(\vec{x}, t)\phi = [u_k - (u_k)|_{n=0}] \frac{\partial \phi}{\partial x_k}. \quad (6)$$

The Taylor's expansion of $A(x \rightarrow, t)$ can be obtained as an arbitrary high-order approximate form as

$$A(\vec{x}, t) = A_0 + A_1 n + A_2 n^2 + O(n^3) \quad (7)$$

This approach simplifies the implementation of the level-set method in contrast with the extension speed method; however, a return to the re-initialization mechanism is needed. It is possible to significantly reduce the number of re-initializations. The hyperbolic tangent function was introduced as a level-set function by Olsson, etc. In the interface bounded field, it is secondhand precision and sufficient for mass conservation. This defines the hyperbolic tangent function

$$\psi(\vec{x}, t) = \frac{1}{2} \left(\tanh h \left(\frac{\phi(\vec{x}, t)}{2\varepsilon} \right) + 1 \right) \quad (8)$$

$\varepsilon =$ a parameter to control the profile thickness.

Table 1
Energy losses in the diesel train [2]

| | Intercity DEMU | Regional DHMU |
|--------------------|----------------|---------------|
| | Class 221 | Class 170 |
| Engine Losses | 68% | 68% |
| Engine Idle | 5% | 5% |
| Auxiliary Use | 5% | 5% |
| Transmission Loss | 4% | 3% |
| Running resistance | 14% | 6% |
| Inertia | 4% | 13% |

This formulation makes a correlation between the hyperbolic tangent function and level set function. $\phi = 0$ defined by the location of iso-surface $\psi = 0.5$ as Eq. (9).

$$\frac{\partial \psi}{\partial \tau} + \nabla \cdot (\psi(1 - \psi)\vec{n}) = \nabla \cdot (\varepsilon(\nabla \psi \cdot \vec{n})\vec{n}). \quad (9)$$

Table 2
Comparison of transmission systems in diesel traction

| | Diesel-mechanic | Diesel-electric | Diesel-hydraulic |
|---|-----------------|-----------------|------------------|
| Engine efficiency | equal | equal | equal |
| Transmission efficiency (approximately) | 95% | 85% | 85% |
| Possibility for optimum engine load | high | high | low |

1.2.2 Improvement of the Re-Initialization Process

Sussman et al. [30] proposed PDE based re-initialization process using the equation $\phi_\tau = L(\phi_0, \phi) = \text{sgn}(\phi_0)(1 - |\nabla\phi|)$, so sgn is applied to keep ϕ_0 unchanged on the interface as Eq. (10)

$$s_\varepsilon(\phi_0) = \frac{\phi_0}{\sqrt{\phi_0^2 + \varepsilon^2}}. \quad (10)$$

$$\partial_2 \int_\Omega H(\phi) = 0 \quad (11)$$

H = a smoothed out approximation of sign function as

$$H_\varepsilon(\phi) = \begin{cases} \frac{1}{2} & \text{if } \phi > \varepsilon \\ -\frac{1}{2} & \text{if } \phi < -\varepsilon \\ \frac{1}{2} \left(\frac{\phi}{\varepsilon} + \frac{1}{\pi} \sin(\pi\phi / \varepsilon) \right) & \text{otherwise} \end{cases} \quad (12)$$

$$\phi_\tau = L(\phi_0, \phi) + Af(\phi) \quad (13)$$

$$A = \frac{-\int_\Omega H(\phi)L(\phi_0, \phi)}{H(\phi)f(\phi)} \quad (14)$$

$$\phi_\tau + \text{sign}(\phi_0)(|\nabla\phi| - 1) = \alpha f \quad (15)$$

$$\frac{\partial\phi}{\partial\tau} + (A_0 - A(t))(-p + k)|\nabla\phi| = 0 \quad (16)$$

The re-initialization equation was modified for McCaslin and Desjardins to take into account considerable spatial variations in the fixed level transport. This local reset is dependent on the local deformation of the flow and numerical diffusion. The re-initialization equation for yields has a spatially and temporally different element

$$\frac{\partial\psi}{\partial\tau} = \nabla \cdot (\alpha(\varepsilon(\nabla\psi \cdot \vec{n}) - \psi(1 - \psi)\vec{n})) \quad (17)$$

The local interfacial value of α is defined as

$$\alpha(\vec{x}_\Gamma, t) = \max(\lambda_n |u_\Gamma \cdot \vec{n}|, \lambda_s |\vec{n}^T, s_\Gamma \cdot \vec{n}| \varepsilon) \quad (18)$$

$\lambda_n |u| \rightarrow \Gamma \cdot n \rightarrow$ *measures the numerical diffusion*

$\lambda_s |n \rightarrow T \cdot S\Gamma \cdot n \rightarrow$ *measures the deformation of local flow kinematics*

$$\begin{aligned} & \max(D_{\bar{x}}\phi_{i,j,k} - D_x^+\phi_{i,j,k}, 0)^2 + \max(D_{\bar{y}}\phi_{i,j,k} - D_y^+\phi_{i,j,k}, 0)^2 \\ & + \max(D_{\bar{z}}\phi_{i,j,k} - D_z^+\phi_{i,j,k}, 0)^2 - 1 = 0 \end{aligned} \quad (19)$$

$D_{x,y,z\pm}$ = *the first order upwind finite difference notations*

The direction and the radius of each particle applied to correct the error to the level set are stored. The radius is:

$$r_p = \begin{cases} r_{max} & \text{if } s_p \phi(\vec{x}_p) > r_{max} \\ s_p \phi(\vec{x}_p) & \text{if } r_{min} \leq s_p \phi(\vec{x}_p) \leq r_{max} \\ r_{min} & \text{if } s_p \phi(\vec{x}_p) < r_{min} \end{cases} \quad (20)$$

Because evaporation rates are normally determined from the jumping conditions in areas just next door to the interfaces, the governing equations for incompressible evaporating gas-liquid fluxes are as "Jump State Form"

$$\nabla \cdot \vec{u} = 0 \quad (21)$$

$$\frac{\partial \rho \vec{u}}{\partial t} + \nabla \cdot (\rho \vec{u} \otimes \vec{u}) = -\nabla p + \nabla(\mu[\nabla \cdot \vec{u} + \nabla \cdot \vec{u}^t]) + \rho \vec{g} \quad (22)$$

$$\frac{\partial \rho C_p T}{\partial t} + \nabla \cdot (\rho C_p \vec{u} T) = \nabla \cdot (\lambda \nabla T) \quad (23)$$

$$\frac{\partial \rho Y}{\partial t} \nabla \cdot (\rho \vec{u} Y) = \nabla \cdot (\rho D_m \nabla Y) \quad (24)$$

T = the temperature

λ = the thermal conductivity

C_p = the specific heat at constant pressure

Y = the mass fraction,

D_m = the mass diffusion coefficient

The vapor pressure on the interface is described to be the saturation pressure P_{vap}^Γ , which and Y_{vap}^Γ can be given by the Clausius-Clapeyron relation as:

$$P_{vap}^\Gamma = p_{atm} \exp\left(-\frac{h_{lg} m_{vap}}{R} \left(\frac{1}{T^\Gamma} - \frac{1}{T_B}\right)\right) \quad (25)$$

$$Y_{vap}^\Gamma = \frac{P_{vap}^\Gamma m_{vap}}{(p_{atm} - P_{vap}^\Gamma) m_g + P_{vap}^\Gamma m_{vap}} \quad (26)$$

$$\dot{\omega} = \frac{\rho_g D_m \nabla Y \cdot \vec{n}|_g^\Gamma}{1 - Y_{vap}^\Gamma} \quad (27)$$

$$T^\Gamma = \frac{h_{lg} m_{vap} T_B}{h_{lg} m_{vap} - R T_B \ln \frac{P_{vap}^\Gamma}{p_{atm}}} \quad (28)$$

P_{vap}^Γ is computed as

$$P_{vap}^\Gamma = \frac{-Y p_{atm} m_g}{(m_g - m_{vap}) Y_{vap}^\Gamma - m_{vap}} \quad (29)$$

Table 3
Annual financial saving and carbon emissions' saving
(Source: London Midland Internal Documents)

| | Savings in kWh/day @23.5kW | Annual Savings in kWh | Annual savings @ 9p/kWh | Annual savings in kg of CO2 |
|-------------------------------|----------------------------|-----------------------|-------------------------|-----------------------------|
| SX daytime stabling | 4814.945 | 962989 | £86,669.01 | 469746.0342 |
| SX over night stabling | 8174.805 | 1634961 | £147,146.49 | 797533.9758 |
| SO day and overnight stabling | 25144.894 | 1005795.76 | £90,521.62 | 490627.1717 |
| SU day and overnight stabling | 16770.175 | 670807 | £60,372.63 | 327219.6546 |
| Total Annual Savings | 54904.819 | 4274552.76 | £384,709.75 | 2085126.836 |
| Annual savings minus losses | 49414.3371 | 3847097.484 | £346,238.77 | 1876614.153 |

3 Level Set Simulation

3.1 Cost Function Variations Due to the Unknowns

Assuming that the 1th and 2nd order Fréchet derivatives of $R(p)$ show them as $R'(p)[\cdot]$ and $R''(p)[\cdot, \cdot]$. The first order Fréchet derivative of a function (if it exists) is a bounded and linear operator. The Fréchet derivatives of the second order are also bounded, but bilinear, meaning that the operator operates on two arguments and is linear for each [32]. Table 3 shows the annual financial saving and carbon emissions' saving. Table 4 shows the modification financial saving.

$$R(P + \varepsilon \delta P) = R(P) + \varepsilon \dot{R}(P)[\delta P] + \frac{\varepsilon^2}{2} R''(P)[\delta P, \delta P] + O(\varepsilon^3) \quad (30)$$

Rewriting $F(p)$ as

$$F(P) = \frac{1}{2} \langle R(P), R(P) \rangle_{S_u} \quad (31)$$

$$F(P + \varepsilon \delta P) = F(p) + \varepsilon F'(p)[\delta P] + \frac{\varepsilon^2}{2} F''(P)[\delta P, \delta P] + O(\varepsilon^3) \quad (32)$$

$$F'(p)[p_1] = Re \langle \dot{R}(P)[p_1], R(P) \rangle_{S_u} \quad (11)$$

$$F''(P)[p_1, p_2] = Re \langle \dot{R}(P)[p_1], \dot{R}(P)[p_2] \rangle_{S_u} + Re \langle R''(P)[p_1, p_2], R(P) \rangle_{S_u} \quad (33)$$

$$\langle \hat{u}, \dot{R}(P)[\hat{p}] \rangle_{S_u} = \langle \dot{R}(P) * [\hat{u}], \hat{p} \rangle_{S_p}, \quad \forall \hat{u} \in S_u, \forall \hat{p} \in S_p \quad (34)$$

can be written as

$$F'(p)[p_1] = Re \langle \dot{R}(P) *, R(p), p_1 \rangle_{S_p} \quad (35)$$

Regarding that the existence of the 1th and 2nd order Fréchet derivatives of p regarded to v , showed as $p'(v)[\cdot]$ and $p''(v)[\cdot, \cdot]$, the 1th and 2nd order Fréchet derivatives of F regarded to v is

$$\hat{F}(v)[v_1] = \hat{F}(v)[p'(v)v_1] \quad (36)$$

$$F''[v_1, v_2] = F''(v)[p'(v)[p_1], p'(v)[p_2]] + \hat{F}(p)[p''(v)[v_1, v_2]] \quad (37)$$

$$v_1, v_2 \in Sv$$

Equations (36) and (37) themselves can be shown in terms of $R(p)$ and its derivatives using (11) and (12):

for a $c \in \mathbb{R}$

$$\begin{cases} \phi(X, \mu) > c & \forall x \in D \\ \phi(X, \mu) = c & \forall x \in \partial D \\ \phi(X, \mu) < c & \forall x \in \Omega \setminus D \end{cases} \quad (38)$$

$$P(X, \mu) = p_i(x)H(p_o(X, \mu) - c) + p_o(1 - H(\phi(X, \mu) - c)) \quad (39)$$

$$\frac{\partial p}{\partial \phi} = (p_i - p_o)\delta_{rg}(\phi - c) \quad (40)$$

$$\frac{\partial p}{\partial \mu_j} = \frac{\partial p}{\partial \phi} \frac{\partial \phi}{\partial \mu_j} = (p_i - p_o)\delta_{rg}(\phi - c) \frac{\partial \phi}{\partial \mu_j} \quad (25)$$

Now using (25) with (15) and (14), the gradient vector for F is

$$\frac{\partial F}{\partial \mu_j} = \hat{F}(p) \left[\frac{\partial p}{\partial \mu_j} \right] = \text{Re} \langle R(p), \hat{R}(p) \left[\frac{\partial p}{\partial \mu_j} \right] \rangle s_u \quad (41)$$

$$= \text{Re} \langle \hat{R}(p) * \left[R(p), (p_i - p_o)\delta_{rg}(\phi - c) \frac{\partial \phi}{\partial \mu_j} \right] \rangle s_p \quad (42)$$

$$\frac{\partial^2 p}{\partial \mu_j \partial \mu_k} = (p_i - p_o) \left(\delta_{rg}(\phi - c) \frac{\partial^2 \phi}{\partial \mu_j \partial \mu_k} + \delta'_{rg}(\phi - c) \frac{\partial \phi}{\partial \mu_j} \frac{\partial \phi}{\partial \mu_k} \right) \quad (43)$$

where $\delta'_{rg}(\cdot)$ is the derivative of the regularized Dirac delta function. Based on (16) and (12) we have

$$\begin{aligned} \frac{\partial^2 F}{\partial \mu_j \partial \mu_k} &= F''(p) \left[\frac{\partial p}{\partial \mu_j}, \frac{\partial p}{\partial \mu_k} \right] + F(p) \frac{\partial^2 p}{\partial \mu_j \partial \mu_k} \\ &= \text{Re} \langle \hat{R}(p) \left[\frac{\partial p}{\partial \mu_j} \right], \hat{R}(p) \left[\frac{\partial p}{\partial \mu_k} \right] \rangle s_u + \text{Re} \langle R''(P) \left[\frac{\partial p}{\partial \mu_j}, \frac{\partial p}{\partial \mu_k} \right], R(P) \rangle s_u + \\ &\quad \text{Re} \langle \hat{R}(P) *, [R(P)], \frac{\partial^2 p}{\partial \mu_j \partial \mu_k} \rangle s_p. \end{aligned} \quad (44)$$

$$\frac{\partial^2 F}{\partial \mu_j \partial \mu_k} \simeq \text{Re}$$

$$\left\langle \hat{R}(p) \left[\frac{\partial p}{\partial \mu_j} \right], \hat{R}(p) \left[\frac{\partial p}{\partial \mu_k} \right] \right\rangle s_u \quad (45)$$

$$= Re \left\langle \dot{R}(p) \left[(p_i - p_o) \delta_{rg} (\phi - c) \frac{\partial \phi}{\partial \mu_j} \right], \dot{R}(p) \left[(p_i - p_o) \delta_{rg} (\phi - c) \frac{\partial \phi}{\partial \mu_k} \right] \right\rangle S_u \quad (32)$$

$$\left[\tilde{H}_\mu(F) |_{\mu=\mu^{(t)}} + \lambda^{(t)} I \right] (\mu^{(t+1)} - \mu^{(t)}) = -J_\mu(F) |_{\mu=\mu^{(t)}} \quad t \geq 0 \quad (46)$$

$$\frac{\partial \phi}{\partial \beta_j} = \alpha_j \beta_j \frac{\|x - X_j\|^2}{\|\beta_j(x - X_j)\|^\dagger} \psi(\|\beta_j(x - X_j)\|^\dagger) \quad (47)$$

$$\frac{\partial \phi}{\partial x_j^{(k)}} = \alpha_j \beta_j^2 \frac{X_j^{(k)} - x^{(k)}}{\|\beta_j(x - X_j)\|^\dagger} \psi(\|\beta_j(x - X_j)\|^\dagger) \quad (48)$$

Table 4
Modification financial saving (Source: London Midland internal reports)

| | | Pessimistic | Realistic | Optimistic |
|------------------|---|-------------|-------------|-------------|
| Fuel amount | Total fuel consumption per day (in litres) | 117 | 234 | 351 |
| | Total fuel consumption per week (in litres) | 819 | 1638 | 2457 |
| | Total fuel consumption per year (in litres) | 42588 | 85176 | 127764 |
| Financial saving | Fuel cost in pounds per litre | £ 0.64 | £ 0.64 | £ 0.64 |
| | Amount of fuel saved per year (in pounds) | £ 27,256.32 | £ 54,512.64 | £ 81,768.96 |

Conclusions

This article presents potential ways to improve the energy efficiency of diesel and hybrid trains without affecting their dynamics. This technologies (on board and off board storage) improve the life cycle of these units and the efficiency of low- and medium-sized traffic energy networks. Several options were assessed to achieve these goals: Save dynamic braking systems fuel resources and cut the size of the diesel engine. For the improvement of the utility of simulations train feature models, Distributed Energy Resources (DER) were combined and aggregated. For this reason, super-capacitors and various battery technologies were selected. The brake energy of the cars and railways can be recovered, and energy efficiency increased. Energy savings by 10-20% and an increase in load factor and peak shavings by nearly 70 percent was recorded. In addition, the stochastic aspects of such occurrences in railways, such as time delays have been analyzed with regard to timing. Delays can have a positive or negative effect in regenerative braking on power efficiencies (and also, their impact on timetable performance). Simulations are accurate for the chosen route in the example, but the program will use the same approach for any other rail line operated by other vehicles. In addition, detailed physical and heat models of batteries will be developed and validated in the future developments of this work with a view to improving integration of energy storage systems in railways, in particular on board solutions, with space, weight and thermal needs to be avoided. The future contribution and assistance of the reporting versatility of the railways modelled on paper will contribute to an efficient energy balance (volatility) in the 2030-2050 Eco energy scenario.

References

- [1] Churella, A., *From steam to diesel: Managerial customs and organizational capabilities in the twentieth-century American Locomotive Industry*. 1998: Princeton University Press
- [2] Peckham, C., *Improving the Efficiency of Traction Energy Use: Summary Report*. 2007
- [3] Garcia-Garre, A. and A. Gabaldon, *Analysis, evaluation and simulation of railway diesel-electric and hybrid units as distributed energy resources*. Applied Sciences, 2019, **9**(17): p. 3605
- [4] Li, S., et al., *A sustainable transport competitiveness analysis of the China railway express in the context of the belt and road initiative*. Sustainability, 2019, **11**(10): p. 2896
- [5] Li, W. and O.-P. Hilmola, *Belt and Road Initiative and Railway Sector Efficiency—Application of Networked Benchmarking Analysis*. Sustainability, 2019, **11**(7): p. 2070
- [6] Khayyam, S., et al., *Railway system energy management optimization demonstrated at offline and online case studies*. IEEE Transactions on Intelligent Transportation Systems, 2018, **19**(11): pp. 3570-3583
- [7] Razik, L., et al., *REM-S—railway energy management in real rail operation*. IEEE Transactions on Vehicular Technology, 2018, **68**(2): p. 1266-1277
- [8] Arboleya, P., et al., *BFS algorithm for voltage-constrained meshed DC traction networks with nonsmooth voltage-dependent loads and generators*. IEEE Transactions on Power Systems, 2015. **31**(2): pp. 1526-1536
- [9] Takagi, R., *Application of energy storage systems for DC electric railways*. WIT Transactions on Ecology and the Environment, 2009, **121**
- [10] Németh, A., & Fischer, S. (2021) Investigation of the glued insulated rail joints applied to cwr tracks. Facta Universitatis, Series: Mechanical Engineering, doi: 10.22190/FUME210331040N
- [11] Sysyn, M., Nabochenko, O., Kovalchuk, V., Przybyłowicz, M., & Fischer, S. (2021) Investigation of interlocking effect of crushed stone ballast during dynamic loading. Reports in Mechanical Engineering, 2(1), 65-76, <https://doi.org/10.31181/rme200102065s>
- [12] Kuchak, A. J. T., Marinkovic, D., Zehn, M. Parametric Investigation of a Rail Damper Design Based on a Lab-Scaled Model (2021) Journal of Vibration Engineering and Technologies, 9 (1), pp. 51-60
- [13] Tigh Kuchak, A. J., Marinkovic, D., Zehn, M. Finite element model updating - Case study of a rail damper (2020) Structural Engineering and Mechanics, 73 (1), pp. 27-35

- [14] Shatrov, Mikhail G. et al. Influence of pressure oscillations in common rail injector on fuel injection rate. *Facta Universitatis, Series: Mechanical Engineering*, [S.l.], v. 18, n. 4, p. 579-593, Dec. 2020

Structural Design of Safety Steel Device of Railway Vehicles Through Analytical and Experimental Investigations

Jovan Tanaskovic¹, Francis Franklin², Nenad Radovic³, Fatima Zivic⁴

¹University of Belgrade Faculty of Mechanical Engineering, Kraljice Marije 16, 11000 Belgrade, Serbia, jtanaskovic@mas.bg.ac.rs

²School of Engineering, Newcastle University, Newcastle upon Tyne NE1 7RU, United Kingdom, francis.franklin@ncl.ac.uk

³University of Belgrade Faculty of Technology and Metallurgy, Karnegijeva 4, 11000 Belgrade, Serbia, nenrad@tmf.bg.ac.rs

⁴University of Kragujevac Faculty of Engineering, Sestre Janjic 6, Kragujevac 34000, Serbia, zivic@kg.ac.rs

Abstract: The subject of this paper is the structural design of a safety steel device that is located between the standard wagon buffer and the collision energy absorber. The safety steel device is a sacrificial part able to withstand normal operating loads from the buffer across the absorber to the vehicle bearing structure without any permanent deformation, but experiences fully controlled fracture when the load exceeds the defined threshold. Following fracture, the load path is through the energy absorber. The sacrificial part is a ring made from quenched and tempered low alloyed steel with precisely defined heat treatment and material properties. Experimental investigations of scaled samples were performed to get mechanical characteristics of the material and geometry. A full-scale prototype of the safety device was produced, and final quasi-static and dynamic experiments were conducted. The results validate the analytical predictions, and thus validate the design method used here for dimensioning the safety steel device.

Keywords: Safety Steel Device; Controlled Fracture; Analytical Dimensioning; Experimental Investigations

1 Introduction

Development and design of standard elements of railway vehicles present a classical job for an experienced designer or researcher. When it comes to design of special parts that are installed in the current bearing structure, especially if those parts have

a role to control fracture at the exactly defined load, the design is more challenging. Such sacrificial parts are often included in passive safety elements and have a direct impact on the safety, primarily passengers but also vehicles and railway infrastructure. To maximise reliability and safety, research must focus on the right choice of grade of material and shape of geometry as well as the most appropriate way of controlled deformation. Deformation must be absolutely controlled, and it is necessary to analyse in detail loads and requirements defined in standards for the strength of railway vehicles [1, 2].

There are many different ways to connect active and passive safety elements (for controlled activation of energy absorbers) in the railway vehicles structure [3-5]. The anti-climb device and energy absorber are parts of the passive safety assembly and one method for connecting these is based on the process of cutting the outer surface of the wall of steel and aluminium tubes. The impact of cutting depth, the geometry of dies, and stroke of cutting were analysed by experimental investigations in the quasi-static and dynamic behaviour. Experimental results showed that the cutting deformation mode is more stable for aluminium tube and that longitudinal cutting force is correspondingly larger for harder materials and larger cutting depths. Including a shrinking tube energy absorber in the process of collision kinetic energy absorption is one more way for the connection of active and passive absorption elements, and this was analysed by Moreno *et al.* [6]. This paper describes the shrinking process of energy absorption and imperfection that may arise during deformation. During normal exploitation, an automatic coupler absorbs forces through the elastic device without the need for activation of passive safety elements. At the moment of collision, contact forces increase rapidly and leading to activation of passive safety elements installed behind the anti-climbing device. The authors developed and validated a numerical model also that can be used for additional analyses. Absorption characteristics of square cross-section tube that use the folding process for energy absorption have been analysed [7]. Initial force is determined as the critical value of force that causes local buckling of the tube. These passive elements are also installed behind the anti-climb system and take the role of energy absorption when the contact forces exceed normal exploitation values. Results of experimental and numerical investigations of shrinking, folding, curling, splitting, combined tube collision energy absorbers, and sliding friction and wear are discussed in Refs [8-14]. Next to the requests defined in the standard, the condition of the rail track has a significant role in dynamic stability as well as railway safety in general [15, 16]. A new idea for connection of active and passive safety elements is presented here. A safety device consisting of a sacrificial element to control the load path, joins the standard buffer and tube absorber, Fig. 1. The role of it is to transfer normal exploitation loads from standard buffer to the wagon bearing structure by passing the absorber and preventing therefore undesired any permanent deformation. Exceeding normal exploitation loads, in the case of collision, leads to controlled fracture of safety device at the exactly defined shearing area, and to activation of the tube absorber. This paper in detail describes analytically dimensioning of safety device and experimental validation of defined

dimensions and material properties. A developed analytical model can be used for further dimensioning this type of safety device as well as similar devices which are a part of collision energy absorber or for some other purpose that requires controlled fracture.

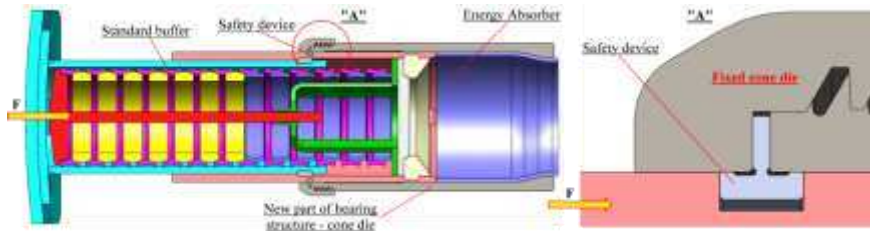


Figure 1

Working principle of safety device

2 Material Characterisation and Proof Design

The geometry and dimensioning of the safety device is critically dependent on the material properties. Material characterization combined analytical determination of critical load using scaled samples with experimental investigations on scaled samples, leading to the final analytical determination of dimensions of the cross-section of a full-scale model of a prototype safety device.

2.1 Preliminary Analytical Design of Safety Device

Safety steel device has a role to transfer normal exploitation loads from the standard buffering elements, bypassing the absorption element, to the vehicle bearing structure, and to break in controlled manner if exploitation loads exceed limit values. The structure of standard buffering elements and the implementation of an energy absorber in line with it requires that the safety device breaks through a clean shearing process. To achieve a controlled break, normal operating stresses need to be below the yield point, which needs to be clearly defined, and ideally below the fatigue limit also, so that there is no failure or plastic deformation of the sacrificial component. The threshold load for activation of the energy damper should be sufficient to exceed the yield stress or the fracture stress. Since the strength, as a crucial design parameter, depends on material composition and quality, heat treatment and to some extent geometry, a scaled model of the safety device was prepared to check performance against values of tensile strength defined in the standards [17].

The geometry and function of the safety device led to the choice of quench and tempered low alloyed steel in grade 42CrMo4 for production. This grade of steel has guaranteed chemical composition while the desired values of mechanical

properties can be obtained by adequate heat treatment. Two different values of hardness were analysed, 42 and 52 HRC, as well as two different cross-sections of safety device, Fig. 2.

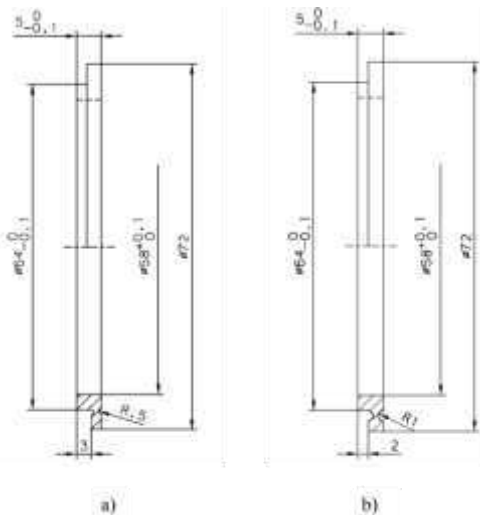


Figure 2

Dimensions of scaled safety devices: a) initial radius at shearing area 0.5 mm,
b) initial radius at shearing area 1.0 mm

Values of tensile strength σ_M , for hardness 42 HRC and 52 HRC, are ≈ 1330 MPa and ≈ 1800 MPa respectively [18-20]. The estimated breaking force is calculated in Table 1, where the ratio (s_f) of limiting shear stress to limiting tensile stress was determined in Ref. [21], and the standard formula for maximum shear stress (VQ/Ib) is used for bending of a rectangular section. Based purely on shear area calculations, therefore, the expected values of breaking force, for two different values of hardness 42 HRC and 52 HRC, are approximately 231 kN and 312 kN respectively. These can be regarded as upper limits, however, with lower limits provided by the bending calculation, i.e., 154 kN and 208 kN respectively. A threshold is set for activation of the energy absorber just above the upper limit.

2.2 Experimental Investigation of the Safety Device

In accordance with the dimensions, defined in Fig. 2, scaled samples were prepared as well as supporting testing tool, Fig. 3a. Samples were made from quench and tempered low alloyed steel in grade 42CrMo4. Three samples were prepared and passed heat treatments. Two samples, manufactured in accordance to dimensions showed in Fig. 2a and Fig. 2b, after heat treatment have a hardness of 42 HRC. One sample was manufactured in accordance to dimensions showed in Fig. 2a with hardness of 52 HRC after heat treatment. Preliminary experimental investigations

were performed on the electro-mechanical testing machine at Institute GOSA that has a maximum load of 250 kN, Fig. 3b. Following experimental investigations, the microstructure of the fractured samples was studied and discussed.

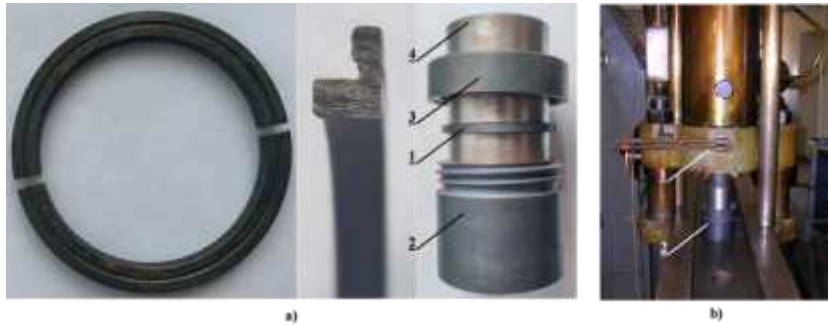


Figure 3

Sample and testing machine: a) Sample of safety device and support tool: 1 - Safety device, 2 – Base of support tool, 3 – Safety nut and 4 – Bushing with circular groove; b) Electro-mechanical testing machine: 1 – Sample ready for test; 2 – Machine head

Table 1

Estimation of breaking force using simple shear and bending shear stress calculations

| Geometry | | | |
|--|------------|------|-----------------|
| Thickness of shearing cross-section | b | 1 | mm |
| Diameter at shearing cross-section | D_s | 65 | mm |
| Area of shearing cross-section = $\pi D_s b$ | A_s | 204 | mm ² |
| 2 nd Moment of area of shearing cross-section (treated as rectangular section) = $\pi D_s b^3 / 12$ | I_s | 17 | mm ⁴ |
| Common Factors | | | |
| Ratio of limiting shear stress to limiting tensile stress i.e., τ_M / σ_M | s_f | 0.85 | |
| Ratio of limiting stress to activation stress (τ_M / τ_r) | s | 0.98 | |
| Grade 42CrMo4: Hardness 42 HRC | | | |
| Tensile strength | σ_M | 1330 | MPa |
| Limiting shear stress = $s_f \sigma_M$ | τ_M | 1130 | MPa |
| Critical load (simple shear) = $\tau_M A_s$ | F_s | 231 | kN |
| Critical load (maximum shear stress from bending) $F_b = F_s / 1.5$ | F_b | 154 | kN |
| Activation load = F_s / s | F_a | 236 | kN |
| Grade 42CrMo4: Hardness 52 HRC | | | |
| Tensile strength [18-20] | σ_M | 1800 | MPa |
| Limiting shear stress = $s_f \sigma_M$ | τ_M | 1530 | MPa |
| Critical load (simple shear) = $\tau_M A_s$ | F_s | 312 | kN |
| Critical load (maximum shear stress from bending) $F_b = F_s / 1.5$ | F_b | 208 | kN |
| Activation load = F_s / s | F_a | 319 | kN |

2.3 Experimental Results

During experiments on the scaled samples, deformation resistance was measured. Recorded load-displacement curves showing the breaking force are shown in Fig. 4a-c.

Experimental and analytical values of breaking force are presented in Table 2. Values of deformation resistance and tensile strength obtained by the experimental test are a close match to the lower limit obtained by analytical calculation. This indicates that bending stresses are critical, which are not included in the shear area calculation. The similarity of results in Fig. 4a and 4b indicates that the difference in notch radius is not hugely significant; as would be expected, the larger notch radius corresponds to a high failure load, but further testing and analysis would be needed to verify this.

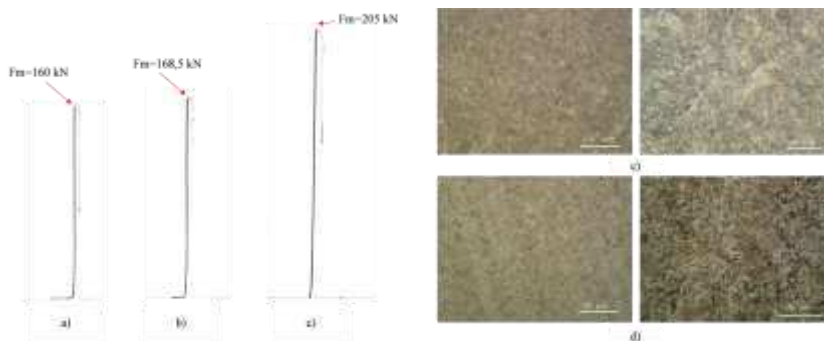


Figure 4

Diagram of breaking force F_m : a) 42 HRC, Fig. 2a; b) 42 HRC, Fig. 2b; c) 52 HRC, Fig. 2a; and Microstructure of braked safety device: c) hardness 42 HRC; d) hardness - 52 HRC

Table 2

Experimental and analytical values of breaking force

| | 42HRC | | 52HRC | |
|---------------------|-------------|------------------|------------|------------------|
| | F_M [kN] | σ_M [MPa] | F_M [kN] | σ_M [MPa] |
| Analytical values | 154 – 231 | 1330 | 208 – 312 | 1800 |
| Experimental values | 160 – 168.5 | 783 | 205 | 1004 |

2.4 Microstructure of Tested Scaled Safety Device

The microstructure of the shearing area was studied using microscope Neofit 30. Fig. 4c,d show the microstructure of the fractured scaled samples.

Both hardness grades show material structures characteristic of typical tempered martensite. After quenching, obtained martensitic microstructure was subjected to tempering. During tempering, chromium based carbides are formed. Depending on tempering temperature, different rate of carbide nucleation and growth of carbides

can be obtained, providing variation in size of particles, as shown in Fig. 4c,d. Therefore, due to variation of carbide size, resistance to deformation is not the same, providing difference in mechanical properties [22, 23].

Based on this, including experimental results and the position of the safety device in the assembly, and the need to function during normal exploitation as well as during collision, hardness 42 HRC is chosen for the safety device. The lower value of hardness is more acceptable for a dynamically loaded design element because a higher value leads to an increase in brittleness and a decrease in toughness.

3 Experimental Research

After analysis of preliminary design and results obtained by tests of scaled safety device, the final design of safety device was prepared and checked via following tests: a) quasi-static test on the hydraulic press and b) dynamic test via collision of two passenger wagons on the industrial railway track at GOSA Rolling Stock Company.

3.1 Determination of Final Design Dimensions

To match the standard buffer, the full scale device requires a shear diameter of 220 mm (compared to 65 mm for the scale device) and a target activation load of 800 kN. Column A in Table 3 indicates that for Grade 42CrMo4 (42 HRC) a thickness of 1.5 mm is appropriate for the shearing cross-section.

Fig. 5a shows the main dimensions of the safety device cross-section. The geometry of the cross-section has been redesigned to provide a clean shear, i.e., breaking of safety device. Manufacture of the safety device is straightforward, but requires high precision. Fig. 5b shows the prototype of a safety device prepared for experimental investigations. After machining by scraping and realised final heat treatment, the safety device cut in two equal parts for assembling in the absorber assembly.

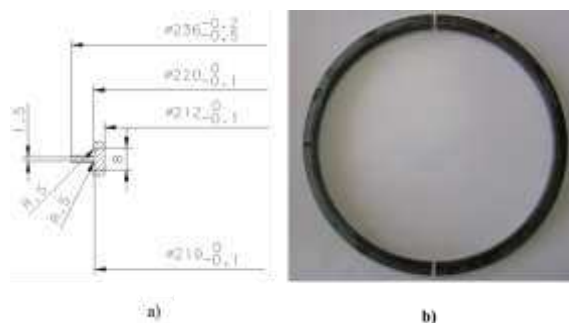


Figure 5

Final design of safety device: a) Dimensions of full scaled safety device; b) Prototype

Table 3

Estimation of breaking force for full scale device with target activation load 800 kN. A: Initial estimate. B: Ratio s adjusted to match experimental results. C: Adjusted thickness to match target.

| Geometry | | A | B | C | |
|--|------------|----------|-------------|------------|-----------------|
| Thickness of shearing cross-section | b | 1.5 | 1.5 | 1.7 | mm |
| Diameter at shearing cross-section | D_s | 220 | 220 | 220 | mm |
| Area of shearing cross-section = $\pi D_s b$ | A_s | 1037 | 1037 | 1175 | mm ² |
| 2 nd Moment of area of shearing cross-section (treated as rectangular section) = $\pi D_s b^3 / 12$ | I_s | 194 | 194 | 283 | mm ⁴ |
| Common Factors | | | | | |
| Ratio of limiting shear stress to limiting tensile stress i.e., τ_M / σ_M | s_f | 0.85 | 0.85 | 0.85 | |
| Ratio of limiting stress to activation stress (τ_M / τ_f) | s | 0.98 | 1.11 | 1.11 | |
| Grade 42CrMo4: Hardness 42 HRC | | | | | |
| Tensile strength [18-20] | σ_M | 1330 | 1330 | 1330 | MPa |
| Limiting shear stress = $s_f \sigma_M$ | τ_M | 1130 | 1130 | 1130 | MPa |
| Critical load (simple shear) = $\tau_M A_s$ | F_s | 1172 | 1172 | 1328 | kN |
| Critical load (maximum shear stress from bending) $F_b = F_s / 1.5$ | F_b | 781 | 781 | 886 | kN |
| Activation load (bending) = F_b / s | F_a | 797 | 704 | 798 | kN |

3.2 Experimental Investigations

The goal of experimental investigations was to check defined geometry of safety device under exactly defined loads as well as the way of deformation of it. Safety device has a role to join standard buffer and absorber and to transfer normal exploitation loads without any permanent deformation. When loads exceed the exactly defined value, comes to controlled break of safety device and absorber starts to work. The following tests were performed: a) quasi-static test on the hydraulic press LITOSTROJ 2500 kN and b) dynamic “crash” test on the open railway track at GOSA Rolling Stock Company, Fig. 6.

During the quasi-static test, reaction force was measured at defined speed of machine head of 50 mm/s. The dynamic test was realized with a wagon speed of 3.4 m/s, while the reaction force and displacement were measured. To get requested way of deformation of safety device, i.e. clean shear, a special tool shown in Fig. 6c was used.

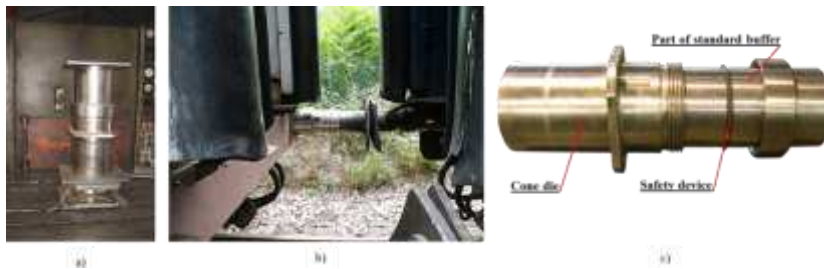


Figure 6

Experimental investigations of prototype: a) Quasi-static test; b) Dynamic - Crash test; c) Test assembly

3.2.1 Results of Experimental Investigations

Figs. 7 and 8 show results obtained by experimental investigations, through force vs. time and force vs. displacement diagrams. Two samples in quasi-static behaviour were tested. Very close values of breaking forces of 824 kN and 843 kN were measured, Fig. 7. Both curves show brittle fracture of safety devices.

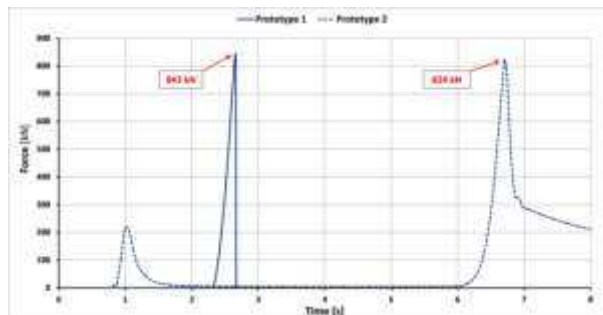


Figure 7

Breaking force of safety device - Quasi-static test

A full collision test of two passenger wagons gave force vs. displacement diagrams that characterize three zones, Fig. 8: the first zone presents work of standard buffer; the second zone presents fracture of safety device and the third zone presents work of absorber. Brittle fracture of safety device can be seen in these diagrams as well. Values of fracture forces measured during the dynamic test are 705 kN and 816 kN, respectively.

Fig. 8b,c shows look of safety device before and after fracture. It can be seen clearly that the safety device is fractured at an exactly designed place (shearing area of width 1.5 mm).

The safety device is designed to transfer a load up to 800 kN without plastic deformation. This means that the normal exploitation load under this value is acceptable and will not lead to the fracture of the safety device.

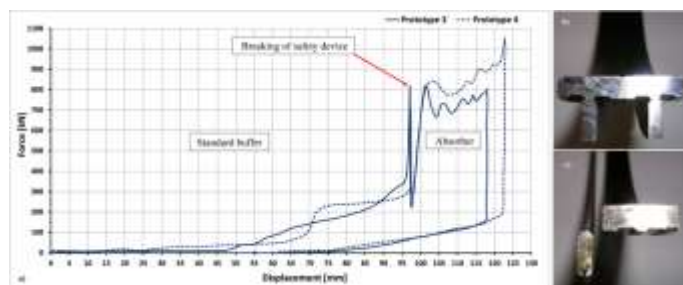


Figure 8

Breaking force of safety device: a) Dynamic crash test, b) Cross section before fracture, c) Cross section after fracture

Results obtained by experimental investigations shown values of fracture force that are slightly higher than 800 kN, which confirms the stability of the safety device and validates the analytical determination of cross-section dimensions of the safety device. The exception represents the fracture force value obtained by the dynamic test of 705 kN, which is assumed to be related to the imperfection of production and inevitable asymmetry of collision contacts. The maximal deviation of the value of fracture force of the safety device is about 5%, which is acceptable and confirms the dimensioning analytical method as appropriate for further dimensioning of different types of safety device as well as similar devices.

The consistency of results across quasi-static and dynamic tests suggests strain rate-dependent effects can be neglected. This is very important from the aspect of working principles of safety devices and dynamic behaviour in exploitation. However, if the outlier result of 705 kN is representative, this would correspond to a lower activation stress and a value of $s = 1.11$ in the calculation (Column B in Table 3). To prevent premature activation, a thicker cross-section width of 1.7 mm would be advisable (Column C in Table 3).

There are further questions that need to be addressed in future research, in particular the fatigue response of the safety devices to normal operating loads, and the likelihood of crack initiation at the free ends of the split ring.

Conclusions

The development of the passive safety elements is a very challenging and complex job that requires precise design and manufacture, careful choice of materials and properties, as well as mounting in a new or current bearing wagon structure. One of the most important design steps is the correct design of the connection between active and passive elements. This paper has presented in detail the design of a sacrificial component that has a role to be fractured at a defined load and thus to redirect the load path away from the energy absorber until an impact event.

The precise fracture requires careful choice of material and heat treatment to control mechanical properties. Calculation and testing during the design process are

necessary to get reliable parameters for dimensioning of elements. Experimental results show that values of tensile strength of quench and tempered low alloyed steel in grade 42CrMo4 obtained by standard tensile tests and experimental tests of scaled samples of safety device have a close match to bending failure predictions.

A full-scale safety device was designed and tested in quasi-static and dynamic experimental investigations. Generally close and consistent results indicate strain-rate dependence is not a major factor, which suggests sufficiently ductile material, despite evidence of brittle fracture. Some further research is necessary to determine suitable safety factors and to study fatigue response in normal operation, but the experimental results presented here provide partial validation of the design methodology for the proposed safety device.

Acknowledgement

This work was supported by the Ministry of Education, Science and Technological Development of Republic of Serbia, Project No. 451-03-9/2021-14/200105 and 451-03-9/2021-14/200107.

References

- [1] EN 15227:2008; Railway applications - Crashworthiness requirements for railway vehicle body
- [2] EN 12663-1:2015; Railway applications - Structural requirements of railway vehicle bodies - Part 1: Locomotives and passenger rolling stock (and alternative method for freight wagons)
- [3] Guangjun G., Weiyuan G., Jian L., Haipeng D., Xiang Z., Wei C., Experimental investigation of an active-passive integration energy absorber for railway vehicles, *Thin-Walled Structures*, Vol. 117, pp. 89-97, 2017
- [4] Weiyuan G., Guangjun G., Jian L., Yao Y., Crushing analysis and multi-objective optimization of a cutting aluminium tube absorber for railway vehicles under quasi-static loading, *Thin-Walled Structures*, Vol. 123, pp. 395-408, 2018
- [5] Junyan W., Zhajun L., Mu Z., Tianjun W., Chengming S., Haihong L., Coupled thermal-structural analysis and multi-objective optimization of a cutting-type energy-absorbing structure for subway vehicles, *Thin-Walled Structures*, Vol. 141, pp. 360-373, 2019
- [6] Moreno C., Winnett J., Williams T., On the effect of anisotropy on the performance and simulation of shrinking tubes used as energy absorbers for railway vehicles, *Thin-Walled Structures*, Vol. 161, <https://doi.org/10.1016/j.tws.2021.107513>, 2021
- [7] Jian L., Guangjun G., Haipeng D., Crushing analysis and multi-objective optimization of a railway vehicle driver's cab, *Thin-Walled Structures*, Vol. 107, pp. 554-563, 2016

-
- [8] Tanasković J., Milković D., Lučanin V., Miloradović N., Experimental and numerical analysis of the characteristics of combined collision energy absorber, *Facta Universitatis, Series: Mechanical Engineering*, Vol. 10, No. 2, pp. 125-136, 2012
- [9] Hosseini A., Hosseini Tehrani P., Study on new crashworthy buffers in railway, *International Journal of Railway Research*, Vol. 1, No. 2, pp. 59-73, 2014
- [10] Tanaskovic J., Milkovic D., Lucanin V., Vasic Franklin G., Experimental investigations of the shrinking–splitting tube collision energy absorber, *Thin-Walled Structures*, Vol. 86, pp. 142-147, 2015
- [11] Tanasković J., Franklin F., Dišić A., Mišković Ž., Numerical validation of the combined extrusion-splitting process of energy absorption through experimental study, *Exp Tech*, Vol. 41, pp. 421-431, 2017
- [12] Tanasković J., Franklin F., Mitrović A., Dišić A., Experimental research of absorption properties of rigid foam filled circular seamless tube energy absorber under quasi-static axial load, *Proc IMechE Part F: J Rail and Rapid Transit*, <http://dx.doi.org/10.1177/0954409720976034>
- [13] Harouz R., Lakehal A., Khelil K., Dedry O., Hashemi N., Boudebane S., Dry siliding friction and wear of the WC/TiC-CO in contact with Al₂O₃ for two sliding speeds, *Facta Universitatis, Series: Mechanical Engineering*, 2020, <https://doi.org/10.22190/FUME200310039H>
- [14] Shilko V. E., Grigoriev S. A., Yu. Smolin Yu. A., A discrete element formalism for modelling wear particle formation in contact between sliding metals, *Facta Universitatis, Series: Mechanical Engineering*, Vol. 19, No. 1, pp. 7-22, 2021
- [15] A. Németh, S. Fischer, Investigation of the glued insulated rail joints applied to CWR track, *Facta Universitatis, Series: Mechanical Engineering*, 2021, doi: 10.22190/FUME210331040N
- [16] M. Sysyn, O. Nabochenko, V. Kovalchuk, M. Przybyłowicz, S. Fischer, Investigation of interlocking effect of crushed stone ballast during dynamic loading. *Reports in Mechanical Engineering*, Vol. 2, No. 1, pp. 65-76, 2021, <https://doi.org/10.31181/rme200102065s>
- [17] DIN EN 10083-3:2007; Steels for quenching and tempering – Part 3: Technical delivery conditions for alloy steels
- [18] Kraut B., *Mechanical engineering manual*, Technical book, Croatia, Zagreb, 1976 (in Serbian-Croatian)
- [19] EN 10132-3:2000; Cold rolled narrow steel strip for heat treatment – Technical delivery conditions - Part 3: Steels for quenching and tempering
- [20] Szala M., Winiarski G., Wójcik L., Bulzak T., Effect of Annealing Time and Temperature Parameters on the Microstructure, Hardness, and Strain-

Hardening Coefficients of 42CrMo4 Steel, Materials, 13(9), 2022,
<http://dx.doi.org/10.3390/ma13092022>

- [21] Veriga S., Mechanical elements 1 - First book General part, University of Belgrade Faculty of Mechanical Engineering, Belgrade, 1990
- [22] Smallman R. E., Bishop J., Modern Physical Metallurgy and Materials Engineering, Science, process, applications, Sixth Edition Butterworth-Heinemann, Oxford, 1999
- [23] Dieter G. E. Mechanical Metallurgy. SI Metric Edition, Mc Graw-Hill Book Co., New York, 1988

Designing a Petri Net Model to Organize the Transport of Goods in the European Rail Chain

Nermin Čabrić ¹, Ratko Đuričić ², Vladimir Malčić ²,
Željko Stević ²

¹ University of Sarajevo, Faculty of Transport and Communications, Zmaja od Bosne 8, 71000 Sarajevo, Bosnia and Herzegovina;
nermin.cabric@fsk.unsa.ba

² University of East Sarajevo, Faculty of Transport and Traffic Engineering Dobož, Vojvode Mišića 52, 74000 Dobož, Bosnia and Herzegovina;
ratko.djuricic@sf.ues.rs.ba, vladimir.malcic@sf.ues.rs.ba,
zeljko.stevic@sf.ues.rs.ba

Abstract: A new railway concept where there is more than one company participating in the transportation chain, Lead Railway Undertaking – LRU, should be in charge of managing and controlling the transportation chain. Using a timed Petri net – TPN, a model of organizing European railway transport will be introduced as a system with discreet events whose state depends on the occurrence of discreet events from the moment of ordering the transportation until the moment of delivering the goods to the client. The tracking of wagons/goods is presented with a token that moves through a designed petri organization model. With the example of a possibility of shortening the estimated time of the wagon retention in stations by shortening the time of commercial checkups of goods, the PN model portrays a strong diagram of all the operations that include wagons, as well as the processes that occur parallel and in sync all along the railway chain.

Keywords: TSI TAF; Petri net; European railway; ITUs

1 Introduction

An intelligent technological information system enables continuity in cross-border data transmission. Data transmissions through the European Railway System is the key element to assure the quality service provision in the international railway. Today, railway companies of all sizes face the need for control and integration of operative information. The most thriving technology for operative information control is creating a mass net of all the participating parties in the transportation chain from the user to the supplier of the transportation service. The network infrastructure is developed on a global level, and it allows the connection of physical

and virtual devices using interoperable communication protocols and intelligent interfaces. In order to achieve an economically acceptable, reliable and safe process, an efficient operative data transmission is implemented using an established technical frame through the technical specification of interoperability, which refers to the element of a “loaded traffic application” of the subsystem of a “telematics application”, and belongs to the functional area of Appendix II of the Directive (EU) 2017/797 (Technical Specification for Interoperability relating to Telematics Applications for Freight Services – TSI TAF). The main goal of this research is organizing the transport of goods in the European railway chain using Petri nets. The created model enables the leading railway carrier to provide the user of railway transportation all of the necessary information, especially: route information; Information about train schedule for arranged points of reporting, including starting point, point of exchange/handover and destination of arranged transport; Predicted time of arrival to final destination, rated stations and intermodal terminals; Traffic interruptions (when the leading railway carrier learns of traffic interruption, it timely informs the service user). The aims and contributions can be manifested through the following. The developed model allows the leading railway carrier the following: To be more efficient in defining a transportation service by stating the price of service and time needed for its implementation, as well as determining the availability of wagons depending on a type of goods that is to be transported; To have precise and timely information about the position on the railway network and predicted arrival of wagons and intermodal freight units, as well as place of loading of empty wagons; To deliver a complete service in a reliable and consistent manner by using common business processes and related information systems to all interested parties (infrastructure managers, service users, customs, etc.) who must have computers for data exchange; To assess the quality of implemented service based on defined values. A primary motive for writing this paper is a current insufficient correlation between all participants in a railway transport supply chain, especially between the railway carrier, infrastructure manager and users of transportation service. This paper also contributes to better wagon management.

2 Related Papers

The Petri Net (PN) model is used in different fields. Harifi et Nakjavanlo [1] use PN as a support system for directing and managing police cars. Cavone et al. [2] have used PN for intelligent, safe and ecologically acceptable management of transport systems by using intelligent transport systems that combine innovative technologies and transportation frames with a goal of finding appropriate solutions for all transportation problems. While providing a service “Car-sharing”, Clemente et al. [3], contrary to the prevailing approach, propose a methodology for determining an optimal threshold that explicitly considers stochastic buyer reactions on stimulating the use of such service. It is presented a support system for deciding

on solving problems of relocating vehicles based on an economic incentive of the service user. Fanti and Ukovich [4] have examined the existence of great need for integrating and coordination of previously autonomous elements and systems in order to reach a mutual goal that otherwise is not achievable. It has been formalized a structural and combined frame for support of decision makers through the implementation of integrated systems of larger scale that are heterogeneous and work independently, but are networked together for the sake of achieving a mutual goal. Sohag and Yiannis [5], in their paper, present a summary of Bayes nets (BN) and PN application in an analysis of system security, assessment of reliability and risk. This paper emphasizes a potential use of approaches based on BN and PN in relation to other classical approaches, and their relative strength and weaknesses in different practical application scenarios. The paper [6] presents a general approach to modeling intermodal terminals in a chain of goods transportation. The model presented allows the assessment of operational performances of intermodal transport system, assessment of efficiency level of intermodal terminal and identification of “bottle-neck” based on appropriate system performance indicators. This model is done by implementation of Timed Petri Nets (TPN) where places are resources, capacities or conditions while crossings represent flow and activities in the terminal. Tokens represent intermodal freight units or means for transporting freight units. Transport of goods is converted from one form to intermodal transport where goods are loaded into an intermodal freight unit, which allows a more flexible, reliable and sustainable transportation service. Besides modeling an intermodal transport system, PN are a great tool for analyzing logistic systems [7]. Even though it is not possible to show operation complexity in an intermodal transportation chain, their graphic aspects provide certain advantages for graphic presentations and model inspections. In [8], it is proposed a procedure of meta-modeling that gives a reference model used by decision makers while assessing performances of intermodal transport network. In order to obtain a generic model that describes a non-specific, from the point of its structure and behavior, intermodal transport network, it is used a Meta approach, actually, modeling from top to bottom and procedures of modeling. The model is presented in a standard language for a visual presentation, Unified Modelling Language – UML, that uses a graphic and textual method of presenting structural and dynamic system behavior. Kabashkin [9] has developed the Decision Support System (DSS) for the selection of alternative directions in a large traffic system that includes a heuristic approach and integration of simulation. The practical implementation of DSS simulation based on the PN model has been proposed. In their paper, Bao et al. [10] propose a hybrid ELM-PS method for predicting train delays that not only gives enough time to make additional decisions but it also has practical importance for improvement of information quality delivered to railway workers and assistance for passengers in estimation of travel time duration. Khakdaman et al. [11], in their paper, have explored the readiness of sender to delegate the selection of transportation mode by using an analysis of discrete transport. The results show that, under certain conditions, most of senders are willing to authorize the selection of transportation

to the service provider. Cooperation and connection of all participants in transportation of goods by railway network is very important and it is established through a TSI TAF platform. Our work through the application of PN has found efficient solutions for directing railway wagons to loading places, actually it efficiently and operatively manages carts. The importance of this cooperation in the ever-growing market of road transportation has been presented in paper [12]. The main challenge of PN use is reasonable model construction that demands certain skills. More and more, it is used for security, reliability and risk assessment in the system. TSI TAF as a functional sub-system of railway network directly affects the reliability of railway system and therefore, indirectly, its safety.

3 TAF TSI Description and Characteristics

TSI TAF sets mandatory functional and technical specifications for data exchange in a harmonized format between Infrastructure Managers (IMs), railway Undertakings (RUs) and other participants. For creating a chain of trains, it is necessary that RU has data about: Limitations of railway infrastructure; Technical data on wagons (Rolling Stock Reference Database – RSRD); Dangerous goods – RID materials that are found in a reference database; Updated wagon information status; Operational database implemented by RUs, IMs, Wagon Keepers and users of transportation services. Besides data exchange, TSI TAF describes an operational process that involves IMs and RUs. Therefore, TSI TAF has a great impact on existing business processes of railway infrastructure. TSI TAF, or at least an information interface with other partners, must be implemented in a similar way by all users of TSI TAF, including IMs and RUs. TSI TAF functions define data processing in regard to following variables: When (at what moment)? What (which information and content) should be sent? Who (partner or partners)? How (in which format) data must be exchanged? The purpose of TSI TAF is to ensure an efficient data exchange by determining technical frameworks in order to maintain a process of transportation in an acceptable price range. It encompasses applications in providing transportation services of railway undertakings in freight transportation and management of connections/chains with other forms of transportation in a continuous intermodal transportation chain. TSI TAF has an influence on conditions under which users use railway transport.

3.1 Architecture of Data Exchange

Data exchange is done through “Peer to Peer - P2P”. This is the model of data exchange where every entity of network is a client and a server. In informatics, it means a concept of networking computers without a server, where every computer is an intelligent work station that finds other computers over an Ethernet package as the most commonly used technology for local networks and it communicates

with them directly, without needed authorization on a central server. Communication P2P through IP networks between IMs and RUs, as well as with other users through a central database and individual databases, is established with a common interface (CI). The architecture of data exchange is developed in such a way that databases of wagon keepers (WK), RUs, IMs, station managers (SM), rolling stocks and users of transportation services are mutually connected through communication processes and protocols. The intelligent railway system can be defined as a modern city that functions in an intelligent and sustainable way in order to ensure its sustainability and efficiency. This goal can be reached by integrating diverse infrastructure and services into joint units, so the intelligent devices can monitor and control them.

3.2 TSI TAF Process

The process of planning begins with loading the wagons, maneuvering and setting up the loaded wagons on the tracks ready for shipment. If the railway chain includes more than one carrier in railway traffic, then that becomes the leading railway carrier (Lead Railway Undertaking - LRU) which is accountable to organize and control the transport line. The user sends a bill of lading to the leading railway carrier. The bill of lading must contain all of the needed data about the transport of goods (Contract of International Carriage of Goods by Rail – CIM), unique rules of the contract for the usage of carriages in international railway traffic (Uniform Rules concerning Contracts of Use of Vehicles in International Rail Traffic – CUV) and valid national rules. According to the contract, LRU provides the user of the transportation services information about: The route; The movement of trains on pre-set locations on the wagon trip plan, including at least the beginning point, the trade/handover point and the endpoint of the contracted transport; Estimated Time of Arrival (ETA) to the end destination, including shunting stations and intermodal terminals. In freight transport, the work of LRU considering shipments begins when the user gets the bill of lading. Every railway undertaker (RU/LRU), which participates in the transport is obligated, based on the contract with IM, to insure the train route and control the movement of the train on its section of the trip. Train routes can be either bigger already reserved routes or an ad hoc train route can be requested from IM. Based on data transmission between IMs and RUs the departure time or arrival time of a wagon to a specific location or if it in a transport chain the responsibility moved from one RU to the other. The TSI TAF process consists of a planning phase as well as an operative (executive) phase. The operative phase of the organization process of European railway transport begins with forming a train composition that is a wagon placement in the train structure according to the referral order provided by the train forming plan. Using the train forming plan, wagon flows are being organized in single-group or multi-group freight trains. Single-group trains do not need any kind of changes to their composition on the whole traffic route. Multi-group trains are formed by two or more groups of wagons which are all arranged for themselves according to the stations they are headed.

4 Petri Net Design

Petri Nets (PN) portray an immediate and strong diagram of all needed operations, shared resources as well as processes which are taking a place in a parallel manner and in synchronization. PN as a graphical-mathematical tool is suitable for modeling and shaping various types of dynamical, discreet and distributive systems. The changes occur in a limited number of steps in an observed time space; A distributive system consists of a certain amount of autonomous subsystems, which are inter-twined and share resources when performing some specific tasks. Those subsystems are often physically arranged. TPN is used for the evaluation of system performances, and Colored Petri Nets (CPN) [13] are useful for modeling complex systems which perform a few different tasks because they allow the use of more mutually different tokens. Models with discreet events are often used to describe decision making and operative processes in logistical systems [14]. Even if PN are not able to portray in detail the complexity of planning phase and executive phase in the system of organization of the European railway transport, the use of TSI TAF as simulation tools have certain advantages. Their graphical aspect enables them to concisely and effectively project (design) and check the model, while the mathematical presentation enables a simple simulation which takes into consideration dynamic conditions and changes in the system, like the movement of shipment, i.e. the movement of wagons or Intermodal transport units – ITU from the place of loading to the end destination. In this section, a frame of PN organization of the transport of goods in the European railway chain of traffic is recommended. In the recommended frame, places represent resources and capacities or conditions and activities on the terminal, and tokens are ITUs or means of transportation of ITUs. The recommended frame of PN organization of the transport of goods in the European railway chain of traffic uses a modular approach and it is made of submodules. The main submodules which make the recommended frame of PN organization of the transport of goods is: unloading the train; coming and going of ITUs; realization of train route request function; realization of train preparation function; realization of train ride functions.

4.1 Functions of Reference Files

IMs, RUs, logistic service providers and rolling stock managers must have access to assortment of reference files: types of dangerous goods, IM, RU and service provider codes; codes of transport service user, so the freight trains on the European railway net can be exploited. Databases which will implement RUs, IMs, wagon owners or clients are: RSRD - Rolling Stock Reference Databases; WIMO – Wagon and Intermodal Operational Unit Database; Train Route Database; Reference files which are: Kept and administrated centrally (Coding for all IMs, RUs, service providing companies; Coding clients for freight transport); Kept and administrated locally (reference files of emergency services, connected with dangerous goods data). Data found in reference files and databases must represent the real state in

any moment. In order to enable tracking of moving trains and wagons, data in operative databases for wagons and intermodal units must be updated at every relevant event in real-time.

4.2 Realization of the Train Path Request Function

Train routes define wanted, accepted and real data which need to be stored in databases. Routes determine exploitation and technical train characteristics for every section of the route. Based on the train list, IM has information about the real composition. RU must deliver IM all of the needed data about when and where the train must ride as well as technical characteristics to the extent in which they are connected with the railway infrastructure. If more RUs participate in transport, then it is selected an LRU that will communicate with IM. The Route requested by LRU can be accepted or declined by IM. In the case of declining the route request, IM gives details about the reasons of declining the route which are updated. If the request is accepted, then IM gives LRU details about the train route. When LRU confirms the IM train route, it goes into the next submodel and realization of train preparation function phase. The submodel "Realization of the Train Path Request Function" of the proposed PN design framework for the organization of the transport of goods in the European railway chain is given in Figure 1.

4.3 Realization of the Train Preparation Function

In order for the LRU/RU to give the notice to IM about the train composition, it is necessary that it possesses data about: Infrastructure limitations; Technical data about wagons (RSRD database); Data from the RID reference file; Updating wagon status (WIMO). Train preparations begin with an IM notice about the LRU train composition. In preparation phase, checkups are done in certain databases containing infrastructure limitations, technical and exploitation characteristics of wagons and intermodal freight units. After all, an LRU checkup notice is sent to IM that the train is ready to go. The submodel "Train Preparation Function" of the proposed PN design framework for the organization of the transport of goods in the European railway chain is given in Figure 1.

4.4 Realization of the Train Running Function

With the arrival of the composition on the shipping track, a dialogue is started between IM and RU to insure the exchange of data about the train and its estimated time of travel on the net. IM gives RU and the neighboring IM information regarding the estimated time of departure and the time of arrival to the location of transition to the net of the next IM.

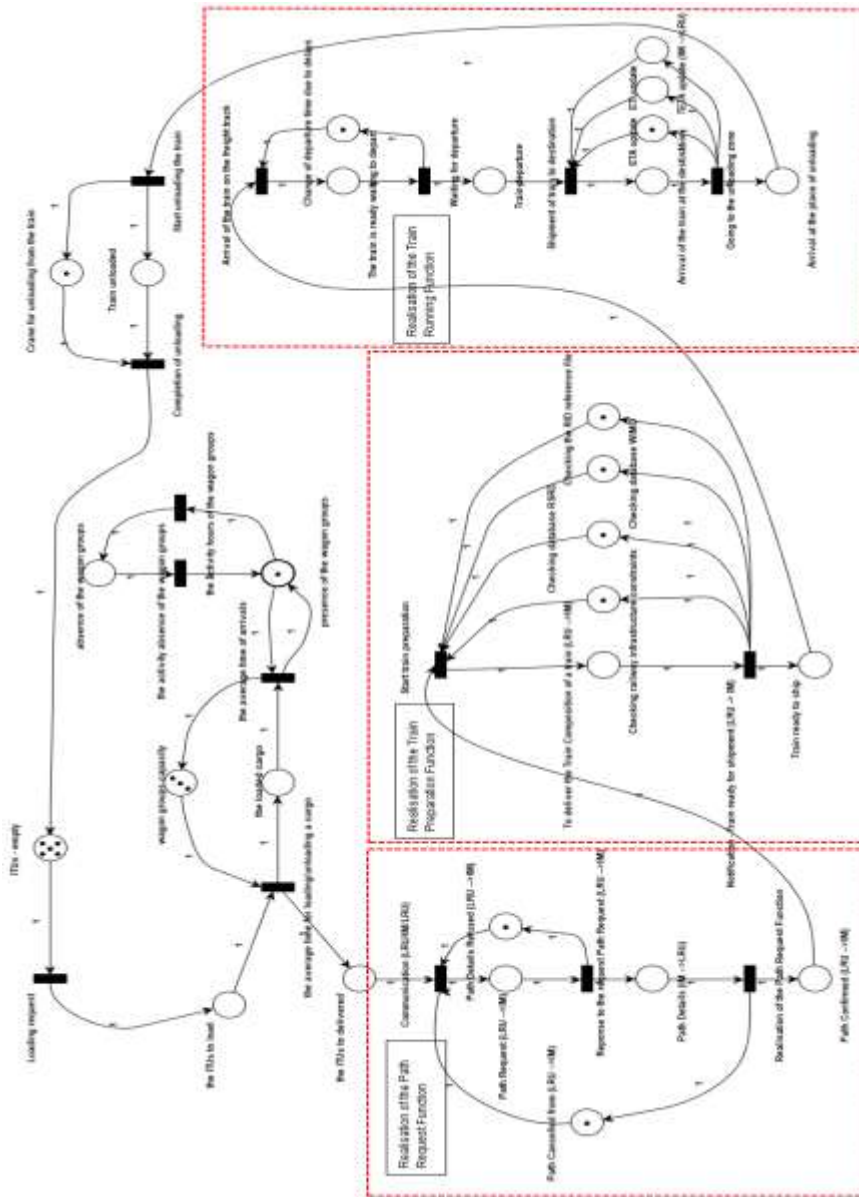


Figure 1

PN design model of the organization of goods transport in the European railway transport chain

Data considering train traffic enables the estimated times of arrival on the observed points agreed upon in the contract of transport, and therefore the relative position of train during the trip to be known. In the contract, the locations of train running briefing are determined. This data exchange happens between IM and the RU which

reserved the route the train rides on. The individual supervision of wagons and intermodal freight units is performed in the communication between RUs which participate in the transport chain and LRU. According to the contractual agreement, LRU will insure the user with the ETA – Estimated Time of Arrival and ETI – Estimated Time of Interchange of wagons from one RU to another on the shipment level. For intermodal freight units which are loaded on the wagons, the ETI of the wagon is also the ETI of the intermodal freight unit. In terms of ETA of intermodal freight units, RU cannot calculate the ETA for different types of transport which participate in the continuous transport chain except the railway part. RU can only deliver to the user of the transport service the ETI of the exchange of intermodal freight units in intermodal terminals where they change the means of transport. The submodel "Train Running Function" of the proposed PN design framework for the organization of the transport of goods in the European railway chain is given in Figure 1.

5 Simulation

In the PN model of organization of transport of goods in the European railway traffic chain, we can model the influence of time needed for data exchange, process and protocols that unwinds through databases which are implemented by RUs, IMs, Wagon Keepers and users of transport services at the time of the delivery of intermodal freight unit t to the end user. Reliable and good quality information shortens the time needed for the technical-commercial checkup of the train which shortens the retention time as well as an earlier time of arrival to the end destination. After the arrival of the train at the end destination, a commercial shipment checkup is done, the receiver is briefed about the shipment delivery and the train is set on a specific place to unload. The receiver is briefed by means of TSI TAF directly about the movement and delivery of shipment.

5.1 Software Tools for Performance Evaluation

For the simulation model of a fictive supply chain problem, the software tool TimeNET 4.3. was used and thereat two new types of tokens were defined. A "Workpiece" token type represents parts, which need to be transported in containers and the "Container" token represents an empty container, which is returned to the receiver to reload after delivery and unloading. The main model contains two submodels "TransportToPlan" and "TransportToSupplier". In examples of stochastic CPN done by the TimeNet software, there is an example of a chain of supply between the supplier and user and the transport takes place on the railway. For the analysis of the influence of time needed for a commercial-technical checkup at the time of inactivity of the factory, in the existing TimeNet supply chain model, an "Inspection" submodel is included (Figure 2).

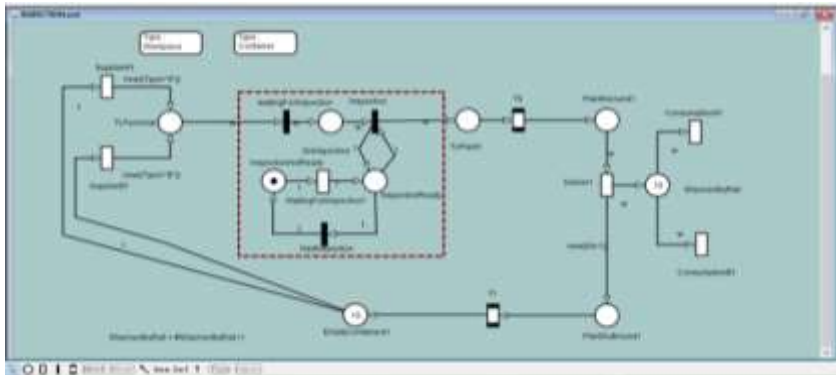


Figure 2

A supply chain model with a commercial vehicle checkup submodel

In the submodel in Figure 2 in the “OnInspection” point, the intermodal freight unit receives its commercial-technical checkup and the needed time is modeled with a transition spot “WaitingForInspection” where we can see the influence of time in a period of factory inactivity by changing the checkup retention time length. ShipmentByRail parameters which define a system of intermodal transport supply chain in the TimeNet software for the submodel of commercial checkups aside from the already given ones for the “Supply Chain” example are as follows:

| Places | | Tokens | | |
|-----------------------|-----------------|---------------|---|-----------|
| Place name | Token type | Token type | Attribute | Data type |
| OnInspection | Workpieces | Workpiece | Type | string |
| InspectionNotReady | integer | Container | N | integer |
| InspectionReady | integer | | | |
| Transition | | | | |
| Transition name | Transition type | Time function | | |
| Inspection | immediate | | | |
| WaitingForInspection | immediate | | | |
| WaitingForInspection1 | timed | Det(0.90) | | |
| NextInspection | immediate | | #OnInspection==0 && #ToTerminal1==1 (glob.) | |

Changing certain parameters like: container retention time on a commercial-technical checkup, train departure timetable or the number of empty containers, we can simulate the influence of the commercial-technical checkup on the total delivery time in the supply chain. In the existing model of the supply chain made with the use of PN with the TimeNET software, if we execute the commercial-technical checkup using the “Inspection” submodel, we can analyze the influence of the time needed for the commercial-technical checkup on the time where the “ShipmentByRail” does not have a token which represents the delivered goods.

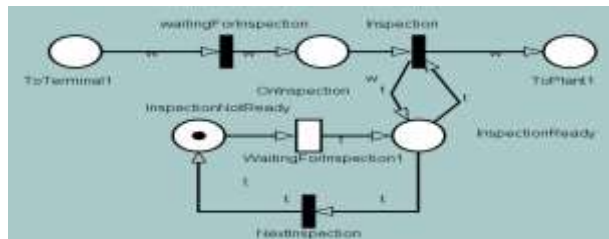


Figure 3

Submodel of a commercial train checkup in a supply chain

5.2 Results and Discussion

Simulations done in the TimeNET software for a hypothetical example of a supply chain show that the average time when the “ShipmentByRail” does not have a token, measured with the expression $(\#ShipmentByRail < 1)$, can be reduced in the following ways: Shortening the interval of freight containers shipments by train, Shortening the time of commercial-technical checkup execution. Shortening the interval of shipment of loaded containers by train influences a change of the predefined train timetable, but shipment is possible through ad hoc routes, which has been found to be a very expensive option, so shortening the time needed for commercial-technical checkup is the remaining option. Assume that the manufacturer and the consumer improve their work processes and that the manufacturer of goods needs empty containers returned as quickly as possible for a new loading and that the consumer needs a more frequent shipment delivery. This can be achieved by shortening the container trading time. Applying the PN software “TimeNET”, first of all, we model the case where the time of the presence of the “OnInspection” token, which represents the time length of the commercial-technical checkup, amounts to one hour and that is the case where there is an electronic bill of lading and TSI TAF is not implemented with the following parameters: The number of containers, $C=10$; Crossing time interval “WaitingForInspection”, $T_{inspection}=1$ hour: Crossing time interval “WaitingForTrain”, $T=100$ hours.

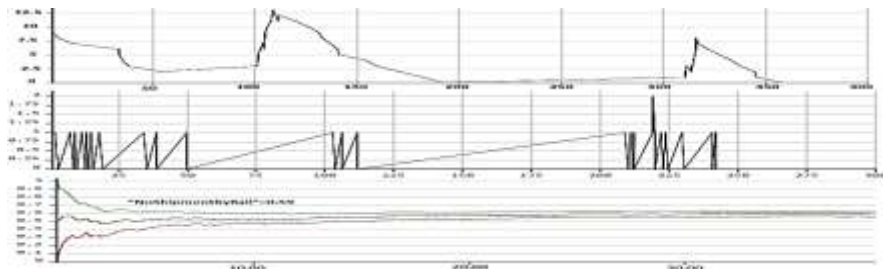


Figure 4

Company inactivity for $C=10$, $T_{inspection}=1$ hour, $T=100$ hours (case example)

Figure 4 is a graph of results in positions “ShipmentbyRail” and “OnInspection” and also as an average time value of “NoShipmentbyRail”=0.59 when in position “ShipmentbyRail” there were no tokens, actually, when wagons from containers did not come and there were no delivery of goods. As an enhanced system, we are modeling the case when token time spent in position “OnInspection” that represents the time of commercial-technical checkup is 0.17 hours, actually when it is in use an electronic shipment document, and TSI TAF is implemented with the following values: Number of containers, $C=10$; Time interval “WaitingforInspection”, $T_{inspection}=0.17$ hours; Time interval “WaitingforTrain”, $T=100$ hours.

Figure 5 represents a graph for given values and it shows the results for tokens being in positions of “ShipmentbyRail” and “OnInspection” as an average value of time “NoShipmentbyRail”=0.55 when in position of “ShipmentbyRail” there was no token.

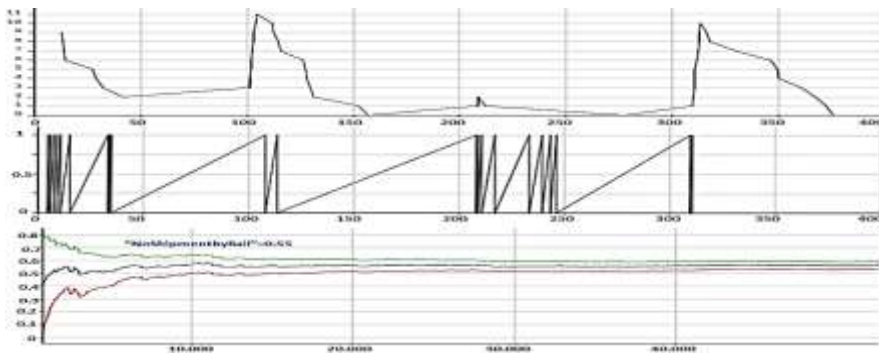


Figure 5

Inactivity of company for $C=10, T_{inspection}=0,17$ hours, $T=100$ hours (case example)

Both graphs show periods when there are no railway container deliveries to the private railway tracks of private transport service users and when the manufacturer has no goods for production, which can create time periods when company does not operate. Possible solutions for improvement are shortening a time interval of train commuting, shortening switching wagons time and shortening the time of commercial-technical checkup execution. Simulations done in the program TimeNET for a supply chain shows that average time when there is no railway cart container delivery, actually average time of company inactivity measured by token ($\#ShipmentbyRail < 1$), can be shortened. Average time when there is no token in position “NoShipmentbyRail”, actually when there is no delivery of goods to the company, can be decreased from the value of “NoShipmentbyRail”=0.59 to “NoShipmentbyRail”=0.55 by efficient data exchange between IMs, RUs, sender receiver and all other participants in a transportation chain. Improvement of financial validity and reliability of transport is contributed by TSI TAF. Bosnia and Herzegovina do not have a liberal market on which international operators can work, so this can be one of the limitations of this study. However, this problem should be solved soon because our country is in a process of market liberalization.

Conclusions

This paper presents the organizational characteristics of transportation of goods in a transportation chain of supply including railway transport. The complex organization of railway transportation in the European railway network and possibility of operational monitoring of the wagons is modeled with Petri nets. The purpose of the model is to describe a discrete system of events as the European railway system of good transportation is. For getting realistic results of the proposed basic model, it is necessary to set realistic railway environment with all data related to wagons and intermodal freight units from the moment of forming a composition to the moment of its arrival to the place of unloading. The proposed model, by using the logic of PN, describes a system of organization and movement of wagons on the European railway network as a system with more discrete events. The communication between RUs and IMs is improved in terms of quality of providing transport services and in terms of accuracy of the estimated arrival time. In this paper, we decided to use PN to acquire a model which would in detail present the system and, from the computer aspect, the diagrams are convenient for tracking the system and measuring its efficiency. The model is modular and can be easily expanded to take into consideration other processes in the continuous intermodal transport chain of supply. The model can also be used for developing the simulation platform for the control of system operations, as well as discovering and preventing dangerous states. With the growing industrial development and population, the role of railways in transportation is going to be crucial in upcoming years [15]. So, in further research, the proposed model should be developed and tested in a real environment

References

- [1] Harifi, S., Nakhjavanlo, B. B., Decision support system based on petri net for a police vehicle command and control system. In Artificial Intelligence and Pattern Recognition (AIPR), International Conference on, pp. 64-69, IEEE, 2016
- [2] Cavone, G., Dotoli, M., Seatzu, C. A Survey on Petri Net Models for Freight Logistics and Transportation Systems. IEEE Transactions on Intelligent Transportation Systems. pp. 1-19, 2017
- [3] Clemente, M., Fanti, M., P., Iacobellis, G., Nolich, M., Ukovich, W., A Decision Support System for User-Based Vehicle Relocation in Car Sharing Systems. IEEE Transactions on Systems, Man, and Cybernetics: Systems. PP. 1-14. 10.1109/TSMC.2017.2665881. 2017
- [4] Fanti, M., P., Ukovich, W., Decision Support Systems and Integrated Platforms: New Approaches for Managing Systems of Systems. IEEE Systems, Man, and Cybernetics Magazine. 3. 18-22, 2017

- [5] Sohag, K., & Yiannis, P., Applications of Bayesian networks and Petri nets in safety, reliability, and risk assessments: A review. *Safety Science*. 115. 154-175, 10.1016/j.ssci.2019.02.009, 2019
- [6] Dotoli, M., Epicoco, N., Falagario, M., Cavone G., A Timed Petri Nets Model for Intermodal Freight Transport Terminals. *IFAC Proceedings Volumes Volume 47, Issue 2, 2014, Pages 176-181, 2014*
- [7] Labadi, K., Chen, H., Modelling, analysis and optimisation of supply chains by using Petri net models: The state-of-the-art. *IJBPSCM*. 2. 188-215, 10.1504/IJBPSCM.2010.036199. 2010
- [8] Boschian, V., Dotoli, M, Fanti, M.P., Iacobellis, G. Ukovich, W., A Metamodelling Approach to the Management of Intermodal Transportation Networks. *IEEE Transactions on Automation Science and Engineering*, Vol. 8, 457-469, ISSN: 1545-5955, 2011
- [9] Kabashkin, I., Heuristic Based Decision Support System for Choice of Alternative Routes in the Large-Scale Transportation Transit System on the Base of Petri Net Model. *Procedia Engineering*. Volume 134, 2016, Pages 359-364, ISSN 1877-7058. 2016
- [10] Bao, X., Li, Y., Li, J., Shi, R., Ding, X., Prediction of Train Arrival Delay Using Hybrid ELM-PSO Approach. *Journal of Advanced Transportation*. 1-15, 10.1155/2021/7763126, 2021
- [11] Khakdaman, M., Rezaei, J., Tavasszy, L. A., Shippers' willingness to delegate modal control in freight transportation, *Transportation Research Part E: Logistics and Transportation Review*, Volume 141, 102027. 2020
- [12] Los, J., Schulte, F., Spaan, M. T. J., Negenborn, R. R., The value of information sharing for platform-based collaborative vehicle routing, *Transportation Research Part E: Logistics and Transportation Review*, Volume 141, 2020, 102011, ISSN 1366-5545. 2020
- [13] Kurt, J., Coloured Petri Nets. a Way to Describe and Analyse Real-World Systems-Without Drowning in Unnecessary Details. 395-401, 1987
- [14] Dotoli, M., Fanti, M. P., Mangini, A. M., Stecco, G. Ukovich, W., The impact of ICT on intermodal transportation systems: a modelling approach by Petri nets. *Control Engineering Practice*, 18 (8), 893-903, 2010
- [15] Banić, M., Miltenović, A., Pavlović, M., & Ćirić, I. (2019) Intelligent machine vision based railway infrastructure inspection and monitoring using UAV. *Facta Universitatis, Series: Mechanical Engineering*, 17(3), 357-364

Train Obstacle Detection System Stabilization and Stochastic Vibrations Analysis Using the Moment Lyapunov Exponent Method

Ivan R. Pavlović, Dušan Stamenković, Vlastimir Nikolić, Aleksandar Miltenović, Nikola Despenić, Marija Stamenković-Atanasov, Goran Janevski

University of Niš, Faculty of Mechanical Engineering
Alesandra Medvedeva 14, 18000 Niš, Serbia;
pivan@masfak.ni.ac.rs, dusan.stamenkovic@masfak.ni.ac.rs,
vlastimir.nikolic@masfak.ni.ac.rs, aleksandar.miltenovic@masfak.ni.ac.rs,
nikola.despenic@masfak.ni.ac.rs, marija.stamenkovic@masfak.ni.ac.rs,
goran.janevski@masfak.ni.ac.rs

Abstract: This paper analyzes stochastic vibrations of a specialised onboard railway obstacle detection system (ODS). The observed system consists of several vision-based sensors mounted in a special housing attached to the locomotive front profile via rubber metal springs and a mounting plate. In this study, the experimental measurements of acceleration were performed in the vertical, longitudinal, and lateral direction for two positions, on the mounting plate rigidly connected to the vehicle body and inside the sensor housing. The ODS stabilization is presented with the results obtained by the moment Lyapunov exponent (MLE) method. Analytical and numerical determination of MLE is firstly presented on a simply supported Euler-Bernoulli beam. Further, the stochastic vibration analysis was performed using the experimentally obtained data. According to these values, the appropriate system parameters essential for the application of the Lyapunov theory to stochastic stability problems were firstly numerically calculated. By means of the Monte Carlo simulation method, whose example was previously shown on a simple beam, the bounds of the almost sure stability of the observed system are given according to the measured accelerations in all of the observed directions.

Keywords: Vibrations; Obstacle Detection; stability; Moment Lyapunov exponent; Monte Carlo simulation

1 Introduction

Railway digitalization and automation has become increasingly important in order to improve its competitiveness and efficiency. For autonomous train movement in GoA3/4 mode of operation it is necessary to detect obstacles in front of the moving train which could lead to collisions. Collisions with obstacles adversely affect train safety, and in most cases trains kill or severely injure any live object they collide with [1]. An obstacle detection system (ODS) is thus a necessary prerequisite for autonomous trains due to high safety requirements of the railway system.

Within the H2020 project SMART [2], an onboard ODS was developed and evaluated. The system combines different vision-based sensors integrated into a housing mounted onto the locomotive front profile. Visual sensors are able to provide very dense and detailed information about the environment. However, in practice their performance depends not just on the ambient lighting and visibility conditions [1], but also on vibrations which are transmitted from the vehicle to the sensors. For instance, edge detector performance in image processing is adversely affected by image distortion induced by vibrations [3]. The image distortion is characterized by the vehicle vibration frequency; the higher the frequency of the vehicle, the more distorted the images [4]. Image stabilization is especially important in autonomous vehicles as the better image acquisition process will increase the feasibility and reliability of the process and the subsequent analysis [5]. In order to prevent the deterioration of image quality due to vibrations, a whole new scientific and engineering area was created, which deals with image stabilization techniques. Image stabilization techniques can be classified into four major categories: optical, digital, electro-mechanical and mechanical stabilization [6]. For mechanical stabilization, the stochastic stability analysis becomes very important to ensure the almost sure stability of the system.

Rail dampers are studied in detail in the works of Kuchak *et al.* [7, 8]. The investigation of the efficiency and influential parameters of a rail damper design based on a lab-scaled model of the rail-damper system and an accurate FE model is presented in [7]. In the author's previous work [8], with the aim to improve the damper model, cone pressure theory is applied in the FE model and the sensitivity analysis is then applied to gradually improve the FE model. Paper [9] deals with the experimental investigation of the interlocking effect of crushed stone ballast material, assessing it as the relationship with the residual and dynamic stresses under the ballast layer. The study of this effect could be potentially useful for many practical problems of railway track design as well as for track maintenance issues.

The modern theory for stochastic stability analysis is based on the Lyapunov exponent (LE) and MLE determination. By using different Lyapunov theories in our previous studies [10, 11], stochastic stability and instability of elastical and viscoelastical systems is analysed for different system parameters. The work of

Arnold et al. [12] presents a small noise expansion of moment Lyapunov exponents for two-dimensional systems. Analytical and numerical determination of LE and MLE was studied in detail for various systems. In [13] using the stochastic averaging method, LE is determined for two elastically connected viscoelastic beams. The regular perturbation method for MLE determination is used in [14] where the LE and MLE of two degrees-of-freedom linear systems subjected to white noise parametric excitation are investigated. The same method is used in [15] where the dynamical behavior of two viscoelastically connected nanobeams under white noise process is analyzed. In the works of Xie [16, 17] MLE is determined for a two-dimensional system under real and bounded noise wideband stochastic processes.

One of the first studies of numerical determination of the moment Lyapunov exponents of stochastic systems using a Monte Carlo simulation approach is presented by Xie in [18]. This method is widely used, and it finds its application in almost every field of study especially when it is very hard or almost impossible to get an analytical expression for MLE. Thus, this method is presented in detail in [19], where stochastic stability of a multi-nanobeam system is analyzed for different types of axial compression on the system ends. In this study, an example of numerical determination of MLE is presented on one simple nanobeam, where numerical results are compared with the analytical ones, with the presented numerical method further using the stability analysis of a higher number of viscoelastically connected nanobeams.

This paper is organized as follows. According to the performed experiment, the essential train acceleration measurements in the vertical, lateral and longitudinal direction are given in Section 2. Section 3 presents the procedure for the analytical and numerical determination of MLE. Using the Euler-Bernoulli beam theory this example is given on an axially compressed simply supported elastic beam. After the verification of the numerical method for MLE determination, this method is further applied for ODS stochastic vibrations analysis (Section 4), where the influence of the viscoelastic medium on the system stabilization is presented. The paper ends with the conclusion section containing the final remarks.

2 Experimental Determination of ODS Vibrations

Within the H2020 project SMART [2], a prototype of the onboard ODS for freight trains was developed. An integrated vision sensor-based onboard ODS for freight trains combines multiple vision sensors integrated into the ODS housing mounted on the locomotive front profile as shown in Figure 1. The ODS housing is mounted on the locomotive front profile to the mounting plate rigidly connected to the locomotive body. The ODS housing is connected to the mounting plate via 4 rubber-metal bushings (Trelleborg M50-40), which passively suppress the vibrations

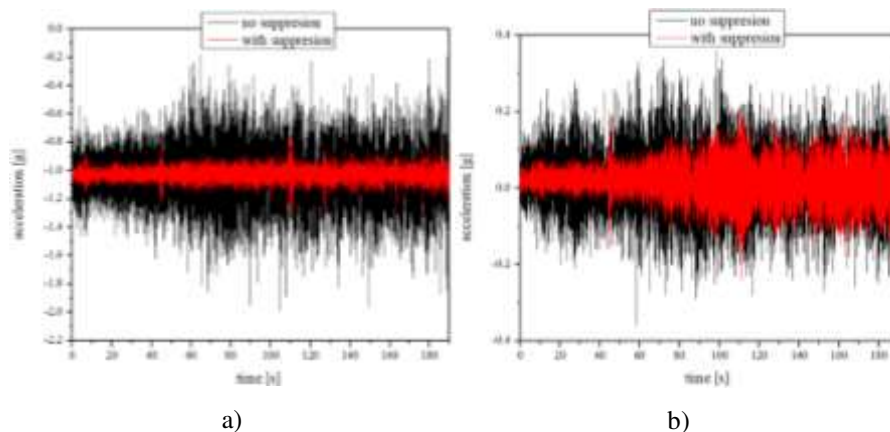
transmitted from the locomotive body to the ODS housing. The design of the housing and the passive vibration suppression system is described in detail in reference [20].

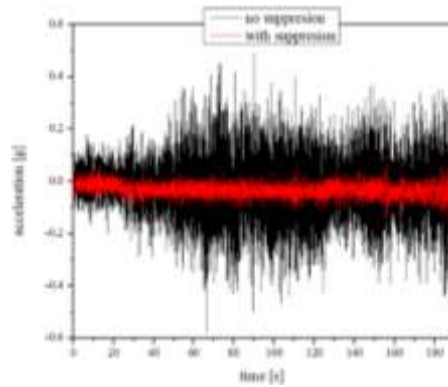


Figure 1

The ODS sensor housing mounted onto the locomotive front profile [1]

The performance of the vibration suppression system was measured during the operational train run at the speed of 80 km/h on a straight portion of the track. The accelerations were measured at two positions - on the mounting plate near the connection point with the rubber metal bushing and in the ODS housing directly above the connection point of the ODS housing with the rubber metal bushing with two triaxial IMUs. The experimental results are shown in Figure 2.





c)

Figure 2

Experimentally determined performance of vibration suppression in three directions: a) vertical, b) lateral, c) longitudinal

3 MLE of a Simply Supported Euler-Bernoulli Beam

For stochastic vibration analysis of the system described in the previous section the MLE numerical determination is suggested. Basic definitions of stochastic stability are the simple or almost sure stability and the stability in the mean of the p -th order, which is based on the concept of the Lyapunov exponent given in Arnold et al. [12]. The almost sure stability is described by the maximal Lyapunov exponent defined as:

$$\lambda_q = \lim_{t \rightarrow \infty} \frac{1}{t} \ln \|q(t; q_0)\| \quad (1)$$

where $q(t; q_0)$ is the solution process of a linear dynamic system. It gives the exponential growth rate of the solution. If $\lambda_q < 0$, then, by definition, $\|q(t; q_0)\|^p \rightarrow 0$ as $t \rightarrow \infty$, the solution is almost surely stable, and $\lambda_q > 0$ implies the instability of the solution in the almost sure sense. The exponential growth rate $E\|q(t; q_0)\|^p$, where E denotes the expectation, is provided by the moment Lyapunov exponent defined as

$$\Lambda_q(p, q_0) = \lim_{t \rightarrow \infty} \frac{1}{t} \ln E \|q(t; q_0)\|^p \quad (2)$$

If $\Lambda_q(p, q_0) < 0$, then by definition, $E\|q(t; q_0)\|^p \rightarrow 0$ as $t \rightarrow \infty$, and those conditions are referred to as the p -th moment stability. MLE provides us with finer stability properties of the random dynamic system.

The example of MLE method is given for the simply supported Euler-Bernoulli beam where the typical beam element is given in Figure 3.

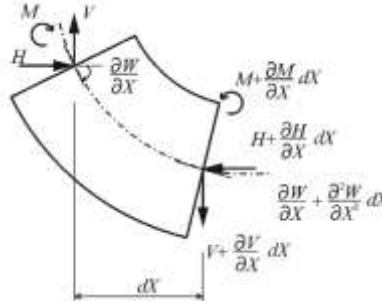


Figure 3

Typical beam element

Following the Euler-Bernoulli method, which is based on a moving field:

$$U = U(X, T) = -Z \frac{\partial W(X, T)}{\partial X}, \quad W = W(X, T) \quad (3)$$

the only deformation different from zero is the dilatation in the X direction:

$$\varepsilon_x = \varepsilon = \frac{\partial U}{\partial X} = -Z \frac{\partial^2 W}{\partial X^2}, \quad (4)$$

Now, according to the beam element from Figure 3 the following dynamical equations can be written:

$$\begin{aligned} m\ddot{a} &= \sum_{i=1}^n \vec{F}_i \Rightarrow \rho A \frac{\partial^2 W}{\partial T^2} + c_1 \frac{\partial W}{\partial T} = \frac{\partial W}{\partial X} - q_1 + q_2, \\ J\ddot{\phi} &= \sum_{i=1}^n \vec{M}_i \Rightarrow \frac{\partial M}{\partial X} - V - H \frac{\partial W}{\partial X} = 0, \end{aligned} \quad (5)$$

where ρ is the mass density, c_1 is the viscous damping coefficient, q_1 and q_2 are the continual loads on the lower and upper side of the beam, and V and H are the components of the main vector of internal forces.

The acting moment from equation (5) is:

$$M = -EI \frac{\partial^2 W}{\partial X^2} \quad (6)$$

A combination of equations (3), (4) and (5) gives:

$$\rho A \frac{\partial^2 W}{\partial T^2} + c \frac{\partial W}{\partial T} + \frac{\partial}{\partial X} \left(\frac{\partial H}{\partial X} \right) + q_1 - q_2 + \frac{\partial^2}{\partial X^2} \left(EI \frac{\partial^2 W}{\partial X^2} \right) = 0, \quad (7)$$

For a time-dependent axially loaded beam with the constant cross-section, $H=F(T)$, the relation (7) becomes:

$$\rho A \frac{\partial^2 W}{\partial T^2} + c \frac{\partial W}{\partial T} + F(T) \frac{\partial^2 W}{\partial X^2} + EI \frac{\partial^4 W}{\partial X^4} = 0, \quad (8)$$

where T is the time, EI presents the beam bending stiffness and $F(T)$ is the time-dependent stochastic process.

Finally, by substituting the following parameters:

$$T = k_t t, \quad W = Lw, \quad X = Lx, \quad k_t = L^2 \sqrt{\frac{\rho A}{EI}},$$

$$2\varepsilon\beta = \frac{ck_t}{\rho A}, \quad \sqrt{\varepsilon} f(t) = \frac{F(t)}{\rho AL^2},$$

in equation (8) the following nondimensional form of the beam is obtained:

$$\frac{\partial^2 w}{\partial t^2} + 2\varepsilon\beta \frac{\partial w}{\partial t} + \sqrt{\varepsilon} f(t) \frac{\partial^2 w}{\partial x^2} + \frac{\partial^4 w}{\partial x^4} = 0, \quad (9)$$

Now, by substituting the solution

$$w = q \sin(\pi x), \quad (10)$$

in (9), the discretized form of the equations of motions of the beam system in the first mode becomes:

$$\ddot{q} + 2\varepsilon\beta \dot{q} + \pi^4 q - \sqrt{\varepsilon} \pi^2 f_1(T) q = 0. \quad (11)$$

In the previous equation, β and ε are the damping coefficient and the small fluctuation parameter, respectively.

Finally, according to [19], the analytical expression for MLE for system (11) is obtained in the following form:

$$\Lambda(p) = \varepsilon \left[\frac{p(3p+10)}{64} \sigma^2 - p\beta \right]. \quad (12)$$

The parameter σ^2 in equation (12) is the intensity of the white noise process.

Now, according to the procedure in our previous papers, MLE is numerically calculated with the aim of comparing it with the results from equation (12).

As presented in reference [19], the system given with equation (11) is simulated 2000 times where the states q and \dot{q} are estimated after each simulation and replaced in equation (2) to obtain a numerical value of MLE. The simulation lasts for 10 s, with the step size being 0.1 s. The numerically obtained results are now used to compare with the results from (12) and presented in Figure 4 with the aim of approving the suggested numerical method for further use.

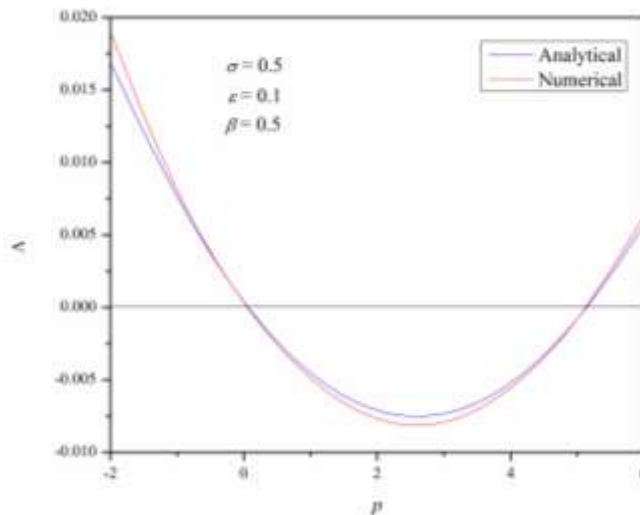


Figure 4

Comparison of analytical and numerical results of MLE for eq. (12)

3 Numerical Results and Discussion

A Monte Carlo simulation numerical method for determining the p -th MLE of stochastic systems is now applied to the obtained experimental results. This method is very useful in the cases when it is very hard or impossible to obtain an analytical expression for MLE.

According to the performed experiment, the averaged measured accelerations and their standard deviations in the vertical, longitudinal, and lateral direction are used to obtain the parameters important for the numerical determination of MLE given by expression (2). According to the Monte Carlo simulation method and using the MATLAB software these parameters were determined for 2000 calculated and integrated values in the range of the standard acceleration deviations, where 2000 different norms in equation (2) were calculated with the aim of numerically obtaining MLE for the analyzed system.

Firstly, stability analysis is given for stochastic vibrations in the vertical direction. This analysis is the most important in the study of the system stability because of the largest system vibrations which occur in this direction. According to the available experiment dataset, the results in this direction are firstly separated in seven points as the train velocity grows from 20 km/h (point-I) to 80 km/h (point-VII) and presented in Figure 5. This figure presents the averaged accelerations and their standard deviations calculated for both observed cases (with and without suppression).

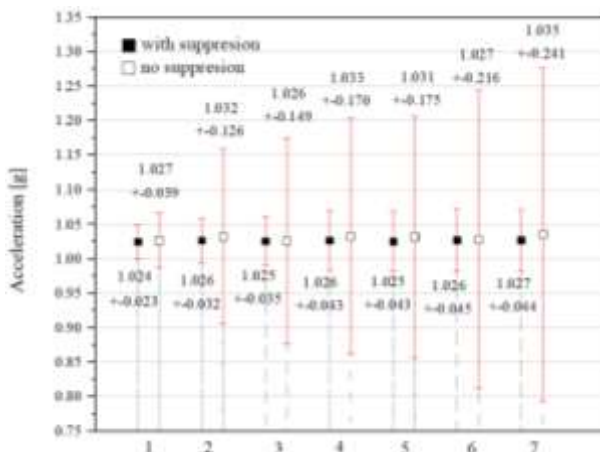


Figure 5

Averaged acceleration values and their standard deviations in the observed period

Now, by means of the Monte Carlo simulation method, the data from this figure are firstly integrated in the ranges in their standard deviations to determine the input states essential for the numerical determination of MLE.

By following the procedure for MLE numerical determination in the previous section and according to the experimental measurement in the vertical direction, the following numerical values of MLE are obtained and presented in Figure 6 and Figure 7. These figures present the variation in the almost sure stability regions for the observed train acceleration period. The results are presented in the 3D plane of MLE λ , norm degree p and train change in velocity (20-80 km/h).

Figure 6 shows the stability surface according to the vibrations of the train. For every tested point the results show significantly larger values of MLE even for low values of the norm degree p .

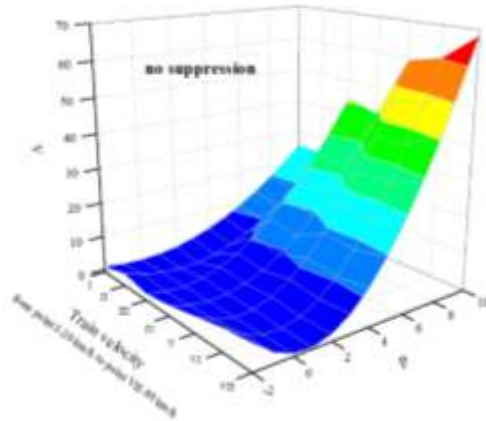


Figure 6

Stability surface according to the measurement values in the vertical direction (without suppression)

The results in Figure 7 are given for the case where suppression is applied. Contrary to Figure 6, significantly lower values of MLE are evident. Also, parameter Λ is negative in the range from $p=0$ to $p=7$, which guarantees the system stability. In comparison to Figure 6, the stabilization is especially evident for the largest values of the norm degree p , which are presented with very big differences in Λ ($p=9,10$).

The vibrations in the lateral and longitudinal directions are much smaller as evident from the experiment results. Thus, the system stabilization in these directions is observed only for the highest train velocity (corresponding values of point 7 from Figure 6 in the lateral and longitudinal direction).

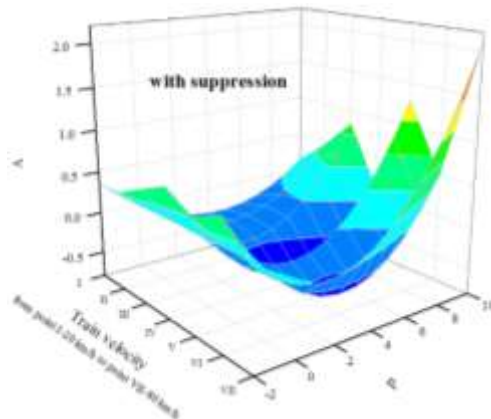


Figure 7

Stability surface according to the measurement values in the vertical direction (with suppression)

Figure 8 presents the boundaries of the almost sure stability where the red line presents the lateral stability of the train and the blue line presents the system stabilization after suppression is applied. As in Figures 6 and 7, the influence of viscoelastic suppression is also evident in this figure, where it can be seen that MLE growth for the highest values of the norm degree is almost negligible.

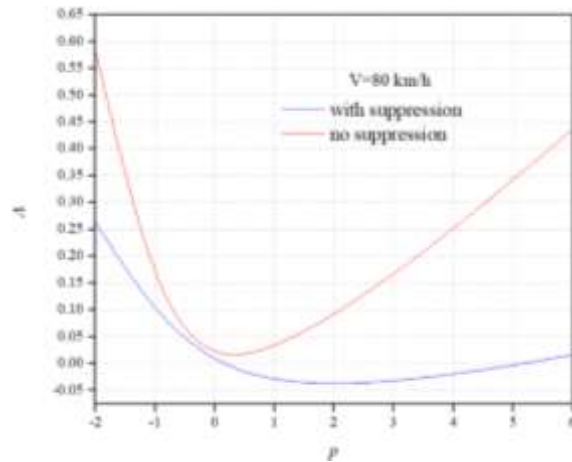


Figure 8

Stability boundaries in the lateral direction

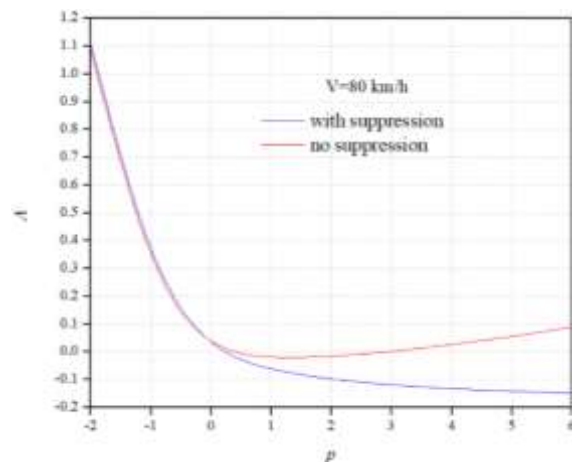


Figure 9

Stability boundaries in the longitudinal direction

Stability boundaries in the longitudinal direction are presented in Figure 9. This direction yields the smallest vibrations. When suppression is applied (blue line), the values of MLE are negative for all positive values of degree p .

Conclusions

This paper deals with stochastic vibrations of a railway ODS. The camera vibrations play a very important role because of their impact on the final picture quality. The experimental study considered the measuring of accelerations at two positions to assess the performance of the applied vibration suppression. In order to present the influence of the viscoelastic medium on ODS stabilization, the MLE method was applied. This method was firstly presented and verified on a simple Euler-Bernoulli beam with the aim of applying it to the analysis of the observed stochastic system. According to the experimental data and by means of the MLE method, the regions of the almost sure stability were given in the transversal, longitudinal and lateral directions. For this purpose the Monte Carlo simulation method was applied. This numerical method was found to be very useful in the stability problem analysis when it is hard or impossible to obtain an analytical solution, which was the case here. According to the performed numerical study, it is evident that the suggested viscoelastic element for the optical system successfully deals with stochastic vibrations where the resulting stabilization of the optical system is presented in all observed directions. This is most prominent in the study of the vertical direction dynamics, where the largest disturbances occur.

Acknowledgement

This research is conducted within the Horizon 2020 Shift2Rail project "Smart Automation of Rail Transport - SMART". The authors would like to thank the Serbian Railway Infrastructure for issuing a permit and providing operational assistance for testing, as well as Serbia Cargo for enabling the vibration measurement in an operational environment.

References

- [1] Ristić-Durrant, D., Haseeb, M. A., Banić, M., Stamenković, D., Simonović, M. and Nikolić, D., (2021) SMART On-Board Multi-Sensor Obstacle Detection System for Improvement of Rail Transport Safety. Proceedings of the Institution of Mechanical Engineers, Part F: Journal of Rail and Rapid Transit, p. 09544097211032738, DOI: 10.1177/09544097211032738
- [2] <https://cordis.europa.eu/project/id/730836>, accessed on 26.09.2021
- [3] Pavlović, M., Nikolić, V., Simonović, M., Mitrović, V. and Ćirić, I., (2019) Edge Detection Parameter Optimization Based on the Genetic Algorithm for Rail Track Detection. Facta Universitatis, Series: Mechanical Engineering, 17(3), pp. 333-344, DOI: 10.22190/FUME190426038P
- [4] Abolmaali, A., Fernandez, R., Kamangar, F., Ramirez, G. and Le, T., (2008) Vibration Reduction and Control for Traffic Cameras: Technical Report (No. FHWA/TX-08/0-5251-2)

- [5] Zhao, G. W. and Yuta, S. I., (1993) January. Obstacle Detection by Vision System for an Autonomous Vehicle. In 1993 Intelligent Vehicles Symposium, IV 1993, pp. 31-36, ISBN: 0780313704
- [6] SMART project, Deliverable 1.1. Obstacle Detection System Requirements and Specification. <https://cordis.europa.eu/project/id/730836/results>
- [7] Kuchak, A. J. T., Marinkovic, D. and Zehn, M., (2021) Parametric Investigation of a Rail Damper Design Based on a Lab-Scaled Model. *Journal of Vibration Engineering and Technologies*, 9(1), pp. 51-60, DOI: 10.1007/s42417-020-00209-2
- [8] Kuchak, A. J. T, Marinkovic, D. and Zehn, M. Finite Element Model Updating - Case Study of a Rail Damper (2020) *Structural Engineering and Mechanics*, 73(1), pp. 27-35, DOI: 10.12989/sem.2020.73.1.027
- [9] Sysyn, M., Nabochenko, O., Kovalchuk, V., Przybyłowicz, M. and Fischer, S. (2021) Investigation of Interlocking Effect of Crushed Stone Ballast During Dynamic Loading. *Reports in Mechanical Engineering*, 2(1), 65-76, DOI: 10.31181/rme200102065s
- [10] Pavlović, I., Pavlović, R. and Janevski, G., (2016) Dynamic Instability of Coupled Nanobeam Systems. *Meccanica*, 51(5), pp. 1167-1180, DOI: 10.1007/s11012-015-0278-x
- [11] Pavlović, I., Pavlović, R. and Janevski, G., (2019) Dynamic Stability and Instability of Nanobeams Based on the Higher-Order Nonlocal Strain Gradient Theory. *The Quarterly Journal of Mechanics and Applied Mathematics*, 72(2), pp. 157-178, DOI: 10.1093/qjmam/hby024
- [12] Arnold, L., Doyle, M. M. and Sri Namachchivaya, N., (1997) Small Noise Expansion of Moment Lyapunov Exponents for Two-Dimensional Systems. *Dynamics and Stability of Systems*, 12(3), pp. 187-211, DOI: 10.1080/02681119708806244
- [13] Pavlović, I., Pavlović, R., Kozić, P. and Janevski, G., (2013) Almost Sure Stochastic Stability of a Viscoelastic Double-Beam System. *Archive of Applied Mechanics*, 83(11), pp. 1591-1605, DOI: 10.1007/s00419-013-0767-0
- [14] Janevski, G., Kozić, P., Pavlović, R. and Posavljak, S., (2021) Moment Lyapunov Exponents and Stochastic Stability of a Thin-Walled Beam Subjected to Axial Loads and End Moments. *Facta Universitatis, Series: Mechanical Engineering*, 19(2), pp. 209-228, DOI: 10.22190/FUME191127014J
- [15] Pavlović, I., Pavlović, R., Janevski, G., Despenić, N. and Pajković, V., (2020) Dynamic behavior of two elastically connected nanobeams under a white noise process. *Facta Universitatis, Series: Mechanical Engineering*, 18(2), pp. 219-227, DOI: 10.22190/FUME190415008P

- [16] Xie, W. C., (2003) Moment Lyapunov Exponents of a Two-Dimensional System Under Bounded Noise Parametric Excitation. *Journal of Sound and Vibration*, 263(3), pp. 593-616, DOI: 10.1016/S0022-460X(02)01068-4
- [17] Xie, W. C., (2001) Moment Lyapunov Exponents of a Two-Dimensional System Under Real-Noise Excitation. *Journal of Sound and Vibration*, 239(1), pp. 139-155, DOI: 10.1006/jsvi.2000.3211
- [18] Xie, W. C., (2005) Monte Carlo Simulation of Moment Lyapunov Exponents. *J. Appl. Mech.*, 72(2), pp. 269-275, DOI: 10.1115/1.1839592
- [19] Pavlović, I., Karličić, D., Pavlović, R., Janevski, G. and Ćirić, I., (2016) Stochastic Stability of Multi-Nanobeam Systems. *International Journal of Engineering Science*, 109, pp. 88-105, DOI: 10.1016/j.ijengsci.2016.09.006
- [20] Banić, M., Stamenković, D., Miltenović, A., Simonović, M. and Milošević, M., (2019) Design of Housing and Vibration Suppression for Obstacle Detection System in Railways. *Proceedings of 24th International conference "Current Problems in Rail Vehicles" - PRORAIL 2019*, 1, Žilina, Slovakia, 17-19, September, pp. 23-31, ISBN 978-80-89276-58-5

Effect of Geocell, on the Mechanical Behavior of Railway Embankments, Using FE Modeling

Farshad Astaraki¹, Majid Movahedi Rad¹, Reza Esfandiari Mehni², Guixian Liu³, Morteza Esmaeili², Guoqing Jing⁴

¹Department of Structural and Geotechnical Engineering, Széchenyi István University, Egyetem tér 1, Győr 9026, Hungary; astaraki.farshad@hallgato.sze.hu; majidmr@sze.hu

²Department of Railway Track & Structures Engineering, School of Railway Engineering, Iran University of Science and Technology, Narmak 13114-16846, Tehran, Iran; afrough_masoud98@rail.iust.ac.ir; m_esmaeili@iust.ac.ir

³Infrastructure Inspection Research Institute, China Academy of Railway Sciences Co., Ltd., Beijing 100081, China; liuguixian@rails.cn

⁴School of Civil Engineering, Beijing Jiaotong University, Beijing, 100044, China; gqjing@bjtu.edu.cn

Abstract: In nature, the mechanical properties of soils, vary from region to region and in some areas, high-strength soil resources lack is a serious difficulty that geotechnical engineers may face where constructing earthworks such as railway and road embankments is required. Although a wide range of soil improvement techniques exists to improve such soils, the effect of geocell, as an effective solution, has not yet been investigated for railway embankments, hence, the present study aims to develop a three-dimensional (3D) Finite Element (FE) model, to fill the gap. To do this, first, six, 1/20 scaled-down railway embankments, including an unreinforced and 5 reinforced ones, were constructed in the lab and their load-settlement behavior, was assessed. Second, a 3D FE model was validated by experimental results and then, using a parametric study, the effect of geocell opening size and geocell layers number, were investigated on bearing capacity and settlement of the embankments, for five various types of soil ranging from poor soils (ST1), to high strength soils (ST5). The outcomes indicated, although adding geocell layers up to 15 layers, results in reducing the exerted stress in railway embankments by a maximum of near 50%, the crest settlement is not efficiently affected. Moreover, it was found that geocell's opening size has a negligible effect on decreasing the embankment's settlement, while it affects the bearing capacity significantly, up to a maximum of 50%.

Keywords: Geocell-reinforced Railway embankment; railway embankment FE model; railway embankment improvement; Geosynthetics

1 Introduction

Nowadays, Geosynthetic materials, especially geocells, are frequently used for different geotechnics' purposes where soil improvement is needed. Among all, the use of such materials in transportation infrastructure, cannot be overlooked as they are a development index for societies and countries. However, amongst the various modes of transportation, railway transportation has a special role due to the high potential for mass transportation of passengers and freight in the safest way. Up to now, a considerable amount of literature has been published on superstructure components of railway tracks especially, rail and ballast aggregates for different purposes [1-11]. However, railway embankments as an essential part of the infrastructure need special attention where construction and renovation of the tracks are needed.

From a Geotechnics Engineering point of view, since soil types vary from region to region, improvement and renovation of railway embankments, as a part of railway substructure, has always been a challenge. Since in some regions access to high strength soil resources is difficult and sometimes uneconomical, geosynthetic material such as geocells and geogrids, are being widely used as a solution to satisfy geotechnical criteria as constructing railway embankments is the matter [12-16].

The geocell foundation mattress is a polymeric, honeycomb-like structure that is formed a series of interlocking strips (Bush et al. 1990) [17]. Due to geocell's special physical structure and confining features, it can keep soil in the integrated state without spearing. Increasing the soil bearing capacity and its settlement reduction in comparison with non-geocell soils is another advantage of geocells, which makes possible use of poor soil materials [18]. Geocell acts as a rigid mattress and distributes the applied load into a deeper depth of underlying soil layers, so the pressure intensity on the soft soil decreases [19]. Hence, the use of geocell mattresses over the soft soil can reduce the settlement and increase the bearing capacity [20].

A number of researchers have reported the effect of geocell, on the mechanical behavior of soft soils through experimental and numerical studies. Zhang et al. (2009) [21], highlighted deformation as one of the main concerns of the designing process using analytic studies on the Winkler foundation model. The results revealed that in order to economize and optimize the design the effect of interface resistance between the geocell blanket and soil should be considered. However, it was found that the more EI rigidity increase, the more would be the deformation minimization. In another study carried out by Zhang et al. (2010) [20] a calculation method was proposed to measure bearing capacity of geocell-supported road embankment over the soft subgrade. The outcomes showed the use of geocell reinforcement resulted in preventing lateral dispersion, increasing the shear strength of materials, load distribution on a wider surface, increasing the bearing capacity of the subgrade soil, and reducing vertical deformation. Mehdipour et al (2013) [22] performed a numerical study on geocell- reinforced slopes considering its bending

effect. In this regard, a comprehensive parametric study was carried out considering different depth layer locations, the number of geocell layers, the vertical spacing between reinforced layers, length, thickness, and the Yung modulus of the geocell. The effects of slope geometry, shear strength characteristics, and soil density on the behavior of the reinforced slopes have also been discussed. The results revealed that the use of geocell layers led to an increase in the safety factor of slopes and a decrease in lateral displacement. Besides, findings indicated that geocells prevent surface failures and redistribute load on a wider surface. Song et al. (2018) investigated failure modes of geocelled retaining wall. It was found that alike the failure mode of rigid retaining walls, sliding rupture occurred in geocell-reinforced retaining walls in case of enlarged value for the apparent cohesion [23]. A series of plate load tests were performed by Gh Tavakoli Mehrjardi et al. (2019) to investigate the behavior of geocell-reinforced soil. In this study different soil grains sizes, geocell dimensions and size of loading plate were examined. Their findings indicated that the bearing capacity of geocell-reinforced soil was significantly gained by 524% compared to the unreinforced one [24]. Recently, Astaraki et al. constructed a series of 6, 1/20 scaled-down laboratory railway embankments, including one unreinforced and five geocell-reinforced embankments. Then, the load-settlement behavior of each embankment was assessed under a simulated uniform railway load. The results indicated that using geocell layers in the embankment body, increased bearing capacity and decreased the crest settlement. However, the maximum bearing capacity and minimum settlement were achieved for reinforced embankment with four geocell layers by 38.6% and 37%, respectively [25].

Despite using geocell for improving mechanical properties of soft and problematic soils, some attempts have been made to investigate the use of geocell layers in ballast and sub-ballast materials. instance, Leshchinsky and Ling through some experimental and numerical simulations showed that the geocell-confined ballast increased the stiffness and resistance of the ballast particles effectively and reduced the related vertical settlement and lateral dispersion [18] [26]. Biabani et al studies revealed that considering concurrent economic issues using geocell and sub-ballast with relatively low compressive strength has a proper performance. The cell surface and the lateral pressure are affecting factors for the geocell strips. Numerical results showed that with the increase of geocell hardness, the mobilized tensile strength of the geocell increases while the inactive resistance decreases [27]. Lately, a comprehensive numerical study was conducted to understand the distribution of stress in railway substructures as using geocell layers as ballast reinforcement. It was found that stress distribution improves where the ballast layer is reinforced using geocell layers [28].

However, far too little attention has been paid to assessing the effect of geocell layers on bearing capacity and crest settlement of real railway embankments. Therefore, the current study aims to fill this gap through a parametric study using the ABAQUS software. In this study, firstly numerical results were validated with

the results obtained experimentally in the previous study carried out by the authors [25]. Afterwards, a wide range of poor to high strength embankment soils named ST1 to ST5, three geocell opening sizes of 245*210, 340*290, and 448*520 mm with a wall height of 100 mm, and five geocell layers, numbered 0, 5, 10, 15 and 20 were examined to determine their influence on stress distribution and settlement of real railway embankments. It should be pointed out the geocell layers were non-spacing placed top-down starting from the crest in the upper part of the embankment body.

2 FEM Modeling of Lab Embankments

In this section, a FE model will be developed based on a previous experimental study carried out by the authors in which a series of six 1/20 scaled-down railway embankments includes five geocell-reinforced and a reference embankment were constructed and examined in the lab environment [25].

In order to simulate the load-settlement behavior of the lab embankments, six 3D models were developed using ABAQUS software [29] and their results were compared with obtained experimental outcomes. In this regard A 15-node quadratic triangular prism (C3D15), An 8-node quadrilateral membrane, reduced integration (M3D8R) and A 20-node quadratic brick, reduced integration (C3D20R) elements were chosen for embankment soil and modified subgrade, subgrade, geocell, and loading plate respectively. Considering soil-geocell interaction, it is noticeable that the geocell has been embedded into the soil. Moreover, for providing a perfect connection between the loading plate and the embankment crest avoiding any lateral displacement or rotation between them, the interaction type of “tie” was applied between them. Boundary conditions of the models were considered like those were imposed in the experimental embankments. Hence, the y-z vertical planes were restrained from the lateral deformation in the x-direction. Likewise, the vertical front and rear planes of the embankments in the x-y plane were limited against lateral deformation in the z-direction and the base of the model was restrained from any displacements and rotations (see Figure 1).

The obtained numerical results in terms of stress-settlement curves are compared to the laboratory outcomes as shown in Figure 2. It should be clarified that the lab and FE models were named based on the number of geocell layers used in the embankments. Therefore, ELM0 to ELM5 refers to the lab embankments with 0 to 5 geocell layers and ANM0 to ANM5 assigns to the numerical models reinforced by 0 to 5 layers, respectively. Figure presents stress-settlement curve of both numerical and laboratory models. As can be seen in the numerical diagrams, using more geocell layers can increase the bearing capacity of the embankments as already inferred in laboratory models. Comparing numerical and laboratory models, it is obvious that the numerical models behave more rigidly, than those experimental

ones however, the numerical models exhibit less settlement compared to laboratory ones.

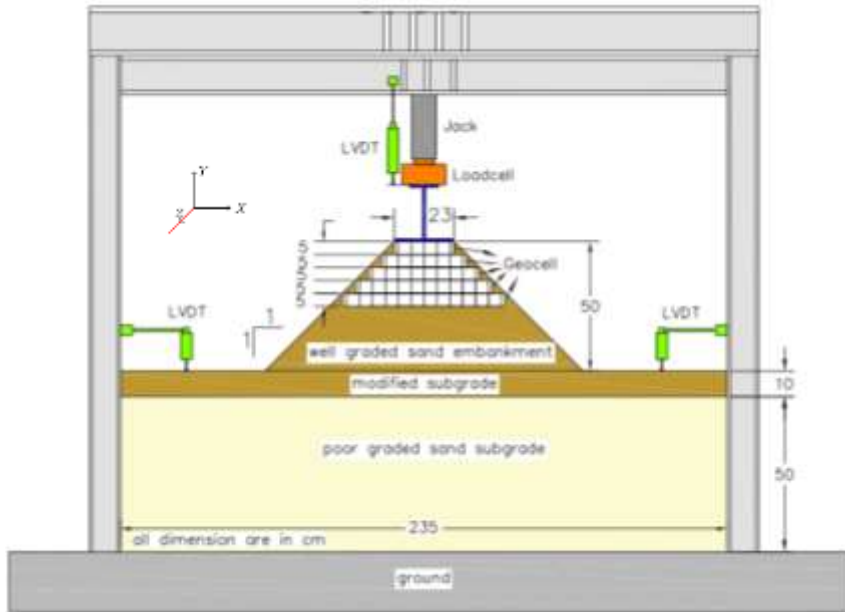
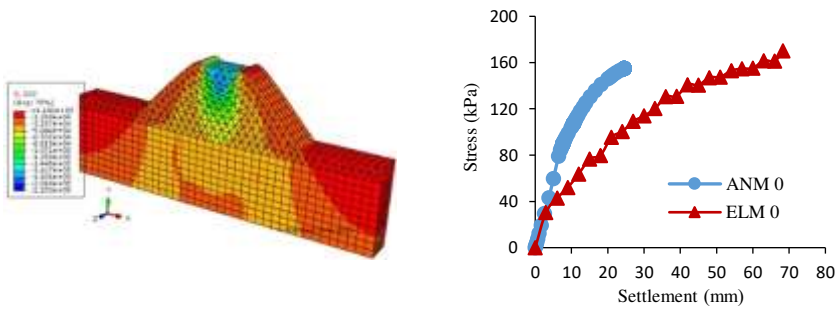
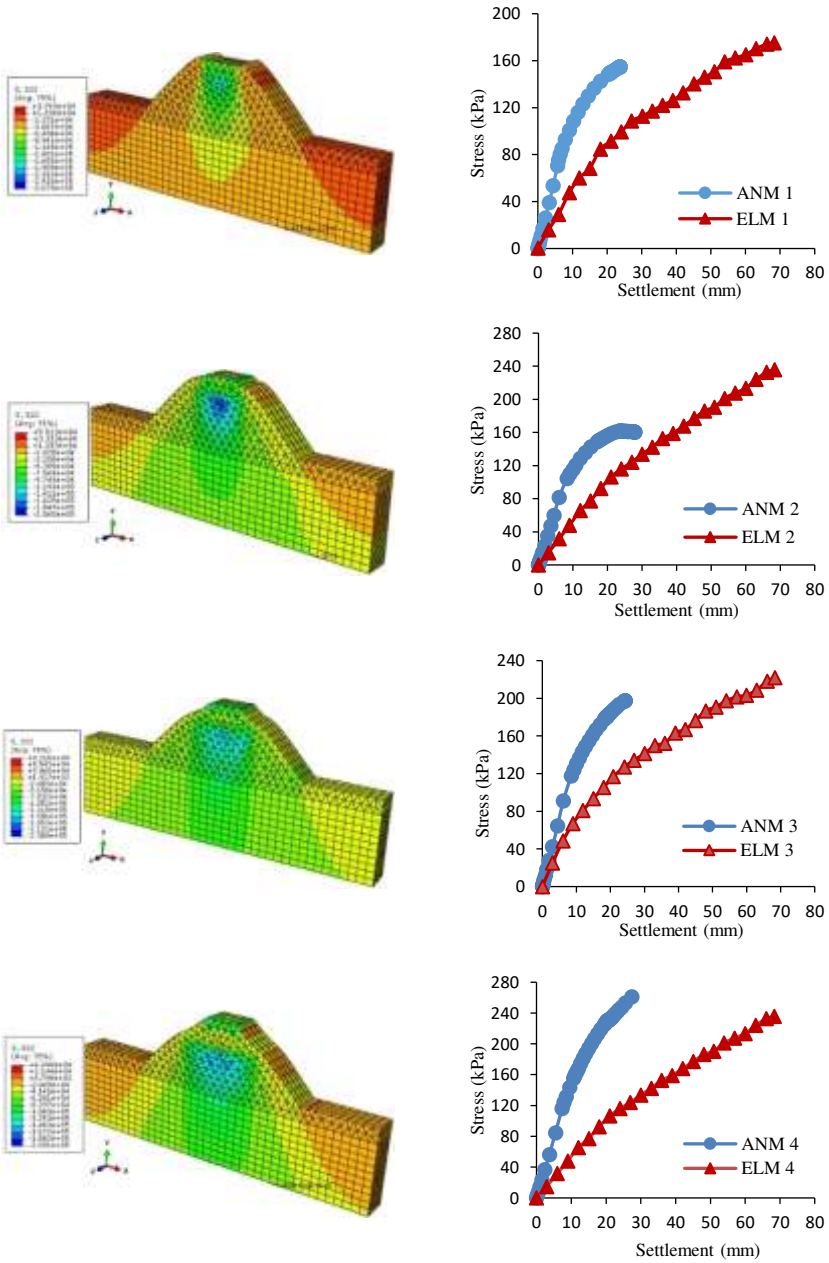


Figure 1

The laboratory geocell-reinforced embankment including 5 geocell layers [25]





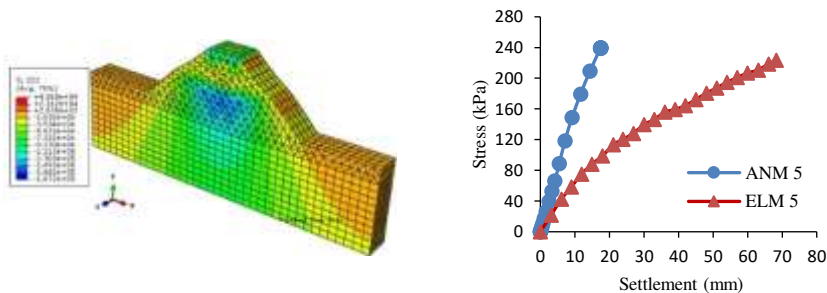


Figure 2

Stress-settlement curve of laboratory and numerical embankments

The main reasons for inadequate confirmation between the numerical results and laboratory results can be defined as follows:

- 1) Difference in loading velocity for lab and numerical models, so that in the lab the load was exerted using a manual hydraulic jack which is hard to apply load continuously at exact velocity.
- 2) The handmade geocell had non-integrated connections and adequate stiffness similar to real geocell and did not have enough integrity and displacement during loading thus the laboratory results showed less bearing capacity and more crest settlement than FE models.
- 3) The effect of soil compaction is evidence for the increase in bearing. In the laboratory, due to the presence of the geocell, it is impossible to compact embankment soil to reach the desired compaction.

3 Parametric Study

After validation of numerical model, by adopting the Mohr-Coulomb law, the effect of different embankment soil types, number of geocell layers and geocell's pocket size was investigated on the distribution of stress and settlement of real embankments using the ABAQUS software [29]. For this purpose, laboratory model dimensions were scaled up [30] to real scale embankment as given in Table 1. Afterward, initially, the effect of different soil types (ST1 to ST4) on induced stress and the settlement of railway embankments were evaluated through an unreinforced embankment model loaded according to the LM71 pattern (Fig) (EN 1991-2, 2003) [31]. Then, the embankments were reinforced using geocell layers according to the laboratory model pattern from top to down to assess the effect of geocell layers number and their pocket size. It must be acknowledged that a length of 4 m was chosen for the embankments as a result of sensitivity analysis carried out on the length and mesh size of the model.

Table 1

Full-scale and laboratory railway embankment dimensions (scale factor of 1:20)

| Parameter | Laboratory model | Real embankment |
|-------------------------|------------------|-----------------|
| Embankment height | 0.5 m | 10 m |
| Embankment length | 2.4 m | 48 m |
| Slopes angle | 45° | 45° |
| Slope length | 0.71 m | 14.2m |
| Crest width | 0.23 m | 4.6 m |
| Subgrade depth | 0.6 m | 12 m |
| Modified subgrade depth | 0.1 m | 2 m |
| Bed sides width | 0.56 m | 11.2 m |

3.1 Material Specifications

In the current study, five various soil types named ST1 to ST5 were utilized for the embankment body and modified subgrade with given specifications in Table 2. The subgrade soil properties were taken similar to the laboratory embankments. Regarding geocell, following the PRS Geo Technologies Co catalogues [32], three geocell pocket sizes of 245×210 mm, 340×290 mm, and 448×520 mm with the wall height of 100 mm and specified properties in Table 3 were used.

Table 2

Characteristics of the soil utilized in numerical study

| Soil type | Dry density (kN/m^3) | Elasticity modulus, E (kN/m^2) | Poisson's ratio | Friction angle, φ (degree) | Cohesion c (kN/m^2) |
|-----------|-----------------------------|---------------------------------------|--------------------|---------------------------------------|----------------------------|
| ST1 | 17 | 2.0e4 | 0.45 | 25 | 20 |
| ST2 | 18 | 4.0e4 | 0.4 | 28 | 23 |
| ST3 | 19 | 6.0e4 | 0.35 | 32 | 27 |
| ST4 | 20 | 8.0e4 | 0.3 | 35 | 30 |
| ST5 | 21 | 1.0e5 | 0.3 | 38 | 33 |

Table 3

Specifications of used geocell in the parametric study

| Density (kg/m^3) | Elastic stiffness (MPa) | Poisson's ratio | Coefficient of Soil- Cell Friction |
|-------------------------|----------------------------|--------------------|---------------------------------------|
| 900 | 1400 | 0.3 | 0.95 |

3.4.2 Loading Pattern

In this section, a longitudinal loading pattern of LM71 presented in the Euro code standard of EN 1991-2 [31] has been used. In order to apply uniform load on the embankment crest, the following equation was used:

$$q = \frac{4 \times Q_{vk}}{(3a + 2b) \times B} \quad (kN/m^2) \quad (1)$$

Where Q_{vk} is the concentrated load of 250 kN (see Figure 3) according to Iranian railway tracks axle load, a and b are the geometrical parameters equal to 1.6 m and 0.8 m respectively. Also, B is linked to the load width equal to a railway sleeper length of 2.6 m. Because of the dynamic nature of the railway system, in this study for slope stability investigation, the dynamic load is substituted by a quasi-static load by considering the impact factor parameter. In present research, impact factor for quasi-static loading was used rather than including velocity and train wheel radius effects according to the AREMA (2006) [33] equation:

$$\alpha = 1 + 5.21 \frac{V}{D} \quad (2)$$

Where α is the impact factor, V is the train speed (km/h), and R is the wheel diameter (mm). For this study, velocity and wheel diameter are assumed to be equal to 160 km/h and 1m respectively. Finally, a distributed load of 115 kN/m^2 was obtained.

Finally, considering a sleeper length of 2.6 m, 0.5 m for ballast depth and a stress distribution angle of 1:1 for the ballast layer under sleeper and impact factor of 1.83 a uniform load of 115 kN/m^2 was applied over embankment crest. It should be noted that this uniform load was applied on effective loading width of 3.2 m.

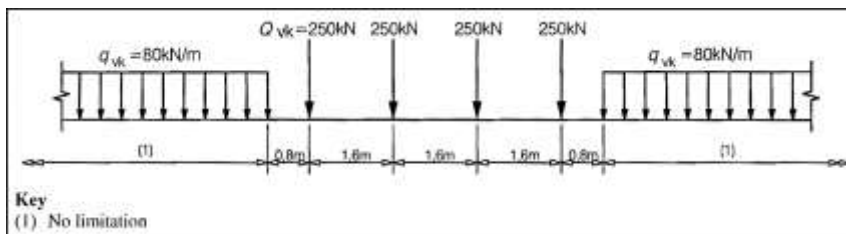


Figure 3

Load model 71 pattern and characteristic values for vertical loads [31, 34]

4 Results and Discussions

In this section, the effect of different soil types, number of geocell layers, and geocell pocket size on the mechanical behavior of railway embankments will be discussed. It should be mentioned that the center point located at the top of the embankment's crest was selected to pick the data as the distributed load of 115 was linearly applied. Models are named based on the soil type used and the number of geocell layers; for instance, ST1-20G refers to an embankment containing ST1 soil type and 20 geocell layers. Furthermore, the geocell layers are placed top-down starting from the crest, similar to experimental models (see Figure 1).

4.1 Effect of Soil Type

To investigate the effect of five different soil types on the exerted stress and the settlement of the railway embankment under service load, five unreinforced embankments were modeled. Figure 4 depicts that the higher the strength of soils, the less existing stress and settlement achieve. From the graph, it can also be understood that high-strength soils decrease crest settlement significantly, while distributed stress is not highly affected. However, compared to ST1-0G, the maximum decrease of settlement and stress was observed for ST5-0G embankment by 54.85% and 11.75%, respectively. The data are summarized in Table 4. From the results, it can be concluded that though using high-strength soil without reinforcement can be a decent alternative where decreasing the settlement is needed, reducing induced stress using reinforcements seems to be a better choice.

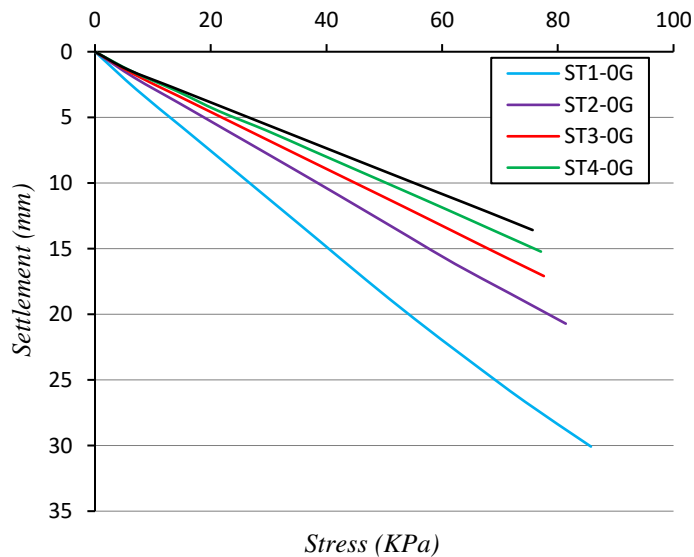


Figure 4

Diagram of settlement-stress of non-geocelled embankments with five different soil types

4.2 Effect of Geocell Layers

Totally 25 real embankments considering 5 soil types and 0, 5, 10, 15, and 20 geocell layers are modeled, in order to assess the influence of geocell layers on the stress and the settlement of railway embankments. Figure 5 shows exerted stress versus the number of geocell layers used inside the embankment body.

Table 4

Effect of soil types on bearing capacity and settlement of embankments according to ST1-0G

| Embankment name | Soil Type | Existing stress in embankment soil (KPa) | Stress reduction (%) | Crest settlement (mm) | Settlement decreasing (%) |
|-----------------|-----------|--|----------------------|-----------------------|---------------------------|
| ST1-0G | ST1 | 85.71 | - | 30.08 | - |
| ST2-0G | ST2 | 81.37 | 5.06 | 20.72 | 31.12 |
| ST3-0G | ST3 | 77.58 | 9.48 | 17.09 | 43.18 |
| ST4-0G | ST4 | 77.08 | 10.07 | 15.23 | 49.37 |
| ST5-0G | ST5 | 75.64 | 11.75 | 13.58 | 54.85 |

The graphs illustrate that irrespective of the soil type, using geocell reinforcement up to 15 layers decreases the exerted stress to the embankments for all soil types. It can also obviously be seen that this effect is noticeable for the weaker soils so that the maximum decrease observed for ST1-15G by around 50% compared to the ST1-0G model. From the data it can be realized that using 20 layers resulted in the almost the same level of stress which means that using 15 geocell layers is the optimum in this case. On top of that, as shown using a black circle, there is a point on the curves, associated with 2 geocell layers, which shows that the level of inserted stress is the same regardless of the soil types used. These results showed a good agreement with the lab results (see Figure 6) which can be interpreted that using geocell layers, up to 2 layers, has the same results irrespective of soil type.

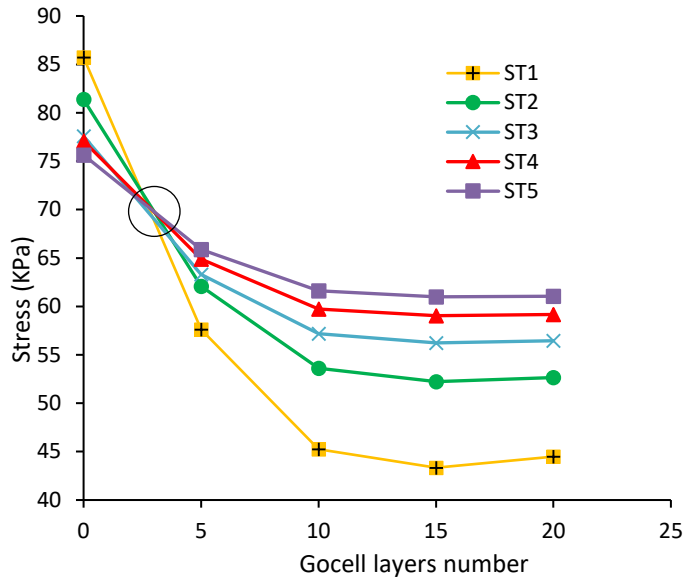


Figure 5

Stress-geocell layers number curves for different soil types

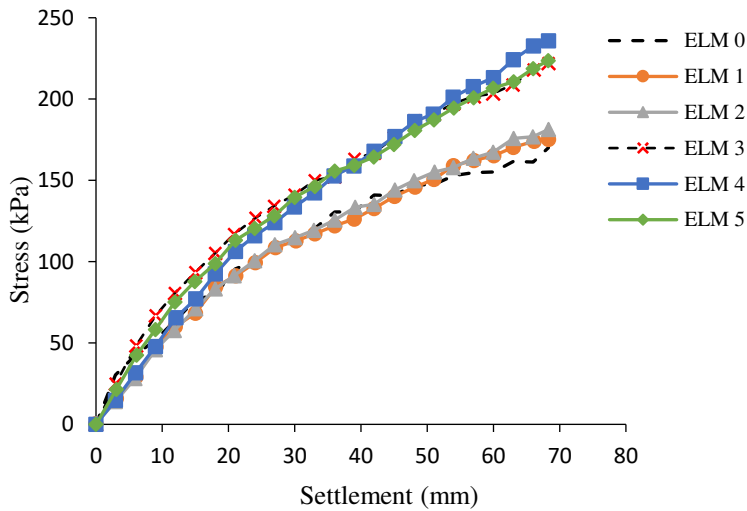


Figure 6

Load-settlement behavior of experimental geocell-reinforced and reference models [19]

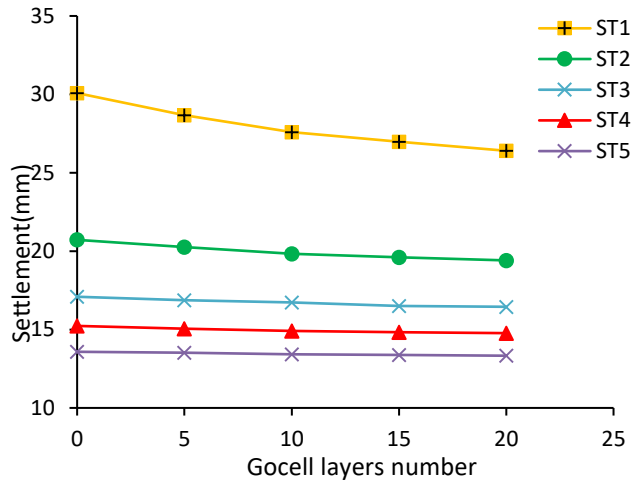


Figure 7

Settlement-geocell layers number curves for different soil types

Figure 7 shows the embankment settlement against the number of geocell layers. As can be seen, increasing geocell layers number is more effective for weaker soils. As the graphs show, except for ST1 and ST2 embankments, the effect of geocell layers number on the settlement is almost negligible. However, the maximum gain in terms of settlement decrease is associated with S1-20G by 12.23% compared to ST1-0G.

4.3 Effect of Geocell Pocket Size

In this sub-section, the effect of geocell pocket size on exerted stress and the settlement of the railway embankments has been assessed. To do this, ST2 soil type reinforced by geocell layers with three different cell pocket sizes of 245×210 mm (small), 340×290 mm (medium), and 448×520 mm (large) with the height of 100 mm according to “PRS Geo Technologies Ltd.” D category [27].

From the graphs (see Figure 8), it can be understood smaller the geocell pocket-size the more effective they are on reducing exerted stress. In other words, the magnitudes of existing stress of the embankment body decrease where geocell with the smaller pocket size is used. On top of that, with increasing the number of geocell layers the effect of pocket-size gradually fades so that using 15 and 20 layers shows the same result for different pocket sizes. Comparatively, the maximum stress reduction was met for ST2-15G by 16.7% for small geocell pocket-size compared to the large one.

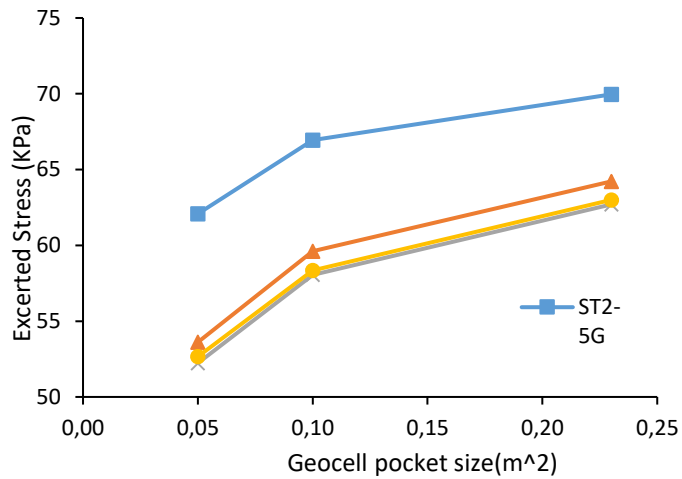


Figure 8
Exerted stress versus geocell pocket size for ST2 soi type

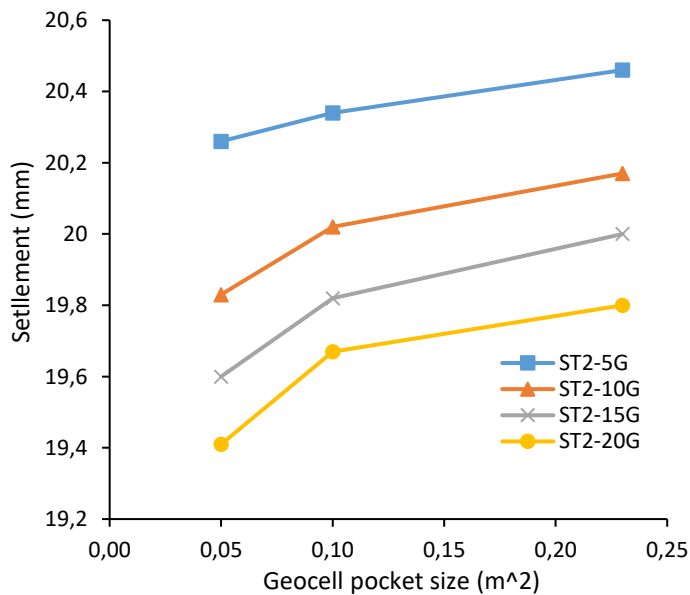


Figure 9
Exerted stress versus geocell pocket size for ST2 soi type

Figure 9 illustrates magnitudes of crest settlement of the railway embankments against three different geocell pocket sizes of small, medium and large. Overall, diminishing the cell dimensions, results in enhancing the settlement. However, it's effect is insignificant as the maximum settlement reduction associated with small pocket-size ST2-15G contained by 2% compare to the large cells.

In summary, the results indicate that constructing railway embankments, using high-strength soils, can guarantee the crest settlement while using reinforcement is recommended where bearing capacity and inserted stress are the topics. Based on the outcomes, using geocells up to 15 layers, considerably reduces the distributed stress in the embankment body. Regarding geocell's opening size, its impact on the embankments' settlement can be ignored. However, depending on the number of layers, using geocell layers with small pocket sizes, can decrease the stress maximum by approximately 17%.

Conclusions

The current study is dedicated to investigating the effect of soil types, geocell layers number and geocell opening size, on settlement and exerted stress of railway embankments through 3D FE modelling using the ABAQUS software. Hence, after developing a FE validated model, five different soil types, ranging from poor (ST1) to high strength (ST5), five geocell layer numbers of 0, 5, 10, 15 and 20, and three geocell opening sizes of 245×210 mm (small), 340×290 mm (medium), and 448×520 mm (large) were examined, to determine their effect on the mechanical properties of the embankments. The main achievements of the study can be summarized as follows:

- 1) Although improving soil properties had a minor effect on exerted stress, the crest settlement decreased significantly when high-strength soils used. Though, the maximum decrease in terms of settlement and existing stress was seen for ST5-0G by 54.85% and 11.75% respectively in comparison with ST1-0G.
- 2) Overall, adding geocell layers number in the embankments resulted in decreasing exerted stress for different soil types with maximum value of 49.44% for ST1-15G compared to ST1-0G. Except for ST1 and ST2, adding more geocell layers could not improve the crest settlement of the embankments. The maximum decrease in terms of crest settlement observed for S1-20G by 12.23% compared to ST1-0G.
- 3) The existing stress level of the embankment body affected by geocell opening size so that its magnitude decreased where geocell with the smaller pocket size is used. The maximum decrease in terms of exerted stress was reported for ST2-15G by 16.7% for small geocell pocket-size compared to the large one. Oppositely, geocell opening size affected the crest settlement minimally, so that a maximum reduction of 2% was linked to ST2-15G with a small pocket size compared to the large pocket.

However, there are some limitation in this study, such as, the assumption of the ballast and sub-ballast layers, as a rigid layer. In addition, in the current paper, the dynamic railway load is replaced by a quasi-static uniform load. For future work, in order to omit the mentioned limitations, the authors suggest remodeling the different layers using DE modeling, under real dynamic loads.

References

- [1] Juhász, E., & Fischer, S. (2019) Investigation of railroad ballast particle breakage. *Pollack Periodica*, 14(2), 3-14
- [2] Németh, A., & Fischer, S. (2018) Investigation of glued insulated rail joints with special fiber-glass reinforced synthetic fishplates using in continuously welded tracks. *Pollack Periodica*, 13(2), 77-86
- [3] Fathali, M., Chalabii, J., Astaraki, F., & Esmaeili, M. (2021) A new degradation model for life cycle assessment of railway ballast materials. *Construction and Building Materials*, 270, 121437
- [4] Kurhan, M., Kurhan, D., Novik, R., Baydak, S., & Hmelevska, N. (2020, November). Improvement of the railway track efficiency by minimizing the rail wear in curves. In *IOP Conference Series: Materials Science and Engineering* (Vol. 985, No. 1, p. 012001) IOP Publishing
- [5] Fischer, S. (2017) Breakage test of railway ballast materials with new laboratory method. *Periodica Polytechnica Civil Engineering*, 61(4), 794-802
- [6] Kurhan, D., & Kurhan, M. (2019, December) Modeling the dynamic response of railway track. In *IOP Conference Series: Materials Science and Engineering* (Vol. 708, No. 1, p. 012013) IOP Publishing
- [7] Przybyłowicz, M., Sysyn, M., Gerber, U., Kovalchuk, V., & Fischer, S. (2022) Comparison of the effects and efficiency of vertical and side tamping methods for ballasted railway tracks. *Construction and Building Materials*, 314, 125708
- [8] Kuchak, A. T. J., Marinkovic, D., Zehn, M., 2020, Finite element model updating - Case study of a rail damper, *Structural Engineering and Mechanics*, 73(1), pp. 27-35
- [9] Kuchak, A. T. J., Marinkovic, D., Zehn, M., 2021, Parametric Investigation of a Rail Damper Design Based on a Lab-Scaled Model, *Journal of Vibrational Engineering and Technologies*, 9(1), pp. 51-60
- [10] Kurhan, D., Fischer, S. Modeling of the Dynamic Rail Deflection using Elastic Wave Propagation. *Journal of Applied and Computational Mechanics*, 2022; 8(1): 379-387, doi: 10.22055/jacm.2021.38826.3290
- [11] Basili, M., Casini, P., Morelli, L., Vestroni, F. Vibration Mitigation of Rail Noise Barriers by Hysteretic Absorbers. *Journal of Applied and Computational Mechanics*, 2021; 7: 1205-1217. doi: 10.22055/jacm.2020.32360.2044
- [12] Esmaeili, Morteza, Behnood Naderi, Hossein Kalantar Neyestanaki, and Alireza Khodaverdian. "Investigating the effect of geogrid on stabilization of high railway embankments." *Soils and Foundations* 58, No. 2 (2018): 319-332

- [13] Astaraki, F., Roozbini, M. R., Esmaeili, M., & Chalabii, J. (2019) Investigation on Mechanical Behavior of Embedded Geocell in Geocell-Reinforced Railway Embankment. *International Journal of Railway Research*, 6(2), 95-102
- [14] Sadeghi, J., Kian, A. R. T., Ghiasinejad, H., Moqaddam, M. F., & Motevalli, S. (2020) Effectiveness of geogrid reinforcement in improvement of mechanical behavior of sand-contaminated ballast. *Geotextiles and Geomembranes*, 48(6), 768-779
- [15] Ngo, N. T., Indraratna, B., & Rujikiatkamjorn, C. (2016) Modelling geogrid-reinforced railway ballast using the discrete element method. *Transportation Geotechnics*, 8, 86-102
- [16] Jing, G., Siahkouhi, M., Wang, H., & Esmaeili, M. (2021) The improvement of the dynamic behavior of railway bridge transition zone using furnace slag reinforcement: A numerical and experimental study. *Proceedings of the Institution of Mechanical Engineers, Part F: Journal of Rail and Rapid Transit*, 09544097211020603
- [17] Bush, D. I., C. G. Jenner, and R. H. Bassett. "The design and construction of geocell foundation mattresses supporting embankments over soft grounds." *Geotextiles and Geomembranes* 9, No. 1 (1990): 83-98
- [18] Leshchinsky, B. and H. I. Ling, Numerical modeling of behavior of railway ballasted structure with geocell confinement. *Geotextiles and Geomembranes*, 2013, 36: pp. 33-43
- [19] Dash, Sujit Kumar, K. Rajagopal, and N. R. Krishnaswamy. "Behavior of geocell-reinforced sand beds under strip loading." *Canadian Geotechnical Journal* 44, No. 7 (2007): 905-916
- [20] Zhang, L., et al., Bearing capacity of geocell reinforcement in embankment engineering. *Geotextiles and Geomembranes*, 2010, 28(5): pp. 475-482
- [21] Zhang, L., Zhao, M., Zou, X., & Zhao, H., Deformation analysis of geocell reinforcement using Winkler model. *Computers and Geotechnics*, 2009 36(6), 977-983
- [22] Mehdipour, I., M. Ghazavi, and R. Z. Moayed, Numerical study on stability analysis of geocell reinforced slopes by considering the bending effect. *Geotextiles and Geomembranes*, 2013, 37: pp. 23-34
- [23] Song, F., et al., Numerical analysis of geocell-reinforced retaining wall failure modes. *Geotextiles and Geomembranes*, 2018, 46(3): pp. 284-296
- [24] Mehrjardi, Gh Tavakoli, R. Behrad, and SN Moghaddas Tafreshi. "Scale effect on the behavior of geocell-reinforced soil." *Geotextiles and Geomembranes* 47, No. 2 (2019): 154-163

- [25] Astaraki, F., Esmaeili, M., & Reza Roozbini, M. (2020) Influence of geocell on bearing capacity and settlement of railway embankments: an experimental study. *Geomechanics and Geoengineering*, 1-17
- [26] Leshchinsky, B. and H. Ling, Effects of geocell confinement on strength and deformation behavior of gravel. *Journal of Geotechnical and Geoenvironmental Engineering*, 2012, 139(2): pp. 340-352
- [27] Biabani, M. M., N. T. Ngo, and B. Indraratna, Performance evaluation of railway subballast stabilised with geocell based on pull-out testing. *Geotextiles and Geomembranes*, 2016. 44(4): pp. 579-591
- [28] Nayyar, A. S., & Sahu, A. K. (2021) Numerical analysis of railway substructure with geocell-reinforced ballast. *Geomechanics and Geoengineering*, 1-11
- [29] Zhuang, H. Y., Chen, G. X., Liang, Y. X., & XU, M. (2007) A developed dynamic viscoelastic constitutive relations of soil and implemented by ABAQUS software. *Rock and Soil Mechanics-Wuhan-*, 28(3), 436 (For Abaqus Reference)
- [30] Wood, D. M., *Geotechnical modelling*. Vol. 1, 2003: CRC Press
- [31] Standardization, E. C. f., European Standard (EN 1991–2). Ref. no. EN 1991-2:2003 E. 2003
- [32] PRS GeoTechnologies Ltd. <https://www.prs-med.com/engineering-services/geotechnical-project-design/specifications/>
- [33] AREMA, American Railway Engineering and Maintenance of Way Association Manual for Railway Engineering. *Economics of Railway Engineering and Operations-construction and Maintenance Operations*, 2006, Vol. 4, chapter 16, part 10
- [34] UIC, E., *Track-Bed Layers for Railway Lines*, UIC Code 719 R. International Union of Railways, Paris, France, 1994

Influence of the Head Wind on Determining Braking Performance of Zacs Tank Wagon

**Saša Radulović¹, Dragan Milković¹, Milan Raković²,
Goran Simić¹, Aleksandra Kostić¹**

¹Laboratory of rail vehicles, University of Belgrade, Faculty of Mechanical Engineering, Kraljice Marije 16, 11120 Belgrade, Serbia
e-mails: sradulovic@mas.bg.ac.rs, dmilkovic@mas.bg.ac.rs,
gsimic@mas.bg.ac.rs, akostic@mas.bg.ac.rs

²Department of fluid dynamics, University of Belgrade, Faculty of Mechanical Engineering, Kraljice Marije 16, 11120 Belgrade, Serbia
e-mail: mrakovic@mas.bg.ac.rs

Abstract: From the aspect of safety, brakes of rail vehicles are an extremely important system on the vehicle. Braking performance affects the normal functioning of vehicles and interoperability of rail vehicles in classic railway train compositions. All trains, classic and different type of motor trains must conform with the available stopping distances, which are predefined by the railway signalling, i.e. control length of a signal and depends on the maximum allowable speed for which the track section is designed. Apart from that, in classic wagons, which are combined and participate in the formation of different train compositions, mutual compatibility must be ensured from the aspect of used braking equipment and connection subassemblies, but even more important, braking performance of all wagons in the train has to be uniform within certain tolerances. This prevents weaker braked wagons from running into stronger braked ones, which can cause longitudinal jerks and may in extremes lead to a train rupture. Stopping distance during brake application depends on train braking performances, longitudinal running resistance and presence of wind and its direction. This paper deals with the influence of wind conditions on the results of slip brake tests and the estimation of a single vehicle's braking performance. Based on experimental measurements, simulations using CFD and comparison with the obtained results, this paper proposes a possibility to extract air drag resistance and wind force from the total resistance force. Presented methodology and obtained results may serve for further simulations of aerodynamic characteristics apart from braking performance, such as vehicle running resistance, energy consumption, etc. and for optimization of the wagon shape and design.

Keywords: stopping distance; slip brake tests; head wind influence; drag coefficient; numerical simulations

1 Introduction

TSI (Technical Specifications for Interoperability) and EN (European standards) define the method of determining the braking performance that is most often performed by measuring stopping distances in case of freight wagons, or by measuring deceleration of passenger coaches, motor units and high speed trains.

By keeping these parameters within the prescribed limits, uniform braking of all wagons in the classic train composition is achieved. With closed train sets, this problem is less pronounced because all units usually have the same brake system, similar or equal weight, load capacity and load level. These train sets do not separate from or connect to other vehicles during regular operation.

This paper deals with the influence of the head wind on the test results during slip tests and measured stopping distance. Depending on the wind speed, measured stopping distances may differ significantly.

The influence of wind on railway vehicles can be considered from several aspects. As an effect influencing safety and stability of vehicles [1-3] and as appearance that affects train running resistance and braking distance [4-8]. Safety and stability against overturning depend on cross wind. Head and tail wind predominantly influence running resistance and braking.

This paper focuses on the aerodynamic drag and the presence of head wind during determining the braking performance of conventional freight wagons. Wind influence is more expressed in the case of single vehicles tests and less expressed and not critical for the trains. Empty wagons vs. loaded wagon are more influenced due to smaller share of resultant force, compared to resistance force, in train motion equation. The tests with and without the presence of head wind were performed on the empty tank wagon Zacs type. The analysis included numerical simulation in the OpenFoam program and experimental measurements on the Zacs type tank wagon. According to relevant standard [9], regular atmospheric conditions for tests are described as with the minimum wind and to ride on dry rails.

This issue was treated by UIC¹ Committee in Technical & Research Report B 126/DT 422 [4] without any binding limits of wind speed, due to large number of influencing factors and inability to generalize them. Wind changes speed and direction unpredictably, so during measurements, along with other atmospheric conditions, these need to be monitored.

In this research we used both, deceleration and stopping distance measurements. Deceleration was used as the most appropriate parameter for calculation of the difference in resistance force, in the presence and without presence of wind. The paper presents how this may lead to false conclusions when expressing brake

¹ UIC – The International Union of Railways (French: Union Internationale des Chemins de Fer)

weight based on the braking distance measurements. Brake weight is the main and only indicator of braking performance inscribed on each passenger and freight wagon, practically used in service when forming train compositions for estimation of the whole train braking performance.

Simulation and comparison with experimental results are performed using OpenFoam software considering the air as an incompressible medium and steady state conditions of flow. Geometric model of the wagon is somewhat simplified and adapted for CFD simulations.

The results of this research are vehicle's stopping distances measured under different wind conditions and drag force and drag coefficient, determined experimentally and numerically.

2 Braking Performance Test

Determining the braking performance of freight wagons with top speed up to 120 km/h and composite K-brake blocks requires slip tests with a single vehicle [9]. This is a full-scale test, during which the vehicle accelerates up to the required speed for braking. At this speed, an emergency (rapid) brake applies and at the same time or short time after the wagon is uncoupled from the test train composition and starts to brake until stop. The test speeds for freight wagons designed for top speed 120 km/h are 100 km/h and 120 km/h. Four valid tests need to be performed for determining the mean value of stopping distance. This value is then corrected for nominal test conditions and then braked weight percentage and brake weight is determined using assessment graphs or formulae given in [9]. Regular braking performance test methodology in the case of freight wagons assumes, among other preconditions, no wind or minimal wind during testing (no maximum wind speed is specified). Determining braking performance of one vehicle requires extensive preparation involving significant logistics, such as: locomotive, passenger coach for test team and installation of uncoupling device, closure of the test track section due to safety issues, etc.

This paper presents testing of the tank wagon type Zacns [5] (Figure 1), with K-block brakes, which are composite tread brakes, rated for 120 km/h maximum speed. When empty this wagon runs at 120 km/h and in the fully loaded conditions the maximum speed is 100 km/h. During slip tests the following braking parameters vs. time were recorded: wagon speed, stopping distance, main brake pipe pressure, brake cylinder pressure and deceleration of the wagon in the longitudinal direction.



Figure 1

Tank wagon Zacs in the test train composition [5]

Wagon speed and stopping distance were measured by using OMRON optical sensor by counting wheelset revolution and by radar doppler high performance transducer Delta DRS1000, GMH Engineering, independent of the wheelset revolution speed and in that way insensitive to slip and/or micro slip during braking. The total unadjusted error of the Doppler radar sensor for the speed range up to 120 km/h is about $\pm 0.5\%$. Figure 2 shows installed speed sensors on the testing wagon.



Figure 2

Speed and stopping distance sensors

Other measured parameters, pressures and deceleration in train motion direction, were measured using sensors and data acquisition system manufactured by Hottinger Baldwin Messtechnik. Based on the deceleration sensor characteristics (lateral sensitivity, linearity and hysteresis) and its calibration, expanded measurement uncertainty with a coverage factor 2 is about 1.4%.

The weather station (Figure 3) serves for checking the test conditions regularly. This station records: environmental temperature, atmospheric pressure, air humidity, wind speed and direction. It was placed on the test section in the middle of the stopping distance of the wagon.



Figure 3

Weather station position [10]

Figure 4 shows a typical measurement record when testing the brake with all the measured values shown, brake pipe pressure (BP), brake cylinder pressure (C), stopping distance (s) and vehicle speed (v), which are later used for further data processing and drawing conclusions about the braking performance.

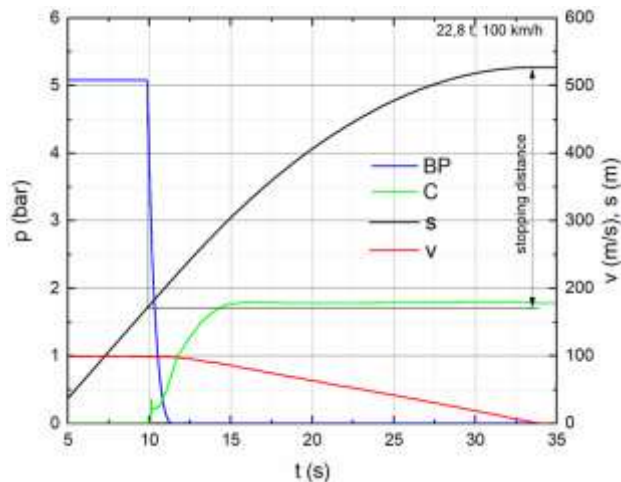


Figure 4

Typical record of measured parameters vs. time during braking of freight wagons [5]

3 Correcting the Stopping Distance

The stopping distance obtained during testing is corrected in order to take into account nominal speed in relation to the initial speed measured in the test and possible presence of gradient on the test track.

Considering that during braking process, most of the parameters are changing in a random way [11]. After determining the mean stopping distance out of four measurements ($j=1..4$), test validity and level of dissipation of the results are estimated by using following statistical criteria related to mean value and standard deviation:

$$\frac{\sigma_n}{s} \leq 0.03 \quad (1)$$

$$|s_e - \bar{s}| \leq 1,95 \cdot \sigma_n \quad (2)$$

where:

$$\sigma_n = \sqrt{\frac{\sum (s_j - \bar{s})^2}{n}} \quad (3)$$

and:

s_j – stopping distance measured during test "j" [m],

n – number of valid test [-],

σ – standard deviation of test results [-],

\bar{s} – mean stopping distance [m],

s_e – individual stopping distance furthest from the mean value [m].

The next step is correction of the mean stopping distance by the following criteria:

- basic principle - adaptation of the existing condition of the test vehicle to the actual characteristics of design series,
- additional correction - the actual filling time will be corrected in relation to the nominal value.

$$s_{\text{corr}} = t_e \cdot v_{\text{nom}} + \frac{F_{\text{test}} + F_R}{F_{\text{corr}} + F_R} \cdot (\bar{s} - v_{\text{nom}} \cdot t_e) \quad (4)$$

$$t_e = t_o + \frac{t_s}{2} \quad (5)$$

$$F_{test} = M \cdot \frac{v_{nom}^2}{2(\bar{s} - v_{nom} \cdot t_e)} - F_R \quad (6)$$

$$F_{corr} = F_{test} \cdot \frac{\eta_{dyn}}{\eta_{dyn,test}} \cdot \frac{d_{test}}{d_m} \cdot \left[\frac{p_{nom} - p_{feder}}{p_{test} - p_{feder}} \right] \quad (7)$$

S_{corr} – corrected mean stopping distance [m],

\bar{s} – mean stopping distance of test [m],

t_e – equivalent time for development of brake force [s],

t_s – mean measured brake cylinder filling time [s],

v_{nom} – nominal initial speed during tests [m/s],

F_{corr} – corrected brake force [N],

F_{test} – mean brake force during the test [N],

F_R – mean value of resistance to forward movement [N],

d_{test} – mean wheel diameter on test wagon,

d_m – diameter of semi-worn wheel [mm]; for block brakes $d_m = d_{test}$,

η_{dyn} – mean efficiency of brake rigging during operation,

$\eta_{dyn,test}$ – efficiency of brake rigging during test,

p_{nom} – nominal brake cylinder pressure [bar],

p_{test} – brake cylinder pressure on test vehicle [bar],

p_{feder} – pressure of retaining springs relative to the effective brake cylinder piston surface area [bar],

v_o – initial braking speed [m/s],

M – mass of the vehicle including rotational inertia [kg].

4 Determination of the Drag Coefficient

Proposed methodology for determination of the drag coefficient uses differences in resistance force acting on a railway vehicle during braking, in the case of absence and presence of wind. Running resistance is a significant characteristic of all forms of transport and all transport modes [6-9, 12-15]. It is a total force acting on a vehicle against its direction of travel. In the case of a railway vehicle, it consists of several components: mechanical resistance, aerodynamic resistance and grade

resistance. Mechanical resistance is mainly due to wheel rolling on the rail and increases during curves negotiation. Aerodynamic resistance is typically proportional to the square of the speed. It is additionally influenced by wind speed and its direction. Grade resistance depends on vehicle and track characteristics. During brake testing grade should be within $\pm 3\%$ [9].

The mean value of resistance to forward movement F_R is represented by a formula (8):

$$F_R = A + B \cdot v_0 + C \cdot v_0^2 \quad (8)$$

which consists of:

- one term independent of vehicle speed,
- the second term proportional to the speed, dealing mostly with the mechanical components resistance (vehicle-track),
- the third term proportional to the square of the speed (aerodynamic resistance),

where A, B, C are specific coefficients depending on vehicle type, selected according to [16] or obtained by measurements [6].

Since the creation of the Davis quadratic equation, it has been noticed that it includes the most significant factors influencing the resistance to movement, but that in some cases there are deviations that cannot be described in this equation form. Therefore, over time, a large number of authors have proposed different empirical expressions, which in specific cases better describe the dependence of resistance on different influential parameters.

Running resistance of freight trains is reported in [7]. Running resistance of passenger coaches was analyzed in ORE C179 [8]. Hara 1967 in Japan investigated influence of the aerodynamics on high-speed Shinkansen trains [12].

Running resistance is possible to be determined using different test methods:

- 1) Tractive effort methods,
- 2) Dynamometer drawbar methods,
- 3) Coasting methods [6].

The most suitable method, which can be used as a basis for assessment of wind drag during braking test, is adapted Coasting method. This method implies that the wagon or train accelerates to a certain speed. Then, the traction power and brakes are switched off and from that moment starts recording of speed vs. time on the track section without gradient or with known gradient along tracks. Coasting train will start to reduce speed and kinetic energy. Decelerations calculated from the speed vs. time function or directly measured by using appropriate deceleration transducer vs. vehicle speed, serves for estimation of train running resistance.

Unlike the coasting method in our case traction power is switched off, but the brakes are switched on and fully applied. Assuming that for one wagon, tested on the same track section, all test conditions are the same, the absence or presence of wind will cause a difference in deceleration, which is a consequence of wind drag force against vehicle travel direction.

The total force acting on a railway vehicle according to Newton's second law of mechanics is:

$$F_T - F_B - F_R = M \frac{dv}{dt} \quad (9)$$

where:

F_T – traction force [N] ,

F_B – total brake force [N],

F_R – total resistance force [N],

v – vehicle speed [m/s].

During braking, traction is off and the traction force is equal to zero. Development of brake force depends on the brake system characteristics. Total resistance force depends on A, B, C coefficients, where B and C participate in the members of the equation that are a function of vehicle speed. Assuming that brake force, first and second terms of resistance force are equal or almost equal under all other same conditions, differences in measured decelerations caused by wind presence and absence, multiplied by vehicle mass, represents third term of air resistance force $C \cdot v^2$ in both cases. In that way, it is possible to compare calculated and measured drag coefficients C_D and to validate numerical model for further analysis.

5 Aerodynamic Resistance Caused by Wind

Apart from the aerodynamic resistance included in the total running resistance, additional force acting on the vehicle is induced by wind blowing on the vehicle frontal side. Head wind generally helps the braking system and decreases stopping distance. Opposite, tail wind increases stopping distance. The following formula calculates drag force [17]:

$$F_D = \frac{1}{2} \cdot \rho \cdot A_f \cdot C_D(\beta) \cdot v_{rel}^2 \quad (10)$$

In the case of direct head wind ($\beta=0^\circ$):

$$F_D = \frac{1}{2} \cdot \rho \cdot A_f \cdot C_D(0^\circ) \cdot (v + v_{wind})^2 \quad (11)$$

where:

ρ – air density [kg/m^3],

C_D – air drag coefficient [kg/m^2],

β – yaw angle of wind [$^\circ$],

A_f – drag area [m^2],

v_{rel} – relative air speed [m/s],

v_{wind} – wind speed [m/s],

v – current speed of the vehicle [m/s].

Use of this equation for additional wind resistance, requires the third term in the equation (8) to be excluded and replaced with equation (11). Minor influence of speed change exists in the second term of equation (8) depending on the speed, but it could be neglected in this analysis as of smaller order of magnitude comparing to the third term, and especially if taking into account that all other test conditions are the same or similar.

6 Test Results

This analysis focuses on pure head wind. The yaw angle β between wind direction and train travel direction during experiments was less than $\pm 8^\circ$. The existence of this angle slightly reduces resulting head wind force and induce consequent side component of the wind force. Side wind may cause minor increase of running resistance related to mechanical components. This was neglected in this analysis since the yaw angle was quite small and better conditions in real test measurements are almost impossible to achieve. As stated above, this paper deals only with head wind component, as the worst possible scenario, considering that all other influences are known and equal during all tests. The main difference is the presence or absence of wind. One series of tests was performed without wind and one with head wind having the magnitude 7-9 m/s.

Table 1 presents test results for stopping distance in the case of wind presence and absence [10] and table 2 presents hypothetical difference in estimation of the braking performance using measured stopping distances, if the head wind influence was intentionally neglected. Test results show that in the case of Zacns tank wagon, head wind with the magnitude of $v_{\text{wind}} = 7-9$ m/s reduces stopping distance for about 27 m from initial speed $v_0=100$ km/h and from speed $v_0=120$ km/h for about 54 m. Consequently, determined brake weight B, if the wind was neglected, differs for 2-3 tonnes, which is unacceptably false result for assessment of the wagon braking performance.

Table 1
Measured stopping distance [9]

| Initial speed (km/h) | Stopping distance (m) | |
|-------------------------|-----------------------|---------|
| | Wind 7-9 m/s | No wind |
| 100 | 337.4 | 370.2 |
| | 340.9 | 378.3 |
| | 340.0 | 381.2 |
| | 342.2 | 350.7 |
| 120 | 473.2 | 508.0 |
| | 471.4 | 527.0 |
| | 476.2 | 508.6 |
| | 479.7 | 515.5 |

Table 2
Corrected mean stopping distance, brake weight percentage and brake weight

| Initial speed (km/h) | Wind 7 m/s | | | No wind | | |
|-------------------------|----------------|---------------|-------|----------------|---------------|-------|
| | s_{corr} (m) | λ (%) | B (t) | s_{corr} (m) | λ (%) | B (t) |
| 100 | 373.6 | 131.4 | 28.6 | 400.8 | 121.8 | 26.6 |
| 120 | 525.9 | 140.0 | 30.5 | 579.9 | 125.2 | 27.3 |

For determining the drag coefficient and wind force F_w , the results of measuring decelerations during braking are presented. The diagrams in Figures 5 and 6 show the records during four brakings from speeds of 100 and 120 km/h in both cases, with and without wind.

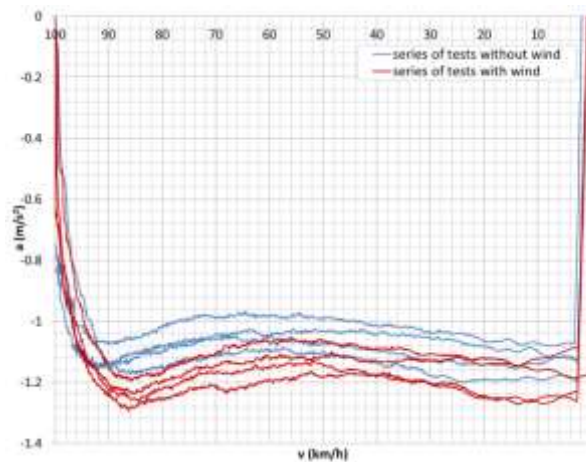


Figure 5
Series of deceleration vs. speed measurements at initial speed of braking 100 km/h

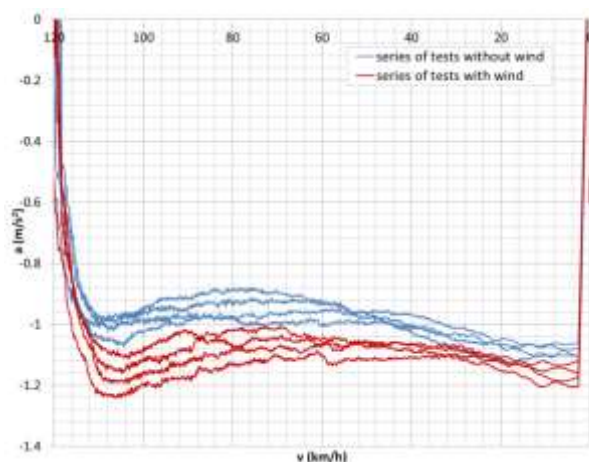


Figure 6

Series of deceleration vs. speed measurements at initial speed of braking 120 km/h

During the measurements at 100 km/h, some deviations were noticed, but the stopping distances were still within the limits according to the criteria of standard deviations. Most likely this is a consequence of insufficient bedding-in of the brake shoes during the first measurements. At 120 km/h this phenomenon was less pronounced.

For further analysis the mean values of measured decelerations were used. Figures 7 and 8 present mean values of each of the four measurements at different speeds and wind conditions.

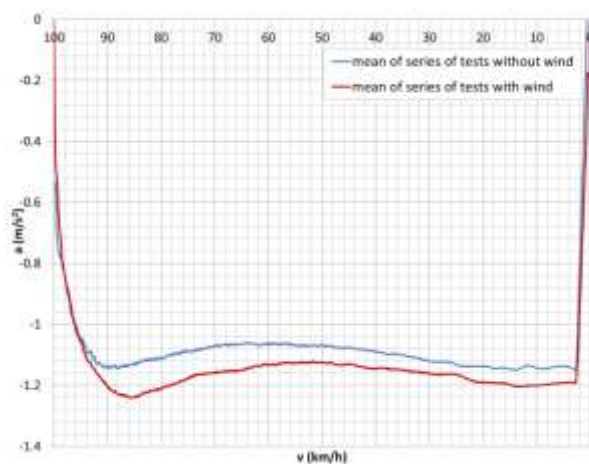


Figure 7

Mean values of deceleration vs. speed measurements at initial speed of braking 100 km/h

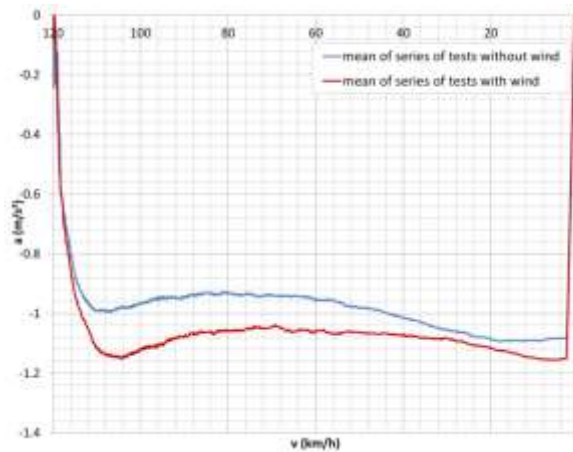


Figure 8

Mean values of deceleration vs. speed measurements at initial speed of braking 120 km/h

Based on the measured differences in decelerations Δa , it is possible to determine the share of wind force F_w in the total force, acting on the vehicle during its braking. Wind force in the longitudinal direction can be calculated as:

$$F_w = M \cdot \Delta a \quad (12)$$

By transforming expression (11), calculated drag coefficient using measured decelerations can be determined using next equation:

$$C_D = \frac{2 \cdot M \cdot \Delta a}{\rho \cdot A_f \cdot (v_{wind}^2 - 2 \cdot v \cdot v_{wind})} \quad (13)$$

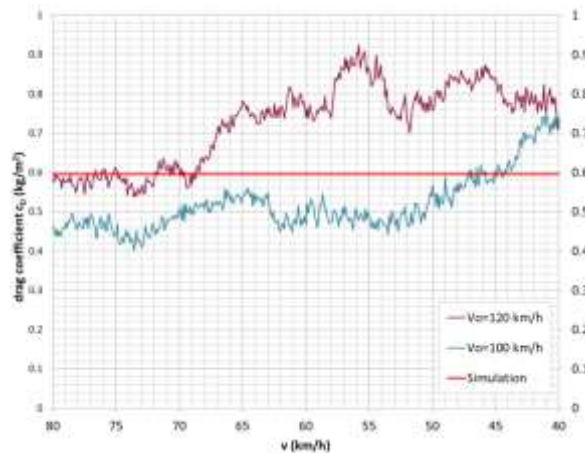


Figure 9

Calculated drag coefficient based on the measured wind influence on braking

The diagram in Figure 9 shows the drag coefficient C_D obtained by experimental measurements in the speed range in which the braking force reached the maximum value and became approximately constant, assuming that during braking the wind blew in the range of 7-9 m/s i.e. by using its mean value 8 m/s. C_D values obtained experimentally are relatively close to cca 0.6 kg/m² that was obtained by using numerical simulations presented below.

7 Numerical Simulations

There are many computer programs around the world dealing with train resistance simulations. They are power tools, serving for estimation of the energy consumption, for determining trains running time, etc. The computer programs specialized for running resistance including aerodynamic forces, use CFD and include wind magnitude, wind yaw angle, wind speed distribution, flow around the vehicle [1, 6, 12]. These programs may help solve different problems and performance of a vast number of simulations. In this paper, we use OpenFoam for comparison and widening possible conclusions about wind influence on braking performance test.

For numerical simulations of air flow around a rail tank wagon, the Reynolds averaged Navier-Stokes (RANS) approach is sufficiently accurate for this research [1]. Considering that maximal speed value is 120 km/h (33.3 m/s) and maximal Mach number less than 0.1, it is justified to assume that the flow is incompressible. During braking, vehicle speed changes almost uniformly, so with some approximations, it is possible to use assumptions of flow steadiness.

The main challenge in this type of simulation is to optimize computational mesh and to select computational method and turbulence modelling. The mesh is created with automated algorithm starting from triangulated surface geometries in Stereolithography (STL) format. After mesh independence test, it appeared that the optimum number of cells is about 5,700,000. The cells are generally hexagonal shape. For modelling turbulence, viscosity $k-\omega$ SST turbulence model is used and SIMPLE algorithm was used for solving system of discretized equations. Figure 10 shows air pressure distribution at 100 km/h. Figures 11 and 12 show air flow lines and air speed distribution.

The pressure distribution and the change in flow depend on the shape of the vehicle, but also on the boundary conditions of the modeled space, which include track geometry and its mechanical characteristics. The surface of the wagon is treated as no-slip walls. The ground is modeled as moving flat surface. Additionally, there is an impact of the equipment installed under the vehicle on flow characteristics, so it can be expected that real resistance to movement is a bit greater and actual drag coefficient is slightly higher compared to the one obtained in the simulations. This impact will be the subject of further research, in order to improve the model itself and the simulations accuracy.

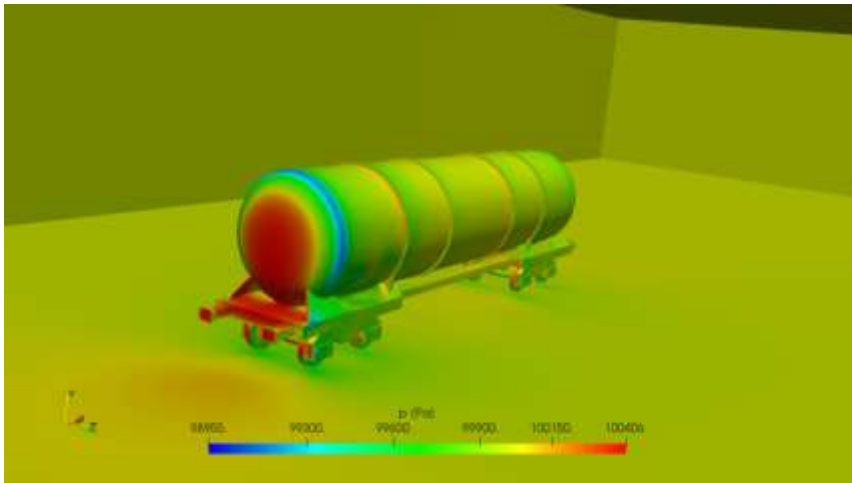


Figure 10
Air pressure distribution at 100 km/h

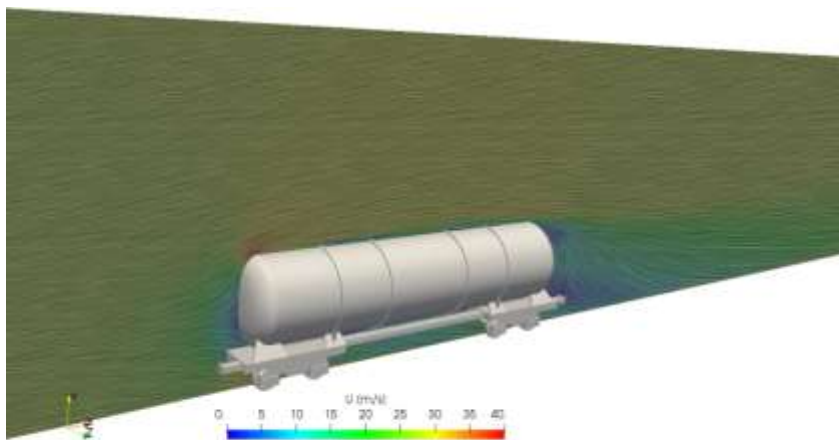


Figure 11
Air flow lines and air velocity distribution around the vehicle at 100 km/h

Computations were performed with air speed values in the range from 20 km/h to 120 km/h (Table 3), with the goal to calculate air drag force F_D and drag coefficient C_D . The total drag force generally consists of two parts: the pressure drag force that depends on the pressure distribution on the body surface and the viscous drag force that results from the friction between the air and the surface. The values of these forces obtained by simulations are presented in Table 3.

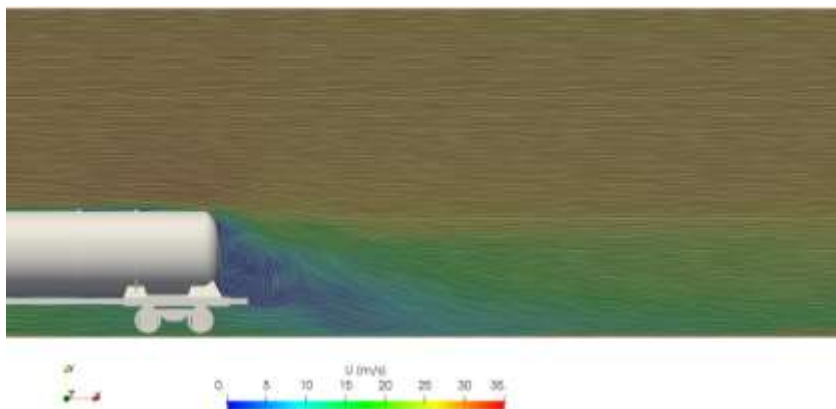


Figure 12

Air flow lines and air velocity distribution at rear of the vehicle at 100 km/h

Table 3

Review of the simulations results

| U [m/s] | U [km/h] | C_D [kg/m ²] | Drag force [N] | Pressure force [N] | Viscous force [N] |
|---------|----------|-------------------------------|-------------------|-----------------------|----------------------|
| 5.56 | 20 | 0.593 | 102 | 81 | 21 |
| 8.33 | 30 | 0.595 | 231 | 183 | 47 |
| 11.1 | 40 | 0.596 | 411 | 330 | 81 |
| 13.9 | 50 | 0.592 | 637 | 500 | 137 |
| 16.7 | 60 | 0.592 | 918 | 738 | 180 |
| 19.4 | 70 | 0.593 | 1251 | 1018 | 233 |
| 22.2 | 80 | 0.596 | 1643 | 1312 | 331 |
| 25.0 | 90 | 0.594 | 2073 | 1661 | 412 |
| 27.8 | 100 | 0.601 | 2588 | 2105 | 483 |
| 30.6 | 110 | 0.601 | 3131 | 2481 | 650 |
| 33.3 | 120 | 0.600 | 3720 | 2909 | 811 |

It is noticed that drag coefficient changes very slightly when the Re changes. This independence is typical of all bodies of a similar shape to the shape of tank wagon, at high values of Re [19]. Typical value for the dimensionless wall distance y^+ for the first cell layer used in this analysis was 30.

Conclusions

As required by the relevant European standards and as stated in UIC Technical Reports [4, 9, 16], when testing braking performance, the influence of wind should be excluded, by choosing test site and time of the test without presence of wind. The presence of wind will further complicate an already complex procedure for correcting measured stopping distance and reduce reliability of measurements.

Wind causes additional running resistance force that acts on the vehicle and the train compositions. Based on the available information from the railway practice and service, significant problems related to wind influence on braking process are not reported, however the test results show that in the case slip test of Zacns tank wagon, the head wind of magnitude 7 to 9 m/s reduces stopping distance for about 54 m during braking from initial speed 120 km/h. Consequently, this may lead to unacceptably false concluding and assessment of the vehicle's braking performance.

Recent editions of valid European standards [1, 6, 16] for any further analyses related to railway vehicles aerodynamics, suggest the use of CFD and experimentally determined resistance coefficients for each vehicle and not using general coefficients from the databases for similar vehicles, given in [18].

In order to obtain reliable indicators of the validity of applied analytical expressions and numerical simulations, further analyses should include more experimental tests under different wind magnitudes and directions of blowing. More realistic boundary characteristics and more detailed vehicle model will additionally increase simulations accuracy.

In addition to the main goal of this research, the paper proposes a way to separate the influence of the wind and air drag from the total resistance force acting on the vehicle. This allows us to determine drag coefficient of the tested vehicle based on the measurements of stopping distances during braking of a wagon, in the presence and absence of head wind of known wind speed.

Acknowledgement

Authors express gratitude to Ministry of Education, Science and Technological Development of Republic of Serbia, Project Contract 451-03-9/2021-14/200105.

References

- [1] EN 14067-6:2018+A1:2020 : Railway applications - Aerodynamics - Part 6: Requirements and test procedures for cross wind assessment
- [2] M. Yu, R. Jiang, Q. Zhang, *et al.*, Crosswind Stability Evaluation of High-Speed Train Using Different Wind Models. *Chin. J. Mech. Eng.* **32**, 40 (2019) <https://doi.org/10.1186/s10033-019-0353-7>
- [3] C. Baker, F. Chelli, A. Orellano, N. Paradot, C. Proppe, D. Rocchi, Crosswind effects on road and rail vehicles, *Vehicle System Dynamics* 47(8), 2009, pp. 983-1022
- [4] UIC B 126/DT 422 : Influence of head and tail wind on the braking distance of trains and single vehicles, Paris, December 2011
- [5] D. Milković, Brake performance test of Zacns wagon, No. LSV-I-7/20, Technical Report, University of Belgrade, Faculty of Mechanical Engineering, Laboratory of rail vehicles, Belgrade 2020

- [6] EN 14067-4:2013+A1:2018 : Railway applications - Aerodynamics - Part 4: Requirements and test procedures for aerodynamics on open track
- [7] ERRI A168.2/RP8 : Line tests with a view to reducing the aerodynamic drag of freight vehicles, Utrecht, 1992
- [8] ORE C179/RP2 : Determination of train resistance in the open air over typical track, using coasting method - BR analysis, Utrecht, 1991
- [9] EN 16834:2019: Railway applications - Braking – Brake performance
- [10] D. Milković, S. Radulović, G. Simić, J. Tanasković, Influence of head wind on the braking distance of single railway vehicle, Proc. of XIX International Scientific-expert Conference on Railway Railcon '20, October 15-16, 2020, Niš, Serbia, pp.13-16, ISBN: 978-86-6055-134-6
- [11] S. Koch, E. Köppen, N. Gräbner and U. von Wagner, On the influence of multiple equilibrium positions on brake nose, *Facta Universitatis, Series: Mechanical Engineering*, 2021, <https://doi.org/10.22190/FUME210106020K>
- [12] T. Hara, J. Ohkushi, B. Nishimura, Aerodynamic drag of trains QR of RTRI, 8 (4), 1967
- [13] Z. Nunić, M. Ajanović, D. Miletić, R. Lojić, Determination of the rolling resistance coefficient under different traffic conditions, *Facta Universitatis Series: Mechanical Engineering*, Vol. 18, No. 4, 2020, pp. 653-664
- [14] R. Tarakka, N. Salam, Jalaluddin, M. Ihsan, Effect of Blowing Flow Control and Front Geometry Towards the Reduction of Aerodynamic Drag on Vehicle Models, *FME Transactions*, Vol. 47, No. 3, 2019, pp. 552-559
- [15] H. S. Hansen, M. U. Nawaz, N. Olsson, Using operational data to estimate the running resistance of trains. Estimation of the resistance in a set of Norwegian tunnels, *Journal of Rail Transport Planning & Management*, Vol. 7, Issues 1-2, 2017, pp. 62-76, ISSN 2210-9706
- [16] EN 14531-1:2015 : Railway applications - Methods for calculation of stopping and slowing distances and immobilization braking - Part 1: General algorithms utilizing mean value calculation for train sets or single vehicles
- [17] P. Lukaszewicz, Energy consumption and running time for trains, Royal Institute of Technology, Stockholm, Doctoral Thesis, 2001
- [18] EN 14531-1:2005: Railway applications - Methods for calculation of stopping and slowing distances and immobilization braking - Part 1: General algorithms utilizing mean value calculation for train sets or single vehicles (withdrawn)
- [19] J. J. Kim, L. Sangseung, M. Kim, M., D. You, S. J. Lee, Salient drag reduction of heavy vehicle using modified cab-roof fairings, *Journal of Wind Engineering and Industrial Aerodynamics*, Vol. 164, 2017, pp. 138-151

Evaluation of Alternative Solutions of General Design of Railway Lines with Regards to Environmental Protection

Ljubo Marković¹, Ljiljana Milić Marković², Srđan Jović³, Miloš Milovančević⁴

¹ Faculty of Technical Sciences, University of Pristina, Kosovska Mitrovica, Serbia, ljubo.markovic@pr.ac.rs

² Faculty of Architecture, Civil Engineering and Geodesy, Univeristy of Banja Luka, Vojvode Stepe Stepanovića 77/3, Bosnia and Herzegovina, ljiljana.milic.markovic@aggf.unibl.org

³ Faculty of Technical Sciences, University of Pristina, Kosovska Mitrovica, Serbia; srdjan.jovic@pr.ac.rs

⁴ University of Niš, Faculty of Mechanical Engineering, Aleksandra Medvedeva 14, 18000 Niš, Serbia, milovancevic@masfak.ni.ac.rs

Abstract: The railway, by its physical size, is a specific continuous object in an area whose impact on the environment can be extremely unfavorable. The changes occurring under the influence of these effects have a strong feedback effect that can lead to new negative states and often very dramatic consequences. In this paper, within the General project for the construction of infrastructure corridor in the central part of the Kolubara basin, the evaluation of alternative solutions for rail sections is shown for the protection of the environment through methodology of multi-criteria compromise ranking. Identified and quantified are adverse impacts on the environment in an area that is a potential corridor. To analyze the impact, taking into account their specific characteristics and spatial relationships, certain indicators for each of the alternative solutions are determined. The procedure and results of multi-criteria evaluation is also presented.

Keywords: General Design; railroad; environmental protection; multi-criteria evaluation

1 Introduction

With the development of technology man has greatly affected the environment not taking care of its preservation and protection from the negative impact of such development. The question of how to protect the nature from man that is "oneself from oneself" has become not only the theme of the day, but the concept without

which it is impossible to reflect the modern world. Numerous experts in various studies are dealing with the identification of the key problems that we face in the environmental protection [1].

The European Union (EU) is also actively engaged in the issues of environmental protection. Currently, VI Action environmental program is in effect, which is implemented since 2002. The priorities of this program are: climate changes, nature and biodiversity, environment, health and quality of life, natural resources and waste.

Railway is one of the most efficient and environmental-friendly ways to transport people and goods. The results in article [2] have indicated that the environmental efficiency slowly increased during 2006-2011 and it exhibits regional disparities with the eastern area having the highest environmental efficiency and the western area being the lowest one and it was found a significant positive impact of railway transportation on higher environmental efficiency. Ballasted railway tracks, despite their benefits, present some limitations and drawbacks, mainly associated with geometry degradation due to ballast settlement and particle breakage [3]. The current closed, government-dominated decision making, opaque information provisioning, and lack of communication with and involvement of residents cause low levels of trust in railway-related local governmental agencies and companies [4]. There is increasing concern about environmental pollution by diffuse emissions of various environmental hazards emitted by transportation activities and selected studies may establish an understanding on relevant processes and environmental risk of railway emissions to soil, drainage water and groundwater [5]. Transport infrastructure is closely linked to several sustainability issues of main policy relevance, and significant impacts on biodiversity as well as resource use and construction costs relate to the corridor design and location in the landscape [6].

2 Environmental Protection Parameters in the Railway Lines Designing Process

The rapid economic growth and development directly affect the increased volume of all forms of transport. In the area of environmental protection, railway is the most acceptable form of transportation. Advantages of the use of railways in relation to other modes of transport (road and air) is reflected in the reduction of noise and air pollution, smaller impacts on flora and fauna, rail corridors occupy less arable land from a road, and the lower the cost of rehabilitation of the damaged environment [7]. European railway administrations, in accordance with the concept of sustainable transport EST (Environmentally Sustainable Transport) [8], are undertaking the following activities to protect the environment.

In the process of planning and design, the designers of railway examine all relationships between railway lines-environment. The success of design in the field of environmental protection from the negative impacts of the railroad requires a comprehensive review and definition of the effective parameters in relation to the main elements of the environment: climate, sound, soil, water, flora and fauna, landscape (Table 1).

Table 1
Matrix of relation railway and the environment [9]

| | Settlements | | | Rest Zones | | Protection Zones | | Water supply | | Agriculture | | | | Schemes |
|------------------------------|-------------|-------|------------|-------------------|---------------------|------------------|----------------|---------------|--------|-------------|----------|------------------|--------------------|---------|
| | Urban type | Mixed | Rural type | Individual points | Rest zones surfaces | Natural reserves | Natural wholes | Water sources | Waters | Farmland | Orchards | Special cultures | Pastures and turfs | |
| Microclimate | | | | | | | | | | | | | | |
| Air turbulation | | | | | | | | | | * | * | * | * | * |
| Potential frost | | | | | | | | | | * | * | * | * | * |
| Appearance of fog | | | | | | | | | | * | * | * | * | * |
| Sound | | | | | | | | | | | | | | |
| Noise | * | * | * | * | * | | | | | | | | | |
| Vibrations | * | * | * | * | * | | | | | | | | | |
| Soil | | | | | | | | | | | | | | |
| Erosion | | | | | | | | | | * | * | * | | |
| Compaction | | | | | | | | | | | | | * | |
| Pollution | | | | | | | | | | * | * | * | * | * |
| Water | | | | | | | | | | | | | | |
| Surface waters pollution | | | | * | * | | | * | * | | | | | |
| Underground waters pollution | | | | | | | | * | * | | | | | |
| Changes in level | | | | | | * | * | | | * | * | * | * | * |
| Fauna | | | | | | | | | | | | | | |
| Species extinction | | | | | * | * | * | | | | | | | * |
| Extinction | | | | | * | * | * | | | | | | | * |
| Seizure of territory | | | | | | | | | | | | | | |
| Flora | | | | | | | | | | | | | | |
| Species extinction | | | | | * | * | * | | | | | | | |
| Obstruction | | | | | * | * | * | | | | | | | |
| Landscape | | | | | | | | | | | | | | |
| Visual disturbances | * | * | * | * | * | * | * | | | | | | | |
| Changes of relief | * | * | * | * | * | * | * | | | | | | | |
| Intersecting the wholes | * | * | * | * | * | * | * | * | * | | | | | * |

The process of creating design solutions for railway is designing real corridors - the routes the end result of which are various solutions on the corresponding substrates. In the railway design methodology four phases are defined: general design, conceptual design, operational project and archive project. In each of these phases also included is defining the environmental impact. Each project within a single methodology begins and ends with clear viewpoints as to provide optimal solutions.

2.1 Evaluation of Alternative Solutions in the Phase of General Project

The result of the general project is a defined corridor with offered alternatives – and the routes within it. In the process of valuation of the alternatives, for the choice of the optimal solution variation methods of multi-criteria evaluation (PROMETHEE, AHP, ELECTRE, VIKOR) are used. As a basis for the evaluation of alternative solutions an ordered list of objectives is formed: A – Construction costs; B – Costs of maintenance and management; C - Implications for users; D - Safety and comfort; E - Development and spatial effects; F – Environmental protection. Within each of these objectives the associated criteria and indicators are defined. Definition of goals, criteria and indicators is one of the most sensitive steps in the overall process of evaluating alternative solutions. The list defines the influences relevant to the offered route, quantifies their importance in specific conditions, i.e., it is about the procedures directly affecting the results of the evaluation of alternative solutions.

3 Environmental Protection (Objective F)

This objective includes minimizing adverse effects on the environment caused by the construction of the future route of the railway in terms of increased levels of noise, vibration, climate and microclimate, soil pollution, water pollution, soil occupation, degradation of flora and fauna. The omission of the aims from the evaluation process can have far-reaching consequences that culminate over time and lead to all serious forms of environmental degradation. Within the goal, defined criteria and indicators include the effects related to the consequences of the construction of the railway track to the environment. The basis for their definition are results supporting environmental studies and synthesis maps of limitation. The criteria are expressed in terms of partial utility score (P) of each criterion, i.e. evaluation of partial benefits for the individual criteria are added together with the use of relative weights. All the indicators of mentioned criteria are quantitative in nature. Table 2 provides an overview of the criteria and indicators that have been adopted on the basis of the analysis developed for the general design railways. Determination of relative weight of criteria and indicators is the obligation of the project team. Designers should critically consider, adopt or provide their proposals in accordance with the knowledge of specific areas and specific characteristics. Weight coefficients of the criteria and indicators cannot be determined on the basis of precisely defined data, but they are determined through expert judgment (survey procedure on specific groups of professionals) and/or by analysis of previous assessments, decisions and reactions of certain population groups through which the attitude of the community towards the above issues is quantified.

Table 2
Criteria and Indicators of F goal

| CRITERION K | INDICATOR P _i | DIMENSIONS OF THE INDICATOR |
|--|---|---|
| K_{F1} NOISE | | min |
| 1.1. | Noise level during the day in settled areas | The area of number of people under the applicable levels |
| 1.2. | Noise level during the night in settled areas | The area of number of people under the applicable levels |
| K_{F2} VIBRATIONS | | min |
| 2.1. | Vibrations level during the day in settled areas | The area of number of people under the applicable levels |
| 2.2. | Vibrations level during the night in settled areas | The area of number of people under the applicable levels |
| 2.3. | The facilities with sensitive equipment exposed to (day/night) vibrations | The area of number of people under the applicable levels |
| K_{F3} ELECTROMAGNETIC RADIATIONS | | min |
| 3.1. | Electromagnetic radiation in urban areas | The area of number of people under the applicable levels |
| K_{F4} WATER POLLUTION AND THE REGIME CHANGES | | min |
| 4.1. | Existing and planned areas for water supply | The surface of zone exposed to pollutants |
| 4.2. | Surface water (liquid or stagnant) exposed to pollutants from traffic systems | Surface of areas endangered along the coast |
| 4.3. | Changes in the underground regime | The area with the changes in the regime |
| 4.4. | Changes in the surface water regime | The area with the changes in the regime |
| K_{F5} POLLUTION AND SOIL DEGRADATION | | min |
| 5.1. | Soil pollution (liquid solid pollutants) from the traffic system | The terrain surface being polluted or the pollutants quantity |
| 5.2. | Soil degradation by erosion, landslide due to railway construction | Degraded soil surface |
| 5.3. | Soil affected by the change of permeability | The area with the changes of permeability |
| K_{F6} FLORA AND FAUNA | | min |
| 6.1. | Presence of characteristic flora in areas along the tracks | The area with the characteristic flora |
| 6.2. | Protected plant species endangered by the transport | The area underprotected plant species being endangered |
| 6.3. | Protected animal species endangered by the transport | The area underprotected animal species being endangered |
| 6.4. | Biodiversity | Number of certain plant and animal species being reduced |
| K_{F7} CLIMATE AND MICRO-CLIMATE | | min |
| 7.1. | Changes in climate characteristics | The area with altered climate characteristics |
| 7.2. | Changes in micro-climate characteristics | The area with altered micro-climate characteristics |
| K_{F8} OCCUPYING AREAS | | min |
| 8.1. | Changes in the terrain morphology | The area with altered morphology |
| 8.2. | Changes in terrain vegetation | The area with altered vegetation |
| 8.3. | Changes in surface waters | The area with changes in surface waters |
| K_{F9} RAILWAY CONSTRUCTION RESOURCES | | min |
| 9.1. | Resources consumption for construction by type | The area with altered regime |

Criterion K_{F1} : Noise

The sections are defined of the route passing through populated areas and the intensity of the noise equivalent level to medium (during the day and during the night) is determined and its impact in the area of 25 m and 100 m from the axis line. The noise impact, i.e. the level of noise endanger is expressed by the surface noise or by the number of people that are under applicable noise level during the day (an indicator $P_{F1,1}$) or night (indicator $P_{F1,2}$) in urban areas. Value of the criterion is obtained through the criteria function f_{F1} :

$$f_{F1} = \sum_{i=1}^2 \omega_i P_{F1,i} \quad (1)$$

$$\omega_i - \text{weight coefficients for which applies, and } \sum_{i=1}^2 \omega_i = 1 \quad (2)$$

Criterion K_{F2} : Vibrations

The sections are defined of the route passing through populated areas and the intensity of the vibrations through the level during the day ($P_{F2,1}$), and during the night ($P_{F2,2}$) is determined and its impact in the area of 100 m from the axis track line. The effect of vibrations is expressed by the surface or the number of people under the applicable level of vibration during the day or night in the urban areas, or the number of buildings with sensitive equipment that is under applicable vibration levels during the day and night ($P_{F2,3}$). Values of the indicators are shown through partial benefit in the score of 1 to 10. Value of the criterion K_{F2} is obtained through the criteria function f_{F2} :

$$f_{F2} = \sum_{i=1}^3 \omega_i P'_{F2,i} \quad (3)$$

where: $P'_{F2,i}$ - the values of the indicators reported through partial use

$$\omega_i - \text{weight coefficients for which applies, and } \sum_{i=1}^3 \omega_i = 1 \quad (4)$$

Criterion K_{F3} : Electromagnetic Radiation

The sections of the route passing through populated areas are defined and the intensity of electromagnetic radiation and their influence in the corridor of the track is determined. This affect ($P_{F3,1}$) is shown by the area or group of people who are under the applicable level. The criteria value K_{F3} is obtained through the function f_{F3} :

$$f_{F3} = P_{F3,1} = \sum_{j=1}^n q_{F3,1,j} \quad (5)$$

where $q_{F3.1,j}$ - the surface or number of people in the j -th section of the route is under the applicable electromagnetic radiation.

Criterion K_{F4} : Water Pollution and Changes in the Regime

The sections of the route are determined passing by the existing or future water supply zone, along the surface waters, the area where there is a change in the regime of water level and the level of contamination of water supply zones and coastal area due to contaminants of the transport system reaching the water is determined, that is the degree of change in the water level regime. These effects are shown through analytical indicators ($P_{F4,i}$):

$$P_{F4,i} = \sum_{j=1}^n P_{F4,i,j} \quad (6)$$

Value of the criterion K_{F4} is obtained through the criteria function f_{F4} , by summarizing the above indicators $P_{F4,i}$ and the corresponding weight coefficients:

$$f_{F4} = \sum_{i=1}^4 \omega_i P_{F4,i} \quad (7)$$

$$\omega_i - \text{weight coefficients for which applies, and } \sum_{i=1}^4 \omega_i = 1 \quad (8)$$

Criterion K_{F5} : Pollution and Soil Degradation

The sections are determined where contamination can occur by a ground transportation system, degradation of soil by erosion and creeping due to railroad construction and changes in permeability. Value of the criterion K_{F5} is obtained through the criteria function f_{F5} , by summarizing the above indicators $P_{F5,i}$ and the corresponding weight coefficients:

$$P_{F5,i} = \sum_{j=1}^n P_{F5,i,j} \quad (9)$$

$$f_{F5} = \sum_{i=1}^4 \omega_i P_{F5,i} \quad (10)$$

$$\omega_i - \text{weight coefficients for which applies and } \sum_{i=1}^4 \omega_i = 1 \quad (11)$$

Criterion K_{F6}: Flora and Fauna

It is determined which sections of the route pass through an area of protected plant and animal species and the impact on the area is determined, as analytically indicated by the indicators:

$$P_{6,i} = \sum_{j=1}^n P_{F6,i,j} \quad (12)$$

where n is a number of protected plant and animal species.

Value of the criterion is obtained through the criteria function f_{F6} , by summarizing the above transformed indicators and the corresponding weight coefficients:

$$f_{F6} = \sum_{i=1}^4 \omega_i P'_{F6,i} \quad (13)$$

where: $P_{F6,i}$ - the indicator is expressed through the partial benefit

$$\omega_i - \text{weight coefficients for which applies and } \sum_{i=1}^4 \omega_i = 1 \quad (14)$$

Criterion K_{F7}: Climate and Micro-Climate

The sections of the route are determined where the consequences in the form of climate change, i.e. microclimate will occur. This is expressed analytically through indicators:

$$P_{F7,i} = \sum_{j=1}^n P_{F7,i,j} \quad (15)$$

where n is a number of consequences in the form of climate change.

The value of the criterion K_{F7} is obtained through the criteria function f_{F7} , by summarizing the above indicators $P_{F7,i}$ and the corresponding weight coefficients:

$$f_{F7} = \sum_{i=1}^2 \omega_i P_{F7,i} \quad (16)$$

$$\omega_i - \text{weight coefficients for which applies and } \sum_{i=1}^2 \omega_i = 1 \quad (17)$$

Criterion K_{F8}: Occupying Areas

The sections of the route are determined where there will be a change in morphology of the terrain, changes in vegetation composition and changes in surface water. These effects are shown analytically through the indicator:

$$P_{F8,i} = \sum_{j=1}^n P_{F8,i,j} \quad (18)$$

where n is a number of in morphology of the terrain, changes in vegetation composition and changes in surface water.

The value of the criterion K_{F8} is obtained through the criteria function f_{F8} , by summarizing the above indicator $P_{F8,i}$ and the corresponding weight coefficients:

$$f_{F8} = \sum_{i=1}^3 \omega_i P_{F8,i} \quad (19)$$

$$\omega_i - \text{weight coefficients for which applies and } \sum_{i=1}^3 \omega_i = 1 \quad (20)$$

Criterion K_{F9} : Railway Construction Resources

Consumption of natural resources (gravel, sand, crushed stone, wood) to build the railway is expressed through K_{F9} criterion and the criterion function f_{F9} that is by the indicator $P_{F9,1}$. The value of the $P_{F9,1}$ indicator is obtained by summing the resources spent by type for certain positions of the construction works:

$$P_{F9,1} = \sum_{j=1}^n \omega_j a_j \quad (21)$$

where:

$P_{F9,1}$ - is the indicator defining the total amount of natural resources that will be spent for the construction of the railway

a_j - quantity of natural resources (j -th type) spent for the construction works of the railway;

ω_j - weight coefficients, which demonstrate the importance of a particular resource for the construction works.

K_{F9} criterion is obtained through the criterion function f_{F9} that is based on the indicator $P_{F9,1}$:

$$f_{F9} = P_{F9,1} \quad (22)$$

4 Example of Valuation Method Application

The industrial company Mining Basin "KOLUBARA" Ltd., in order to ensure safety in the operation of the entire power system of Serbia must open a new open pit mines as replacement capacity for existing mines due to increased production of TPP "Kolubara B". The main prerequisite for the construction of new mines is the relocation of significant infrastructure facilities: rivers, roads, railroads, industrial facilities, as well as settlements. In this regard, the formation of a new transport corridor is analyzed, which is defined in planning documents [10] [11]. Within the general project [12] for the relocation of infrastructure four alternative solutions for relocation of railroad sections of the railway Belgrade - Bar have been proposed. Also, proposed is the formation and development of studies on the impact on the environment of forming a corridor for the relocation of infrastructure [813].

4.1 Solutions of Relocation of the Railroad in the Central Part of the Kolubara Basin

Variation solutions (Figure 1) of the main railway Belgrade - Bar on the area in question were created in relation to a given corridor, the area for stable plants of mining complex, the position of relocated channel of the river Kolubara, technological bridge position and the mutual spatial relations of the river, railway and road. Boundary elements of the plan and profile are determined based on the given calculated speed $V_r = 160$ m/h. A cross-section of double track formation with a width of planum of 11.20 m has been adopted.

Variation Solution 1

In the first variation model solution the railway is relocated so that after leaving the existing corridor of the existing traffic the railroad crosses through the relocated channel of the river Kolubara in place of a technological bridge. In this solution railway crosses using an overpass of the technological bridge. Further the railroad is parallel to the displaced bed of the river Kolubara. Length of railroad dislocation per this version is 13.07 kilometers.

Variation Solution 2

In the second variation the railroad is relocated by the line running down the left side of the Kolubara River, passing under the technological bridge, continues parallel to the displaced river bed, crosses the South Peštan and fits into existing railroad. Length of railroad dislocation per this version is 12.01 kilometers.

Variation Solution 3

The third version of the track layout plan is fully consistent with option 2, but in this variation the track crosses the technology bridge with an overpass.

Variant Solution 4

In the fourth variant solution the railroad is displaced so that after leaving the existing traffic corridor the railway crosses the relocated Kolubara river bed in the third stage before the technological bridge, and then the technological bridge which after crossing the river has lowered down to the projected levels of the terrain. Further the railroad is parallel to the displaced bed of the river Kolubara (the left bank). Length of railroad dislocation per this version is 13.07 kilometers.

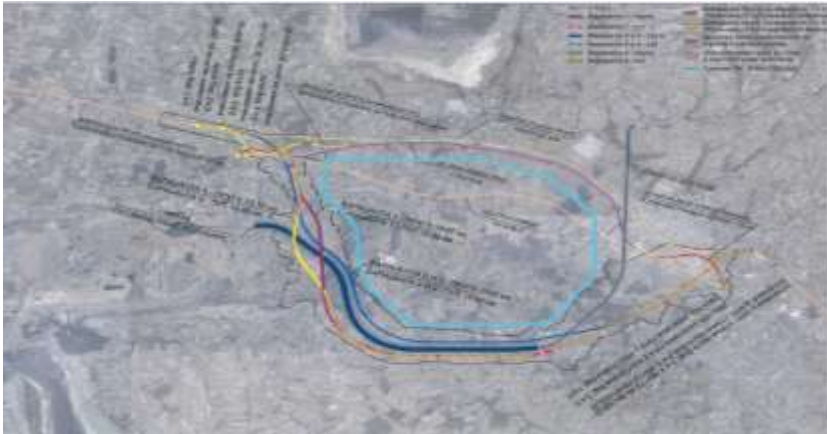


Figure 1

Overview map of the variant solutions [12]

4.2 Variant Solutions Valuation from the Aspect of Environmental Protection

The process of evaluating of variant solutions in terms of the impact on the environment aims at minimum adverse effects. Evaluation of the proposed variant solutions in terms of environmental protection has been performed using multi-criteria compromise ranking [14]. This method solves the optimization problem with multiple heterogeneous and conflicting criteria. The resulting solution is a compromise; it may be unique or represent sets of related solutions. The compromise solution is the one permissible solution that is closest to the ideal. The ideal solution is defined on the basis of best values criteria and is usually not in a given set of alternative solutions.

4.2.1 Variants, the Applicable Criteria and Relative Weights

The process of evaluating started by four alternative solutions of displacement of the Belgrade-Bar into the reserved corridor proposed at the level of General project [14]. Selection of the criteria and their partial participation (relative weight) were made based on experience in implementation of similar studies, project documentation and surveys where multidisciplinary team members took part.

To determine the relative weights of the criteria a simplified Delphi method on a sample of 30 respondents with average years of service over 30 was applied. Participants in the survey analyzed the importance of each criterion with respect to general knowledge and specific site conditions (Table 3).

Table 3
Criteria and criterion weight

| Ord.no | Criterion | Criterion weight |
|--------|---|------------------|
| 1. | Noise | 0.24 |
| 2. | Vibrations | 0.13 |
| 3. | Water pollution and changes in the regime | 0.16 |
| 4. | Pollution and soil degradation | 0.17 |
| 5. | Flora and fauna | 0.11 |
| 6. | Climate and micro-climate | 0.06 |
| 7. | Occupying areas | 0.13 |

For selected criteria the parameters and their quantitative representation have been defined. For each of the criteria the indicators are defined (Table 4) and their weights determined: P – Pronounced effect ($\omega_1=0,67$); LP – Less pronounced effect ($\omega_2=0,33$) and N – No effect ($\omega_3=0$). All effects are reduced to a common unit (meter of track).

Table 4
Criteria, indicators and their quantitative views

| Criterion (effect) | Indicator | Quantitative overview |
|---|----------------------|---|
| Noise | Pronounced (P) | Length of the route through settlement |
| | Less pronounced (LP) | Settlements in the impact zone of 1,000 m |
| | No effect (N) | Remaining length of the route |
| Vibrations | Pronounced (P) | Length of the route through the archaeological sites |
| | Less pronounced (LP) | Length of the route through settlements |
| | No effect (N) | Remaining length of the route |
| Water pollution and changes in the regime | Pronounced (P) | The length of the route with watercourses closer than 100 m |
| | Less pronounced (LP) | Other watercourses in the area of 1000 |
| | No effect (N) | Remaining length of the route |
| Pollution and soil degradation | Pronounced (P) | Length of the route through orchards, vineyards and fields |
| | Less pronounced (LP) | Length of the route through pastures, forests and other |
| | No effect (N) | Bridges, tunnels and settlements |
| Flora and fauna | Pronounced (P) | Length of the route through forests |
| | Less pronounced (LP) | All except forests and settlements |
| | No effect (N) | Length of the route through settlements |

| Criterion (effect) | Indicator | Quantitative overview |
|---------------------------|----------------------|--|
| Climate and micro-climate | Pronounced (P) | The length of the embankment and the cut over 6 m |
| | Less pronounced (LP) | Other cuts and embankments |
| | No effect (N) | Tunnels and bridges |
| Occupying areas | Pronounced (P) | Route length through settlements, military and economic structures |
| | Less pronounced (LP) | Length of the route through the agricultural zones |
| | No effect (N) | Remaining length of the route |

By reading the relevant data from thematic maps and by the quantification of the effects, the input data for the evaluation of variant solutions according to the adopted criteria were obtained (Table 5).

Table 5
Indicators for evaluating the effects

| Variant solution | Degree of the pronounced effect | Noise | Vibrations | Water pollution | Pollution and soil degradation | Flora and fauna | Climate and micro-climate | Occupying areas |
|------------------|---------------------------------|-------|------------|-----------------|--------------------------------|-----------------|---------------------------|-----------------|
| Variant 1 | P | 1060 | 7500 | 2455 | 57 | 250 | 3814 | 1060 |
| | LP | 3300 | 1060 | 1283 | 2343 | 1060 | 6275 | 2512 |
| | N | 8710 | 4509 | 9331 | 10669 | 11759 | 1283 | 9497 |
| Variant 2 | P | 190 | 6560 | 2403 | 8 | 615 | 3026 | 190 |
| | LP | 2750 | 190 | 140 | 330 | 190 | 7163 | 2411 |
| | N | 9073 | 5263 | 9470 | 11675 | 11208 | 140 | 9412 |
| Variant 3 | P | 190 | 6560 | 2403 | 8 | 615 | 1839 | 190 |
| | LP | 2750 | 190 | 1574 | 1764 | 190 | 6917 | 2411 |
| | N | 9073 | 5263 | 8036 | 10241 | 11208 | 1574 | 9412 |
| Variant 4 | P | 1103 | 7425 | 2565 | 57 | 213 | 3376 | 1103 |
| | LP | 3245 | 1103 | 1210 | 2313 | 1103 | 6324 | 2621 |
| | N | 8758 | 4578 | 9331 | 10736 | 11790 | 1190 | 9382 |

4.2.2 The Results of Calculation and Analysis

Based on the performed procedures of evaluating variant solutions at the observed area using multi-criteria method of compromise ranking results were obtained by which the Variant 2 from the aspect of environmental protection has an advantage of 39.3% compared to Variant 3, 98.9% compared to Variant 4, while as compared to Variant 1 has an advantage of 99.3%. The obtained results of the valuation are presented in Table 6.

Table 6
Variant solutions ranking

| Ord.no. | Advantage in % | Variant solution |
|---------|----------------|------------------|
| 1) | 0 | Variant 2 |
| 2) | 39,3 | Variant 3 |
| 3) | 98,9 | Variant 4 |
| 4) | 99,3 | Variant 1 |

Conclusions

Environmental protection is now a first-rate social problem. The protection of the environment in the process of designing railway is access in the earliest stages of making the technical documentation and it occupies the very top of the matrix of aims to evaluate the offered alternatives. This approach reduces the contingency fund for the execution of technical measures of precautions, i.e. reduces investment costs. In order to include the aspects of environmental protection into the methodology of evaluation of alternative solutions their comprehensive knowledge and determination is necessary. This paper presents a method of multi-criteria compromise ranking of alternative solutions and its application for the variant solutions evaluation as well as unambiguous definition of the optimal solution route for the protection of the environment during the preparation of the General Project of the railway. Based on the analysis of its effects it is concluded that the offered various solutions for the rail sections defined in the project will have a certain negative impact on the environment. Using these criteria of benefits of the area, from the standpoint of environmental protection, the optimal route of the railway in the studied corridor was adopted, which along with the necessary minimal measures of protection reduces the potential impact during the future railway exploitation to the smallest possible measure. As a result of application of the multi-criteria compromise ranking method the variant solution 2 was given priority as a compromise solution for making the final decision on the selection of optimal route.

For future investigation there is a need to increase protection modes and solutions [15, 16]. Also artificial intelligence techniques could be incorporated as well in the system.

References

- [1] W. J. Sutherland et al.: Identification of 100 fundamental ecological questions. *Journal of Ecology*, 101, 2013, pp. 58-67
- [2] Song, M., Zhang, G., Zeng, W., Liu, J., & Fang, K. (2016) Railway transportation and environmental efficiency in China. *Transportation Research Part D: Transport and Environment*, 48, 488-498
- [3] Sol-Sánchez, M., & D'Angelo, G. (2017) Review of the design and maintenance technologies used to decelerate the deterioration of ballasted railway tracks. *Construction and Building Materials*, 157, 402-415

- [4] He, G., Mol, A. P., Zhang, L., & Lu, Y. (2015) Environmental risks of high-speed railway in China: public participation, perception and trust. *Environmental Development*, 14, 37-52
- [5] Burkhardt, M., Rossi, L., & Boller, M. (2008) Diffuse release of environmental hazards by railways. *Desalination*, 226(1-3), 106-113
- [6] Karlson, M., Karlsson, C. S. J., Mörtberg, U., Olofsson, B., & Balfors, B. (2016) Design and evaluation of railway corridors based on spatial ecological and geological criteria. *Transportation Research Part D: Transport and Environment*, 46, 207-228
- [7] Economical and Ecological Comparison of Transport Modes: Road, Railways, Inland Waterways, Summary of Findings, PLANCO Consulting GmbH, Essen, November, 2007
- [8] OECD Guidelines towards Environmentally Sustainable Transport, OECD, 2002
- [9] M. Kosijer: Contribution to the methodology of valuation variants for high-speed lines at the level of the General Project, Thesis, The Faculty of Civil Engineering, Belgrade, in 1994 (in Serbian)
- [10] Shatrov, Mikhail G. et al. Influence of pressure oscillations in common rail injector on fuel injection rate. *Facta Universitatis, Series: Mechanical Engineering*, [S.l.], v. 18, n. 4, pp. 579-593, Dec. 2020
- [11] Kuchak, A. J. T., Marinkovic, D., Zehn, M. Parametric Investigation of a Rail Damper Design Based on a Lab-Scaled Model (2021) *Journal of Vibration Engineering and Technologies*, 9 (1), pp. 51-60
- [12] Tigh Kuchak, A. J., Marinkovic, D., Zehn, M. Finite element model updating - Case study of a rail damper (2020) *Structural Engineering and Mechanics*, 73 (1), pp. 27-35
- [13] Traffic Institute CIP: Previous analysis of the impact of forming a corridor for the relocation of infrastructure facilities on the environment, Belgrade, June 2010 (in Serbian)
- [14] S. Fischer, Investigation of effect of water content on railway granular supplementary layers, *Naukovyi Visnyk Natsionalnoho Hirnychoho Universytetu*, ISSN 2071-2227, E-ISSN 2223-2362, 2021, № 3, doi.org/10.33271/nvngu/2021-3/064
- [15] Németh, A., & Fischer, S. (2021) Investigation of the glued insulated rail joints applied to cwr tracks. *Facta Universitatis, Series: Mechanical Engineering*, doi: 10.22190/FUME210331040N
- [16] Sysyn, M., Nabochenko, O., Kovalchuk, V., Przybyłowicz, M., & Fischer, S. (2021) Investigation of interlocking effect of crushed stone ballast during dynamic loading. *Reports in Mechanical Engineering*, 2(1), 65-76, <https://doi.org/10.31181/rme200102065s>

Maintenance Reliability of Railway Curves Using Their Design Parameters

Mykola Kurhan, Dmytro Kurhan, Nelya Hmelevska

Department of Transport Infrastructure, Dnipro National University of Railway
Transport named after Academician V. Lazaryan
Lazaryan st. 2, 49010 Dnipro, Ukraine
{mykolakurhan, kurhan.d, hmelevnela}@diit.edu.ua

Abstract: Based on the conducted monitoring of the railway track operation, it is shown, that most curves fail to meet the source nameplate data. Proposals have been developed to reduce the intensity of the track disorder, due to the reduction of curve parameters to the normative requirements, operating in Ukraine. Recommendations obtained in this work will contribute to the effectiveness of design decisions, determine the quality of the reconstruction projects in general and the expediency of its implementation in particular, they will be useful for carrying out activities to improve the smoothness of trains movement, increase the speed and level of travel comfort, in the curved tracks, especially in the future development of high-speed train implementations.

Keywords: railway; railway curve; survey of curves; accuracy assessment; reliability

1 Introduction

Since the beginning of railways, research was carried out in all industrialized countries, in order to increase the speed of trains. The maximum speed of trains was and remains the measurement of the technical progress and economic development of a country. A distinctive point dividing the usual movement from the high-speed one, was the round figure of 100 mp/h (160.9 km/h).

Setting the maximum permissible speed according to the parameters and the state of curves is a complex task, the effectiveness of the high-speed movement implementation of passenger trains, depends on a correct solution.

The methods used today to determine the optimal parameters of the curves, are imperfect, since subjectivity, the performer's qualifications and other factors are introduced into the end result. The geometric parameters of curves indicated on the longitudinal profile, often do not coincide with the actual data.

The reconstruction of the section, with placing the track centerline into the project position, in the profile and the plan with the restoration of the design radii, is especially relevant. In this case, the parameters of the track must correspond to the maximum speed, safety, smoothness, comfort and the costs of restructuring the track within the rational parameters must reconcile. Today, the maintenance of the track, in the absence of sufficient funding and other objective reasons, are not fully implemented, and therefore, the reliability to keep parameter values of the plan, within the time limits that characterizes the ability to perform the necessary functions in specified operating conditions, is reduced.

Considering the reliability of a technical object, in a broad sense, the authors mean the ability of the railway track to be trouble-free, in operation, during the life cycle, due to the time, in the execution of the set task. In good working order, the track must meet all the requirements established for it, by normative-technical and design documentation. The inconsistency of at least one of the requirements, defines an object into the category, of defective.

The purpose of this work is to analyze the existing methods of a survey of horizontal curves, study the impact of the errors in measuring the plan parameters, on the permissible speed of trains traffic and development proposals for reducing the intensity of the track disorder, by bringing the parameters of curves to regulatory requirements operating in Ukraine, for the future directions of implementation of the high-speed train implementation.

2 Analysis of Current Literature

Currently, there are known methods for a plan survey of a railway, each of which, has advantages and disadvantages. Thus, in works [1-3] an analysis of the plan survey accuracy for the railway track is presented. The authors come to the conclusion, that at a full survey by the method of arrows, it is necessary to determine the coordinates of individual points in 100-150 m (tacheometric, GPS survey, intersection sights from the reference stations). Then, the disadvantages of the survey of arrows, associated with an increasing error, will be eliminated. At the same time, the coordinates of individual points adjusted in the arrow measurements, will also become more accurate.

Article [2] discusses the question of determining the horizontal curvature of a railway track, noting that this is most often done on the basis of the measured versines from the chord stretched along the track. Further usage of this method would not be substantiated if there was a direct method of determining the curvature. A new method of determining the horizontal curvature, which is based on changing the angles of slope to a chord in the Cartesian coordinate system [4], is considered. The verification of the proposed method was conducted on a clearly

defined geometric track system consisting of a circular curve and two symmetrically located transitional curves.

It should be noted that the measurement of versines, historically, is the basis for the diagnostic methods relating to the evaluation of the geometric state of railways [5-9]. At the same time, it is deemed necessary to ensure a radical improvement of the existing situation by the method of mobile satellite measurements [10-12]. In Poland, for example, it is a National spatial frame of reference PL 2000. The result of such measurements is a set of numbers that after appropriate processing, form a set of coordinates in the corresponding Cartesian system.

In addition to the American GPS and Russian Glonass, which are present on the market, it is planned to use the Galileo satellite network, which is currently being developed in Europe. Galileo Global Navigation Satellite System is created by the European Union to ensure the independence of member countries, in the field of coordinate and navigation support [13].

Today, the business network of stations, in the improvement of positioning on the Earth, the TNT GNSS Network, is actively operating in the territory of Ukraine, which provides users with access to the GNSS data, via the Internet. Also, there the possibility of access to the correction information, in the RTCM format according to the NTRIP protocol and within the operational area of stations, it is possible to execute the work in RTK mode (Real-Time Kinematic), with an accuracy of 1 mm [14].

Each time, with the next appearance of an updated GPS positioning system, Scientists conduct research in the direction of determining the coordinates of machines in motion, using these systems, but without strengthening them in base stations on Earth. But still, the results of these studies do not allow determination of the position of the track, with sufficient accuracy to perform work on the surfacing [15].

The track surfacing is one of the labor-intensive processes and at the same time, the most significant, since the operational characteristics depends on the track surfacing (smoothness of movement, the traveling speed, etc.), the safety of movement, the costs of current repair and maintenance [16-22]. Track surfacing is carried out with all types of repair, reconstruction and new construction.

An analysis of the plan of the line in the directions of the accelerated train traffic (141-160 km/h) in Ukraine showed that there was a correlation dependence between the specific gravity of the lengths of curves and the percentage in the implementation of the maximum traffic speed (Fig. 1).

During operation, train loads affect the railway track. Over time, the deformation accumulates, the track disorders begin to be observed which cause operating restrictions that directly affect the speed and safety of motion. For example, the authors in [23] demonstrated the results of the analysis of the deterioration of the tram lines geometry. When performing the repair work, it is necessary to bring the

track to the design coordinate position, both in installing a new four-track grating and with current repairs by correctional machines.

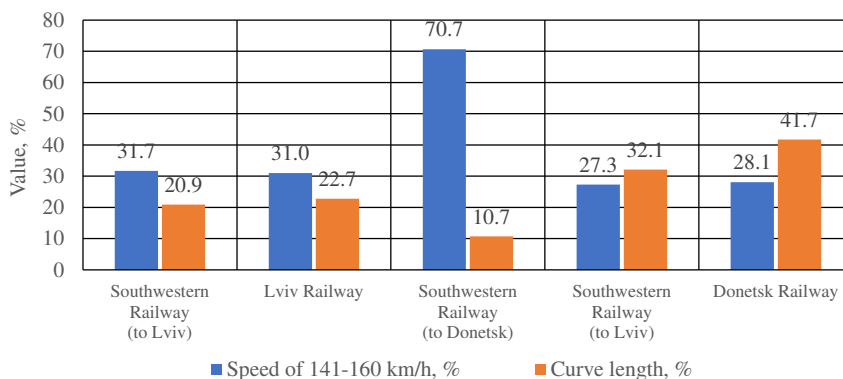


Figure 1

Realization of speed of 141-160 km/h in the directions of accelerated train traffic

3 Comparison of Curves Characteristics

In accordance with the requirements of the instructions (for Ukraine it's CP-0269 [24] and CP-0236 [25]) before the implementation of high-speed trains, railway tracks, rolling stock and other railways service should be brought to a state that provides trains with allowed speeds. Consequently, there is a task of assessing the state of each curve, to ensure the safety, smoothness of the movement and travel comfort.

To compare the full-scale position of the curve with the design one, a technical passport is drawn up for each curve. Authors present an analysis of the passport data for the period from 2017 to 2021 for the curve located on the odd track on the Slavhorod-Novohupalivka section at the regional branch "Prydniprovskya Railway", 1058-1059 km. The source data of the curve is obtained by the survey of the method of arrows from a 20-meter chord (versines) and elevation of the outer rail at the same points (Fig. 2).

The passport specifications of each curve must meet the following requirements:

- requirement 1* Compliance with the recommendations of existing regulatory documents on the construction and maintenance of the track and implementation of allowed permissible speeds
- requirement 2* The position of the curve in the plan may differ from the existing no more than extremely possible track shifts, limited by overall, technical, technological and other requirements

requirement 3 Passport specifications of the curve construction (by curvature, the elevation of the outer rail, the length of transient curves) should provide the rational rates of the non-compensated acceleration (α , m/s^2), the speed of its change (ψ , m/s^3) and relocation of elevation of the outer rail (i_g , ‰) at the allowed and actual speeds of trains

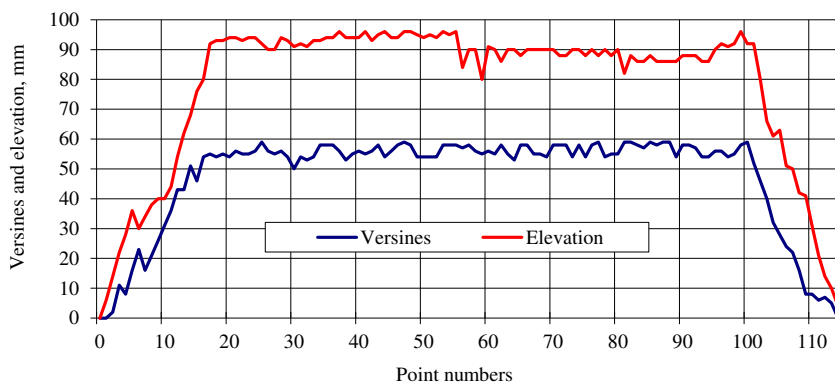


Figure 2

Versines and elevation of outer rail in curves in accordance with date from 01.01.2021

The method of research involves checking the passport specifications of the curves. If the existing curve parameters differ from requirements (1-3), then the rational parameters of the curve are calculated for a given range of speeds that ensure the implementation of existing normative documents, optimization of the power interaction between rolling stock and tracks with minimum displacement and the elevation of the outer rail.

The calculated design passport specifications of the curve after approval by the track service must be implemented in planned repair works or reconstruction of the track.

Verification of compliance with the requirement 1. The curve is considered to be dynamically smooth, if the deviation in the versines do not exceed the nominal values, that is the difference of versines in adjacent points in 10 m at the length of the chord 20 m.

On the existing railways, the form of the transition curve remains in the form of a radioidal spiral with a linear relocation of the superelevation and the curvature, and the permissible traffic speed is allowed [24], depending on the steepness of the relocation. For the maximum permissible speed of 120 km/h, the steepness of the relocation of the superelevation (mm/m) is taken in the range of more than 0.7 to 1.0 incl.

According to the passport of the curve, the radius of the existing curve is 867 m, the length of transition curves is 150 and 140 meters, superelevation is 95 mm.

The greatest difference of adjacent versines of an outer rail in a circular curve 8 mm, and the greatest deviations from the uniform growth of versines on the transition curves is 5 mm [24].

Thus, from Fig. 3, it follows that within the transition curves, that is, deviations from uniform growth of versines on a transition curve, reach 8-9 mm at a permissible 5 mm.

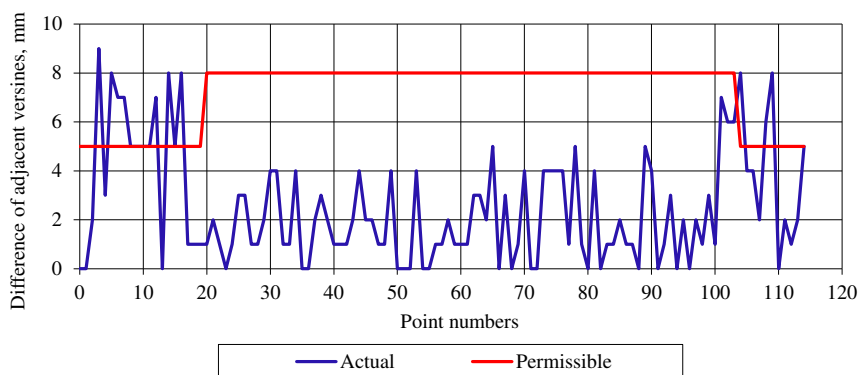


Figure 3

Difference of adjacent versines: actual and permissible

According to [24], for a speed of 120 km/h, the maximum permissible steepness of the relocation of the superelevation in the curve is 1.0 mm/m. From the analysis of Fig. 4, it follows that on transition curves and in a circular curve there is an excess of the gradient of 1.0 mm/m, which determines the state of the curve that does not provide smoothness and comfort of the travel.

The parameters of the curves are updated annually by measuring the magnitudes of the versines and elevation of the outer rail. By measured versines, the angle of rotation, radius and all elements of the curve are determined. The measure of the angle of rotation does not depend on the radius of the curve and the degree of its disorder and is constant for this curve. The monitoring of surveying works on the curve, which is taken for an example at the Slavhorod-Novohupalivka section, should be admitted unsatisfactory (Table 1), since the angle of rotation of the curve for five years (from 2017 to 2021) differs by 5-8%, the radius of the curve by 6-10%, and the length of the curve is 3-6% of the average number.

Compliance verification with requirements 2. When reconstructing the track, the correction of horizontal curves is performed with the restoration of the design radii and bringing the lengths of transition curves to the allowed norms.

Since the existing curve parameters are different from the above requirements (1-3), then the rational parameters of the curve are calculated to provide a allowed maximum speed of passenger trains 120 km/h. As options, one-, two- and three-radius curves were considered (Table 2).

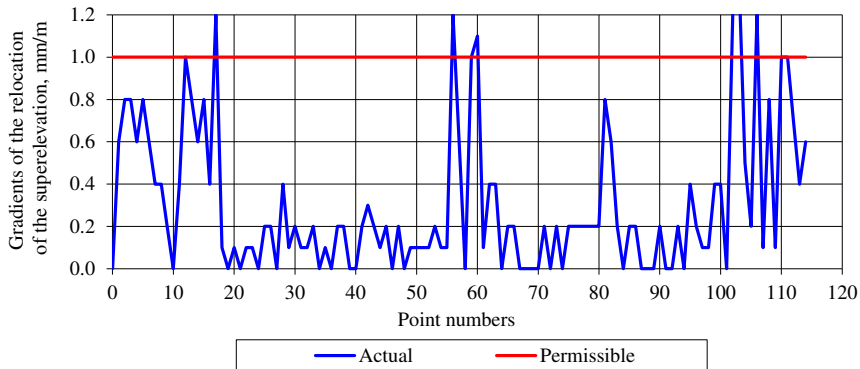


Figure 4

Gradients of the relocation of the superelevation at the points of the curve survey

Table 1

The value of the curve parameters and the appropriate permissible traffic speed

| Curve parameters | The values of the curve parameters obtained in different years | | | | |
|---|--|--------|--------|--------|--------|
| | 2017 | 2018 | 2019 | 2020 | 2021 |
| The angle of rotation | 56°23' | 64°09' | 63°55' | 58°53' | 62°17' |
| Radius, m | 998 | 858 | 857 | 948 | 889 |
| 1 st transition (chloide), m | 40 | 110 | 140 | 130 | 190 |
| Circular, m | 892.04 | 825.62 | 821.07 | 839.36 | 816.35 |
| 2 nd transition (chloide), m | 140 | 160 | 130 | 140 | 110 |
| Superelevation, mm | 35 | 85 | 85 | 75 | 85 |
| The sum of landslides | 4920 | 5598 | 5578 | 5139 | 5435 |

In determining the design parameters of the curve, the criterion of working cost was used to reorganize the plan of a line. In this case, when optimizing, the cost of track alignment, relaying of a track, additional ballast, the transfer of the contact network and SCB devices, additional volumes of heaping the roadbed are taken into consideration. The need for certain additional works was determined programmatically depending on the displacement value at the specified point of the curve.

Total cost of works on the restructuring of the curve was performed by the equation:

$$K = \sum_{i=1}^4 a_i l_i + \sum_{i=5}^7 a_i l_i + \sum_{i=8}^{10} a_i Q_i \quad (1)$$

where $a_1 \dots a_4$ – costs on displacement of the existing track centerline respectively up to 60 mm, 61-120 mm, 121-250 mm and more than 250 mm; $l_1 \dots l_4$ – length of sections with a corresponding range of landslides; $a_5 \dots a_7$ – expenses respectively to the relaying of the permanent way, transferring the network, SCB devices; $l_5 \dots l_7$ – length of sections of relaying tracks, transferring the contact network, SCB cables; $a_8 \dots a_{10}$ – the cost of the 1 m³ ballast, soil for expanding the existing roadbed and soil for heaping the roadbed on a new route; $Q_8 \dots Q_{10}$ – the volume of ballast, soil for expanding the existing roadbed and soil for heaping the new roadbed.

When track alignment to a distance of more than 60 mm, additional volumes of work arise that are related to the works on the contact network and the filling up of ballast will occur. And if the displacement exceeds the given value (for example a_4), then instead of costs for alignment, the cost of relaying tracks, transferring the contact network and SCS devices are calculated.

Volume cost indicators on the options in reorganizing the plan of a line are given in Table 2.

From analysis of Table 2, it follows that, taking into account the financial position, the option of a three-radius curve, at which the track surfacing is provided within the main site of the roadbed with minimal expenses.

Verification of compliance with the requirement 3. Controlled values of the curve according to which evaluation of the actual parameters of the curve are:

- The magnitude of the horizontal acceleration (α), calculated on the entire curve according to the actual values of the curvature and elevation of the outer rail with regard to their local deviations with a length of not less than 30 m
- The rate of change of non-compensated acceleration on the sections of variable curvature (ψ , m/s³)
- The steepness of the relocation of the superelevation (i_g , ‰) in transient curves

Figure 5 shows graphs of non-compensated accelerations and the speed of their change along the curve. From the graphs it follows that at a maximum speed of 120 km/h, after correction of the curve, the conditions of not exceeding the speed of the non-compensated acceleration on the sections of variable curvature $\psi \leq 0.6$ m/s³, and non-compensated acceleration α on the section from 55th to 100th point reach 0.75-0.80 m/s².

Table 2
Volume cost indicators on the options

| Radius of curve (R_i), m | Transition curves (L_i), m | Superelevation (h_i), mm | Maximum displacement, mm | The sum of landslides, mm | Costs, Euro |
|---|--|--------------------------------------|--------------------------|---------------------------|-------------|
| $R_1=889$ | $L_1=190$; $L_2=110$ | $h_1=85$ | + 277 - 178 | 11972 | 3679 |
| $R_1=899$; $R_2=879$ | $L_1=160$; $L_2=80$; $L_3=140$ | $h_1=80$; $h_2=85$ | + 83 - 77 | 3852 | 731 |
| $R_1=902$; $R_2=889$; $R_3=877$ | $L_1=160$; $L_2=30$; $L_3=40$; $L_4=140$ | $h_1=80$; $h_2=85$; $h_3=85$ | + 47 - 61 | 1876 | 309 |

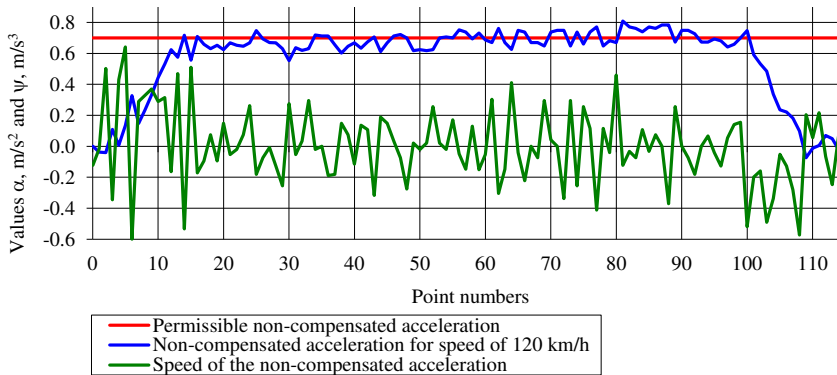


Figure 5

Non-compensated acceleration and speed of their change along the curve

The comparison of various methods of the survey for one of the curves on the Synelnikove – Chapline, Regional Branch "Prydniprovskya railway" [1] was performed. The survey was performed by the method of arrows, Honikberg's method and coordinate one, with the use of an electronic tacheometer.

Comparison of the results in straightening the curves according to the source data obtained by various methods of the survey is shown in Table 3.

As it can be seen from Table. 3, permissible speeds by various methods of the survey are different. From this and other examples it follows that for the proper solution to the issues of reconstruction of the track and track buildings in order to provide the speed of 161-200 km/h in the internal transport corridors, it is necessary to conduct the works on the conditioning of curves and establishing a real permissible speed of movement on them at the current level.

Table 3

The value of the curve parameters and the corresponding permissible speed of motion

| Curve parameters and the permissible speed | The values of the curve parameters obtained by different methods of the survey | | |
|--|--|--------------------|-------------------|
| | Method of arrows | Honikberg's method | Coordinate survey |
| The angle of rotation | 15°09.6' | 14°47' | 14°49.5' |
| Radius, m | 1156 | 1110 | 1156 |
| 1 st transition (chloide), m | 90 | 60 | 100 |
| Circular, m | 199.29 | 226.40 | 197.03 |
| 2 nd transition (chloide), m | 100 | 60 | 110 |
| Maximum permissible speed, km/h | 130 | 120 | 126 |
| Extreme landslides, mm | + 23 - 43 | + 24 - 106 | + 15 - 84 |

Conclusions

To date, there are many techniques that are used to measure the parameters and the states of curves. It is the existence of various techniques that have practical application, suggests that each of them has its own advantages and disadvantages. To select a technique, it is necessary to have both a statistical and a mathematical justification.

Comparing the results of the curve survey by various methods, it can be established, how much they differ from each other, but, it is impossible to determine their differences, in relation to the absolutely correct values, since the exact position of the curve remains unknown. It is also obvious that the accuracy of the results will depend, not only on the parameters of the measuring devices and the ability of the executors, but also on the methodology that defines the technology of measurement and the needed mathematical transformations of the data obtained, for example, in the curvature of a curve.

The most effective method is the method of the survey, by a track-measuring car, correctional-tamping-gauging machines, as well as, a survey method using GPS sensors and a survey using track-measuring trucks. When they are used simultaneously, a plan survey and longitudinal profile of the railway track are carried out. But each of them has their inherent advantages and disadvantages. The most accurate method, with the greatest degree of process automation, can be considered a survey method using GPS sensors, but for this accuracy, it requires a developed network of baseline GPS stations located on Earth.

For all curves that limit the speed of movement, as well as, those that are maintained with deviations, an on-site inspection, with the fulfillment of the complete calculation cycle, for their certification, must be carried out.

The certification of curves will contribute to reducing the intensity of the railway disorders, reducing labor costs in maintaining the track in the plan, increasing the smoothness and comfort of riding.

Today, the business network of stations, for the improvement of positioning on Earth, is the TNT GNSS Network, is actively operating in the territory of Ukraine and provides users with direct access to GNSS data, via the Internet. Without significantly upgrading the technique, for the survey and track surfacing, one can start certification and track surfacing, using the global coordinate system. In the future, the usage and development of this network and prospects, are open for full certification of the track, in the global coordinate system, the creation of a virtual reference system and the track surfacing preparation, by heavy machines, including project coordinates, without the need for physical measurement visits.

Acknowledgement

The curves were calculated using the RWPlan software developed under the guidance of Assoc. Prof. I. Korzhenevich [26].

References

- [1] M. B. Kurhan, D. M. Kurhan, S. Y. Baidak, N. P. Khmelevska. Research of railway track parameters in the plan based on the different methods of survey. *Science and Transport Progress*, Vol. 2(74), 2018, pp. 77-86
- [2] W. Koc. Analysis of Moving Chord Inclination Angles when Determining Curvature of Track Axis. *Current Journal of Applied Science and Technology*, Vol. 40(10), 2021, pp. 92-103
- [3] C. Specht, W. Koc, P. Chrostowski, J. Szmagliński. Accuracy assessment of mobile satellite measurements in relation to the geometrical layout of rail tracks. *Metrology and Measurement Systems*, Vol. 26, 2019, No. 2, pp. 309-321
- [4] W. Koc. The Method of Determining Horizontal Curvature in Geometrical Layouts of Railway Track with the Use of Moving Chord. *Archives of Civil Engineering*, Vol. 66(4), 2020, pp. 579-591
- [5] L. Marx. Satellitengestützte Gleisvermessung: auch beim Oberbau. *Der Eisenbahningenieur*, Vol. 58, 2007, Num 6, pp. 9-14
- [6] Y. Naganuma, T. Yada, T. Uematsu. Development of an inertial track geometry measuring trolley and utilization of its highprecision data. *International Journal of Transport Development and Integration*, Vol. 3(3), 2019, pp. 271-285
- [7] Q. Chen et al. A Railway Track Geometry Measuring Trolley System Based on Aided INS. *Sensors*, Vol. 18(2), 2018, 538
- [8] T. Strübing. Kalibrierung und Auswertung von lasertriangulationsbasierten Multisensorsystemen am Beispiel des Gleisvermessungssystems RACER

- II. Schriften des Instituts für Geodäsie der Universität der Bundeswehr München, Vol. 91, 2015
- [9] T. Weinold, A. Grimm-Pitzinger. Die Lagerung der Gleisvermessungen der ÖBB. *Vermessung & Geoinformation*, Vol. 7(3), 2012, pp. 348-352
- [10] M. Specht *et al.* Road Tests of the Positioning Accuracy of INS/GNSS Systems Based on MEMS Technology for Navigating Railway Vehicles. *Energies*, Vol. 13(17), 2020, 4463
- [11] K. Czaplewski *et al.* Application of Least Squares with Conditional Equations Method for Railway Track Inventory Using GNSS Observations. *Sensors*, Vol. 20(17), 2020, 4948
- [12] H. M. Yehia, H. N. El-kenani Effect of the Gravity and Magnetic Field to Find Regular Precessions of a Satellite-gyostat with Principal Axes on a Circular Orbit, *J. Appl. Comput. Mech.*, 7(4), 2021, 2120-2128
- [13] C. Specht *et al.* Diagnostics of the tram track shape with the use of the global positioning satellite systems (GPS/Glonass) measurements with a 20 Hz frequency sampling. *Journal of Vibroengineering*, Vol. 16(6), 2014, pp. 3076-3085
- [14] RTK Network HUB. <https://net.tnt-tpi.com/page> [online, last visited on: 2021.11.23]
- [15] A. Wilk *et al.* Determination of the tram track axis using a multi receiver GNSS measurement system. *Transportation Overview - Przegląd Komunikacyjny*, Vol. 75(4), 2020, pp. 1-117
- [16] R. Wenty. High-capacity, precision and reliability in track maintenance. *Railway technical review*. Vol. 46(3), 2006, pp. 24-32
- [17] D. Kurhan, M. Havrylov. The Mathematical Support of Machine Surfacing for the Railway Track. *Acta Technica Jaurinensis*, Vol. 13(3), 2020, pp. 246-267
- [18] A. Németh, S. Fischer. Investigation of glued insulated rail joints applied to CWR tracks. *Facta Universitatis Series Mechanical Engineering*, 2021, 7642
- [19] A. O. Shvets. Analysis of the dynamics of freight cars with lateral displacement of the front bogie. *Advanced Mathematical Models and Applications*, Vol. 6(1), 2021, pp. 45-58
- [20] D. Kurhan, S. Fischer. Modeling of the Dynamic Rail Deflection using Elastic Wave Propagation, *J. Appl. Comput. Mech.*, 8(1), 2022, 379-387
- [21] M. Przybyłowicz, M. Sysyn, U. Gerber, V. Kovalchuk, S. Fischer. Comparison of the effects and efficiency of vertical and side tamping methods for ballasted railway tracks. *Construction and Building Materials*, Vol. 314 (Part B), 2022, 125708

- [22] M. Kurhan, D. Kurhan, R. Novik, S. Baydak, N. Hmelevska. Improvement of the railway track efficiency by minimizing the rail wear in curves. IOP Conf. Ser.: Materials Science and Engineering, Vol. 985, 2020, 165475
- [23] V. Jóvér., L. Gáspár, S. Fischer. Investigation of geometrical deterioration of tramway tracks. Science and Transport Progress, Vol. 2(86), 2020, pp. 46-59
- [24] Instructions for the arrangement and maintenance of the railway of Ukraine (CP-0269). Ukraine, Kyiv, 2012, 456 p.
- [25] Rules for determining the increase of the outer rail and setting the allowable speeds in the curved sections of the track (CP-0236). Ukraine, Kyiv, 2010, 52 p.
- [26] Brain Rail System. RWPlan. https://brailsys.com/RWPlan_0.htm [online, last visited on: 2021.11.23]

Effects of Wheel Surface Defects on Ground Borne Vibration

Milad Kazemian¹, Farshad Astaraki², Ahmad Mohammadi doost³, Milad Akbarivarmaziar⁴, Majid Movahedi Rad², Szabolcs Fischer²

¹Faculty of Civil Engineering, Islamic Azad University Science and Research Branch, Hesarak 1477893855, Tehran, Iran; Milad.kazemian@srbiau.ac.ir

²Department of Structural and Geotechnical Engineering, Széchenyi István University, Egyetem tér 1, Győr 9026, Hungary; Astaraki.farshad@hallgato.sze.hu; majidmr@sze.hu; fischersz@sze.hu

³Department of Railway Rolling Stock Engineering, School of Railway Engineering, Iran University of Science and Technology, Narmak 13114-16846, Tehran, Iran; Ahmad_mohammadi@rail.iust.ac.ir

⁴Department of Railway Track & Structures Engineering, School of Railway Engineering, Iran University of Science and Technology, Narmak 13114-16846, Tehran, Iran; a_hoseinkhani@rail.iust.ac.ir

Abstract: Wheel ground borne vibrations, may have a significant impact on human activity and on nearby buildings. In metropolitan cities, metro lines and their development may cause such vibrations. Despite many works and solutions for path and receiver, the excitation source could also have a great effect. Wheel and rail damages are the two sources of vibration which can increase the damage impact by a factor of 5x. Wheel damage would increase dynamic vertical force noticeably and an increase in ground-borne vibration is expected. In this study with the help of finite element modelling, wheel damage including wheel flat, spalling and wheel oval is studied for a slab track and results are discussed. The studied parameters are velocity and wheel damage and their effect on ground-borne vibrations are examined.

Keywords: ground-borne vibration; FEM; metro; wheel defect; moving load

1 Introduction

Excessive ground vibrations may have a significant impact on human comfort and on the built environment. Ground vibration may also have a detrimental effect on the railway safety, with the deterioration of the embankment and fatigue effect on

rail. Vibrations in the frequency range relevant to the whole-body perception from tracks onto the ground surface, propagate parallel to the ground surface via Rayleigh wave modes with low rates of attenuation with distance [1]. Analysis of these effects requires realistic models of ground vibration generation and propagation. In particular, it has been shown that it is important to include the effects of both the railway track structure and the layered structure of the ground [2-7]. During the last decade various approaches which different accuracy have been carried out to investigate vibration levels from the lines, and also to design tracks and constructional measures to reduce vibration levels. The methods can be classified as either numerical, analytical or empirical methods. Some studies based on analytical approaches can be found in Kausel [8], Krylov and Ferguson [9], and Barber [10] as an effective tool for solving the wave propagation problems. Numerical models using the finite and boundary element method are under development for analysis of wave propagation problems in solids with emphasis on dynamic soil-structure interaction due to the passage of a train [11] [12]. Ground-borne vibrations induced by underground railways are a major environmental concern in urban areas. These vibrations propagate through the tunnel and surrounding soil into nearby buildings causing annoyance to people. Vibration is perceived directly or it is sensed indirectly as re-radiated noise. Tang *et al.* [13] studied the dynamic response and pore pressure model of the soft clay around the tunnel under vibration loading of Shanghai subway. Their results offered a valuable reference to the design loading, construction and the safe operation of the subway tunnel. Gupta *et al.* [14] compared two modular prediction tools for estimating vibrations due to underground railway traffic. It was demonstrated how the Craig-Bampton sub structuring technique allows to efficiently incorporate a track in the tunnel and to analyze the vibration isolation efficiency of a floating slab track in the tunnel, without the need to recompute the impedance of the soil. Degrande *et al.* [15] presented a numerical model to predict vibrations in the free field from excitation due to subway trains in tunnel. The responses of two different types of tunnel due to a harmonic load on the tunnel invert were compared. The first tunnel was a shallow cut-and-cover masonry tunnel on the Paris subway network, embedded in layers of sand, while the second tunnel is a deep bored tunnel of London underground, with a cast iron lining and embedded in the London clay. Hussein and Hunt [16] developed a numerical model for calculating vibration from underground railways. Further, they investigated the wave-guided solution of the track, the tunnel, the surrounding soil and the coupled system. They also showed that the dynamics of the track have significant effect on the results calculated in the wavenumber-frequency domain and therefore an important role on controlling vibration from underground railways.

Auersch *et al.* [17] studied train-track-soil interaction using field test in Germany and Switzerland. Tests consist of measuring train, track and soil vibration, while the train passes with 9 different speeds. Studied tracks are two ballasted track (one on a concrete bridge and the other on ground) and a slab one. Up to 10 points in Switzerland are measured and in some points axle box measurements are done.

They were able to determine the transmission function of the wave propagation from hammer tests and use it to determine the wheel dynamic force spectrum which showed a good agreement with the axle box tests. As a result of their work, the comparison of axle box and ground measurements confirms the prediction of ground-borne vibrations caused by trains using continuum mechanics models. dos Santos et al. [18] conducted a comprehensive study of ground-borne vibrations caused by train in Portugal railway. Their work consisted of three basic parts including determining ground and track characteristics and measuring the vibrations caused train. Accelerometers were mounted both on the rails and on different distances from the track. They also used a system consisting of several lasers to measure the vertical displacement of the track and in total 20 train passages were recorded. In another study, he presented a three-dimensional numerical model for predicting vibrations caused by train [19]. He used the field test data in ref. [18] to validate the results of this model. Green functions were used to describe the response of the ground.

There are few researches on effects of wheel damages on ground vibration compare to solutions on path and receiver. One of the dynamic impact forces which have significant effect on ground vibration is generated by wheel flat. When a steel wheel, such as these fitted to all railway rolling stock, is braked too heavily causing wheel-locking, the effect of sliding along the rail is to machine or grind a small flat on the wheel rim. This occur still on older rolling stock; however, modern anti-lock braking systems seek to avoid this occurrence. The result is a wheel which can impart periodic damage to the rail during subsequent motion, until the 'flat' is removed by re-grinding or re-profiling for larger flats. Existence of wheel flat induces additional damage beyond the rolling contact fatigue. Furthermore, the discontinuity of slope between the smooth circular part of the rim and the flat induces harsh vibration of track. So, in this paper by FE modelling of a slab track for Tehran metro, effects of velocity and damage dimension is studied. Three damage possibilities are considered: wheel flat, wheel RCF, which causes spalling and wheel ovaling.

2 FE Modelling

The developed model involves the vehicle loads, the track and the ground. Since the load is assumed to be symmetrically distributed on the two rails, half of the track is sufficient to derive the train model. Only vertical vibrations are taken into account. To overcome plane stress/strain limitations, third dimension is modeled explicitly. Galvin et al, [20] uses a coupled FEM/BEM approach where the track is modeled using FEM and the unbounded domain is accounted for by BEM. However, a pure FEM solution is utilized by Banimahd et al, [21] and Kouroussis et al. [22]. A challenge presented by this approach is that absorbing boundary conditions must be implemented at model boundaries to prevent spurious waves

contaminating the solution. The authors employed absorbing layers, to mitigate such a wave, by using Dashpot elements, in the ABAQUS software.

2.1 Track Modeling

Track geometry and material properties were modelled in accordance with international union of railways [23] specifications. 20 m of slab track was modeled in accordance with Tehran metro line. The model was symmetrical in the track direction, so only half of all track components and half of the supporting soil was modeled. The rail was modeled as a continuously welded beam with I section profile in accordance with UIC54 profile, Figure 1. The rail was connected to the slab section by using rail pad and base plate sections.

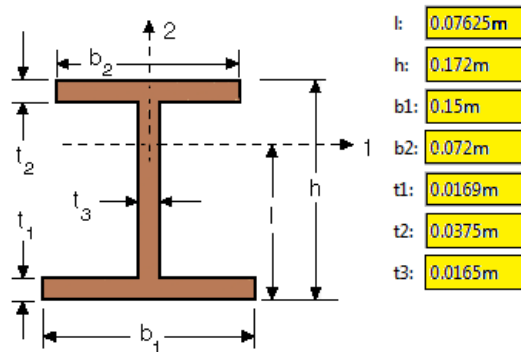


Figure 1
Rail profile dimensions

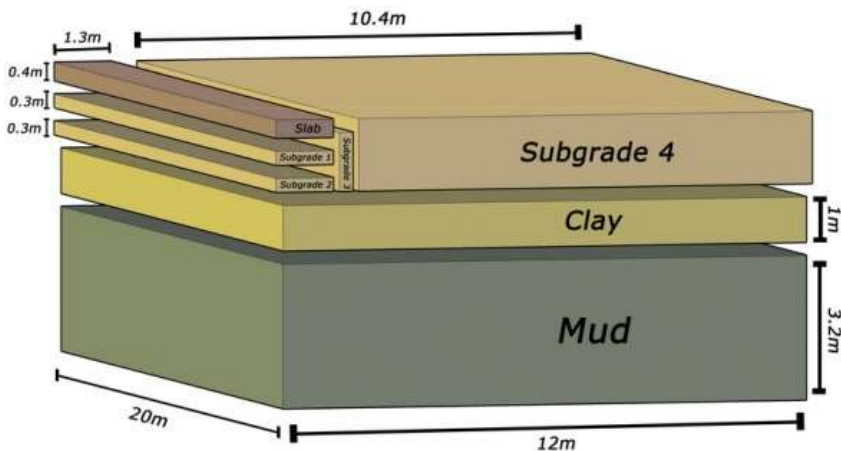


Figure 2
Soil components modeling

2.2 Soil Modeling

Soil properties of the test site was modeled as a stratified linear elastic material consisting of three layers with varying material properties as defined in Kouroussis et al [24].

The uppermost layer consisted of 0.4 m of slab section and the second layer consisted of 0.6 m of subgrade. The third layer consisted of 1 m of clay section and the fourth layer consisted of 3.2 m of mud section, the bottom of which was bounded by an absorbing boundary condition to simulate an unbounded domain. A summary of soil material properties is found in Table 1.

Table 1
Track and soil material properties

| FEM part description | Young's modulus (GPa) | Poisson's ration | Density (Kg/m ³) | Thickness (m) |
|----------------------|-----------------------|------------------|------------------------------|---------------|
| Rail | 207 | 0.3 | 7850 | - |
| Slab | 30.8 | 0.2 | 2400 | 0.4 |
| Subgrade 1 | 22.9 | 0.2 | 2400 | 0.3 |
| Subgrade 2 | 3.54 | 0.24 | 1900 | 0.3 |
| Subgrade 3 | 3.4 | 0.24 | 1900 | 0.3 |
| Subgrade 4 | 3.37 | 0.24 | 1870 | 1.2 |
| Clay | 0.035 | 0.24 | 1850 | 1 |
| Mud | 0.003 MPa | 0.25 | 1800 | 3.2 |

A uniform stiffness proportional Rayleigh damping value of $\beta=0.0004s$ was assumed for all layers in accordance with Kouroussis et al [22]. This implementation was essential to accurately model energy dissipation in the soil layers.

2.3 Commercial FEM Software Implementation

Modeling the vehicle interaction with track is time consuming specially in 3D domain and may cause problems in convergence especially in high frequency excitations. Therefore, ABAQUS moving load was defined using Subroutine. This subroutine defines distribution of non-uniform load magnitudes as a function of time and position, at a set of predefined integration points. The moving load codes consisted of axle load of vehicle and the wheel flat impact load which applied to the rail in each 3 m in track length. Parameters of model which are used in this study are listed in Table 2.

Table 2
Parameters in FE dynamic analyses

| Axle load (KN) | Wheel profile | Wheel diameter (m) | Train speed (m/s) | Flat size (m) |
|----------------|---------------|--------------------|-------------------|---------------|
| 80 | S1002 | 0.86 | 5, 13, 22 | 0, 0.02, 0.04 |

The model consists of total 42710 elements, 35826 C3D8R solid elements for soil, 6884 B31 beam elements for rail, Figure 3.

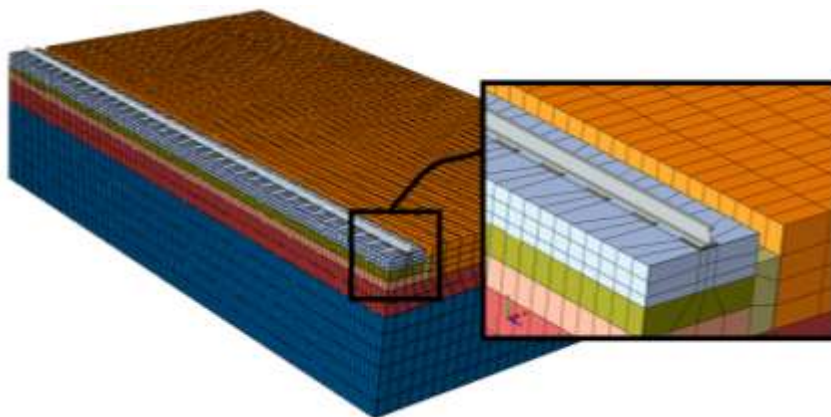


Figure 3

Track and soil mesh generation

The phenomenon of wheel flat in the railway occurs usually because of various reasons, such as locking the wheels when braking or reducing the adhesion force between the wheels and the rail. This failure creates not only impact forces that cause damage to trains and tracks but also cause noise and vibration. Figure 4 shows an example of wheel flat. Other common train wheel failures such as out of roundness (OOR) are really usual. In this type of failure, unlike the wheel flats, no impact occurs. In fact, OOR causes the amount of contact force amplitude to increase. Figure 5 shows a wheel that the length and the depth of the flat are a and b , respectively. The flatness of the wheel is indicated by a circular chord.



Figure 4

An example of a wheel flat

In this study three types of wheel-flat are modeled. These wheel flats include RCF, oval and wheel flat. Each wheel-flat is modeled with several different sizes, RCF includes 0, 6 and 12 millimeters, oval includes 0, 1, 2 and 6 millimeters and flats including 0, 20 and 40 millimeters. In this paper, we mean the RCF defect, which is a series of spalling on the tread of the wheel. In this model [25], It is assumed that the angular velocity of the wheel (ω) is constant. When the wheel is placed on the flat, the distance between the center of the wheel and the rail, $y(t)$, is minimum, which is obtained because of the difference between the radius of the wheel and the depth of the flat. Figure 6 shows the distance between the center of gravity of the wheel and the rail as a function of time.

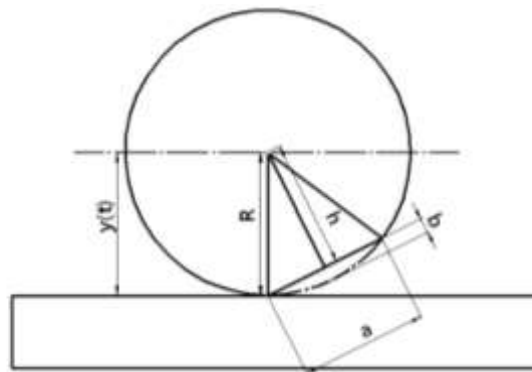


Figure 5

A train wheel with a flat of length a and width b

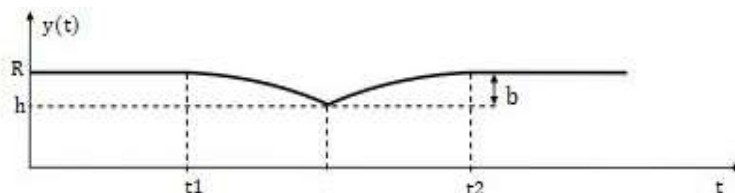


Figure 6

Displacement of the center of the wheel during the passing of the flat

When the circle segments in $y(t)$ are approximated by a second-order polynomial, its time derivative, when it represents the vertical velocity of the wheel, appears as linear functions, and in fact, the vertical linear momentum of the wheel $p(t)$ corresponds to it. The dynamic component of the vertical contact force between the wheel and the rail is easily obtained from the time derivative of the vertical momentum according to $F(t) = \dot{p}(t) = m\dot{y}$. This value appears to be a negative constant value between t_1 and t_2 and the Dirac delta function $t = (t_1 + t_2) / 2$, which means that its value increases infinitely over extremely small period of time at that moment. In this paper, the above theory is used to model the force due to the wheel flat, in which the impact force cause by the wheel flat is applied alternately at time

intervals equal to a full wheel round on the contact patch. For the other two faults, the same method has been used to model the fault force. The data point is located 10 meters from the center of the track, as shown in Figure 7.

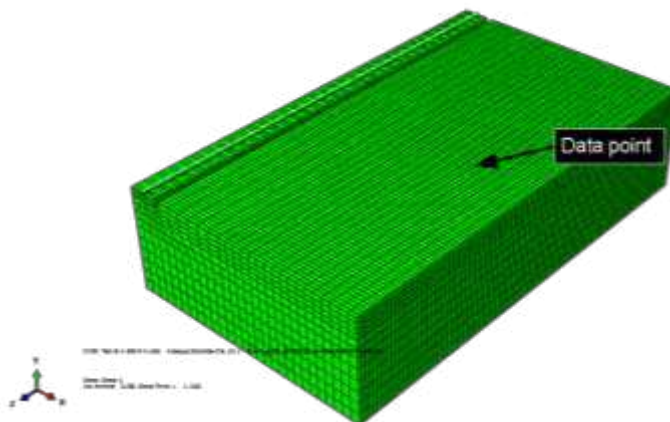


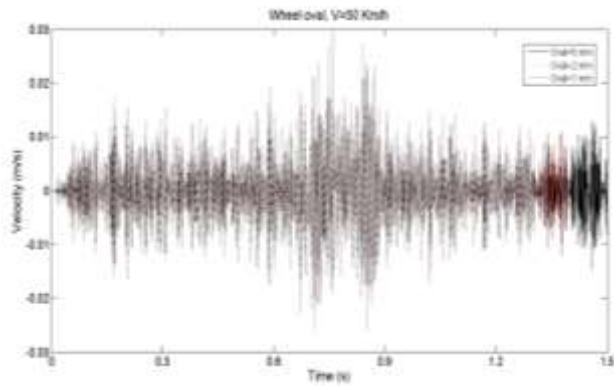
Figure 7
Position of the data point

3 Numerical Results

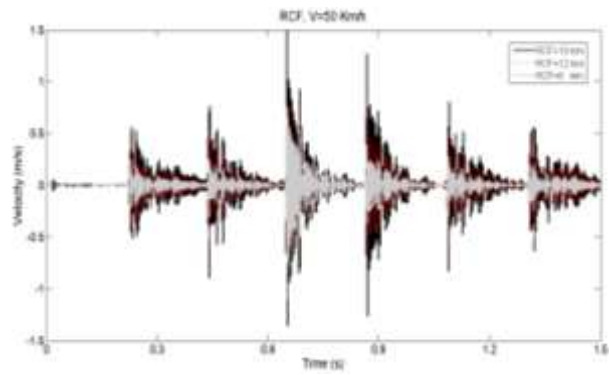
In this Study, three different wheel defects and defect size are considered for modelling. Using the finite element model, 3 different velocities for the moving load were analyzed. The examined velocities were 10, 20 and 50 km/h, respectively. To investigate the ground-borne vibrations caused by these passages, vertical velocity at 10 meters from the center of the track was considered as the output. The time domain results of vertical velocity at the surface of the ground for each of defects is shown in Figure 8. The maximum values of each signal for each velocity and each defect is shown in Table 5.

Table 5
Flat results

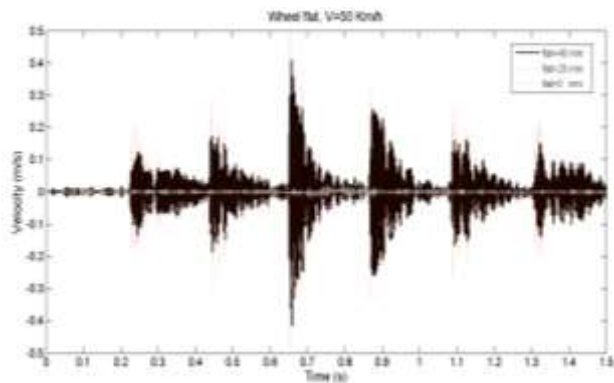
| Velocity (km/h) | New wheel | Wheel flat | | Wheel oval | | | RCF | | |
|-----------------|-----------|------------|--------|------------|--------|--------|--------|--------|--------|
| | | 20 mm | 40 mm | 1 mm | 2 mm | 6 mm | 6 mm | 12 mm | 18 mm |
| 20 | 0.0222 | 0.2101 | 0.1748 | 0.0485 | 0.0485 | 0.0485 | 0.3719 | 0.7444 | 1.1145 |
| 50 | 0.0217 | 0.4951 | 0.4151 | 0.0318 | 0.0318 | 0.0318 | 0.7512 | 0.9475 | 1.4903 |
| 80 | 0.0185 | 0.4911 | 0.5414 | 0.023 | 0.023 | 0.023 | 0.4646 | 0.8604 | 1.3012 |



(a)



(b)

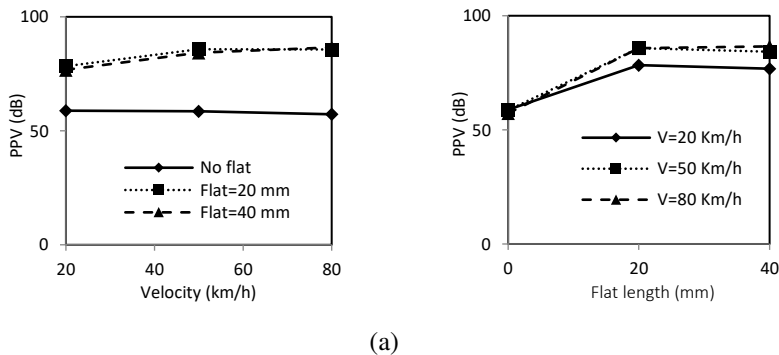


(c)

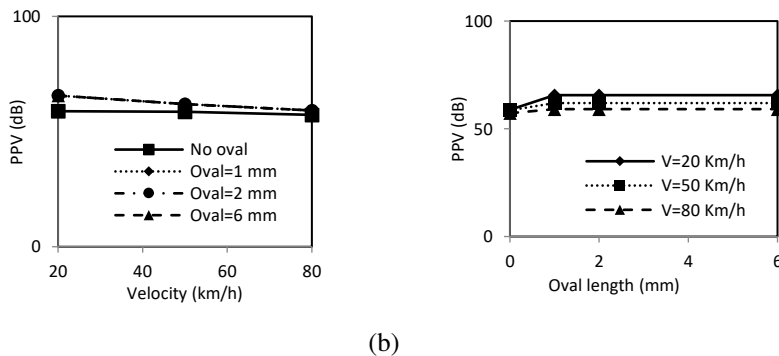
Figure 8

An example for the time domain results for $v=50$ km/h
a) wheel oval b) RCF and c) wheel flat

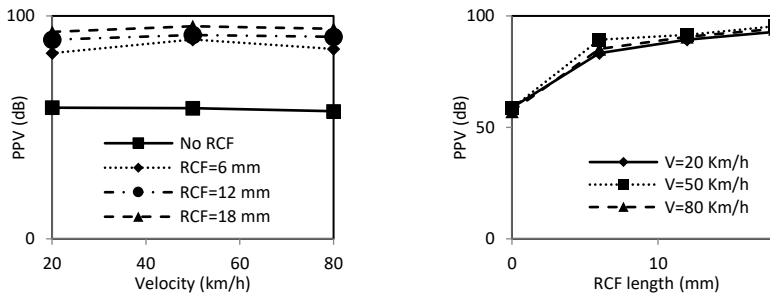
For better comparison, these values are converted to dB (reference 10^{-6} inch/s) and can be compared in Figure 9. According to Figure 9a, it can be concluded that effects of flat length is dominant compared to speed. So, for a wheel flat larger than 20 mm, decrease in speed in order to vibration reduction has no effect. Figure 9b for Oval type failure shows that the velocity is inversely related to the increase in vibrations caused by this defect. In other words, this failure mostly shows its effect on vibrations at low speed. Also, increasing the size of this defect does not show any effect on increasing the vibrations, or in other words, this defect is only a function of speed while studying ground-borne vibration. In fact, increasing or decreasing the defect length of the oval has no effect on the amount of vibrations, and it is only the presence or absence of this defect that can affect the vibrations. Also, from Figure 9c, which is plotted for RCF defect, it can be seen that, unlike the early stage, the size of the defect has a great effect on vibrations. As can be seen from Figure 9c on the left, increasing the size of the defect has a direct effect on the level of vibration and also the presence or absence of this defect has a greater effect on vibration level compared to other mentioned defects. The diagram also shows that increasing the speed has almost no effect on the vibration level and even in small failures, increasing the speed will reduce vibrations caused by this defect type.



(a)



(b)



(c)

Figure 9

Wheel damage effect on PPV value (dB) for a) wheel flat b) wheel oval and c) RCF

Conclusions

This paper studied the effect of wheel surface defects and train speed, on ground-borne vibrations. For this purpose, the Finite Element Method (FEM) has been used to model railway track and its super structure. 20 meters of slab track was modeled according to Tehran metro line specifications. Three different wheel defects were considered including wheel flat, oval and RCF. For each type of defect, three velocities of 20, 50 and 80 km/h were considered, and time domain results were converted to dB for better comparison. The results showed that for the wheel flat defects, increasing the speed has less effect compared to speed, on ground-borne vibration. Also, increasing the size of the wheel flat, generally, does not have a significant effect on vibrations. For Oval defects, it was observed that the velocity is inversely related to the increase in vibrations caused by this defect and it mostly showed its effect, on vibrations at low speeds. Also, increasing the size of this defect does not show any effect on increasing the vibration level. In RCF, unlike oval, the defect size has a large effect on the vibration level and the presence or absence of this defect, has a greater effect on vibration levels than the others.

References

- [1] Sheng X, Jones C. J. C, Petyt M. Ground vibration generated by a load moving along a railway track. *Journal of sound and vibration*. 1999. 228 (1). 129-156
- [2] Sysyn, Mykola P., Olga S. Nabochenko, Franziska Kluge, Vitalii V. Kovalchuk, and Andriy Pentsak. "Common crossing structural health analysis with track-side monitoring." (2019)
- [3] M, Gerber U, Nabochenko O, Kovalchuk V. Common crossing fault prediction with track based inertial measurements: statistical vs. Mechanical approach. *Pollack Periodica*. 2019 Aug;14(2):15-26

-
- [4] Kurhan D, Kurhan M. Modeling the dynamic response of railway track. Iniop Conference Series: Materials Science and Engineering 2019 Dec 1 (Vol. 708, No. 1, p. 012013) IOP Publishing
- [5] Kurhan D, Kurhan M, Husak M. Impact of the variable stiffness section on the conditions of track and rolling stock interaction. Iniop Conference Series: Materials Science and Engineering 2020 Nov 1 (Vol. 985, No. 1, p. 012005) IOP Publishing
- [6] C. J. C. JONES C. J. C. Use of numerical models to determine the effectiveness of anti-vibration systems for railways. Proceedings of the Institution of Civil Engineers, Transportation, 1994 105, 43-51
- [7] SHENG X, JONES C. J. C, PETYT M. Ground vibration generated by a harmonic load acting on a railway track. Journal of Sound and vibration 1999, 225(1), 3}28
- [8] Kausel E. Thin-layer method. International Journal for Numerical Methods in Engineering 1994; 37: 927–41
- [9] Krylov VV, Ferguson CC. Recent progress in the theory of railway generated ground vibrations. Proceedings of the Institute of Acoustics 1995; 17(4):55–68
- [10] Barber JR. Surface displacements due to a steadily moving point force. Journal of Applied Mechanics 1996; 63: 245–51
- [11] Mohammadi M, Karabalis DL. Dynamic 3-D soil-railway track interaction by BEM–FEM. Earthquake Engineering and Structural Dynamics 1995; 24: 1177–93
- [12] Yang B. Y, Hung HH. A 2.5D finite/infinite element approach for modelling visco-elastic bodies subjected to moving loads. International Journal for Numerical Methods in Engineering 2001; 240: 1317–36
- [13] Tang Y. Q, Cui Z. D, Zhang X, Zhao Sh. K. Dynamic response and pore pressure model of the saturated soft clay around the tunnel under vibration loading of Shanghai subway. Engineering Geology 98 (2008) 126-132
- [14] Gupta S, Hussein M. F. M, Degrande G, Hunt H. E. M, Clouteau D. A comparison of two numerical models for the prediction of vibrations from underground railway traffic. Soil Dynamics and Earthquake Engineering 27 (2007) 608–624
- [15] Degrande G, Clouteau D, Othman R, Arnst M, Chebli H, Klein R, Chatterjee B. A numerical model for ground-borne vibrations from underground railway traffic based on a periodic finite element–boundary element formulation. Journal of Sound and Vibration. Volume 293, Issues 3-5, 13 June 2006, Pages 645-666

-
- [16] Hussein M. F. M, Hunt H. E. M, A numerical model for calculating vibration from a railway tunnel embedded in a full-space. *Journal of Sound and Vibration*. Volume 305, Issue 3, 21 August 2007, Pages 401-431
- [17] Auersch, L., S. Said, and R. Müller, Measurements on the vehicle-track interaction and the excitation of railway-induced ground vibration. *Procedia engineering*, 2017, 199: p. 2615-2620
- [18] Dos Santos, N. C., et al., Experimental analysis of track-ground vibrations on a stretch of the Portuguese railway network. *Soil Dynamics and Earthquake Engineering*, 2016, **90**: p. 358-380
- [19] Dos Santos, N.C., et al., Track-ground vibrations induced by railway traffic: experimental validation of a 3D numerical model. *Soil Dynamics and Earthquake Engineering*, 2017, **97**: p. 324-344
- [20] Galvin,romeroa,Domínguezj.Fullythree-dimensionalanalysisofhigh-speed train-track-soil-structuredynamicinteraction.journalofsoundand Vibration 2010;329(24):5147-63
- [21] Banimahd M, Kennedy J, Woodward P, Medero G. Behaviour of train-track interaction in stiffness transitions. *Proceedings of the Institution of Civil Engineers* 2010;1(2006):1-10
- [22] Kouroussis G, Verlinden O, Conti C. Ground propagation of vibrations from railway vehicles using a finite/infinite-element model of the soil. *Proceedings of the Institution of Mechanical Engineers, Part F: Journal of Rail and Rapid Transit* 2009;223(4):405-13
- [23] International union of Railways. UIC code 719R: earthworks and trackbed layers for railway lines. UIC.Paris, France; 1994
- [24] Kouroussis G, Verlinden O, Conti C. Free field vibrations caused by high-speed lines: measurement and time domain simulation. *Soil Dynamics and Earth- quake Engineering* 2011;31(4):692-707
- [25] Steenbergen, Michaël Jozef Matthatias Maria. "Wheel-rail interaction at short-wave irregularities." (2008)

Effect of Dynamic Creep Coefficients and External Load on Hunting Velocity in a Railway Vehicle

Seyed Ali Mousavi, Kourosch Heidari Shirazi*, Laleh Fatahi

Mechanical Engineering Department, Faculty of Engineering, Shahid Chamran University of Ahvaz, Ahvaz, Iran
sa-mousavi@stu.scu.ac.ir; k.shirazi@scu.ac.ir; lfatahi@scu.ac.ir

Abstract: The purpose of this research is to provide an accurate and low degree of freedom model to analyze critical hunting velocity for a rail vehicle. Two types of simplifications have been commonly used in investigations, including linearization of nonlinear and trigonometric terms and applying static coefficients in linear wheel/rail contact models such as Kalker model. To find the effect of these simplifications in the accuracy of computed hunting velocity a 3DOF single-axis bogie model with a wheelset possessing 3D motion mobility and constant wheel/rail contact is used. The creep forces and spin moment in the contact model are obtained from the linear Kalker model with dynamic creep coefficients. The contact model coefficients are updated in each moment based on the instant values of normal wheel force and wheelset yaw angle using a proposed algorithm. The critical speed and bifurcation diagram of the hunting frequencies are obtained and a comparison is made between the static creep coefficient model and dynamic creep coefficient model. According to the results, dramatic changes in stability margins and starting point of period doubling in the bifurcation diagram are observed under the presence of dynamic creep coefficients. Also, an increase of normal external load on the wheelset causes the reduction of critical velocity, which is merely predicted in the dynamic coefficient model. This means the static creep coefficient models do not have enough reliability for analyzing the variable weight wagon problems such as freight trains. Another important result is that the simplification of most trigonometric terms has a negligible effect on the accuracy of results.

Keywords: Creep Forces; Creep Coefficients; Stability; Hunting; Bifurcation

1 Introduction

Railway transportation has been played an important role in today's human life. Needs for higher-speed trains to increase the capacity of transportation systems besides the aging of the railway networks arises new engineering and technical challenges for designers. One of the important problems in the field of stability of

the rail vehicles dynamics is hunting behavior. The hunting can lead to an unstable amplitude growth in vibration about the yaw axis of the suspension system (or bogie) that can be ended by wagon derailment. That is why determining the accurate margin of the hunting is of great importance in the multi-body dynamics of rail vehicles. The hunting is inevitable and roots in the intrinsic property of conical wheelset, creep forces, and bogie's mass-stiffness-damper interactions in a parallel rail system. Also, it reduces ride comfort and causes damage to vehicles and rail.

Ahmadian and Yang [1, 2] evaluated the effect of system parameters on the stability of the railway vehicle by considering the nonlinear parameters of yaw damper and wheel-rail contact. The numerical simulation showed that damping coefficient changes could change the critical hunting speed. They also analyzed the Hopf bifurcation phenomenon. The results showed that nonlinear parameters in the primary suspension system, as well as rail and wheel flange contact, will play a significant role in hunting behavior. Also, nonlinear elements in wheel and rail contact and suspension systems affect critical speed and bifurcation. In some cases, the results show that the critical velocity obtained from the linear analysis is higher, than that obtained from the nonlinear analysis. In the work of True and Asmund [3], the dynamic analysis of a freight wagon in the presence of dry friction damper and nonlinear creep forces in the contact area of the wheel and rail was performed. In another work, Lee and Cheng [4, 5], employed Lyapunov's Indirect Method to obtain the critical hunting velocity, under the effects of several physical parameters. They compared the results of their model with a 6 DOF model and observed that the predicted critical hunting speed by the 6 DOF system is much higher than their model. Another interesting finding of this work was that the critical hunting velocity of wagons with new wheels is more than that with worn wheels. Using a nonlinear creep model, Lee and Cheng [6, 7] derived the equations of motion for an 8 DOF system. They compared the results of the 8 DOF model with a 6 DOF model in a curved path. Unlike the previous studies, their investigations showed that the critical hunting velocity for the 8 DOF model is higher than the 6 DOF model, However, they both used nonlinear models, predicting fewer hunting velocities compared with the linear contact model. Also, for 8 DOF model and based on the linear creep model, the effect of the parameters of the secondary suspension system on the critical speed was investigated. Zeng and Wu [8] examined the derailment of a rail vehicle by considering the contact angle of the wheel flange, the coefficient of friction, the creep forces, and the presentation of a new relationship. The results showed that increasing the contact angle of the wheel rim and reducing the coefficient of friction is effective in preventing wheel climb derailment. Cheng *et al.* [9] used a nonlinear heuristic creep model for a 21 DOF wagon model and obtained the critical speed of the wagon as it crossed the curved track. Their results showed that the critical speed obtained for a 6 and a 14 DOF models is much higher than the 20 DOF model. Also, the critical velocity obtained by the nonlinear heuristic creep model is lower than the velocity obtained from the linear creep model. Zboinski and Dusza [10]

studied the stability and self-excited vibrations of a rail vehicle on a curved track and used the fork diagrams for the curved track to examine the effect of different initial conditions. Kim and Seok [11] used the multiple-scale method to study the bifurcation diagrams of a rail vehicle using linear and nonlinear models for lateral wheelset displacements. By presenting a dynamic model of a rail vehicle, Wang and Li [12, 13] investigated the effect of acceleration on the wheel lift. It was observed that the contact patch of the wheel and rail at a contact angle has a critical point, to start the derailment occurs quickly. Zhang and Dai [14] presented a mathematical model of a 2 DOF for a wheelset, to analyze the effect of a yaw damper of secondary suspension on Hopf bifurcation. They also applied the nonlinear contact model of the wheel and the rail, to extract the equations of motion, and study the effect of different parameters on the lateral stability of a particular type of wheelset. Wei and Yabuno [15] examined subcritical Hopf and saddle-node bifurcations in the hunting motion of a railway vehicle by considering cubic and quintic nonlinearities. The results showed that both the cubic and the quintic nonlinearities of the wheel system play an important role. Skerman et al. [16] have investigated the hunting of an unloaded freight wagon fitted with three-piece bogies, which utilize friction wedges for damping and have friction at many interfaces. Several methods of analysis were compared, including simulation on track with irregularities. Also, different initial conditions were used for each bogie to excite different types of hunting at a given speed.

In the present study, the influence of two types of simplifications that are commonly used in the prediction of the hunting velocity, including linearization of nonlinear and trigonometric terms and employing linear contact models with constant coefficients are investigated. In Section 2 dynamic and kinematic equations of motion based on the 3D mobility of wheelset and constant contact of the wheel/rail are derived. In Section 3 linear Kalker model is represented and an algorithm for estimation of dynamical creepage constants is developed. In Section 4, the results are demonstrated and discussed. In Section 5, concluding remarks are presented. The proposed technique could also be useful for the dynamic analysis of two-wheeled robots [17].

2 Governing Equation of a Wheelset

The governing equations of the system include three types of equations, i.e., dynamic equilibrium equations, kinematic compatibility equations, and creepage model constitutive equations for creepage forces and moments. According to Figure 1, to describe the three-dimensional rotation of the wheelset with respect to the ground frame, three coordinate systems with three associated rotations including, ψ rotation angle about the vertical axis (or Z) and φ rotation angle about the longitudinal axis (or X), and θ angular velocity about wheelset lateral

axis can be used. Therefore, the angular velocity of the wheelset and velocity of wheelset midpoint are obtained as follows:

$$\bar{\omega} = \dot{\phi} \hat{i}_1 + (\Omega + \dot{\theta}) \hat{j}_w + \dot{\psi} \hat{k} \tag{1}$$

$$\bar{v} = (V + \dot{x}) \hat{i} + \dot{y} \hat{j} + \dot{z} \hat{k} \tag{2}$$

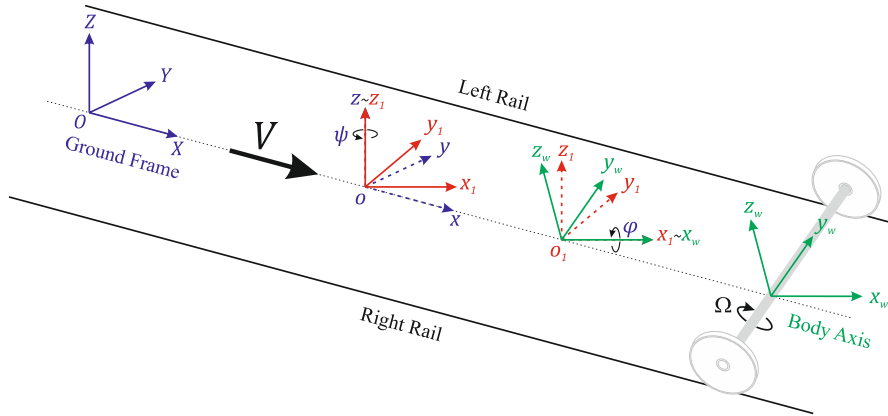


Figure 1
Axes Systems of Wheelset

where, V and Ω are constant parts and \dot{x} and $\dot{\theta}$ are variable parts of the components v_x and ω_y , respectively.

2.1 Kinematics of the Wheelset Contact Point

The front view of the wheelset, normal and tangential components of contact forces, and also the geometry of the wheelset are depicted in Figure 2. By using Figure 2 the position vectors of the contact point for the left and right wheel with respect to the wheelset midpoint are given as follows:

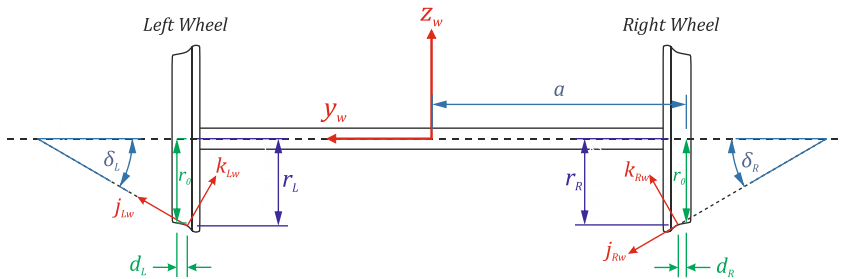


Figure 2
Contact Axes

$$\vec{r}_c^{Lw} = (a - d_L) \hat{j}_w - r_L \hat{k}_w \quad (3)$$

$$\vec{r}_c^{Rw} = -(a + d_R) \hat{j}_w - r_R \hat{k}_w \quad (4)$$

where, a is half-track length. Using proper coordinate transformations, the normal forces can be obtained for each wheel:

$$\vec{N}_L^w = \begin{cases} N_L \sin(\psi) \sin(\delta_L + \varphi) \\ -N_L \cos(\psi) \sin(\delta_L + \varphi) \\ N_L \cos(\delta_L + \varphi) \end{cases} \begin{matrix} i \\ j \\ k \end{matrix} \quad (5)$$

$$\vec{N}_R^w = \begin{cases} -N_R \sin(\psi) \sin(\delta_R - \varphi) \\ +N_R \cos(\psi) \sin(\delta_R - \varphi) \\ N_R \cos(\delta_R - \varphi) \end{cases} \begin{matrix} i \\ j \\ k \end{matrix} \quad (6)$$

Moreover, the angular velocity of the left and right wheel can be expressed in the left and right wheels frames as follows:

$$\vec{\omega}_c^{Lw} = \begin{cases} \dot{\varphi} \\ +(\Omega + \dot{\theta}) \cos \delta_L + \dot{\psi} \sin(\delta_L + \varphi) \\ -(\Omega + \dot{\theta}) \sin \delta_L + \dot{\psi} \cos(\delta_L + \varphi) \end{cases} \begin{matrix} i_{Lw} \\ j_{Lw} \\ k_{Lw} \end{matrix} \quad (7)$$

$$\vec{\omega}_c^{Rw} = \begin{cases} \dot{\varphi} \\ +(\Omega + \dot{\theta}) \cos \delta_R - \dot{\psi} \sin(\delta_R - \varphi) \\ +(\Omega + \dot{\theta}) \sin \delta_R + \dot{\psi} \cos(\delta_R - \varphi) \end{cases} \begin{matrix} i_{Rw} \\ j_{Rw} \\ k_{Rw} \end{matrix} \quad (8)$$

where, \vec{r}_c^{Lw} and \vec{r}_c^{Rw} are position vectors of the left and right contact points relative to the center of the wheelset in the corresponding frames, \vec{N}_L^w and \vec{N}_R^w are normal forces in the ground frame.

2.2 Equation of Motion for the Wheelset

Considering dynamic equilibrium and ground frame the equations of motion can be derived using the well-known Newton's second law as follows:

$$m\ddot{\vec{r}} = \Sigma \vec{F} \quad (9)$$

$$\dot{\vec{H}}_G = \Sigma \vec{M}_G \quad (10)$$

Using, Figure 3 and substituting the wheelset's mass, inertia, midpoint acceleration, and angular velocity and exerting external forces and moments in Eqs. 9 and 10, six Eqs. 11 to 16 will be obtained for the model of a wheelset shown in Figure 3:

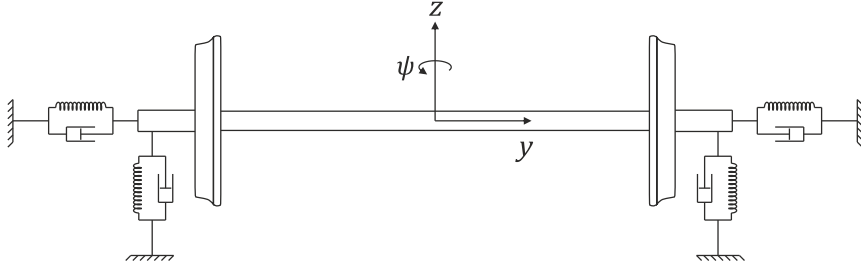


Figure 3
Model of Wheelset

$$m_w \ddot{x} = F_{lx} + F_{rx} + N_{lx} + N_{rx} \quad (11)$$

$$m_w \ddot{y} = F_{ly} + F_{ry} + N_{ly} + N_{ry} + F_s - F_T \quad (12)$$

$$m_w \ddot{z} = F_{lz} + F_{rz} + N_{lz} + N_{rz} - m_w g - W_{ext} \quad (13)$$

$$I_x \ddot{\psi} \cos \psi + u (\phi \dot{\phi}, \dot{\theta}, \ddot{\theta}, \psi, \dot{\psi}, \ddot{\psi}) = +R_{ry} (F_{rz} + N_{rz}) \quad (14)$$

$$-R_{rz} (F_{ry} + N_{ry}) + R_{ly} (F_{lz} + N_{lz}) - R_{lz} (F_{ly} + N_{ly}) + M_{lx} + M_{rx} + M_{sx}$$

$$I_y \ddot{\theta} \cos \phi \cos \psi + v (\phi, \dot{\phi}, \ddot{\phi}, \dot{\psi}, \ddot{\psi}) = +R_{rx} (F_{rz} + N_{rz}) \quad (15)$$

$$-R_{rz} (F_{rx} + N_{rx}) + R_{lx} (F_{lz} + N_{lz}) - R_{lz} (F_{lx} + N_{lx}) + M_{ly} + M_{ry} + M_{sy}$$

$$(I_z \cos^2 \phi + I_y \sin^2 \phi) \ddot{\psi} + w (\phi, \dot{\phi}, \ddot{\phi}, \dot{\psi}, \ddot{\psi}) = +R_{rx} (F_{ry} + N_{ry}) \quad (16)$$

$$-R_{ry} F_{rx} + R_{ly} (F_{ly} + N_{ly}) - R_{ly} F_{lx} + M_{lz} + M_{rz} + M_{sz} - 2bF_d$$

where, F_{ij} , M_{ij} and N_{ij} are creep forces, moments, and normal forces, respectively and R_{ij} are moment arms and $i = \{l, r\}$ & $j = \{x, y, z\}$. Also, suspension force F_s , suspension moment M_s , flange force F_T , and yaw damper moment $2bF_d$ can be derived as follows [2]:

$$\vec{F}_s = -2(K_y y + C_y \dot{y}) \hat{j} \quad (17)$$

$$\vec{M}_s = -2K_\psi b^2 \psi \quad (18)$$

$$F_T = \begin{cases} K_r (y - \delta) & y > \delta \\ 0 & -\delta < y < \delta \\ -K_r (y + \delta) & y < -\delta \end{cases} \quad (19)$$

$$F_d = \begin{cases} C_1 V_\psi + C_2 V_\psi^2 + C_3 V_\psi^3 + C_4 V_\psi^4 & V_\psi > 0 \\ C_1 V_\psi - C_2 V_\psi^2 + C_3 V_\psi^3 - C_4 V_\psi^4 & V_\psi < 0 \end{cases} \quad (20)$$

Eqs. 12 and 16 will be used as the main equations to derive lateral displacement y and the yaw angle ψ . Two unknowns \dot{x} and $\dot{\theta}$ in Eqs. 11 and 15, and the vertical forces of the left and right wheels in Eqs. 13 and 14 can be derived using the two following kinematic constraints:

$$z = -\frac{\lambda a(1 - \cos\psi)}{\cos\psi} + \frac{\lambda ay^2}{(a - \lambda r_0)^2} \quad (21)$$

$$\varphi = \frac{\lambda y}{a - \lambda r_0} \quad (22)$$

2.3 The Creep Forces and Moments

Large forces are generated in the contact area of wheels and rails, and these forces have a significant effect on the dynamics of the vehicle. Among the various modeling methods for approximating the creep forces and moments in the wheel-rail contact patch, Kalker theory [18] is extensively used in the applications. According to Kalker theory, if the longitudinal, lateral, and spin creep parameters are very small, the slip zone is small, and therefore, regardless of slip, the adhesion zone can be considered as the dominant area in wheel-rail contact. Based on this theory, creep forces and spin moment are defined through Eqs. 23, 24, and 25:

$$F_x = -f_{33}\zeta_x \quad (23)$$

$$F_y = -f_{11}\zeta_y - f_{12}\zeta_{sp} \quad (24)$$

$$M_z = f_{12}\zeta_y - f_{22}\zeta_{sp} \quad (25)$$

where, f_{11} , f_{12} , f_{22} , and f_{33} are the creep coefficients and ζ_x , ζ_y and ζ_{sp} are creepage terms. Since the creep forces are defined on the wheel contact plane they should be expressed with respect to the ground frame.

2.4 Creepage Expressions

When two relatively rigid bodies are compressed and rolled, a creep phenomenon occurs, and creep forces are generated. These forces have a significant effect on the dynamic behavior of the wheel and eventually railway vehicles. Based on Carter's work [19] the left and right wheel creepage can be computed as follows:

$$\zeta_x^L = \frac{1}{V} \left[(V + \dot{x}) \cos\psi + \dot{y} \sin\psi - r_L \dot{\psi} \sin\varphi - (a - d_L) \dot{\psi} \cos\varphi - (\Omega + \dot{\theta}) r_L \right] \quad (26)$$

$$\xi_y^L = \frac{1}{V} \left[-(V + \dot{x}) \cos(\delta_L + \varphi) \sin \psi + \dot{y} \cos(\delta_L + \varphi) \cos \psi \right. \\ \left. + \dot{z} \sin(\delta_L + \varphi) + r_L \dot{\phi} \cos \delta_L + (a - d_L) \dot{\phi} \sin \delta_L \right] \quad (27)$$

$$\xi_{sp}^L = \frac{1}{V} \left[-(\Omega + \dot{\theta}) \sin \delta_L + \dot{\psi} \cos(\delta_L + \varphi) \right] \quad (28)$$

$$\xi_x^R = \frac{1}{V} \left[(V + \dot{x}) \cos \psi + \dot{y} \sin \psi - r_R \dot{\psi} \sin \varphi + (a + d_R) \dot{\psi} \cos \varphi - (\Omega + \dot{\theta}) r_R \right] \quad (29)$$

$$\xi_y^R = \frac{1}{V} \left[-(V + \dot{x}) \cos(\delta_R - \varphi) \sin \psi + \dot{y} \cos(\delta_R - \varphi) \cos \psi \right. \\ \left. - \dot{z} \sin(\delta_R - \varphi) + r_R \dot{\phi} \cos \delta_R + (a + d_R) \dot{\phi} \sin \delta_R \right] \quad (30)$$

$$\xi_{sp}^R = \frac{1}{V} \left[(\Omega + \dot{\theta}) \sin \delta_R + \dot{\psi} \cos(\delta_R - \varphi) \right] \quad (31)$$

2.5 Creep and Creepage Coefficients

The creep coefficient f_{11} , f_{12} , f_{22} , and f_{33} are defined as follows:

$$f_{11} = (ab) GC_{22} \quad (32)$$

$$f_{12} = (ab)^{3/2} GC_{23} \quad (33)$$

$$f_{22} = (ab)^2 GC_{33} \quad (34)$$

$$f_{33} = (ab) GC_{11} \quad (35)$$

where, C_{11} , C_{22} , C_{23} , and C_{33} are the creepage and spin coefficients, which depend only on Poisson's ratio (ν) and the ratio of the semi-axis of the contact ellipse (a/b) according to Kalker table of creepage and spin coefficients. Given G and ν , combined rigidity modulus, and combined Poisson's ratio, respectively, as follows:

$$G = \frac{2G_w G_r}{G_w + G_r} \quad (36)$$

$$\nu = \frac{G}{2} \left[\left(\frac{\nu_w}{G_r} \right) + \left(\frac{\nu_w}{G_r} \right) \right] \quad (37)$$

where, a and b are the semi-axis of the contact ellipse in the rolling direction and lateral direction, respectively, such that [20]:

$$a = m \left[3\pi N (K_1 + K_2) / 4K_3 \right]^{1/3} \quad (38)$$

$$b = n \left[3\pi N (K_1 + K_2) / 4K_3 \right]^{1/3} \quad (39)$$

where, N is the normal force, and subscripts w and r denote wheel and rail, respectively and K_1 , K_2 and K_3 are defined as follows:

$$K_1 = \frac{1 - \nu_w^2}{\pi E_w} \quad (40)$$

$$K_2 = \frac{1 - \nu_r^2}{\pi E_r} \quad (41)$$

$$K_3 = \frac{1}{2} \left[\frac{1}{R_w} + \frac{1}{R'_w} + \frac{1}{R_r} + \frac{1}{R'_r} \right] \quad (42)$$

where, R , R' and E denote the rolling radius of the wheel, the transverse radius of curvature of the wheel profile at the point of contact, and Young's modulus of elasticity, respectively.

Given θ and K_4/K_3 , the coefficients m and n in Eqs. 38 and 39 can be estimated using Table of Hertz [20], where θ and K_4 are defined as follows:

$$\theta = \cos^{-1}(K_4/K_3) \quad (43)$$

$$K_4 = \frac{1}{2} \left[\left(\frac{1}{R_w} + \frac{1}{R'_w} \right)^2 + \left(\frac{1}{R_r} + \frac{1}{R'_r} \right)^2 + 2 \left(\frac{1}{R_w} - \frac{1}{R'_w} \right) \left(\frac{1}{R_r} + \frac{1}{R'_r} \right) \cos(2\psi) \right] \quad (44)$$

where, ψ is the angle between the normal planes that contain the curvatures $1/R_1$ and $1/R_2$ such that when the rails are parallel, ψ is the yaw angle of the wheel about the vertical axis.

According to the above-mentioned equations, an algorithm can be suggested for the dynamic updating of creep coefficients. The process of estimation of creep forces includes manipulation of, creepage expressions computation, creepage coefficients, and creep coefficients. The former is obtained from kinematic variables and the latter from the wheel normal force and yaw angle. The flowchart in Figure 4 represents this dependency and order of calculations of the variables. In this flowchart, the yellow boxes contain the constant parameters depending on the mechanical properties of the wheels and rails, the white boxes contain parameters that are a function of the normal wheel force and the yaw angle, and gray boxes contain input variables of the normal wheel force and the yaw angle.

power function for curve fitting is employed to fit ten values of elliptical diameter ratios for row $\nu = 0.28$:

$$C_{ij} = c_1 \left(\frac{b}{a} \right)^{c_2} + c_3 \tag{45}$$

where, c_1 , c_2 and c_3 are three function parameters. Table 1 summarizes the three parameters of each of the power functions for each of C_{ij} 's table. These functions are depicted in Figure 5 (a) to (d). To ensure the accuracy of estimation of each function the value of R-square is represented in Table 1.

Table 1
Power function curve fitting of creepage and spin coefficients for $\nu = 0.28$

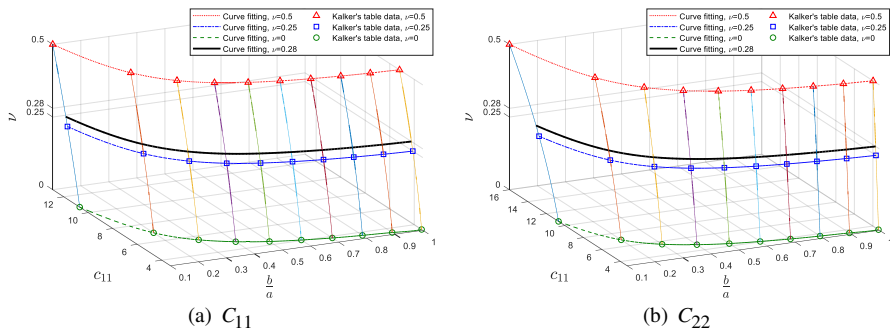
| Coefficient | c_1 | c_2 | c_3 | R^2 |
|-------------|--------|---------|--------|--------|
| C_{11} | 1.2460 | -0.8524 | 2.9650 | 1 |
| C_{22} | 1.6650 | -0.8238 | 2.0310 | 1 |
| C_{23} | 0.8630 | -1.2200 | 0.6391 | 1 |
| C_{33} | 0.7695 | +1.0080 | 0.4180 | 0.9999 |

For estimation of m and n using the Hertz table [20], two types of function are employed, including a three-parameter power function m and a four-parameter exponential function n . These functions are selected using the evaluation of the R-square of the CFtool different functions. Based on the calculations, the functions are as

$$\text{follows: } m = 37.44\theta^{-0.7236} - 0.451 \tag{46} \quad (R^2 = 1)$$

$$n = 0.3626 \exp(0.0113\theta) - 0.259 \exp(-0.107\theta) \tag{47} \quad (R^2 = 0.9995)$$

The curve of the functions of m and n are depicted in Figure 5 (e) and (f).



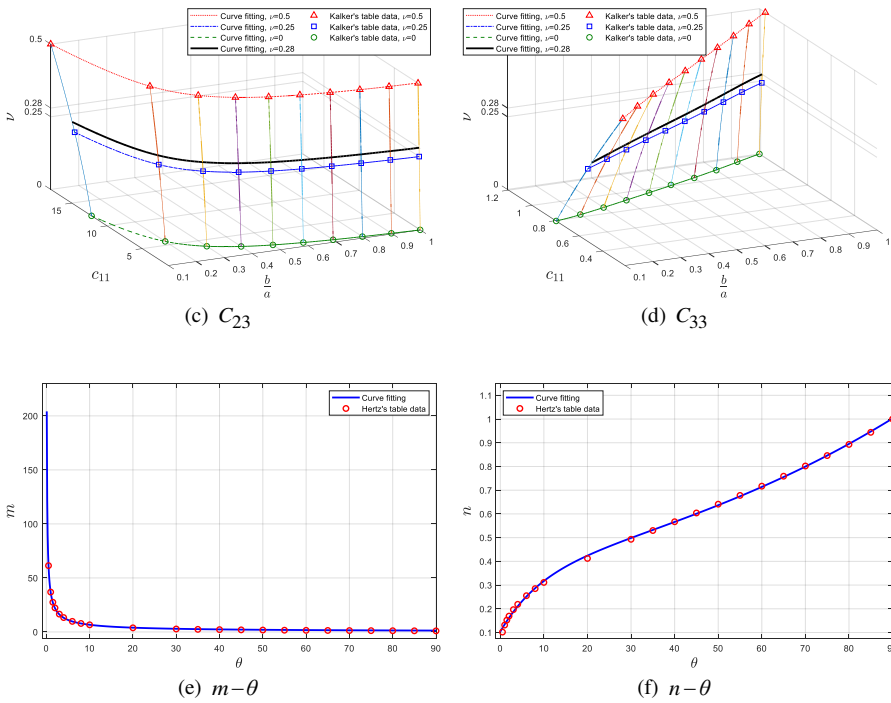


Figure 5
Creep Coefficients Curve Fitting

3 Results

In this section, several studies are performed to clear both the effect of simplification by comparing a simplified 2DOF, with a full terms 3DOF model, as well as the effect of contact model by comparing a static creep coefficient (SCC) model and a dynamic creep coefficient (DCC) model. The numerical values of the parameters and constants of the system are summarized in Table 2. The first study results are depicted in Figure 6. In this study, nonlinear and trigonometric terms of the mathematical model of the considered system are neglected, however, two systems are considered, which are, the simplified model with SCC as well as the simplified model with DCC. Also for the purpose of validation, the results are compared with those presented in [21]. The results are included a bifurcation diagram of lateral vibration amplitude of the wheelset under the velocity up to 60m/s and for three cases of vertical external loading, exerted on the midpoint of the wheelset. It is seen that the results of SCC model are very similar to that of [21] and the increase of external load has no significant effect on the hunting velocity, by which, jumping on the lateral vibration amplitude occurs.

However, for DCC surprisingly a dramatic reduction of hunting velocity for higher external loads is observed. Practically, this means that the heavier the wagon, the more instability and lower the critical velocity.

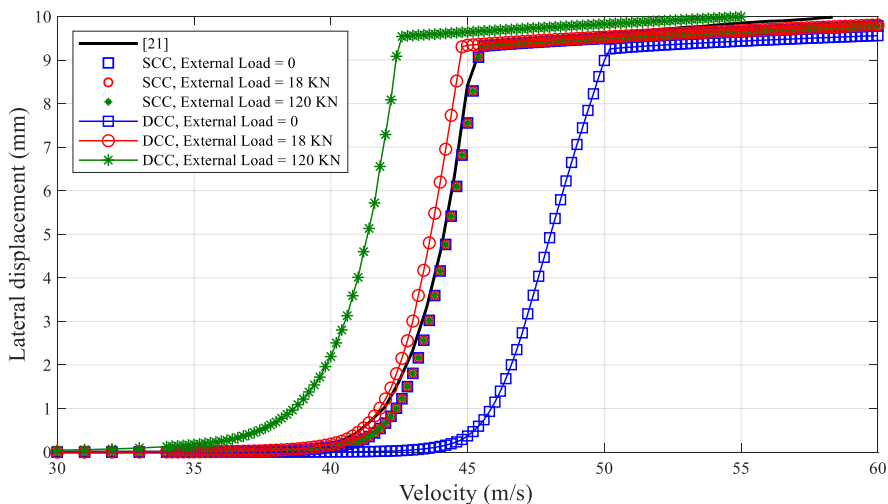


Figure 6

Comparison of bifurcation diagrams for lateral displacement from the simplified equations of motion with Reference [21]

Table 2
System Parameters [2]

| | |
|--------------------------------------|--|
| Half of the track gauge | $a = 0.7176 \text{ m}$ |
| Half of yaw spring arm | $b = 1 \text{ m}$ |
| Lateral damping of suspension | $C_y = 2.1 \times 10^4 \text{ N.s / m}$ |
| Damping coefficients for yaw dampers | $C_1 = 1.9230 \times 10^4$ $C_2 = 5.1400 \times 10^5$ $C_3 = 3.1127 \times 10^6$ $C_4 = 5.1400 \times 10^6$ |
| Lateral creep force coefficient | $f_{11} = 6.728 \times 10^6 \text{ N}$ |
| Spin creep force coefficient | $f_{22} = 1000 \text{ N.m}^2$ |
| Lateral spin creep force coefficient | $f_{12} = 1.2 \times 10^3 \text{ N.m}$ |
| Longitudinal creep force coefficient | $f_{33} = 6.728 \times 10^6 \text{ N}$ |
| Roll moment of inertia of wheelset | $I_{wx} = 625.7 \text{ kg.m}^2$ |

| | |
|--|---------------------------------------|
| Spin moment of inertia of wheelset | $I_{wy} = 133.92 \text{ kg.m}^2$ |
| Lateral rail stiffness | $K_r = 1.617 \times 10^7 \text{ N/m}$ |
| Lateral stiffness of primary suspension | $K_y = 8.67 \times 10^4 \text{ N/m}$ |
| Yaw spring stiffness of primary suspension | $K_x = 8.67 \times 10^4 \text{ N/m}$ |
| Wheelset mass | $m_w = 1800 \text{ kg}$ |
| Wheel radius | $r_0 = 0.533 \text{ m}$ |
| Wheel conicity | $\lambda = 0.05$ |
| Flange clearance | $\delta = 0.923 \text{ cm}$ |

The second study focuses on the effect of degrees of freedom of the model and the effect of the presence of nonlinear terms and additional degrees of freedom in the model. The considered model is a 3DOF model, with 6 generalized coordinates including, x , y , z , φ , ψ and θ . However, because of the presence of the three geometrical constraints, the remaining DOF is 3, e.g., y , ψ and x . Meanwhile, there is a simplified 2DOF model, which is extensively used in nonlinear and perturbation analyses [1], which merely considers y and ψ 2DOF. According to this model, \dot{x} and $\dot{\theta}$ are assumed to be constant. The diagrams in Figure 7 to Figure 9, show that the 2 DOF and 3DOF models have similar responses under the different vertical external loading conditions, whether the model is of SCC type or DCC.

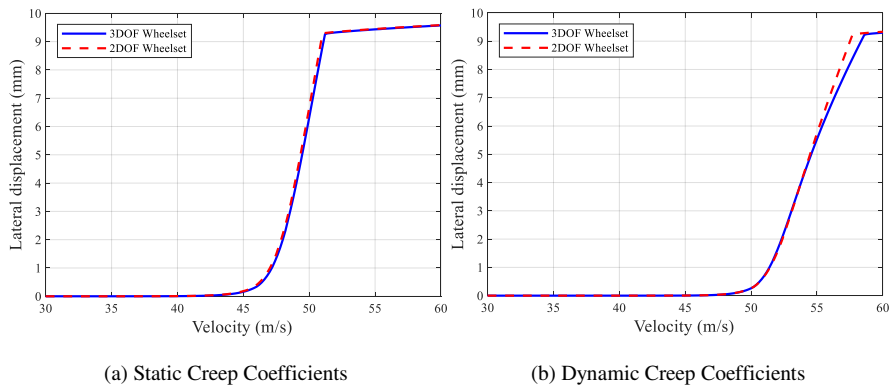


Figure 7
Comparison of 2DOF and 3DOF results, Axle Load = 0

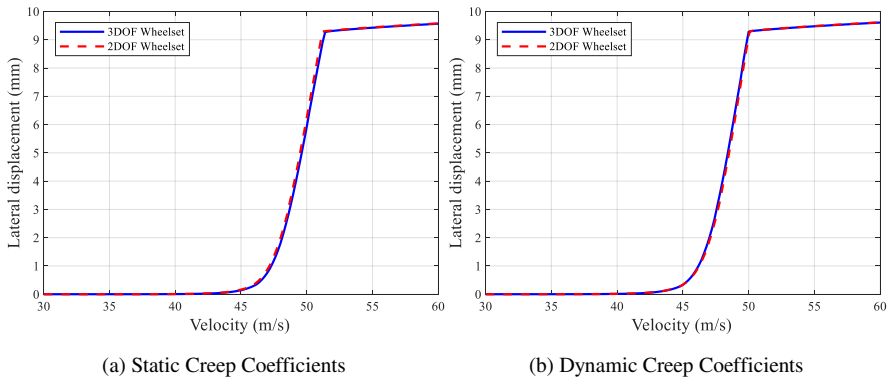


Figure 8
Comparison of 2DOF and 3DOF results, Axle Load = 18 kN

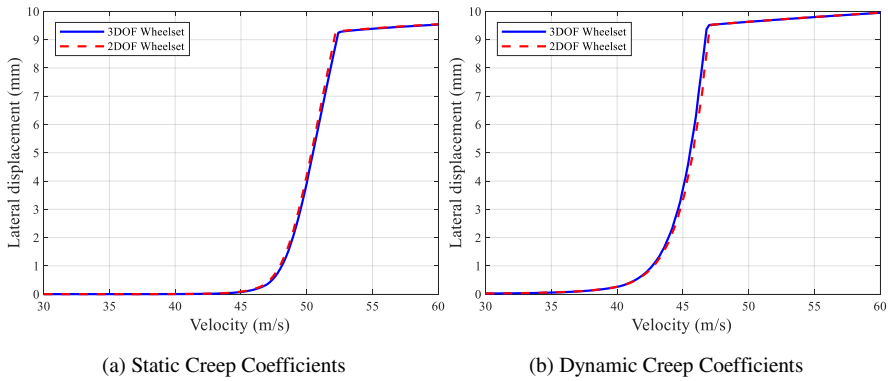


Figure 9
Comparison of 2DOF and 3DOF results, Axle Load = 120 kN

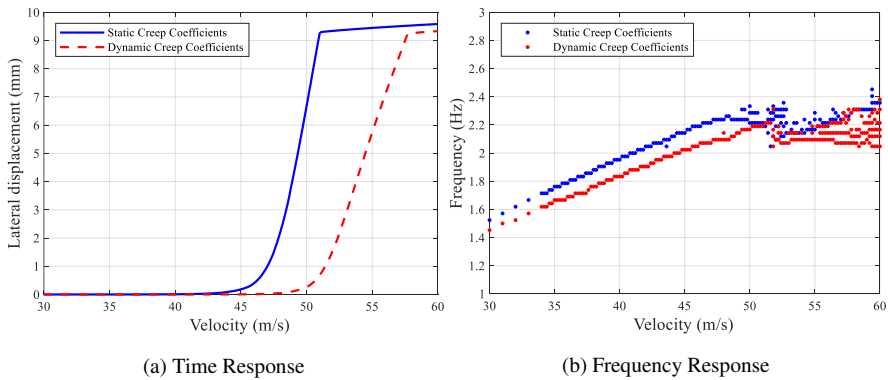


Figure 10
Comparison of bifurcation diagrams for lateral displacement, Axle Load = 0

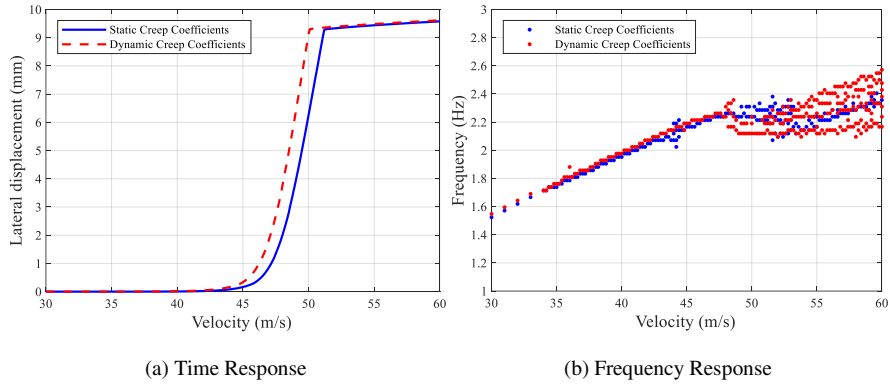


Figure 11

Comparison of bifurcation diagrams for lateral displacement, Axle Load = 18 kN

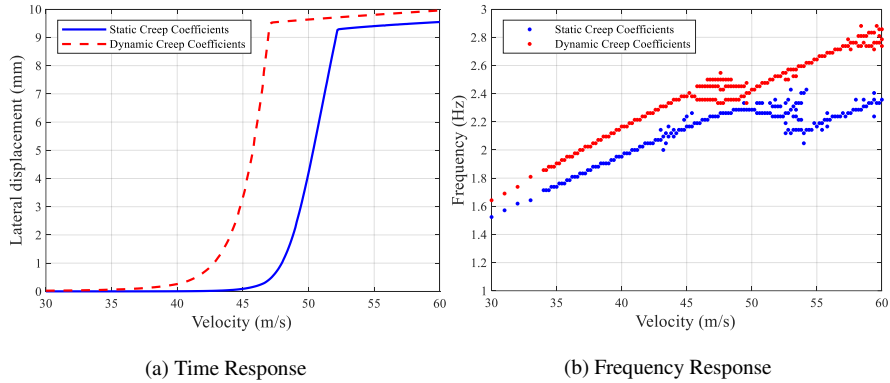


Figure 12

Comparison of bifurcation diagrams for lateral displacement, Axle Load = 120 kN

In the third study, the importance of creep coefficients on the regularity of lateral dynamic behavior of the wheelset is investigated. To this end, the lateral response amplitude of the two SCC 3DOF and DCC 3DOF models under the different vertical loads are analyzed. In addition to the amplitude, the frequency content of the time domain response of the lateral vibration in the different forward velocities are extracted. According to Figure 10(a) to Figure 12(a) not only the DCC model predicts that increase of the vertical external load, causes a decrease in the hunting velocity, but also from Figure 10 (b) to Figure 12(b) it is concluded that the DCC model predicts that entering the behavior to a period-doubling process and burst the chaotic dynamic is more probable for the smaller vertical external loads.

The latter means that as it is depicted from Figure 12(b) the regularity in lateral dynamic behavior for a vertical external load 120 kN is much more than 18 kN and

0 kN cases. While the bifurcation diagram drawn by SCC model has no significant difference for the different vertical external loads.

Another example of the remarkable effect of DCC in the prediction of hunting at different speeds is shown in Figure 13. According to Figure 13 in 55 m/s both the SCC and DCC models predict unstable vibration such that rail-flange contact occurs. However, for the unload case in Figure (a) and Figure (d), the DCC model reports the presence of a stable limit cycle while the SCC model reports unstable growth of amplitude which ends with the flange contact. Also, according to Figure 13(c) and Figure 13(e) and imminent derailment is predicted by the DCC model while the SCC model shows more safe motion. Figure 13 clearly proves that predictions and interpretations of the DCC model in many cases completely differ from those of the SCC model.

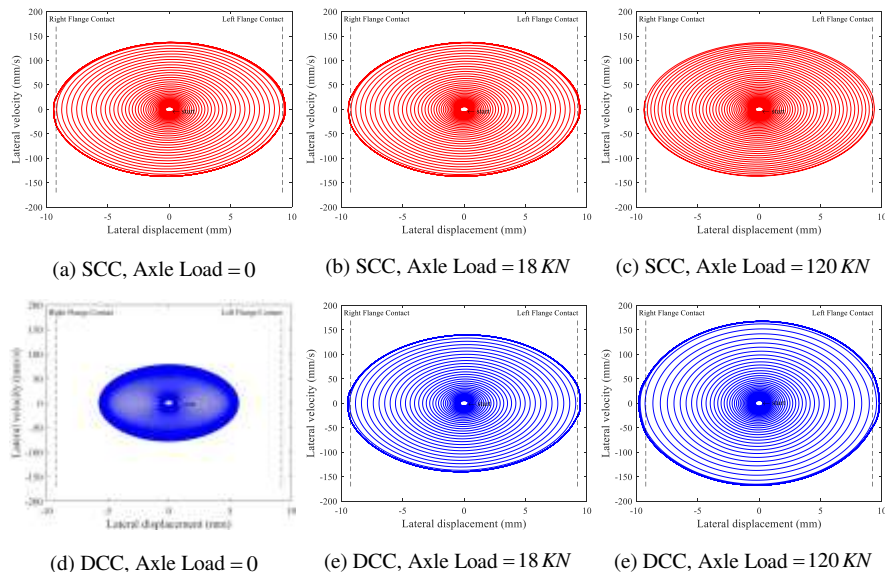


Figure 13

Phase portrait plot for the 3DOF wheelset in velocity $55\frac{\text{m}}{\text{s}}$

Conclusions

In the present work, the effect of some factors in the final prediction of the hunting velocity of a railway vehicle such as the mathematical contact model, degree of freedom of the wheelset, dynamic creep coefficients, and the presence of small nonlinearities in the model have been studied. A simplified 2DOF model and a 3DOF full terms dynamic models are considered. Also, two contact models based on the linear Kalker model with the assumption of SCC and DCC have been compared. The phase diagram as well as amplitude and frequency bifurcation

diagrams for different ranges of velocity and external vertical loads have been generated. The results can be summarized as follows:

The presence of all trigonometric and small nonlinearities in the 3DOF model has no particular effect on the accuracy of results compared to the simplified 2DOF model.

Bogie models with SCC contact assumption are not able to predict the dependency of the hunting velocity to the vertical external load, whereas DCC model show this dependency clearly.

According to the DCC models increase of the external vertical load, causes an increase in the instability of velocity margin and decreases the irregularity during hunting motion.

Due to the important role of external load in hunting velocity, different permissible velocities should be used for the full and empty state of freight trains for more derailment safety.

References

- [1] Ahmadian, M., Yang, S.: Effect of system nonlinearities on locomotive bogie hunting stability. *Veh. Syst. Dyn.*, **29** (6), 1998, pp. 365-384
- [2] Ahmadian, M., Yang, S.: Hopf Bifurcation and Hunting Behavior in a Rail Wheelset with Flange Contact. *Nonlinear Dyn.*, **15** (1), 1998, pp. 15-30
- [3] True, H., Asmund, R.: The Dynamics of a Railway Freight Wagon Wheelset With Dry Friction Damping. *Veh. Syst. Dyn.*, **38** (2), 2002, pp. 149-163
- [4] Lee, S. Y., Cheng, Y. C.: Hunting stability analysis of high-speed railway vehicle trucks on tangent tracks. *J. Sound Vib.*, **282** (3-5), 2005, pp. 881-898
- [5] Lee, S.-Y., Cheng, Y.-C.: Nonlinear Analysis on Hunting Stability for High-Speed Railway Vehicle Trucks on Curved Tracks. *J. Vib. Acoust.*, **127** (4), 2005, pp. 324-332
- [6] Lee, S. Y., Cheng, Y. C.: Influences of the vertical and the roll motions of frames on the hunting stability of trucks moving on curved tracks. *J. Sound Vib.*, **294** (3), 2006, pp. 441-453
- [7] Lee, S.-Y., Cheng, Y.-C.: A New Dynamic Model of High-Speed Railway Vehicle Moving on Curved Tracks. *J. Vib. Acoust.*, **130** (1), 2008, p. 011009
- [8] Zeng, J., Wu, P.: Study on the wheel/rail interaction and derailment safety. *Wear*, **265** (9), 2008, pp. 1452-1459
- [9] Cheng, Y.-C. et al.: Modeling and nonlinear hunting stability analysis of

- high-speed railway vehicle moving on curved tracks. *J. Sound Vib.*, **324** (1), 2009, pp. 139-160
- [10] Zboinski, K., Dusza, M.: Self-exciting vibrations and Hopf's bifurcation in non-linear stability analysis of rail vehicles in a curved track. *Eur. J. Mech. A/Solids*, **29** (2), 2010, pp. 190-203
- [11] Kim, P., Seok, J.: Bifurcation analysis on the hunting behavior of a dual-bogie railway vehicle using the method of multiple scales. *J. Sound Vib.*, **329** (19), 2010, pp. 4017-4039
- [12] Wang, W., Li, G.: Development of high-speed railway vehicle derailment simulation – Part I: A new wheel/rail contact method using the vehicle/rail coupled model. *Eng. Fail. Anal.*, **24**, 2012, pp. 77-92
- [13] Wang, W., Li, G.: Development of high-speed railway vehicle derailment simulation – Part II: Exploring the derailment mechanism. *Eng. Fail. Anal.*, **24**, 2012, pp. 93-111
- [14] Zhang, T., Dai, H.: Bifurcation analysis of high-speed railway wheel-set. *Nonlinear Dyn.*, **83** (3), 2016, pp. 1511-1528
- [15] Wei, W., Yabuno, H.: Subcritical Hopf and saddle-node bifurcations in hunting motion caused by cubic and quintic nonlinearities: experimental identification of nonlinearities in a roller rig. *Nonlinear Dyn.*, **98** (1), 2019, pp. 657-670
- [16] Skerman, D. et al.: Determining the critical speed for hunting of three-piece freight bogies: practice versus simulation approaches. *Veh. Syst. Dyn.*, **0** (0), 2021, pp. 1-22
- [17] Wiech, J. et al.: Virtual spring damper method for nonholonomic robotic swarm self-organization and leader following. *Contin. Mech. Thermodyn.*, **30** (5), 2018, pp. 1091-1102
- [18] Kalker, J. J.: Survey of Wheel/Rail Rolling Contact Theory. *Veh. Syst. Dyn.*, **8** (4), 1979, pp. 317-358
- [19] Carter, F. W.: On the Action of a Locomotive Driving Wheel. *Proc. R. Soc. A Math. Phys. Eng. Sci.*, **112** (760), 1926, pp. 151-157
- [20] Garg, V. K., Dukkipati, R. V.: *Dynamics of Railway Vehicle Systems*. 1984
- [21] Sedighi, H. M., Shirazi, K. H.: Bifurcation analysis in hunting dynamical behavior in a railway bogie: Using novel exact equivalent functions for discontinuous nonlinearities. *Sci. Iran.*, **19** (6), 2012, pp. 1493-1501

Optimization of the Angled Guide Plate for the Vossloh W14-PK Fastener

**Wei Qi¹, Peyman Aela², Guoqing Jing³, Yunyun Tong⁴,
Majid Movahedi Rad⁵**

¹School of Rail Transit, Chengdu Vocational & Technical College of Industry, No. 818, Zhengxing street, Tianfu New District, Chengdu Sichuan, P.R. China, 610218

² Department of Civil and Environmental Engineering, The Hong Kong Polytechnic University, 11 Yuk Choi Rd, Hung Hom, Kowloon, Hong Kong, China

³ School of Civil Engineering, Beijing Jiaotong University, No. 3 Shangyuancun, Haidian District, Beijing, China, 100044

⁴ School of Civil Engineering and Architecture, Zhejiang University of Science & Technology, 318 Liuhe Rd, Xihu Qu, Hangzhou, China, 310023

⁵ Department of Structural and Geotechnical Engineering, Széchenyi István University, Egyetem tér 1, 9026 Győr, Hungary

e-mail: qw9199@my.swjtu.edu.cn, peyman.aela@polyu.edu.hk, gqjing@bjtu.edu.cn, 112013@zust.edu.cn, majidmr@sze.hu

Abstract: Angled guide plates are used to transmit the forces induced by trains, from the rail seat, to the concrete sleepers. Additionally, the design of the angled guide plates, with an appropriate width, supports tilting protection. Considering the updated requirements of the ML-1 railway line, in the Islamic Republic of Pakistan, an optimization design of the angled guide plate of the Vossloh W14-PK fasteners was carried out herein. The design requirements of the angled guide plate need to meet the requirements of structural stress and protect the plates from deterioration. Given the conducted refined model of the Vossloh W14 - PK fastener, it is shown that the force and deformation of the angled guide plate, in the bearing groove adjacent and the outside bolt hole area, are small. Therefore, it was preliminarily recommended that the optimization area of the angled guide plate be divided into the section I, close to the rail groove and section II, outside the bolt hole. The Finite Element Model (FEM) of angled guide plate was established, which is used to analyze the influences of length, width, depth and the number of holes, in section I and section II, on the force distribution, across the angled guide plate. The results show that the scheme of reducing the amount of material and minimizing the influence of force on the structure of the angled guide plate, is to punch three holes in section I and two holes in section II. The holes in section I/II are 20/30 mm in length, 8/8 in width, and 15/8 mm in depth,

respectively. The fatigue test showed that the optimized angled guide plate, had good application effects.

Keywords: Ballasted track; Fastening system; Angled guide plate; Structural design; Fatigue test

1 Introduction

The Islamic Republic of Pakistan will upgrade the railway line ML-1. This project mainly optimizes the ballasted trackbed, sleeper and fastener system. The research on ballast bed has a long history, including ballast crushing [1] [2], ballast bed settlement, ballast aggregate distribution, the force between the sleeper and track bed, ballast flight mechanism analysis, longitudinal and transverse resistance of trackbed, ballast screening, and reuse, etc [3-7]. The route selection scheme for different environments and grades is relatively mature, so the ballasted track of the ML-1 line can directly adopt existing standards.

Sleeper types of the ballasted track include wood sleeper, concrete sleeper, steel sleeper, composite sleeper, et al. The wooden sleeper has good elasticity and easy maintenance, but it has some problems, such as poor durability and unfavorable to environmental protection [8] [9]. Concrete sleepers have uniform quality, low cost, and an extensive application range [10]. Steel sleepers have corrosion, conductivity, and other problems, and are only used in special sections [11] [12]. Composite sleepers can use new materials and environmental protection materials to replace wooden sleepers, but now the cost is high [13] [14]. Therefore, concrete sleepers are suitable for ML1 line

The fastening system is a substantial track component to transfer train loads from the rail to the sleeper, minimize traffic-induced vibrations and impacts, maintain the rail inclination and track gauge, act as an electrical insulator between rails and sleepers, and provide adequate clamping force to rails to ensure lateral, longitudinal and torsional stability of rails [15]. As shown in Figure 1, the fastening system is a set of components, including screw spikes, pads, clips (clamps), insulators, and angled guide plates that connect the rails to sleepers in the track superstructure [16].

Due to the development of new types of railway sleepers and high-speed railways [17] [18], selecting the appropriate types of the fastening system is one of the important issues that should be taken into account. Given that the two terms of structural design and flexibility, railway fastenings are divided into direct/indirect and rigid/elastic types, respectively [19].

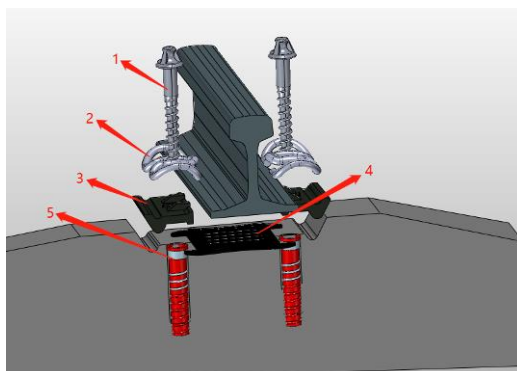


Figure 1

Composition of Vossloh W14-PK fasteners 1-Bolt studs, 2-Fastening clip, 3- Angled guide plate, 4-Rail pad, 5-Preburied casing

As shown in Figure 2, the direct fastenings connect the rail directly to the sleeper through rail pads without using baseplates, while indirect fastenings connect the rail to the sleeper through the rail pad and baseplate pad [20]. The application of direct fastenings causes rail seat deterioration as the consequence of shock loads on loosened fastening clips (Figure 3), while the application of indirect fastenings led to a pulsating force distribution and fluctuating around the initial tension value that prolongs the railway superstructure service life [21]. On the other hand, fastenings could be classified into rigid or elastic types. The rigid fastenings were a common system used in the early 1900s for bolting the rail to the timber sleeper rigidly, whereas the screws are tightened in an elastic rail fastening such that an initial tension is formed through the elastic clip or the spring washers, which allows a slight rail movement within the rail seat. Loosening of rigid fastenings after a relatively short period of operation is the principal disadvantage of this type, which led to over-stressing the clips under high lateral forces and consequential damages of the fastening clips.

The anchorage of the fastening system in the sleeper has an important role in joining the elastic clip or spring part of the assembly to the less resilient sleeper. It should be able to tolerate impact loads and vibration transmitted to the sleeper without cracking or loosening it. While polypropylene and HDPE have been used in the past for light-duty applications, anchorages for threaded fastenings are typically made of nylon or composite materials. To avoid damage in freezing weather, care must be taken to expel any water during the assembly of the fastening. Shoulders for non-threaded fastenings are usually made of ductile cast iron, such as, S.G. Iron (Spheroidal Graphite Iron).

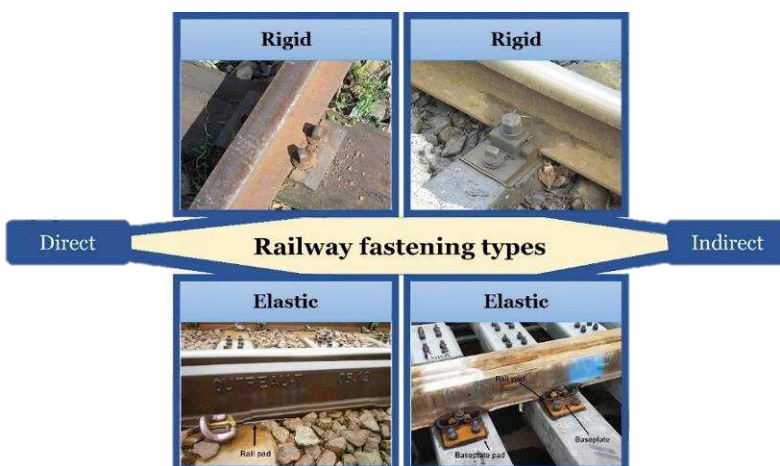


Figure 2

(a) Direct rigid fastening, (b) indirect rigid fastening, (c) direct elastic fastening, (d) indirect elastic fastening [19] [20]

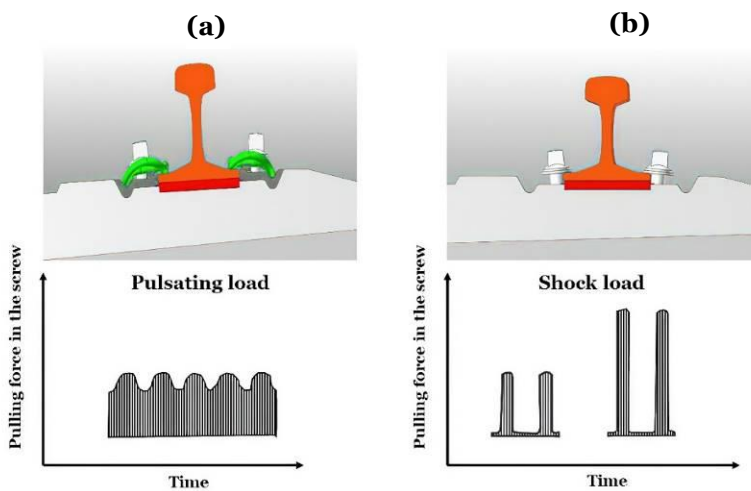


Figure 3

Pulling load distribution for (a) elastic and (b) rigid fastening

The shape of the concrete-encased portion of the shoulder has been refined over time to ensure that it extends down into the prestressed region of the sleeper and securely transmits lateral and torsional forces. Each part of the fastening cast into the sleeper must be able to withstand a 60 kN pullout force without causing damage to the sleeper.

A repeated loading test is a suitable method to evaluate the long-term performance of fasteners subjected to traffic loading caused by passing trains. In this regard,

cyclic loading is applied to the railhead so that the position of applying load is depending on fastening vertical stiffness, track axle load, and curvature. The cyclic load could be applied to an individual rail or both rails on a concrete sleeper, as shown in Figure 4a-b. For non-symmetrical fastening systems, the rail should be fixed between two sleepers or half sleepers. The repeated load could be applied vertically or obliquely depending on the support position (Figure 4c-d). The requirements of British and AREMA standards for conducting repeated load tests are compared in Table 1.

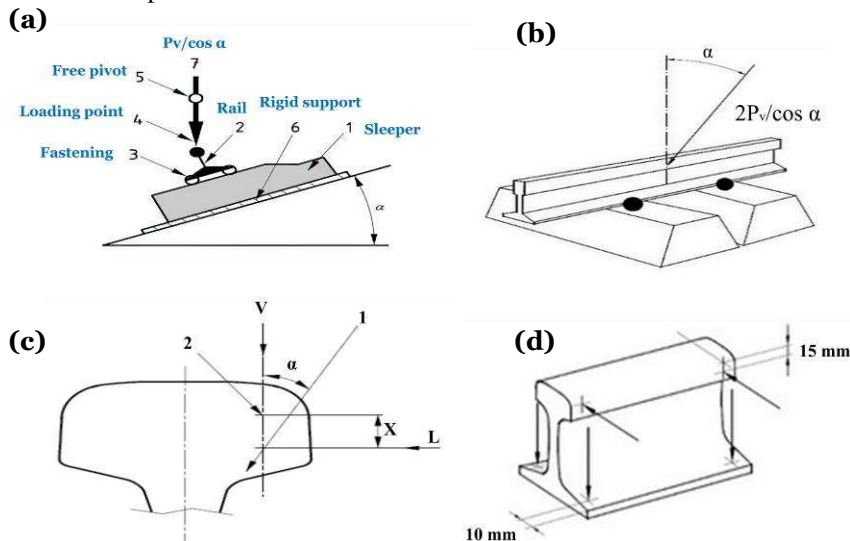


Figure 4

Laboratory tests conditions: (a-b) Repeated load test arrangements, (c) Loading point on the railhead, (d) Displacement measurement positions [22]

Table 1

Repeated loading test requirements according to different standards

| BS EN 13481-2 | AREMA 1-30 |
|---|---|
| The minimum rail length is 500 mm. | The rail length should be 457 mm – 508 mm. |
| The clamping force is determined after the test according to BS EN 13146-7. | The uplift force is determined according to Article 2.6.1. |
| The magnitude and position of load are associated with the track axle load and curve radius presented in Table 4 and Figure 4a-b. Cyclic loading should be continued up to 3×10^6 cycles at a frequency of (4 ± 1) Hz. | The cyclic loading is applied at the angle of 20° relative to the vertical axis of the rail for 3×10^6 cycles at a frequency of 2.5 Hz. The magnitude of upward loading should be 0.6P, and downward load should be $0.6P + 133.5$ kN or 133.5 kN if a single spring/hydraulic ram or double-acting hydraulic ram is used, respectively. |

| | |
|--|---|
| The maximum temperature of fastening components should be lower than 50°C. | The maximum temperature of the rail pad should be lower than 71°C. |
| The maximum loading rate should be 200 kN/min for a single sleeper. | The maximum loading rate should be 22.24 kN/min for a single sleeper. |

In this paper, the long-term performance of W14-PK fasteners was the main concern since the Islamic Republic of Pakistan will upgrade the railway line ML-1, with Vossloh W14-PK fasteners, which is a suitable alternative for ballasted tracks. The fastening system modification requirements for the angled guide plate, are as follows:

- (1) It must fulfill requirements for ballasted track lines with gauge 1676 mm
- (2) It should be capable of connecting 60E1 to 54E1 rails
- (3) It should be able to be supported by China IIIa prestressed concrete sleeper with shoulder retaining
- (4) It can save material while satisfying the force of the angled guide plate

2 Materials and Methods

2.1 Materials

Pakistan ML-1 railway line adopts 54E1 rail and 60E1 rail. The rail material is 350HT. It is a non-porous rail with a length of 25 m. The weight of a rail per meter is 60.21 kg. Its elastic modulus is 210 GPa, the Poisson's ratio is 0.3 and the density is 7830 kg/m³.

The fastener clip is type ω . Its buckle pressure is 10 KN. Its material is 38Si7. Its elastic modulus is 200 GPa, the Poisson's ratio is 0.3, and the density is 7830 kg/m³. Figure 5 is the dimension of the angled guide plate. Angled guide plate material is glass fiber reinforced PA66/PA6. Its elastic modulus is 9.6 Gpa, the Poisson's ratio is 0.35 and the density is 1150 kg/m³. Table 2 is its physical parameters.

Table 2
Physical parameters of the angled guide plate

| No. | Item | Unit | Index |
|-----|----------------------------|------|------------|
| 1 | Tensile strength (23°C) | MPa | ≥ 170 |
| 2 | Tensile strength (70°C) | MPa | ≥ 110 |
| 3 | Elongation at break (23°C) | % | ≤ 4 |
| 4 | Elongation at break (70°C) | % | ≤ 7 |

| | | | |
|---|------------------------------------|----------------------------|----------------|
| 5 | Bend strength (23°C) | MPa | ≥ 250 |
| 6 | Bend strength (70°C) | MPa | ≥ 140 |
| 7 | Volume resistivity (wet state) | $\Omega \cdot \text{cm}^3$ | $\geq 10^{10}$ |
| | Volume resistivity (dry state) | $\Omega \cdot \text{cm}^3$ | $\geq 10^{14}$ |
| 8 | Non-notched impact strength (23°C) | KJ/m ² | ≥ 80 |

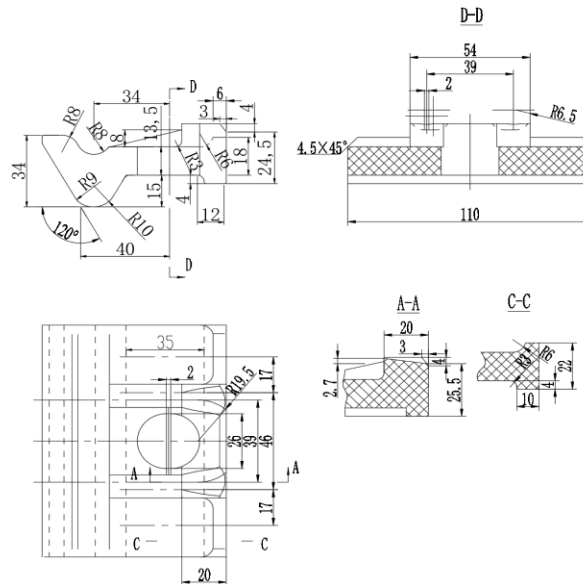


Figure 5

Structural details of the angled guide plate

The material of the rail pad is the CPU. Its strength is 80 kN/mm (23 °C) and its stiffness variation is less than 30% at 70°C. Its elastic modulus is 5 GPa, the Poisson's ratio is 0.4 and the density is 1200 kg/m³. The bolt studs material is high-quality carbon steel or alloy structural steel. Its strength grade is 5.6. The elastic modulus of the bolt studs is 220 GPa, the Poisson's ratio is 0.3, the density is 7830 kg/m³ force is 75 kN. The sleepers' strength grade of concrete should not be less than C60. The elastic modulus is 36 GPa, the Poisson's ratio is 0.2, and the density is 2400 kg/m³.

2.2 Model

2.2.1 Load

Load value is determined according to the Chinese railway track design code (TB 10098-2017). The dynamic load of the wheel is expressed by the maximum

possible value of the equivalent static load. The vertical equivalent static load on a straight track is shown in Eq. (1).

$$\begin{cases} v \leq 120 \text{ km/h} & P_d = P_0 (1 + \alpha) \\ 120 \text{ km/h} < v \leq 160 \text{ km/h} & P_d = P_0 (1 + \alpha + \beta)(1 + \alpha_1) \end{cases} \quad (1)$$

P_d : the vertical equivalent static load of wheel acting on the rail (kN)

P_0 : static wheel weight (kN)

N : Driving speed (km / h)

α, α_1 : speed coefficient, $\alpha = 0.6v / 100$, $\alpha_1 = 0.3 \Delta v / 100$

β : Partial load coefficient

$$\beta = \frac{2 \cdot \Delta h \cdot H}{S^2} \quad (2)$$

Δh : unbalanced superelevation (mm)

H : height of the center of gravity of locomotive or vehicle (mm)

S : center distance between inner and outer rails (mm)

According to the design parameters, the Pakistan railway has the highest running speed of 160 km/h, axle load of 25 t, and a track gauge of 1676 mm. It can be seen from this that the velocity coefficient $\alpha = 0.72$, $\alpha_1 = 0.12$, partial load coefficient $\beta = 0.12$. The static load on the sleeper is about 40% of the axle load. Therefore, the vertical load P_d of dynamic wheel load is 103.04 kN. The lateral force is 0.8 P_d according to the Chinese Railway Track Design Code, so, $P_l = 82$ kN

$$P_d = P_0 (1 + \alpha + \beta)(1 + \alpha_1) = 125000 \times 0.4 \times 1.84 \times 1.12 = 103040 \text{ N} \quad (3)$$

2.2.2 Analytical Model

The angled guide plate is one of the fastening system components, and its stress is mainly affected by the one-sided rail row. In order to optimize the angled guide plate, a finite model of the fastener system under a single rail is established, as shown in Figure 6. The finite element model is used to analyze the influence of the length, width, depth, and the number of holes in section I and section II on the force distribution across the angled guide plate, as shown in Figure 7. The dimensions of length, width, depth, and the number of holes were set according to the specific conditions of the optimization area. The optimum design scheme is shown in Table 3.

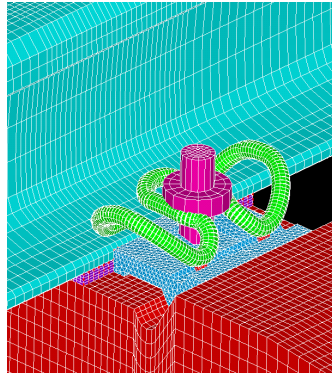


Figure 6

Fine finite element model of fastener system

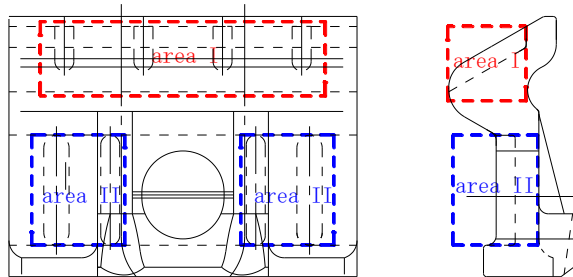


Figure 7

Hole area division of the angled guide plate

Table 3

The optimum design scheme of the angled guide plate

| | No. | Number of holes | Variable | Dimension (Unit: mm) | Abbreviation |
|------------|-----|-----------------|----------|----------------------|--------------|
| Section I | 1 | 3 | length | 5,10,15,20 | I-3-l |
| | 2 | 3 | width | 4,8,12 | I-3-w |
| | 3 | 3 | depth | 5,10,15,20,25 | I-3-d |
| | 4 | 1 | length | 5,10,15 | I-1-l |
| | 5 | 1 | width | 20,30,40 | I-1-w |
| | 6 | 1 | depth | 10,15,20 | I-1-d |
| Section II | 7 | 2 | length | 20,25,30,35 | II-2-l |
| | 8 | 2 | width | 4,8,12,16 | II-2-w |
| | 9 | 2 | depth | 4,8,12 | II-2-d |

2.3 Test Method

2.3.1 Static Test

Static test including hardness, drainage rate, internal porosity, insulation resistance, compression resistance. Hardness is measured by the Brinell hardness tester [23].

The drainage rate test was to allow the gauge baffle to absorb water for 12 hours. Record the weight as the initial weight W_1 . Place the angled guide plate in the heating furnace at 120 ± 3 °C for 2 hours and then weigh it within three minutes, after taking it out, then record the weight as W_2 . See Eq. (4) for drainage rate P .

$$P = \frac{W_1 - W_2}{W_1} \times 100\% \quad (4)$$

The internal porosity was to cut the gauge stop into four pieces along the longitudinal direction, and then detect whether there had porosity inside [24]. The insulation resistance test was completed by a high resistance tester. The angled guide plate was boiled for 2 h, then, wiped the surface moisture with filter paper quickly after taking it out. Aluminum foil was padded on the upper and lower planes of the gauge baffle, and electrodes were placed respectively. After the gauge baffle was placed stably, measured its resistance under 500 V DC voltage [24]. The compressive performance test was to place the mounting frame together with the gauge baffle on the testing machine (Figure 8). Add to 60 kN at the loading speed of 0.5 kN/s, and unload after stabilizing for 10 s. After repeating this three times, remove the mounting frame together with the angled guide plate from the testing machine. The gauge baffle was taken out and placed on the measuring platform to measure its depth of camber.

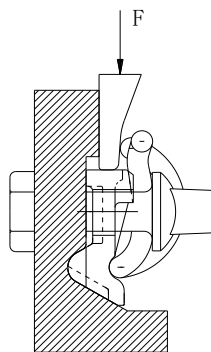


Figure 8

Compressive performance test

2.3.2 Fatigue Test

The fatigue test device is shown in Figure 9. Before the fatigue test, slowly load the test assembly system to the maximum load. The loading rate was 200 kN/min. Repeat the loading 10 times. During the last 3 times of loading, the error of the included angle between the maximum load action line and the vertical line of the rail bottom was within $\pm 0.5^\circ$. Apply fatigue load to the test fastener assembly. The minimum load was 9 kN and the maximum load was 500 kN. Unload after 3×10^6 load cycles, and let the fastener parts for the test stand for 24 h. Then, test rail longitudinal resistance, insulation performance, and uplift resistance of embedded parts.

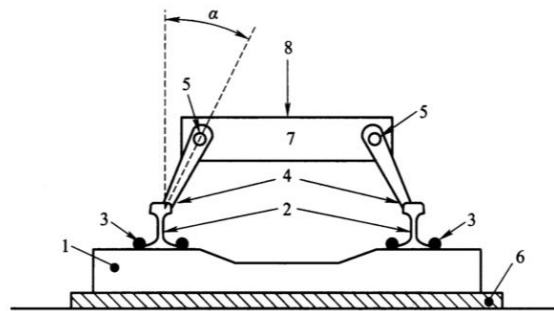


Figure 9

The fatigue test device: 1-sleeper; 2-steel rail; 3-fastener system; 4-loading device; 5-pivot; 6-cushion on rigid foundation; 7-booster frame; 8-Maximum acting load, 500 kN

3 Results and Discussion

3.1 Analysis of Angled Guide Plate

In the three-dimensional direction, the original angled guide plate has small displacement under train load, see Table 3. The displacement of the angled guide plate in the X direction is larger than that in other directions under train load. Three-dimensional stresses under train loads satisfy the requirements, see Table 4. The tensile and compressive stress in the X direction is greater than that in other directions. The principal stress of the angled guide plate is shown in Table 5. The maximum tensile stress of the angled guide plate is 39.4 MPa, which is 35.82% of the allowable stress of the material. The angled guide plate has more material safety margins, and its structure has a larger optimization space.

Table 4
Three-dimensional displacement of angled guide plate under load (Unit: mm)

| displacement of X | | displacement of Y | | displacement of Z | |
|-------------------|----------|-------------------|----------|-------------------|----------|
| Max | Min | Max | Min | Max | Min |
| 1.58E-3 | -1.10E-1 | 2.06E-2 | -1.13E-2 | 7.68E-3 | -4.36E-2 |

Table 5
Three dimensional stress of angled guide plate under load (Unit:MPa)

| Stress of X | | Stress of Y | | Stress of Z | |
|-------------|-------|-------------|-------|-------------|-------|
| Max | Min | Max | Min | Max | Min |
| 37 | -36.4 | 13.2 | -24.8 | 21.2 | -15.5 |

Table 6
Principal stress of angled guide plate under load (Unit: MPa)

| 1st principal stress | | 2nd principal stress | | 3rd principal stress | |
|----------------------|-------|----------------------|-------|----------------------|-------|
| Max | Min | Max | Min | Max | Min |
| 39.4 | -14.5 | 13.2 | -24.9 | 8.84 | -36.5 |

3.2 Analysis Scheme

- Comparison of results under condition I-3-1

Under conditions I-3-1, with the increase of the hole length, most of the stress and displacement of the angled guide plate increase. Except that the displacement in direction Y is greatly affected by the opening length, the variation of most indexes by the increase of opening length is not greater than 50% (Figure 10).

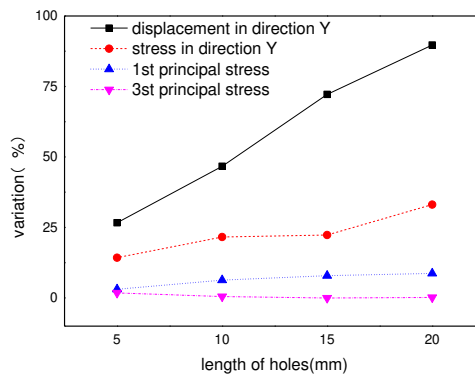


Figure 10
Variation of deformation and stress under condition I-3-1

- Comparison of results under condition I-3-w

Under condition I-3-w, with the increase of the hole width, most of the stress and displacement of the angled guide plate increase. When the hole width exceeds 8mm, the parameters of the angled guide plate increase rapidly (Figure 11).

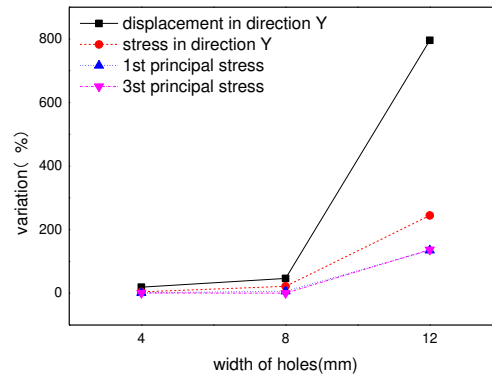


Figure 11

Variation of deformation and stress under condition I-3-w

- Comparison of results under condition I-3-d

Under condition I-3-d, with the increase of the hole depth, most of the stress and displacement of the angled guide plate increase. When the hole depth exceeds 15mm, the parameters of the angled guide plate increase rapidly (Figure 12).

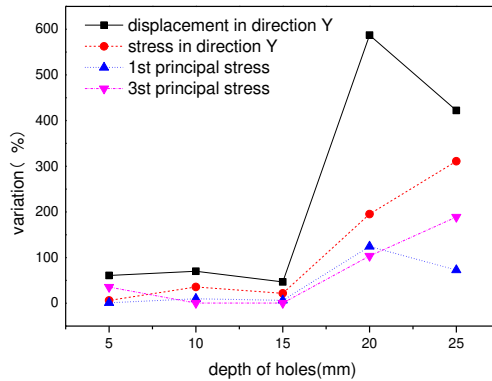


Figure 12

Variation of deformation and stress under condition I-3-d

- Comparison of results under condition I-1-1

Under the condition of a single hole in area I, the stress and displacement parameters of the angled guide plate increase significantly (Figure 13). With the

increase of hole length, the stress on the angled guide plate decreases. However, the variation of each parameter of the angled guide plate exceeds more than 80%.

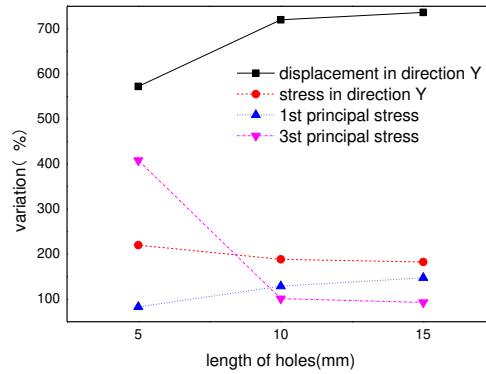


Figure 13

Variation of deformation and stress under condition I-1-l

- Comparison of results under condition I-1-w

Under the condition of a single hole in area I, the stress and displacement parameters of the angled guide plate increase significantly with the width of the hole increase (Figure 14). The displacement in direction Y increases most significantly.

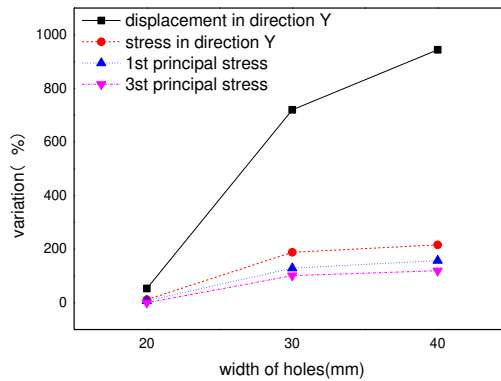


Figure 14

Variation of deformation and stress under condition I-1-w

- Comparison of results under condition I-1-d

Under the condition of a single hole in area I, the stress and displacement parameters of the angled guide plate increase significantly with the depth of the hole increase (Table 15). The displacement in direction Y increases most significantly.

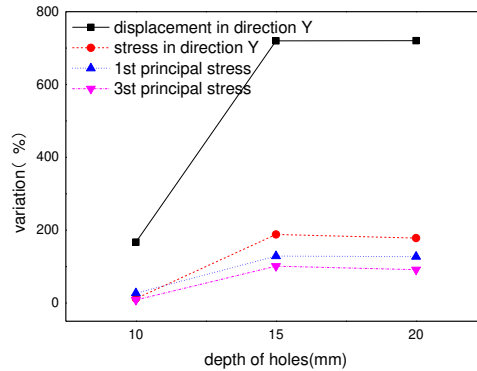


Figure 15

Variation of deformation and stress under condition I-1-d

- Comparison of results under condition II-2-1

Under the condition of two holes in area II, the increase of hole length has little effect on the stress and displacement of the angled guide plate (Figure 16). It was found that only when the length of the hole reaches 35 mm, the displacement in the Y direction exceeds 36%.

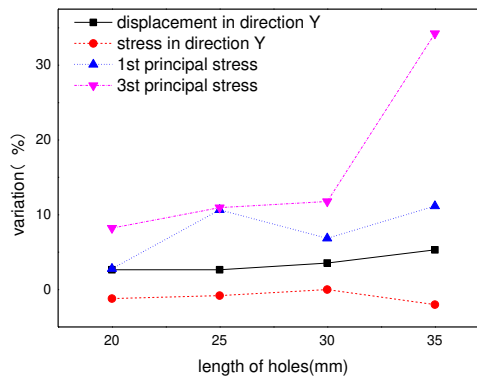


Figure 16

Variation of deformation and stress under condition II-2-1

- Comparison of results under condition II-2-w

Under the condition of two holes in area II, the stress and displacement of the angled guide plate increase with the hole width increase. When the hole width exceeds 12 mm, the parameters of the angled guide plate increase significantly (Figure 17).

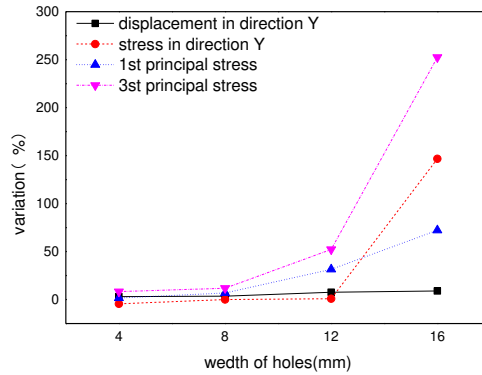


Figure 17

Variation of deformation and stress under condition II-2-w

- Comparison of results under condition II-2-d

Under the condition of two holes in area II, the increase of hole depth has little effect on the stress and displacement of the angled guide plate (Figure 18). Only when the hole depth reaches 12 mm, the 3rd principal stress exceeds 37%.

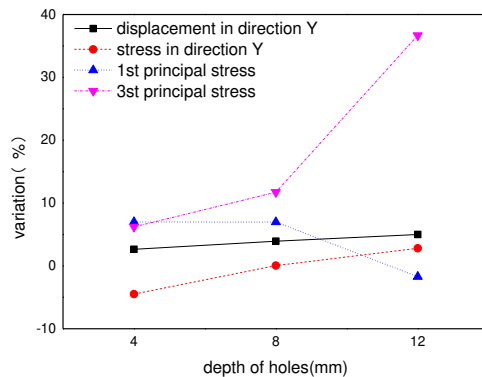


Figure 18

Variation of deformation and stress under condition II-2-d

3.3 Optimization Scheme

By comparing the displacement and stress variation of angled guide plates under different schemes, it can be seen that the effect of the single-hole scheme is poor. According to the spatial distribution, deformation, and stress variation of the angled guide plate's two areas, the optimal design scheme of the angled guide plate is: Area I uses three holes with 20 mm long, 8 mm wide, 15 mm deep.

Area II uses two holes 30 mm long, 8 mm wide, 8 mm deep. The deformation and stress variation of the angled guide plate in this scheme is shown in Table 7~ Table 9. The displacement and stress of the angled guide plate had little variation. This realizes the purpose of ensuring the safety of angled guide plate structure and saving materials.

Table 7

Three-dimensional displacement variation of angled guide plate under load (Unit: mm)

| displacement of X | | displacement of Y | | displacement of Z | |
|-------------------|--------|-------------------|--------|-------------------|--------|
| Max | Min | Max | Min | Max | Min |
| 22.60% | 13.53% | 37.99% | 93.89% | 63.29% | -1.97% |

Table 8

Three-dimensional stress variation of angled guide plate under load (Unit: MPa)

| Stress of X | | Stress of Y | | Stress of Z | |
|-------------|-------|-------------|--------|-------------|--------|
| Max | Min | Max | Min | Max | Min |
| 18.47% | 8.34% | 7.86% | 32.75% | 9.26% | 15.54% |

Table 9

Principal stress variation of angled guide plate under load (Unit: MPa)

| 1st principal stress | | 2nd principal stress | | 3rd principal stress | |
|----------------------|-------|----------------------|--------|----------------------|--------|
| Max | Min | Max | Min | Max | Min |
| 19.04% | 6.35% | 7.77% | -0.13% | -7.64% | 15.64% |

3.4 Test Results

Through static load test and fatigue load test, it is proved that all indexes of the optimized gauge baffle meet the applicable requirements. The results are shown in Table 10 and Table 11.

Table 10

The test results of the angled guide plate

| No. | item | unit | standard | test result |
|-----|-------------------|------|---|----------------------------|
| 1 | hardness | HRR | ≥ 105 | 112 |
| 2 | Drainage rate | % | Drainage rate of angled guide plate after water absorption modulation shall be $\geq 0.4\%$ | 0.85 |
| 3 | internal porosity | / | There should be no bubbles or voids inside | no bubbles or voids inside |

| | | | | |
|---|------------------------|------------|--|--------------------------------------|
| 4 | Insulation resistance | k Ω | $\geq 5 \times 10^6$ | 1.91×10^9 |
| 5 | compression resistance | / | Angled guide plate shall not be damaged after the compression test, and its uplift value shall not exceed 0.5 mm | no damage and uplift value is 0.3 mm |

Table 11
Fatigue test results of the fastener assembly

| No. | item | unit | standard | test result | |
|-----|-------------------------------------|---|------------|---|-------------------------|
| 1 | Rail longitudinal resistance | kN | ≥ 9 | 12.1 | |
| 2 | Insulation performance | k Ω | ≥ 5 | 7.6 | |
| 3 | Uplift resistance of embedded parts | kN | ≥ 100 | After the 100kN pullout test, the embedded parts were not damaged, concrete around embedded parts without visible cracks and mortar peeling | |
| 4 | Assembly fatigue performance | Component state after fatigue | / | Components should not be damaged | No damage to components |
| 5 | | Variation of track gauge expansion | % | ≤ 6 | 3.9 |
| 6 | | Variation of rail longitudinal resistance | % | ≤ 20 | 9.1 |
| 7 | | Variation of assembly buckle pressure | % | ≤ 20 | 9.4 |
| 8 | | Static stiffness variation of assembly | % | ≤ 25 | 13.2 |

Conclusions

The angled guide plate of the Vossloh w14-pk fastener has a large safety margin, under the actions of train loads and exhibits optimization space.

We divided the angled guide plate into Area I, close to the rail groove and Area II, outside the bolt hole. The angled guide plate was then optimized by the placement of holes. The optimization scheme, after the theoretical analysis, is to provide holes in Area I, 20 mm long, 8 mm wide and 15 mm deep, and holes in Area II

that are 30 mm long, 8 mm wide and 8 mm deep. This achieved the goal of ensuring the safety of angled guide plate structure and the economy of material use.

The fatigue test of the optimized angled guide plate showed that the optimized scheme met or, in most cases, exceeded the applications, standard minimal requirements.

Acknowledgement

This work was supported by the Natural Science Foundation of Zhejiang Province (Grant No. LY19E080002).

References

- [1] Y. Guo, V. Markine, X. Zhang, W. Qiang, and G. Jing, "Image analysis for morphology, rheology and degradation study of railway ballast: A review," *Transp. Geotech.*, 2019
- [2] E. Juhász and S. Fischer, "Investigation of railroad ballast particle breakage," *Pollack Period.*, Vol. 14, No. 2, pp. 3-14, 2019
- [3] Y. Guo, V. Markine, J. Song, and G. Jing, "Ballast degradation: Effect of particle size and shape using Los Angeles Abrasion test and image analysis," *Constr. Build. Mater.*, Vol. 169, pp. 414-424, 2018
- [4] Y. Guo, H. Fu, Y. Qian, V. Markine, and G. Jing, "Effect of sleeper bottom texture on lateral resistance with discrete element modelling," *Constr. Build. Mater.*, Vol. 250, p. 118770, 2020, doi: <https://doi.org/10.1016/j.conbuildmat.2020.118770>
- [5] G. Jing, D. Ding, and X. Liu, "High-speed railway ballast flight mechanism analysis and risk management—A literature review," *Constr. Build. Mater.*, Vol. 223, pp. 629-642, 2019
- [6] G. Jing, P. Aela, H. Fu, and M. Esmaeili, "Numerical and Experimental Analysis of Lateral Resistance of Bi-Block Sleeper on Ballasted Tracks," *Int. J. Geomech.*, 2020
- [7] W. Jia, V. Markine, Y. Guo, and G. Jing, "Experimental and numerical investigations on the shear behaviour of recycled railway ballast," *Constr. Build. Mater.*, Vol. 217, pp. 310-320, 2019, doi: <https://doi.org/10.1016/j.conbuildmat.2019.05.020>
- [8] A. M. Zaremski, "Concrete vs. wood ties: Making the economic choice," 1993
- [9] P. Qiao, J. F. Davalos, and M. G. Zipfel, "Modeling and optimal design of composite-reinforced wood railroad crosstie," *Compos. Struct.*, Vol. 41, No. 1, pp. 87-96, 1998
- [10] W. Ferdous, A. Manalo, G. Van Erp, T. Aravinthan, S. Kaewunruen, and A. Remennikov, "Composite railway sleepers—Recent developments, challenges and future prospects," *Compos. Struct.*, Vol. 134, pp. 158-168,

2015

- [11] P. A. Guoqing Jing Hao Fu, “The Contribution of Ballast Layer Components to the Lateral Resistance of Ladder Sleeper Track,” *Constr. Build. Mater.*, Vol. (under rev, 2018
- [12] W. Ferdous and A. Manalo, “Failures of mainline railway sleepers and suggested remedies–review of current practice,” *Eng. Fail. Anal.*, Vol. 44, pp. 17-35, 2014
- [13] A. Manalo, T. Aravinthan, W. Karunasena, and A. Ticoalu, “A review of alternative materials for replacing existing timber sleepers,” *Compos. Struct.*, Vol. 92, No. 3, pp. 603-611, 2010, doi: <https://doi.org/10.1016/j.compstruct.2009.08.046>
- [14] E. R. Anne, “Rubber/plastic composite rail sleepers,” *UK waste Resour. action Program.*, 2006
- [15] S. Fischer, B. Eller, Z. Kada, A. Németh, “Railway Construction,” Univ. Nonprofit Kft, Győr, 2015, 334 p.
- [16] Vossloh, “Sleeper anchor SN,” 2015 [Online] Available: <http://www.vossloh.com>
- [17] G. Jing, M. Siahkouhi, J. Riley Edwards, M. S. Dersch, and N. A. Hoult, “Smart railway sleepers - a review of recent developments, challenges, and future prospects,” *Constr. Build. Mater.*, Vol. 271, p. 121533, 2021, doi: <https://doi.org/10.1016/j.conbuildmat.2020.121533>
- [18] M. J. G. Romero, J. R. Edwards, C. P. L. Barkan, B. Wilson, and J. Mediavilla, “Advancements in fastening system design for North American concrete cross-ties in heavy-haul service,” 2010
- [19] A. Śładkowski and K. Bizoń, “Aspects of Rail Infrastructure Design,” in *Sustainable Rail Transport*, Springer, 2018, pp. 113-145
- [20] I. Grossoni, Y. Bezin, and S. Neves, “Optimisation of support stiffness at railway crossings,” *Veh. Syst. Dyn.*, Vol. 56, No. 7, p. 1072-1096, 2018
- [21] J. Liu, “Influence of the rail fastening components on the lateral deformation and load distribution behavior of the rail.” Technische Universität München, 2013
- [22] E. 13146-4:2020 Standardization, E. C. f., “Railway applications - Track - Test methods for fastening systems - Part 4: Effect of repeated loading,” *CEN*, 2020
- [23] inspection and quarantine of the people’s republic of china General administration of quality supervision, “plastics-determination of hardness-part 2. Rockwell hardness,” *GB T 3398.2*, 2008
- [24] C. N. R. Administration, “Fastening systems for high-speed railway-Part 3 : Type V fastening system,” *TB/T 3395.3*, 2015

Simulation of Parameters of Locomotive Diesel, Gas Diesel and Gas Engines Using Multi-Zone and One-Zone Models

**Vladimir Sinyavski, Mikhail Shatrov, Andrey Vakulenko,
Igor Alekseev**

Moscow Automobile and Road Construction State Technical University (MADI),
Faculty of Energy and Ecology, Leningradski Prospekt 64, 125319 Moscow,
Russia, dvs@madi.ru

Abstract – Modern requirements for reduction of the carbon footprint and toxic emissions of internal combustion engines, as well as their operation cost may be fulfilled by conversion of diesel engines for operation on natural gas. Methane, which is the main component of natural gas, contains by 15% less carbon than diesel fuel, and its heat value is by 15% higher (by mass). Therefore, an engine fed by natural gas may reduce its CO₂ emissions by up to 30% compared to the base diesel engine. The price of natural gas in Russia is almost twice as much less than that of diesel fuel. As locomotive engines often operate 24 hours a day 7 days a week, the gain in fuel costs may be large. Two basic methods of diesel engine conversion for operation on natural gas were analyzed: gas engine and gas diesel (dual-fuel) engine. Simulation of diesel, gas diesel and gas engines for a shunting locomotive was done using the multi-zone AVL FIRE model and one-zone model developed in MADI. The simulation showed that transfer from diesel cycle to gas and gas diesel cycles resulted in considerable decrease in fuel consumption and emissions of particles and NO_x. The gas engine had lower mechanical and thermal stresses compared to diesel and gas diesel versions.

Keywords: conversion of diesel engine; gas engine; dual-fuel engine; engine simulation; one-zone model; multi-zone model; Wiebe formula

1 Introduction

Reduction of the carbon footprint to fight the greenhouse effect is a pressing issue of today's world ecological agenda. Conversion of engines for operation on natural gas makes it possible to decrease considerably emissions of carbon dioxide (CO₂). Natural gas produced in Russia contains 95-98% of methane, which has about 15% less carbon compared to diesel fuel. In addition, the heat value of methane is by 15% higher (by mass) than that of diesel fuel. So, if an engine

operating on natural gas preserves the same effective efficiency as the base diesel engine, its conversion for operation on natural gas may decrease emissions of CO₂ by 30%. Emissions of nitrogen oxide (NO_x) decrease considerably making it possible to comply with the latest severe ecological standards without mounting a complicated and expensive SCR catalyst. Depending on the method of diesel engine conversion for operation on natural gas, emissions of soot decrease many times or become zero.

For conversion of engines to operate on natural gas, two basic methods are used: spark-ignition gas engine and gas diesel (dual-fuel) engine.

A gas engine may operate on a stoichiometric or lean gas-air mixture. Stoichiometric gas-air mixture ensures a good ignition, stable and complete combustion and low chance of knock origination. The traditional three-way catalyst used on petrol engines may be used for the reduction of three basic emissions of spark-ignition engines: carbon monoxide (CO), hydrocarbons (CH) and nitrogen oxide (NO_x). The basic problem of stoichiometric gas engines is the high temperature of their exhaust gases, which may result in the deterioration of their turbine. Therefore, the power augmentation rate by turbocharging of these engines is limited [1].

Spark-ignition gas engines operating on a lean gas-air mixture usually have a low exhaust gases temperature, which enables high power augmentation by turbocharging and decreases emissions of CO and NO_x. For such engines, an oxidation catalyst to reduce the unburned hydrocarbons is required and the chance of knock origination of lean mixtures is higher. At the Moscow Automobile and Road Construction State Technical University (MADI), a truck diesel engine was converted into a lean-mixture gas engine operating with an air excess coefficient of $\lambda = 1.5$. To preserve the power of the base diesel engine, its original turbochargers were replaced by the models ensuring a higher boost pressure. To comply with the ecological standards, a special catalyst containing rhodium was used to reduce the unburned methane [2].

The main problem of using the gas cycle on medium-speed (locomotive) engines is knock. If the cylinder size and power augmentation increase and when the engine operates on a lean gas-air mixture, the probability of its origination increases. The chance of knock appearance also grows at low engine speeds and transient modes.

The medium-speed Jenbacher 6th series gas engine used for electric power generation has a high power augmentation. It has a high brake mean effective pressure $p_e=2.4-2.6$ MPa. The engine operates on a very lean gas-air mixture (air excess coefficient λ close to 2.0). For ignition of a lean gas-air mixture, a prechamber with an enriched mixture is used. Here, the natural gas is ignited by a spark plug and then the sprays of burning gas penetrate into the main combustion chamber and ignite the lean mixture. The Miller cycle is implemented to prevent knock. This also improves the effective efficiency up to 49% and reduces NO_x

emissions. To compensate for the losses in volumetric efficiency caused by the early closure of the intake valves in the Miller cycle, a two-stage turbocharging system is mounted [3]. A combination of the Miller cycle with the two-stage charging system is widely used on internal combustion (IC) engines today. As shown in [4], one turbocharger with a high-pressure compressor and a two-stage charging system with two ordinary turbochargers can provide almost the same engine parameters if the p_e value is 2.7 MPa, but only the two-stage charging system can provide much higher engine boosting with the p_e value of 3.2 MPa.

A serious problem of spark-ignition gas engines is knock. The chance of its origination grows with the increase of the cylinder diameter and boost pressure. In gas diesel engines, this problem is not so critical and they may have much larger cylinder size and higher power augmentation.

Gas diesel engines with mechanical fuel supply systems have a low substitution of diesel fuel by gas: the share of diesel fuel is 20-30% at full loads, increases at low loads and reaches 100% at idle mode [5].

The authors of [6] supposed that the need to increase the igniting portion of diesel fuel at low loads was caused by the growth of fuel drops diameter due to the reduction of both the injection pressure and air counter-pressure in the cylinder because the boost pressure decreases at low loads. The ability of the fuel drop to ignite the air-gas mixture diminishes, and more diesel fuel has to be injected at low loads. Therefore, one has to increase considerably the fuel injection pressure.

The latest gas diesel engines are equipped with Common Rail fuel supply systems, which provide a high injection pressure and multiple injections modes. This ensures a good ignition of natural gas by finely atomized diesel fuel sprays and makes it possible to decrease the share of diesel fuel up to 3-5% at full load and keep it pretty small at low loads and idling mode [7, 8]. These engines have a high substitution of diesel fuel by gas, as well as high fuel efficiency and ecological parameters. The only problem is that the injectors of the base diesel engine tend to overheat as just 3-5% of diesel fuel is injected and this volume of the fuel is not sufficient to cool properly the injector nozzles.

The power, fuel efficiency and ecological parameters of gas diesel engines depend on the parameters of the igniting portion of diesel fuel: ignition pressure [9], fuel distribution within the combustion chamber [10], injection rate shape [11], and pressure oscillations in the fuel system [12].

When switching from diesel to gaseous fuel, the volumetric efficiency of the cylinders decreases due to the partial substitution of the air with gas. Calculation results show that the volumetric efficiency decreases by about 10% in a stoichiometric gas engine and by about 6% in the gas-diesel engine operating at the air excess coefficient of $\lambda = 1.5$ [13]. This drop in engine power is to a large extent compensated by a higher heating value of methane compared to diesel fuel.

The performed analysis shows that both the lean mixture spark-ignition gas engine and gas diesel engine can be used for powering of locomotive, though gas diesel engine is preferable in case of the large engine size and high power augmentation.

Conversion of diesel engines for operation on natural gas requires considerable expenses for engine design modification, building of onboard gas storage systems, creation of gas filling infrastructure. Therefore, it is important to evaluate the amelioration of the basic parameters of a diesel engine in case of its conversion for operation on natural gas and decide if these expenses are reasonable.

The goal of this work is to carry out the simulation of operation parameters of diesel, gas diesel and gas versions of the shunting locomotive engine to predict the improvement of its fuel efficiency and ecological parameters, as well as mechanical and heat strains.

2 Methodology

2.1 Simulation Models and Calculation Method

Evaluation of the engine parameters was carried out using simulation results obtained with the well-known multi-zone AVL FIRE model and a one-zone model of diesel, gas diesel, gas engine simulation developed in MADI [14]. The multi-zone AVL FIRE model needs much calculation time, it simulates only compression-combustion-expansion processes and needs boundary conditions: air pressure and temperature at the cylinder inlet, as well as exhaust gases pressure and temperature at the cylinder outlet. The one-zone MADI model is simple and fast in operation. It provides accurate results if it is calibrated by the engine test results. For calculation of the combustion process by the one-zone MADI model, heat release rate parameters of the I.Viebe empirical formula are needed, which may be calculated by the multi-zone FIRE model. Therefore, the following simulation method was used.

- 1) Calculation of the parameters of the diesel, gas diesel and gas engines by the one-zone MADI model to get the air pressure and temperature at the inlet to the cylinder and the exhaust gases pressure and temperature at the outlet of the cylinder using the approximate values of the I.Viebe heat release rate parameters φ_z and m .
- 2) Calculation of the compression-combustion-expansion processes of all three engines by the multi-zone FIRE model using parameters of the air at the cylinder inlet and exhaust gases at the cylinder outlet calculated by the one-zone MADI model to get more precise values of the I.Viebe heat release rate parameters.

3) Calculation of the parameters of the diesel, gas diesel and gas engines by the one-zone MADI model using more precise values of the I.Viebe heat release rate parameters calculated by the multi-zone FIRE model.

2.2 Input Data

The comparison of operation parameters of three engines was carried out for the 6-cylinder in-line D200 engine of the chanting locomotive. For calibration of the one-zone MADI model, engine test results of diesel and gas diesel versions of the 6-cylinder in-line Cummins KAMA truck engine were used. The gas diesel engine had a modular gas feeding and electronic control systems developed in MADI, which could be used both on high-speed (truck) and medium-speed (locomotive) engines [7]. The one-zone MADI model for a diesel engine was additionally calibrated by the experimental results of testing the D200 locomotive diesel engine by the locomotive characteristic [15].

Table 1 shows parameters of the base diesel engine: cylinder stroke S , cylinder diameter D , compression ratio ε , as well as engine parameters at the rated mode: brake power N_e , brake mean effective pressure p_e , engine speed n .

Table 1
Parameters of the base diesel engine

| S [mm] | D [mm] | ε - | N_e [kW] | p_e [MPa] | n [rpm] |
|-------------|-------------|--------------------|---------------|----------------|--------------|
| 280 | 200 | 14.0:1 | 870 | 2.0 | 1000 |

Experimental compressor and turbine maps of the turbocharger TK-1020 with centrifugal compressor and axial turbine mounted on the D200 diesel engine were used.

The combustion chamber of the base diesel engine D200 and its gas diesel version is shown in Fig. 1. It can't be used for the gas engine because of knock. Therefore, the compression ratio was reduced from 14.0:1 to 10.0:1. The value of the over-piston clearance of the base diesel engine (15 mm) was not changed and compression ratio was reduced by increasing the volume of the combustion chamber in the piston head.

The combustion chamber shape was optimized to ensure complete combustion of the gas fuel and minimal toxic emissions. Poor combustion of the gas fuel and formation of unburned hydrocarbons takes place in the over-piston clearance. Therefore, the diameter of the combustion chamber was increased from 156 to 180 mm to obtain the minimal volume of the over-piston clearance and the hemispheric shape was selected as shown in Fig. 2.

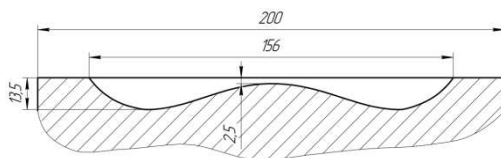


Figure 1

Schematic of the combustion chamber of the diesel and gas diesel engine (compression ratio = 14,0:1)

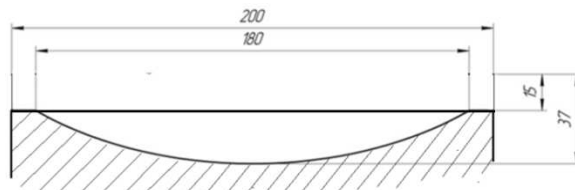


Figure 2

Schematics of the combustion chamber of the gas engine (compression ratio = 10,0:1)

3 Results and Discussions

Calculations of the diesel, gas diesel and gas versions of the D200 locomotive engine were carried out for the rated mode by the multi-zone AVL FIRE model using the boost air and exhaust gases parameters, which were earlier calculated by the one-zone MADI model. The boost air and exhaust gases parameters do not differ much from those obtained after the final calculation by the MADI model indicated in Table 4.

Emissions of NO_x and soot for diesel, gas diesel and gas engines calculated by the multi-zone FIRE model are presented in Table 2.

As can be seen in Table 2, the gas engine produces a minimal amount of NO_x and soot. Compared to the diesel engine, emissions of NO_x are 3.1 times lower and for the gas engine – 13.6 times lower. Soot emissions for the gas diesel and gas engines are very low compared to the diesel engine. Still for the gas engine, they are 1.5 times lower than for the gas diesel engine.

Table 2

Emissions of NO_x and soot by diesel, gas diesel and gas versions of the D200 engine

| | NO_x [g/kWh] | Soot [g/kWh] |
|-------------------|-----------------------|------------------------|
| Diesel engine | 17.742 | 0.0089 |
| Gas diesel engine | 5.743 | $5.3492 \cdot 10^{-5}$ |
| Gas engine | 1.2945 | $3.0173 \cdot 10^{-5}$ |

3.1 Determination of the Coefficients of the I.Viebe Formula for the Heat Release Rate

Figs. 3, 4, and 5 present the heat release rate diagrams for diesel, gas diesel and gas versions of the D200 engine calculated by the multi-zone AVL FIRE model. The heat release rate diagrams calculated by the I.Viebe formula are superimposed on them. The heat release duration φ_z was calculated as an interval between the start and the end of the heat release process. The heat release law parameter m was determined by combining the curves obtained by the multi-zone AVL FIRE model and the heat release rate curves calculated by the I.Viebe formula.

As m and φ_z coefficients of the I.Viebe formula influence greatly the optimal by fuel efficiency ignition advance angle θ_{ign} , the optimal by fuel efficiency θ_{ign} value was found for every operation mode of each engine and all results presented lower were obtained for the optimal θ_{ign} value.

Analysis of the φ_z and m values demonstrates that the heat release duration is reduced by about 20 crank angle rotation degrees ($^{\circ}CA$) after switching from diesel to gas diesel and gas cycles (correspondingly, 70, 36 and $40^{\circ}CA$). This seems reasonable because in a diesel engine, after combustion has already started, fuel injection continues and preparation of new fuel drops for combustion takes some time (fuel drops have to fly away from the injector, disintegrate into smaller drops, evaporate, mix with the air, heat, etc.). In gas diesel and gas engines, the gas-air mixture is already mixed in the intake manifold and in the cylinder during the compression stroke and is ready for combustion, it just needs to be ignited by a spark plug or a small quantity of diesel fuel.

When switching from diesel to gas diesel and gas cycles, the heat release law parameter m increases correspondingly from 0.5 to 1.0 and 2.0, which results in softer combustion and lower noise level and mechanical loads on the engine parts. Diesel noise is largely caused by the “explosion” type ignition of the portion of diesel fuel injected during the ignition delay period. This portion of diesel fuel is the largest in diesel engine, considerably lower in gas diesel engine and is absent in gas engine.

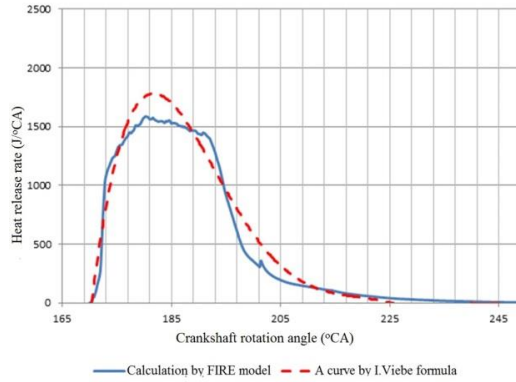


Figure 3

Heat release rate diagram for the D200 diesel engine: $\phi_z = 70^\circ\text{CA}$, $m=0.5$

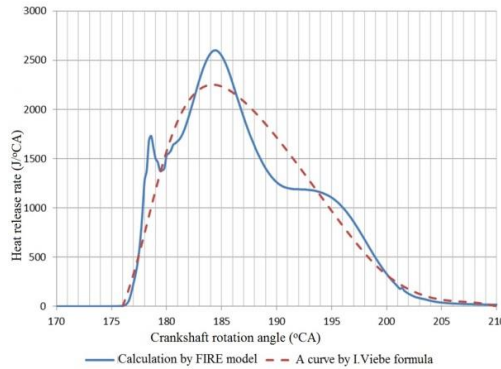


Figure 4

Heat release rate diagram for the D200 gas diesel engine: $\phi_z = 36^\circ\text{CA}$, $m=1$

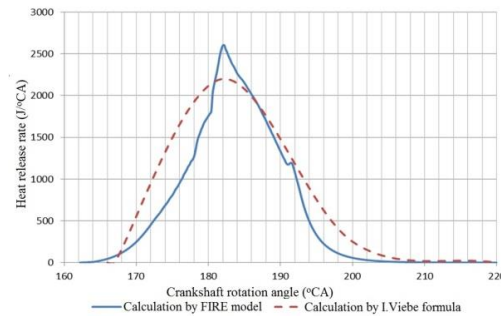


Figure 5

Heat release rate diagram for the D200 gas engine: $\phi_z = 40^\circ\text{CA}$, $m=2$

3.2 Comparison of Operating Parameters of the Locomotive Diesel, Gas Diesel and Gas Engines

Comparison of experimental and simulation operation parameters of the D200 by the locomotive characteristic calculated by the one-zone MAD1 model is presented in Fig. 6 [15]. Here, p_e is the brake mean effective pressure, p_b – boost air pressure, g_e – brake specific fuel consumption, p_z – peak cylinder pressure, G_r – diesel fuel consumption, T_b – boost air temperature. Fig. 6 demonstrates a high convergence of experimental and calculated parameters, both of the diesel engine and its charging system.

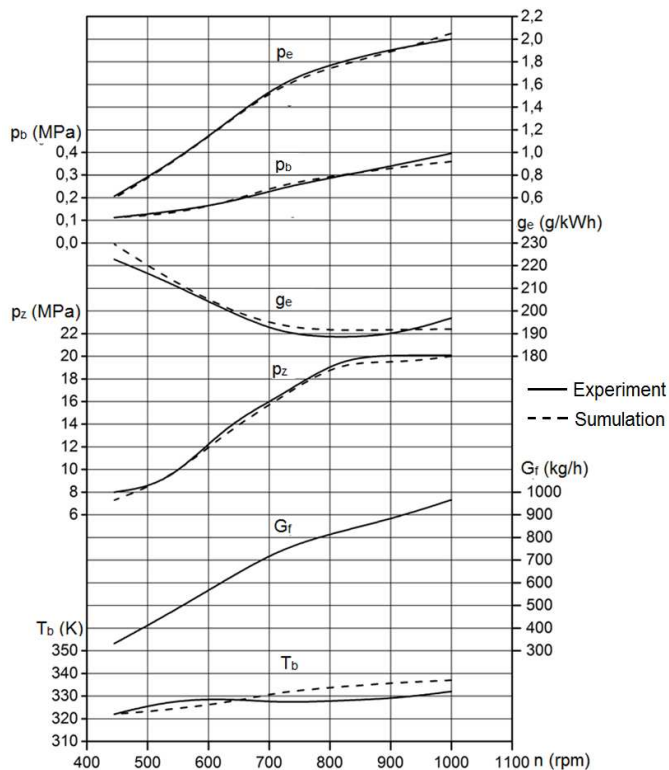


Figure 6

Comparison of experimental and calculated operation parameters of the D200 diesel engine by the locomotive characteristic

To forecast the operation parameters of the locomotive diesel, gas diesel and gas engines, simulation of three engines was carried out at the rated mode by the MAD1 one-zone model using the Wiebe heat release rate parameters calculated earlier by the multi-zone AVL FIRE model. Injection rates of diesel fuel for the diesel engine, gas fuel for the gas engine, gas and diesel fuel for the gas diesel

engine were selected so as to get the same rated power 870 kW. For the gas diesel engine, the percentage of the diesel fuel was 5%.

Table 3 presents the basic input data and operation parameters of the engines. The injection rate of diesel fuel G_{df} and gas fuel G_{gas} , parameters of the I.Viebe formula: heat release duration φ_z and heat release mode m , ignition advance angle θ_{ign} , brake specific fuel consumption g_e , indicated efficiency η_i , effective efficiency η_e and air excess coefficient λ .

Table 3
Parameters of the D200 diesel/gas diesel/gas engine at rated mode

| Engine | G_{df} | G_{gas} | φ_z | m | θ_{ign} | g_e | η_i | η_e | λ |
|------------|------------|------------|-------------|-----|----------------|---------|----------|----------|-----------|
| | [mg/cycle] | [mg/cycle] | [°CA] | - | [°to TDC] | [g/kWh] | - | | - |
| Diesel | 950 | - | 70 | 0.5 | 16 | 193 | 0.488 | 0.439 | 1.76 |
| Gas diesel | 760 | 38 | 36 | 1.0 | 6 | 163 | 0.499 | 0.449 | 1.97 |
| Gas | - | 842 | 40 | 2.0 | 12 | 172 | 0.469 | 0.422 | 2.13 |

As shown in Table 3, for the gas diesel and gas engines, ignition starts closer to the top dead center (TDC) due to a shorter heat release duration φ_z . The value of θ_{ign} for the gas engine is higher than for the gas diesel engine because the gas engine has a higher value of the I.Viebe parameter m . Compared to the diesel engine, the value of g_e for the gas diesel engine is by 15.5% lower and for the gas engine – by 11% lower basically due to a higher heat value of methane, but also partly due to a shorter heat release duration φ_z . The values of η_i and η_e are similar for the diesel and gas diesel engines and are by relatively 4% lower for the gas engine. The gain in the value of g_e is not so high for the gas engine because it has a reduced compression ratio. For the same reason, the values of η_i and η_e for the gas engine are by 4-6% lower than for the diesel and gas diesel engines. The value of λ for the gas engine is by 7% higher than for the gas diesel engine and by 17% higher than for the diesel engine due to a higher exhaust gases temperature T_t caused by a lower compression ratio, which results in a higher turbocharger rotor speed as shown in Table 4.

Table 4 shows the charging system parameters: boost pressure p_b , turbine inlet pressure p_t , boost air temperature T_b , exhaust gases temperature T_t and turbocharger rotor speed n_r . The values of compressor and turbine efficiency are not shown because they are similar for all three engines.

As can be seen in Table 4, for the gas engine, the values of p_b , p_t , T_b are higher than for the diesel and gas diesel engines because the gas engine has a higher value of T_t , which results in a higher value of n_r .

Table 4

Parameters of the charging system of the D200 diesel, gas diesel and gas engines

| Engine | p_b | p_t | T_b | T_t | n_r |
|------------|-------|-------|-------|-------|-------|
| | [MPa] | [MPa] | [K] | [K] | [rpm] |
| Diesel | 0.287 | 0.241 | 339 | 801 | 30287 |
| Gas diesel | 0.282 | 0.238 | 338 | 792 | 30035 |
| Gas | 0.314 | 0.259 | 341 | 815 | 31668 |

Table 5 shows parameters, which characterize mechanical and thermal loads of the engines: peak combustion pressure p_z , maximum pressure rise rate $(dp/d\phi)_{\max}$, which indicates the noise level, temperature resulting from the heat exchange T_{res} , average heat transfer coefficient for the cycle α_{av} and the product $T_{\text{res}} \cdot \alpha_{\text{av}}$, which characterizes the thermal factor of the engine.

Table 5

Parameters of mechanical and thermal loads of the D200 diesel/gas diesel/gas engine

| Engine | p_z | $(dp/d\phi)_{\max}$ | T_{res} | α_{av} | $T_{\text{res}} \cdot \alpha_{\text{av}}$ |
|------------|-------|---------------------|------------------|-----------------------|---|
| | [MPa] | [MPa/°] | [K] | [W/m ² ·K] | [kW/m ²] |
| Diesel | 18.4 | 0.801 | 1110 | 759 | 842.5 |
| Gas diesel | 18.2 | 0.799 | 1100 | 752 | 834.7 |
| Gas | 14.4 | 0.555 | 1040 | 705 | 733.2 |

As seen from Table 5, parameters of mechanical and thermal loads of the diesel and gas diesel engines are close. The value of p_z does not exceed the limit for this engine, which is 20 MPa. Compared to the diesel engine, parameters of mechanical and thermal loads of the gas engine are lower: p_z – by 22% which indicates lower mechanical loads, $(dp/d\phi)_{\max}$ – by 35% which indicates lower mechanical loads and noise level and the product $T_{\text{res}} \cdot \alpha_{\text{av}}$ – by 13% which indicates lower thermal factor.

Conclusions

- 1) Simulation by the AVL FIRE multi-zone model provided coefficients of the I.Viebe formula for the heat release rate, which are needed for engine simulation by the one-zone MADI model. For the locomotive diesel, gas diesel and gas engines, the heat release duration ϕ_z was 70, 36 and 40°CA and the heat release law parameter m was 0.5, 1.0 and 2.0 correspondingly.
- 2) Simulation by the AVL FIRE model showed that compared to the diesel engine, the gas diesel and gas engines have, correspondingly, 3.09 times and 13.7 times lower NO_x emissions. Emissions of soot of the gas diesel and gas engines are close to zero.
- 3) Simulation by the MADI model demonstrated that compared to the diesel engine, the gas diesel engine and gas engine have, correspondingly, by 15.5% and 11% lower brake specific fuel consumption. The indicated and effective efficiency

of the gas diesel engine is by 4% higher due to a shortened heat release duration, and of the gas engine – by 6% lower due to a lower compression ratio, despite a shortened heat release duration. Mechanical and thermal loads of the gas engine are lower than in the diesel and gas diesel engines because of its lower compression ratio.

References

- [1] V. A. Luksho: A complex method of increasing energy efficiency of gas engines with high compression ratio and shortened intake and exhaust strokes, Ph.D. thesis, NAMI, Moscow, 2015, 365 p.
- [2] A. Khatchiyani, V. Kuznetsov, V. Vodejko, I. Shishlov: Results of development of gas engines in MADI (GTU), Avtozapravochni complex + Alternativnoye toplivo, Vol. 3 (21), 2005, pp. 37-41
- [3] J. Klausner, J. Lang, C. Trapp: J624 – Der weltweit erste Gasmotor mit zweistufiger Aufladung, MTZ – Motortechnische Zeitschrift Ausgabe, 04, 2011
- [4] V. V. Sinyavski, M. G. Shatrov, V. V. Kremnev, G. Pronchenko: Forecasting of a boosted locomotive gas diesel engine parameters with one- and two-stage charging systems, Reports in Mechanical Engineering, Vol. 1 (1), 2020, pp. 192-198, DOI: <https://doi.org/10.31181/rme200101192s>
- [5] B. P. Zagorskih, Yu. A. Kozar, Ye. B. Babenich: Perfection of gas supply for diesel engine operation by gas diesel cycle, Avtozapravochni complex + Alternativnoye toplivo, Vol. 5, 2012, pp. 3-6
- [6] L. V. Grehov, N. A. Ivsachenko, V. A. Markov: On ways to improve the gas-diesel cycle, AvtoGasoZapravochniy kompleks + Alternativnoye toplivo, Vol. 7 (100) 2010, pp. 10-14
- [7] M. G. Shatrov, V. V. Sinyavski, A. Yu. Dunin, I. G. Shishlov, A. V. Vakulenko: Method of conversion of high- and middle-speed diesel engines into gas diesel engines. Facta universitatis. Series: Mechanical Engineering. Vol 15 (3) 2017, pp. 383-395, DOI: 10.22190/FUME171004023S
- [8] V. V. Sinyavski, I. V. Alekseev, I. Ye. Ivanov, S. N. Bogdanov, Yu. V. Trofimenko: Physical simulation of high- and medium-speed engines powered by natural gas, Pollution Research, 2017, Vol. 36 (3) pp. 684-690
- [9] M. G. Shatrov, L. N. Golubkov, A. U. Dunin, A. L. Yakovenko, P. V. Dushkin: Influence of high injection pressure on fuel injection performances and diesel engine working process, Thermal Science, Volume 19 (6) 2015, pp. 2245-2253
- [10] M. G. Shatrov, V. I. Malchuk, A. Y. Dunin, I. G. Shishlov, V. V. Sinyavski: A control method of fuel distribution by combustion chamber zones and its dependence on injection conditions, Thermal Science, Vol. 22 (5) 2018, pp. 1425-1434

-
- [11] M. G. Shatrov, L. N. Golubkov, A. Yu. Dunin, P. V. Dushkin, A. L. Yakovenko: A method of control of injection rate shape by acting upon electromagnetic control valve of common rail injector, *International Journal of Mechanical Engineering and Technology*. Vol. 8 (11) 2017, pp. 676-690
- [12] M. G. Shatrov, A. U. Dunin, P. V., Dushkin, A. L. Yakovenko, L. N. Golubkov. V. V. Sinyavski: Influence of pressure oscillations in Common Rail injector on fuel injection rate, *Facta universitatis, Series: Mechanical Engineering*, Vol. 18(4) 2020, pp. 579-593, DOI:10.22190/FUME200611042S
- [13] M. G. Shatrov, L. M. Matyhin, V. V. Sinyavski, A. U. Dunin: An alternative approach to the assessment of internal combustion engine filling and its technical and economic parameters. *International Journal of Emerging Trends in Engineering Research*, Vol. 8 (6) June 2020, pp. 2805-2811
- [14] V. V. Sinyavski, M. G. Shatrov, A. Y. Dunin, I. G. Shishlov, A. V. Vakulenko: A zero-dimensional model for internal combustion engine simulation and some modeling results. *Proceedings of the International Conference on Engineering Management of Communication and Technology (EMCTECH) Vienna, Austria, 2020*, pp. 1-6, DOI: 10.1109/EMCTECH49634.2020.9311546
- [15] M. G. Shatrov, V. V. Sinyavski, I. G. Shishlov, A. V. Vakulenko: Forecasting of parameters of boosted locomotive diesel engine fed by natural gas. *Naukograd Nauka Proizvodstvo Obschestvo*, Vol. 2 (4) 2015, pp. 26-31

Investigating Slope Stability of Geocell-Reinforced Railway Embankments

Morteza Esmaeili^{1*}, Farshad Astaraki², Mohammad Reza Roozbini¹, Majid Movahedi Rad²

¹Department of Railway Track & Structures Engineering, School of Railway Engineering, Iran University of Science and Technology, Narmak 13114-16846, Tehran, Iran

²Department of Structural and Geotechnical Engineering, Széchenyi István University, Egyetem tér 1, Győr 9026, Hungary
e-mail: m_esmaeili@iust.ac.ir, Astaraki.farshad@hallgato.sze.hu, roozbini_90@iust.ac majidmr@sze.hu

*Abstract: The current paper aims to investigate stability of side's slopes of geocell-reinforced railway embankments. For this purpose, firstly a set of six 1:20 scaled models including a reference embankment and geocell-reinforced embankments was constructed in a loading chamber and their load-settlement behaviour was assessed. In the next stage, 3D FEM models of the embankments were developed and the relevant results were verified against the laboratory test outcomes. In continue, on the basis of verified models, the scaled up railway embankments were simulated and the real train loading applied to the models. In this matter, a wide-ranging parametric study was performed on the embankment soil properties ranged from poor (ST1) to high strength (ST5) materials, geocell elasticity modulus (E), number of geocell layers (N) and their vertical location in the embankment body (U) to achieve a minimum embankment sliding safety factor (SF) of 1.5. Outcomes indicate that geocell opening size, stiffness and the placement position play an important role where the concern is to stabilize the embankments' sides slopes. It was found that middle of the embankment was the best position of geocell layers. Elasticity modulus of 1400 MPa and opening size of 245*210 mm were also determined as the optimum for geocell layers.*

Keywords: Geosynthetics; Geocell-reinforced embankment; ballasted railway tracks

1 Introduction

Due to the lack and limitation of good soil resources, constructing new railway embankments is a challenge from geotechnical engineers' viewpoint because of the weak shear strength and bearing capacity of poor soils that cause the failure and instability. Although for increasing axle load and operation speed of railway tracks

superstructure maintenance, geometry correction and renovation of ballast material are important [1, 2, 3], it is essential to enhance the mechanical properties of the embankments' soil. In the past few decades, geosynthetic materials have received many attention from geotechnics engineers to construct different geotechnical infrastructure including railway and roadway construction, coastal protection, foundations, slopes and landfilling. Depending their function, they have been developed in eight main product groups of geogrids, geonets, geotextiles, geosynthetic clay liners, geomembranes, geofoam, geocomposites and geocells. Cellular confinement systems-as known as geocells- are widely used in construction where soil improvement is required. Geocells are the geosynthetic products with a three-dimensional cellular network that made of thin polymeric strips. In spite of the use of geocell reinforcement for various geotechnical purposes, there are limited studies on its utilization in the railway tracks, especially the embankments. In continues, some studies in the field of geosynthetic reinforcement, especially geocells will be explained.

One of the first studies in this field is an experimental study carried out on the stability of a geocell-reinforced soft soil subgrade to assess the effect of geocell opening size, wall height and etc. on the bearing capacity and failure settlement of a two-layer geocell-reinforced subgrade [4]. The main outcomes showed an improvement in load-settlement characteristics while using geocell reinforcement. Furthermore, they suggested a factor that presented improved bearing capacity based on geocell opening size. Avesani Neto *et al.* [5] investigated geocell-reinforced embankments over soft soils. As the main result, an equation was proposed to calculate the safety factor of geocell-reinforced embankments based on the safety factor of the reference embankment, and specifications of utilized geocell and soil. In another study, the effect of prestressing the geosynthetic reinforcement on the safety factor of embankments over soft soil was studied by S. K. Shukla and R. Kumar [6]. Their investigation resulted in proposing a relation between required prestressing force and desired safety factor. Krishnaswamy *et al.* [7] studied the mechanical behaviour of the embankments over a geocell-supported bed in case of soft foundations. Using a geocell layer presented improvement in both bearing capacity and settlement of the embankments and also it was found that tensile stiffness had a significantly important influence on the performance of the geocell-supported embankment. In scope of materials, Leshchinsky and Ling [8] examined the confinement effect of geocell on the behavior of ballasted railway tracks. The results indicated that using geocell layers in ballast caused reducing vertical deformations and settlements by reducing lateral squeeze of the ballast. The effect of the geogrid-box (GBM) method on the bearing capacity of rock-soil slopes was carried out by Moradi *et al.* (2018) [9]. To do this, a series of laboratory tests and finite element analyses were conducted. The results revealed that for slopes reinforced by GBM, bearing capacity can be increased by 11.16% compared to reinforced slopes using a layered geogrid method. The influence of geocell reinforcement on embankments constructed over weak foundation was investigated by Mahdavi Lagha *et al.* [10]. The main outcome of this research was suggesting a

simple method based on slope stability analysis for the primary design of embankments supported on the geocells layer. Sitharam and Hegde [11] presented the case history of the construction of an embankment with 3 m height on the geocelled-foundation over soft soils. Experimental study's outcomes indicated that by using a combination of geogrid and geocell layers, the bearing capacity of foundation increases 4-5 times. They also proposed a simple analytical model to estimate the load-carrying capacity of the reinforced clay bed by a combination of geocell and geogrid. Li et al. [12] did an experimental study on embankments reinforced by geocell and it was found that bearing capacity, vertical and lateral displacements improved compared to reference embankments. Dai et al. [13] by adopted particle image velocimetry (PVI) method investigated performance of reinforced embankments with geocell under static and cyclic loading. The main results indicated that cumulative displacement reduced by using geocell and with increasing embedded depth, the improvement effect of geocell gradually decreased. Zhou and Wen [14] studied geocell-reinforced sand cushion on soft soil. They found that with preparation of a geocell-reinforced sand cushion, the settlement of the underlying soft soil diminished. A design methodology for determining the formation thickness of railway tracks using geosynthetic reinforcement introduced by S. Chawla et al. [15]. The advantage of this new method is diminishing the requirement for formation layer depth by combining geosynthetic. Esmaeili et al. (2018) [16] investigated the performance of geogrid layers in high railway embankments using a series of laboratory and numerical tests. It was found that the larger usage of geogrid layers number the higher the safety factor of the embankments will be achieved. However, the results indicate that the effect of geogrid tensile strength on the reduction of the crest settlement will be diminished for shorter embankments and also while the high strength soils utilized for the construction.

The studies presented thus far provide evidence that there isn't any investigation that has focused on the usage of geocell layers to stable side slopes of the railway embankments. Therefore, this paper deals with the effect of different parameters of geocell layers on improving SF of real-scale railway embankments. For this purpose, previously, six laboratory embankments with a scale of 1:20 were constructed. Hence, five geocell-reinforced embankments and a reference embankment without reinforcement were constructed and examined by in the lab environment to figure out the influence of geocell layers on the mechanical behaviour, settlement and bearing capacity of the railway embankments [17]. Then, by employing the validated 3D numerical procedure carried out by authors [18], the effect of different geocell stiffness, opening sizes, geocell layers number and different vertical locations of geocell layers have been studied on the stability of side's slope of a railway embankment with a 10 m height, slide's slope of 45° for five different soil categories ranged from poor (ST1) to high strength (ST5).

2 Real Railway Embankments Slope Stability Analyses

In current section the effect of soil types, geocell layers number, geocell stiffness and geocell opening size has been investigated on the slope stability of real railway embankments by adopting the Mohr-Coulomb law in the ABAQUS software [19]. For this purpose, laboratory model dimensions scaled up to real scale embankment as can be seen Figure 1. Afterward, reference embankments were modelled and loaded according to the LM71 pattern (Figure 2) (EN 1991-2. 2003) [20] to determine if they meet SF of 1.5 or not. Then, the embankments were reinforced using geocell layers according to the laboratory model pattern. It should be pointed out that the validation and FEM's details are provided in reference [18] already published by the authors.

In current paper each embankment has named based on utilized soil type and geocell layers number. For instance ST2-20 refers to an embankment containing soil type 2 and 20 geocell layers number. The 3D FE analysis is used to calculate the SF of the embankments sides slope based on the temperature-driven strength reduction method proposed by Xu *et al.* (2009) [21]. Also, for confirming the obtained SF by the mentioned method, the failure surface checked using equivalent plastic strain contour (PEEQ) for each embankment's sliding slopes similar to what was used by I-Hsuan Ho, M.ASCE (2014) [22] for assessing the slope stability. It should be noted that geocell layers placed in upper part of embankment from the top of the crest to down alike the laboratory models (see Figure 1).

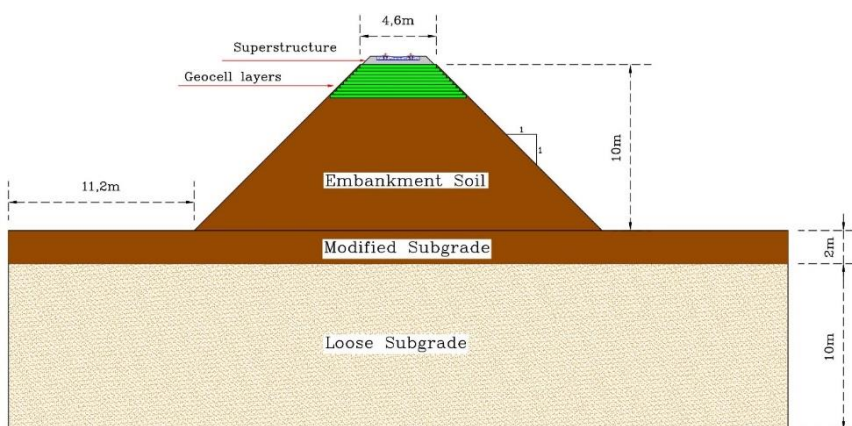


Figure 1

Cross section of the full-scale reinforced-geocell railway embankment

2.1 Loading Model

The proposed loading pattern LM 71 by Euro code standard of EN 1991-2 [20] was used for applying the equivalent uniform load over the embankments' crest (Figure 2).

The following equation can be used for calculating equivalent uniform load:

$$q = \frac{4 \times Q_{vk}}{(3a + 2b) \times B} \quad (kN/m^2) \quad (1)$$

Where Q_{vk} is the point load of 250 kN, a and b refer to the geometrical parameters which their value are 1.6 m and 0.8 m respectively. Also, the B parameter defines as the load width, which is 2.6 m, equal to the length of the railway sleeper.

Because of the dynamic nature of the railway loads, the dynamic load is substituted by a quasi-static load considering the impact factor parameter. In the present research, the impact factor for quasi-static loading was used rather than including velocity and train wheel radius effects according to the AREMA (2006) [23] equation:

$$\alpha = 1 + 5.21 \frac{V}{D} \quad (2)$$

Where α is the impact factor, V is the operation speed (km/h), and D is the wheel diameter (mm) which in the current study are considered 160 km/h and 1000 mm respectively based on Iranian Railway Standard.

By considering a 2.6 m sleeper length, a ballast depth of 0.5 m, and a stress distribution angle of 45 for the ballast layer, a uniform load of 115 kN/m^2 was applied to the embankment. It should be clarified that the uniform load was exerted on effective loading width of 3.2 m.

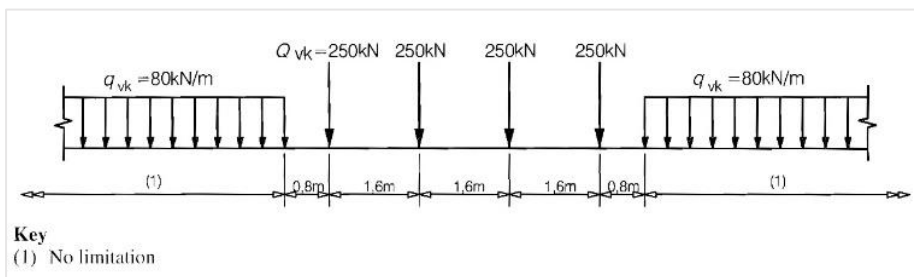


Figure 2

Load model 71 pattern and characteristic values for vertical loads [20]

2.2 Assessment of Safety Factor

As mentioned, the 3D FE analysis is used to determine slope stability based on the ‘temperature-driven strength reduction method’ that has presented by Xu *et al.* (2009) [21]. According to this method, SF computes with actual shear strength, and decrease strength parameters in the finite element program, instead of modifying the input files in the strength reduction factor (SRF). For Applying this method to ABAQUS software should define the temperature depend properties of internal friction angle $\varphi(\theta)$ and cohesion $C(\theta)$ in the input file. Based on this method, linear function are assumed:

$$C_{trial} = (1 - 0.9\theta)C \quad (3)$$

$$\varphi_{trial} = \tan^{-1}[(1 - 0.9\theta)\tan\varphi] \quad (4)$$

Where C_{trial} and φ_{trial} are reduced cohesion and internal friction angle respectively, and C and φ are real cohesion and internal friction angle respectively. It should be noted that θ linearly increase from 0.0 to 1.0. Finally, by define load proportionality factor, $t = \theta$ the SF (F_{trial}) obtained by using below equation:

$$F_{trial} = \frac{1}{1 - 0.9t} \quad (5)$$

Where t varies from 0.0 to 1.0. The relationship between maximum relative displacement, δ and t can be given by the analysis, and the breakpoint of the δ - t curve is considered critical SF. For instance, an example has presented here for calculating SF by this method. As shown in Figure 3(b) for δ - t curve presented for ST1-0 embankment, when t reached at 0.1148 s a sharp break in the displacement occurred. From Eq. (5) a SF of 1.12 is obtained for this embankment. Also, as shown in Figure 3(a) the failures take place at $t=0.1148$ s based on the PEEQ counter (Previously, this parameter has been used for showing failure surface by Ho, I-Hsuan (2014) [22]). Figure 3 shows good confirmation between the temperature-driven strength reduction method and the PEEQ counter.

2.3 Effect of Embankment Length on SF

In this research with scale up the laboratory model dimensions, an embankment with 10 m height, a crest width of 4.6 m, and the slope angle of 45° selected according to the requirements of Iranian Railway Standard. The subgrade depth was 12 m including a 2 m modified subgrade (see Figure 1). To control and analyze the models much easier, a sensitivity analysis was done on two embankments with the same specification but different lengths of 48 and 4 m (see Figure 4). Based on the results the SFs of 1.638 and 1.640 were achieved for the lengths of 4 and 48 m respectively. As results indicate the model length has a negligible effect on SF; accordingly, the embankment length of 4 m selected for this investigation.

2.4 Sensitivity Analyses

In this section, a series of sensitivity analyses were carried out on a wide range of variables including mechanical properties of embankments' soil, geocell elasticity modulus, geocell opening size, number of geocell layers and vertical position of geocell layers undersimulated trainload to investigate their effect on slope stability of full-scaled railway embankment. All variables are summarized in Table 2.

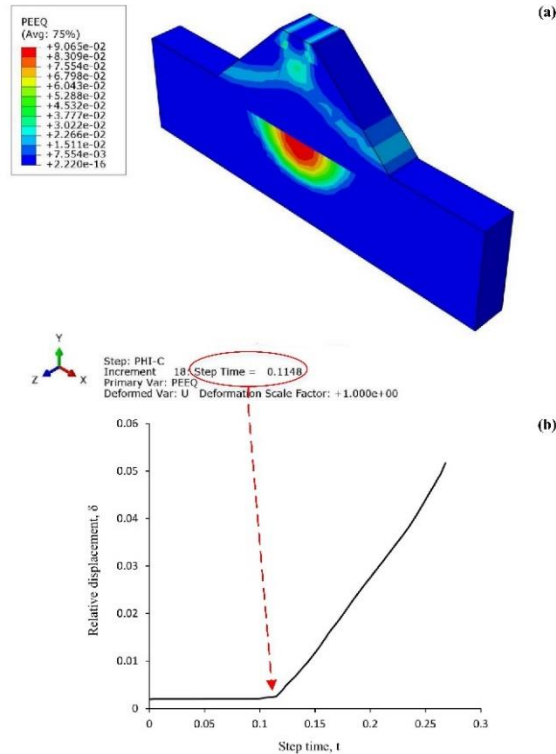


Figure 3

Comparison of PEEQ counter and temperature-driven strength reduction method: (a) PEEQ counters (b) δ - t curve

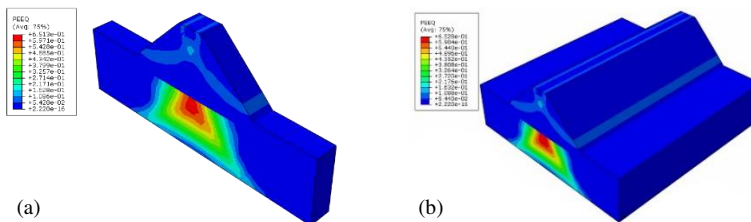


Figure 4

Model length verification a) $L=4$ m b) $L=48$ m

For the sake of soil type effect on the stability of the embankments, five different soil types of ST1 to ST2 with the given properties in Table 2 were analyzed. By choosing this five various soil types the effect of the embankment soil type on slope stability will be investigated in a wide range of poor to high strength soils. Also, the subgrade material properties selected same what exactly utilized in laboratory models. It should be notified that the utilized soil type for both the modified subgrade and embankment body is identical.

The basic geocell properties address in Table 1, which are in accordance with the PRS Geo Technologies Co catalogs [24]. In this study, sensitivity analysis was conducted on geocell stiffness as a significant geocell properties. For this purpose, the effect of eight various geocell stiffness of 150, 300, 700, 1000, 1400, 2000, 2500 and 3000 MPa investigated. Regard to this issue it is noteworthy that the other geocell specification was considered the same based on what is given in Table 1.

To investigate the effect of geocell opening size on slope stability of railway embankments, a sensitivity analysis was done on the reinforced embankments include ST2. It should be noted that after scaling up the laboratory cell dimensions and searching in the industry products there were not geocell dimensions of 1000*1000 mm. For this purpose, three different cell dimensions of 245*210 mm (small), 340*290 mm (medium), and 448*520 mm (large) with a height of 100 mm selected based on “PRS Geo Technologies Ltd [24]” products, category D. The mentioned geocell used for reinforcing the embankments with 5, 10, 15, 20, 25 and 30 geocell layers with the consecutive arrangement in the upper part of the embankments.

The effect of geocell layers on SF of railway embankments investigated by laying down geocell layers in the upper part of embankment continuously (non-spacing). With the aim of meeting SF of 1.5 for unstable embankments, the embankments reinforced by 5, 10, 15, 20, 25 and 30 geocell layers depending on embankment soil type.

With the objective to survey the performance of the geocell layers location on slope stability of railway embankments, firstly geocell layers were just placed in the upper part of the embankment body. Secondly to achieve the higher SF values, different vertical locations, U/H of 0.25, 0.37, 0.5, and 0.75 (see Figure 4 (a)) were examined. Moreover, the effect of geocell layers placement at three locations of the top, middle and bottom of the embankment was investigated together to stable the embankments including poorer soil types (see Figure 4 (b)).

Table 1
Specifications of used geocell in the parametric study

| Density (kg/m ³) | Elastic stiffness (MPa) | Poisson's ratio | Coefficient of Soil-Cell Friction | Opening size |
|------------------------------|-------------------------|-----------------|-----------------------------------|--------------|
| 900 | 1400 | 0.3 | 0.95 | 245*210 mm |

Table 2
A summary of different variables used in parametric study

| Variables | Description | | | | | |
|--|--|--------------------------|-----------------------------------|-----------------|-------------------------------------|----------------------------|
| | Soil type | Dry density (kN/m^3) | Young's modulus, E (kN/m^2) | Poisson's ratio | Friction angle, ϕ ($^\circ$) | Cohesion, c (kN/m^2) |
| Embankment soil | ST1 | 17 | 2.0e4 | 0.45 | 25 | 20 |
| | ST2 | 18 | 4.0e4 | 0.4 | 28 | 23 |
| | ST3 | 19 | 6.0e4 | 0.35 | 32 | 27 |
| | ST4 | 20 | 8.0e4 | 0.3 | 35 | 30 |
| | ST5 | 21 | 1.0e5 | 0.3 | 38 | 33 |
| Geocell number layers | 5, 10, 15, 20, 25 and 30 | | | | | |
| Geocell elasticity module (MPa) | 150, 300, 700, 1000, 1400, 2000, 2500 and 3000 | | | | | |
| Geocell opening size (mm) | 245*210 (small), 340*290 (medium), and 448*520 (large) | | | | | |
| Placement location of geocell layers (U/H) | Just in upper part: U/H=0.05, 0.1, 0.15, 0.2, 0.25 and 0.3 Different parts: U/H=0, 0.25, 0.37, 0.5, 0.75 and 1. | | | | | |

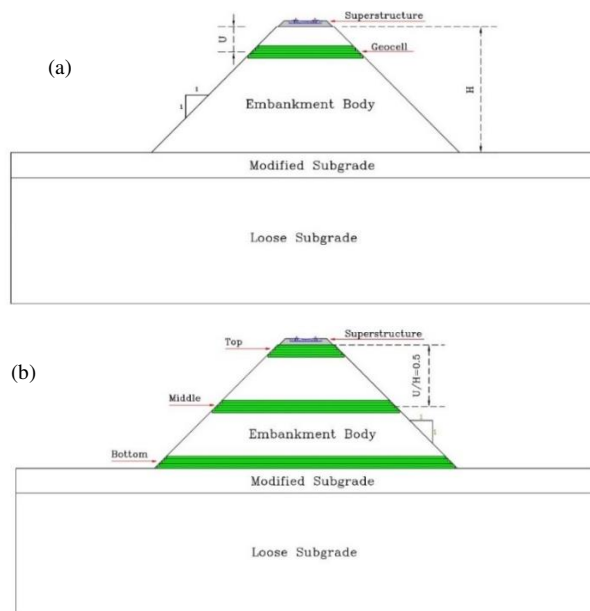


Figure 4

Vertical location of geocell layers according to a) U/H b) top, middle and bottom parts of the embankment

3 Results and Discussions

In this section, the effect of each soil types, elasticity module of geocell (E), geocell opening size, geocell layers number and vertical placing location of geocell layers on the SF of full-scale railway embankments will be debated. At first all unreinforced embankments including ST1 to ST5 soils analysis under qua-static load of $115kN/m^2$. With considering SF of 1.5 as slope stability criterion, the unstable embankments reinforced by geocell layers for satisfying the criterion. At the beginning, sensitivity analysis carrying out on geocell stiffness and geocell opening size to select the best values of them. After that, by placing geocell layers at the upper part of the embankments their influence on the SF was evaluated. Finally, in order to optimally use the geocell, the geocell layers effect were investigated in different vertical positions of the embankments.

3.1 Effect of Soil Types

To investigate the soil type effect on SF of railway embankments, five different soil types by given properties in Table 2 were analyzed. As shown in Figure 7 with improving mechanical properties of embankment soil, the SF of the embankments increased. The maximum and minimum SF values of 1.12 and 1.81 were obtained for ST1-0 and ST5-0 respectively. From the results it is clear, the soil type plays an important role on the slope stability so as to the ST3-0, ST4-0 and ST5-0 are stable without using geocell reinforcement and ST1-0 and ST2-0 have not met the slope stability criterion of 1.5.

3.2 Effect of Geocell Stiffness

The results obtained from the stiffness analysis are presented in Figure 5. From the data in this figure, it is apparent that by increasing geocell stiffness the SF of embankment increased and finally after the elastic module of 2500 MPa remained constant. In addition, the results indicated that the minimum stability criterion is satisfied by applying stiffness of 1400 MPa. Based upon this results for all next sensitively analyses, the elastic moduli of 1400 MPa adopted for geocell layers as optimum stiffness.

3.3 Effect of Geocell Opening Size

As Figure 1 shows, the geocell layers with smaller cell openings showed better performance than the others. From the char it's obvious that the effect of geocell opening size has been significant as increasing the number of geocell layers. It means that for the geocell-reinforced embankments up to 25 layers geocell opening size has a negligible effect. Furthermore, from the chart it is completely

obvious that the improvement has been significant for ST2-30 embankment in terms of SF by using the geocell layers with small opening size instead of large ones so as to it was improved from 1.36 to 1.52.

3.4 Effect of Number of Geocell Layers

The obtained results from analysis of FEM models are presented in Figure 7. The results indicate that SF increased for all the embankments with different soil types, by increasing geocell layers number.

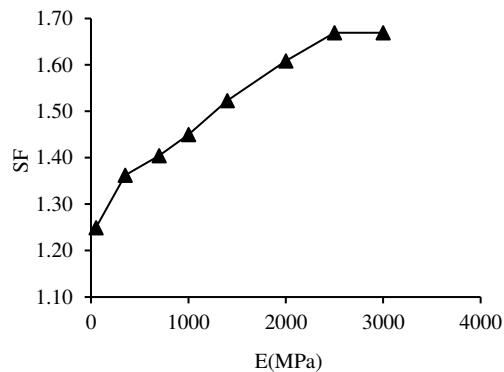


Figure 5

Geocell stiffness against SF for the ST2-30

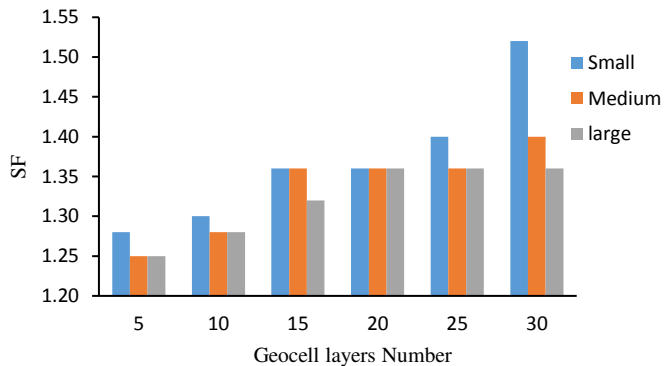


Figure 1

Effect geocell opening size on SF of ST2-30 embankment

Moreover, the effect of geocell layer number on SF increased with improvement of soils mechanical properties. In fact, in the reinforced embankments, the upper part of the embankment has a function same as a rigid foundation and as Figure 8 shows,

the failure take place below this foundation. By considering SF of 1.5 as criterion, as shown in the Figure 7 the embankments containing ST3, ST4 and ST5 are stable without using geocell layers. The important issue is stabling of the embankments include ST1 and ST2 soil types. For this purpose the geocell layer numbers increased up to 30 for meeting demanded safety factor. From the figure the embankment containing ST2 became stable by placing 30 geocell layers in the upper part. However, despite the use of 30 geocell layers, ST1 embankment remained unstable. The main reason is that, the soil under geocell layers ruptured due to the low shear strength of the soil (see Figure 8).

3.5 Effect of Vertical Location of Geocell Layers

As discussed in the previous section, all embankments except those containing ST1 soil met SF of 1.5 or higher by placing geocell layers at the upper part of the embankments. Moreover, Figure 7 shows that for stabling embankments with ST2 30 geocell layers number are needed which looks non-economic.

In this section with the aim of employee minimum geocell layers numbers to stabilization of ST2 embankment and also for stabling ST1 embankment, sensitively analysis performed on the vertical location of geocell layer numbers. For this purpose and in order to find out the best geocell layers placement location, at first one geocell layer placed at different U/H locations of 0.25, 0.37, 0.5, and 0.75 for ST2 embankment (see Figure 4(a)). It should be noted that in this section, the properties of utilized geocell are exactly the same what given in Table 1. As the results shown in Table 3, placing one geocell layer at difference vertical locations had a negligible effect on SF.

In the next step geocell layers extended to 5 layers at the mentioned locations. As reported in the table, for ST2-5 by placing 5 geocell layers at the middle of embankment a SF of 1.54 has been achieved. From this analysis it was found that the best vertical location is U/H=0.5.

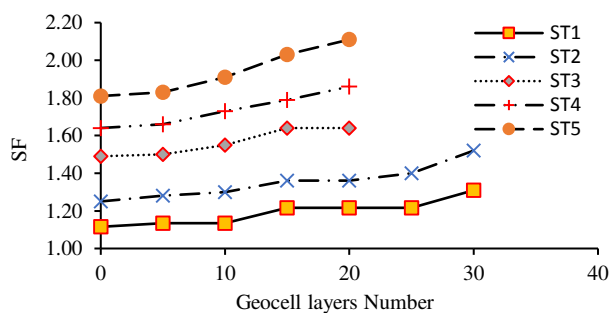


Figure 7

Effect of geocell layers number (N) on SF of real railway embankments for different soil types

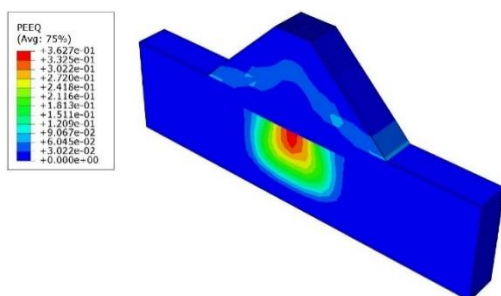


Figure 8

Failure mechanism of ST1-30 embankment by PEEQ counter

In the next step in order to improve and stab ST1 embankment, three different geocell layers of 5, 10 and 15 had tested at $U/H=0.5$ for meeting a desire SF. As reported in Table 3 with increasing geocell layers up to 15 layers in this location the intended SF not achieved. As Figure 9 shows, by utilizing 15 geocell layers at the middle of the embankment the failure occurs in the upper portion of the embankment. Finally by placing 15 geocell layers at three different parts of top, middle and bottom (see Figure 4(b)) of ST1-15 embankment a SF of 1.54 was obtained. All results around vertical position and number of geocell layers for ST1 and ST2 embankments are summarized in Table 3.

Concluding remarks

The purpose of the current study was to determine the effect of geocell layers on slope stability of railway embankments. At first six 1:20 scaled models including a reference and five reinforced embankments with geocell were constructed and examined in the lab. In the next step, using a validated finite element model, the effect of different geocell parameters including geocell stiffness, geocell opening size, number of geocell layers and vertical position of geocell layers investigated on a series of real scale railway embankment including five different soil types. A summary of the main findings are provided in below:

Table 3
SF values for different geocell layers number at different vertical locations for ST1 and ST2 embankments

| Em. name | Location | | | SF | Em. name | Location (U/H) | | | | SF |
|----------|----------|--------|--------|------|----------|----------------|------|-----|------|------|
| | Top | Middle | Bottom | | | 0.25 | 0.37 | 0.5 | 0.75 | |
| ST1-15 | 5 | 5 | 5 | 1.54 | ST2-1 | 1 | 0 | 0 | 0 | 1.25 |
| ST1-10 | 5 | 5 | 0 | 1.31 | ST2-1 | 0 | 1 | 0 | 0 | 1.28 |
| ST1-5 | 0 | 5 | 0 | 1.25 | ST2-1 | 0 | 0 | 1 | 0 | 1.28 |
| ST1-10 | 0 | 10 | 0 | 1.33 | ST2-1 | 0 | 0 | 0 | 1 | 1.28 |
| ST1-15 | 0 | 15 | 0 | 1.36 | ST2-5 | 5 | 0 | 0 | 0 | 1.32 |

| | | | | | | | | | | |
|--------|---|---|---|------|-------|---|---|---|---|------|
| ST2-15 | 5 | 5 | 5 | 1.77 | ST2-5 | 0 | 5 | 0 | 0 | 1.49 |
| ST2-10 | 5 | 5 | 0 | 1.75 | ST2-5 | 0 | 0 | 5 | 0 | 1.56 |
| ST2-5 | 0 | 5 | 0 | 1.56 | ST2-5 | 0 | 0 | 0 | 5 | 1.34 |

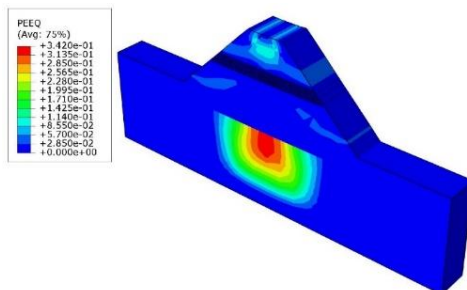


Figure 9

Failure mechanism of ST1-15 by placing all 15 geocell layers at middle of embankment

1) The soil type play a significant role in slope stability of railway embankments so that improving the mechanical properties of the embankment resulted in higher SF. The ST5-0, ST4-0 and ST3-0 embankments were stable without using any geocell layers and ST1-0 and ST2-0 exhibited unstable behavior based on the stability criterion of 1.5. The maximum and minimum SFs of 1.12 and 1.81 were obtained for ST5-0 and ST1-0 embankments respectively.

2) By investigation different geocell stiffness values on ST2-30 embankment, it was found the stiffness parameter played an important role on enhancing SF. The maximum and minimum values of 1.67 and 1.36 were resulted for the stiffness's of 150 and 3000 MPa respectively. Moreover, the stiffness of 1400 MPa selected as an optimum value based on the obtained results.

3) The geocell with small opening size had more effect on SF of reinforced ST2 embankments than medium and large sizes. By using geocell layers with small cells in ST2-30 embankment the SF increased about 11% in compared to large cells. However, opening size of 245*210 mm was determined as optimum.

4) The fourth major FEM finding was that increasing geocell layers number lead to enhance SF for all embankments and it was more noticeable as high strength soils were used. The most increasing was met for ST5-20 with 17 percent increase compared to ST5-0. Furthermore, ST3 and ST2 embankments were stabilized by utilizing 5 and 30 geocell layers respectively.

5) The vertical location of $U/H=0.5$ was found as the best position of geocell layers placement in the embankment body. In this regards by placing 5 geocell layers in the middle part of the embankment instead of using 30 geocell layers at the upper part, the slope stability is satisfied by the premeditated SF criterion which shows also 6 times decrease from an economic point of view. However, for ST1 soil type, although placing 30 geocell layers at the top of the embankment gives a SF of 1.31,

placing 15 geocell layers including five at the top, five in the middle and five at the bottom of the embankment presents a SF of 1.54, which again shows 50% saving money as well as providing higher safety factor.

References

- [1] Fischer Sz, Horvát F. Investigation of the reinforcement and stabilisation effect of geogrid layers under railway ballast. *Slovak Journal of Civil Engineering*. 2011 Sep 1;19(3):22
- [2] Kurhan M, Kurhan D, Novik R, Baydak S, Hmelevska N. Improvement of the railway track efficiency by minimizing the rail wear in curves. *INOP Conference Series: Materials Science and Engineering 2020 Nov 1 (Vol. 985, No. 1, p. 012001) IOP Publishing*
- [3] Przybylowicz M, Sysyn M, Kovalchuk V, Nabochenko O, Parneta B. Experimental and theoretical evaluation of side tamping method for ballasted railway track maintenance. *Transport Problems*. 2020;15
- [4] Mandal, J. N., & Gupta, P. (1994) Stability of geocell-reinforced soil. *Construction and building materials*, 8(1), 55-62
- [5] Neto, J. A., Bueno, B. S., & Futai, M. M. (2015) Evaluation of a calculation method for embankments reinforced with geocells over soft soils using finite-element analysis. *Geosynth. Int.*, 22, 439-451
- [6] Shukla, S. K., & Kumar, R. (2008) Overall slope stability of prestressed geosynthetic-reinforced embankments on soft ground. *Geosynthetics International*, 15(2), 165-171
- [7] Krishnaswamy, N. R., Rajagopal, K., & Latha, G. M. (2000) Model studies on geocell supported embankments constructed over a soft clay foundation. *Geotechnical testing journal*, 23(1), 45-54
- [8] Leshchinsky, B., & Ling, H. I. (2013) Numerical modeling of behavior of railway ballasted structure with geocell confinement. *Geotextiles and Geomembranes*, 36, 33-43
- [9] Moradila, G., Abdolmaleki1b, A., & Soltani, P. (2018) A laboratory and numerical study on the effect of geogrid-box method on bearing capacity of rock-soil slopes. *Geomechanics and Engineering*, 14(4), 345-354
- [10] Madhavi Latha, G., Rajagopal, K., & Krishnaswamy, N. R. (2006) Experimental and theoretical investigations on geocell-supported embankments. *International Journal of Geomechanics*, 6(1), 30-35
- [11] Sitharam, T. G., & Hegde, A. (2013) Design and construction of geocell foundation to support the embankment on settled red mud. *Geotextiles and Geomembranes*, 41, 55-63
- [12] Li, L., Cui, F., Hu, Z., & Xiao, H. (2018) Experimental Study on the Properties of Geocell-Reinforced Embankments. In *Proceedings of China-*

- Europe Conference on Geotechnical Engineering (pp. 1160-1163) Springer, Cham
- [13] Dai, Z., Zhang, M., Yang, L., & Zhu, H. (2018, May) Model Tests on Performance of Embankment Reinforced with Geocell Under Static and Cyclic Loading. In *GeoShanghai International Conference* (pp. 399-410) Springer, Singapore.
- [14] Zhou, H., & Wen, X. (2008) Model studies on geogrid-or geocell-reinforced sand cushion on soft soil. *Geotextiles and Geomembranes*, 26(3), 231-238
- [15] Chawla, S., Shahu, J. T., & Gupta, R. K. (2018) Design methodology for reinforced railway tracks based on threshold stress approach. *Geosynthetics International*, 1-10
- [16] Esmaeili, M., Naderi, B., Neyestanaki, H. K., & Khodaverdian, A. (2018) Investigating the effect of geogrid on stabilization of high railway embankments. *Soils and Foundations*, 58(2), 319-332
- [17] Astaraki, F., Esmaeili, M. and Reza Roozbini, M., (2020) Influence of geocell on bearing capacity and settlement of railway embankments: an experimental study. *Geomechanics and Geoengineering*, pp. 1-17
- [18] Astaraki F, Roozbini MR, Esmaeili M, Chalabii J. Investigation on Mechanical Behavior of Embedded Geocell in Geocell-Reinforced Railway Embankment. *International Journal of Railway Research*. 2019 Dec 10;6(2):95-102
- [19] Simulia, D. S., (2018) ABAQUS 2018 User's manual. Dassault Systems, analysis user's guide volume IV: Elements
- [20] Standardization, E.C.f., European Standard (EN 1991–2). Ref. no. EN 1991-2:2003 E. 2003
- [21] Xu, Q., Yin, H., Cao, X., & Li, Z. (2009) A temperature-driven strength reduction method for slope stability analysis. *Mechanics Research Communications*, 36(2), 224-231
- [22] Ho, I. H. (2014) Numerical study of slope-stabilizing piles in undrained clayey slopes with a weak thin layer. *International Journal of Geomechanics*, 15(5), 06014025
- [23] AREMA, American Railway Engineering and Maintenance of Way Association Manual for Railway Engineering. *Economics of Railway Engineering and Operations-construction and Maintenance Operations*, 2006, Vol. 4, Chapter 16, Part 10
- [24] PRS GeoTechnologies Ltd. <https://www.prs-med.com/engineering-services/geotechnical-project-design/specifications/>

Comparative Study of the Mechanical Behavior of Concrete Railway Sleeper Mix Design, using Waste Rubber and Glass Materials

Mohammad Siahkouhi¹, Chunchao Li², Farshad Astaraki³,
Majid Movahedi Rad³, Szabolcs Fischer³, Guoqing Jing^{1*}

¹ School of Civil Engineering, Beijing Jiaotong University, No.3 Shangyuancun Haidian District, Beijing 100044, P. R. China

² Jitoo UHPC (Shandong) New Material Technology Co., Ltd, Wenshan West Road 1, Wendeng District, Weihai, Shandong 264400, China

³ Department of Structural and Geotechnical Engineering, Széchenyi István University, Egyetem tér 1, Győr 9026, Hungary
e-mail: m.siahkouhi@bjtu.edu.cn, lcc@mingyangrt.com,
astaraki.farshad@hallgato.sze.hu, majidmr@sze.hu, fischersz@sze.hu,
gjqing@bjtu.edu.cn

Abstract: Waste rubber tires and glass powders, are hazardous materials for the environment. One of the methods to consume them, is their application in railway engineering projects. Rubber and glass materials, in this research, are provided from waste tires and glass bottles. Therefore, a modification is conducted to the concrete railway sleeper mix design, incorporated with waste rubber (R) and glass powder (GP). Three mechanical tests, including compressive, flexural and tensile splitting, have been studied on rubber and glass powder concrete specimens. Three different percentages of 5%, 10% and 15% by cement weight, for GP and by fine aggregate volume for R, are investigated herein. The results show that GP concrete has a better performance over the rubber concrete (RC), but lower than Ref. specimens. 5%GP as the best mix design, has compressive, flexural and tensile strengths of 45.4 MPa, 7.5 MPa and 5.82 MPa, respectively. Moreover, these strengths, for compressive and flexural, of 5%GP are about 24% and 6% lower than the Ref. strengths, respectively, while, tensile splitting strength is almost 14% higher than Ref. strength.

Keywords: Concrete railway sleeper; waste rubber; waste glass; recycled materials

1 Introduction

Railway sleepers are an important component of railway tracks, that help to disperse and reduce train loads from the rail foot to the underlying ballast bed and, as a result, to subgrade of the track [1]. Timber, concrete, and steel are used to make traditional

sleepers [2]. The majority of railway tracks were made of wood sleepers, but due to their environmental problems, they were gradually replaced by other types of sleepers [3]. Steel sleepers were utilized instead of wooden sleepers to replace them [4]. When it comes to the performance of steel sleepers, there are concerns with high train speeds and corrosion [5]. In railway engineering, concrete sleepers are widely utilized [6]. Their performance on railway tracks results in lower maintenance costs, increased track stability, and extended track life cycles [7]. Mono-block concrete sleepers are one of the most common types of pre-stressed concrete sleepers used in railway tracks [8].

Jing *et al.* [2] assessed the combination of glass powder and steel fiber as a silica fume replacement in concrete railway sleeper mix design. Results showed that with the consideration of the performance and cost, the combination of 10% GP and 1.5% steel fiber is optimal mix design. Cementitious composites with glass powder were tested by Siad *et al.* [9] to test the concrete's mechanical behavior, glass powder was used instead of fly ash. GP improve the performance of concrete by 20%. In a study, Ramdani *et al.* [10] employed GP coupling with rubber fibers. They demonstrated that combining rubber fiber with GP can improve concrete's mechanical qualities. The performance of GP in concrete has been studied by a number of researchers. Generally, non-crystalline silica, sodium oxide, calcium oxide, and other components are ingredients of GP. As a result, the high silicon concentration of GP material makes it ideal for the concrete industry, making it acceptable for partial cement replacement [11-13]. Some investigations were conducted using UHPC's behavior with GP to better understand glass powder in microstructure [14-16]. The presence of GP decreases chloride penetrability and the corrosion risk of bars placed in concrete sleepers, according to Shayan and Xu [17], especially in high chloride content locations. Kou and Xing [18] founded out that GP content in concrete decreased 7 days compressive strength, however; the cement replacement by GP is very useful in case of rehology.

Rubber concrete (RC) has been widely used in a variety of applications, including the manufacture of sleepers. Jing *et al.* [6] studied manufacturing of a rubber concrete railway sleeper. In this study behavior of a rubber and conventional concrete railway sleepers are compared using digital image correlation (DIC). The results show that the rubber pre-stressed concrete sleeper has a resistance against crack initiation by 20% greater than that of the conventional pre-stressed concrete sleeper. Anilkumar *et al.* [19] demonstrated that rubber concrete sleepers with crumb rubber as fine aggregate have a higher deflection, especially when the rubber content is increased from 5% to 15%, and their impact absorption is higher than that of sleepers without rubber content. In another research, Hameed *et al.* [20] looked at the effects of rubber crumb as a fine aggregate on railway sleeper impact absorption. When compared to pre-stressed concrete sleepers, the impact strength of railway sleepers containing crumb rubber increased by 60%. Larger fracture widths and deflections result from RC's weaker mechanical qualities, including as compressive and flexural strengths [20-22]. Furthermore, their distinct bond

behavior [23], which is primarily attributable to mechanical properties, necessitates assessing their fracture behavior in order to evaluate crack width. Rubber has been widely studied as an aggregate or fiber material in concrete [24-27]. Superior impact absorption [28, 29], stronger ductility [30, 31], better dynamic qualities including damping features [32-34] and higher resistance to the beginning of first cracks in the concrete [35, 36] are the four primary characteristics of rubber concrete which are significantly important for concrete railway sleepers.

None of the referenced papers have compared the behavior of waste rubber and glass materials, in concrete railway sleeper mix design. Consuming these materials can protect the environment and, moreover, can reduce the production cost of concrete railway sleepers, as well as, a reduction of deposits of waste materials. Therefore, in this research, attention to different admixtures, incorporated with waste rubber and glass, and the performance of the concrete railway mix design is studied.

2 Experimental Program

2.1 Materials and Mix Proportion

The materials of seven mixtures of rubber and glass concrete and Ref. concrete are introduced in the current section with 5%, 10% and 15% by cement weight for GP and by fine aggregate volume for R (Table 1). All the materials that are used in this research, excluding rubber and glass particles are the same as those are used by a concrete sleeper factory to produce conventional concrete sleeper. Ordinary Portland cement type (II) has been used for mixtures. The rubber used in this research obtained from waste tires. After gathering and omitting steel wires, they are changed to powder in a factory (Table 2). A poly-carboxylate superplasticizer is used for all the concrete mixtures. The gradation graphs of fine and coarse aggregates are presented in Figure 1. Sand is one of the expensive materials in concrete sleeper production. Considering the important role of sleepers in railway tracks, good quality of materials is expected. Sand is one of the expensive materials as most of the time they are produced using stone crushing machine. The Glass powder that is used in this research is obtained from waste glasses, which were purchased from a factory. After gathering the waste glass and washing them, they are changed to a powder for different purposes (Table 2). The glass powder (GP) material has a maximum particle size of 0.01 mm. To combine powder materials with concrete admixture and also avoid particle agglomeration, they are mixed before the water and a superplasticizer is added. First, the fine aggregates are mixed in the mixer followed by adding the powder materials and mixed for around 4 minutes. Then almost half of the 2% (by cement weight) superplasticizer is diluted in the admixture water and is gradually added within 2 minutes. The remaining

superplasticizer are gradually added, during a next 4 minutes of mixing. The fresh concrete is cast in two kinds of molds, with dimensions of 100 * 100 * 400 mm prismatic and 100 mm cubical. The specimens without movement are covered with plastic sheets and are kept at ambient temperature for a day before demolding. After demolding, the samples are cured in with heat and vapor. The curing method is in this way that specimens are cured at 20 °C for 73 hours of curing time, then the heat is smoothly raised to 90 °C. This heat is stable for 50 hours, afterwards, it is gradually reduced back to 20 °C. For validity of test results, each mix of 3 specimens are manufactured and tested.

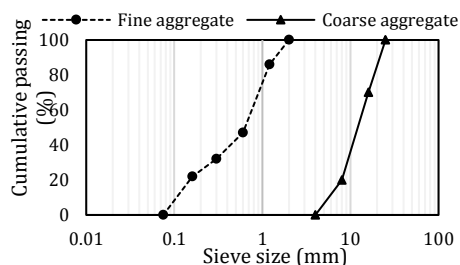


Figure 1

Gradation curve of concrete aggregates


Table 1


Concrete admixtures

| Mix ID | W/C | Cement | Glass powder | Rubber | Fine agg. | Coarse agg. |
|---------|-----|----------------------|--------------|--------|-----------|-------------|
| | | (kg/m ³) | | | | |
| Ref. | 0.3 | 400 | - | - | 691 | 1229 |
| 5GP-0R | | 377 | 23 | - | 691 | 1229 |
| 10GP-0R | | 354 | 46 | - | 691 | 1229 |
| 15GP-0R | | 331 | 69 | - | 691 | 1229 |
| 0GP-5R | | 400 | - | 14.23 | 656.4 | 1229 |
| 0GP-10R | | 400 | - | 28.46 | 621.9 | 1229 |
| 0GP-15R | | 400 | - | 42.69 | 587.3 | 1229 |

Table 2

Glass powder and waste rubber properties

| Type of Material use | Size | Density (g/cm ³) | Pictures |
|----------------------------|---------|------------------------------|--|
| sand aggregate replacement | 0.28 mm | 1.085 |  |

| | | | |
|--------------------|------------|-----|--|
| Cement replacement | 13 μ m | 2.1 |  |
|--------------------|------------|-----|--|

2.2. Compressive Strength Test

Seven concrete specimens, including glass powder, rubber specimens and Ref. are tested in compressive strength test as shown in Figure 2. The results indicate that the presence of glass powder and rubber decrease concrete strengths. A 5% mix of glass powder, has the highest strength between glass powder and rubber specimens, however, it is 25% lower than Ref. strength. 5GP-0R is followed by 0GP-5R specimen with 43.5 MPa compressive strength. The Ref.'s compressive strength is about 60.5 MPa. Overall, increasing rubber and glass powder decreases concrete strengths. 5%, 10% and 15% glass powder by weight of cement specimens have strengths almost 25%, 30% and 40%, respectively, and 5%, 10% and 15% rubber by volume of fine aggregate have about 28%, 29% and 34% lower compressive strength, respectively, than Ref. with 60.5 MPa strength. Therefore, for the case of using waste materials glass powder in 5% of cement weight, shows better performance than other admixtures.



Figure 2

An overview of compressive strength test machine

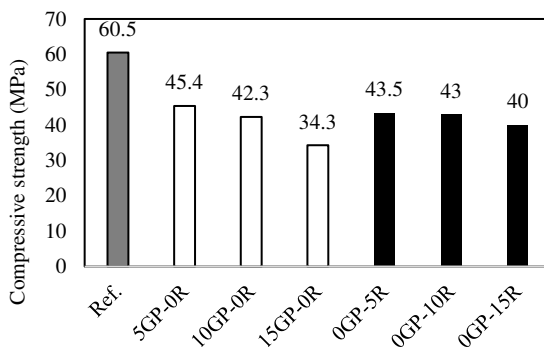


Figure 3

Compressive strength and flowability of concrete specimens

2.3. Flexural Strength Test

Flexural strengths of Ref. specimen decreases in presence of rubber and glass powder. Figure 4 shows an overview of flexural strength of specimens. Ref. specimen has 8 MPa strength almost 6%, 6% and 10% higher than 5GP-0R, 10GP-0R and 15GP-0R specimen's strengths, respectively. These difference percentages for rubber concrete specimens, including 0GP-5R, 0GP-10R and 0GP-15R are 6%, 8% and 10% respectively. Maximum flexural strength is identical between 5GP-0R and 0GP-5R as 7.5 MPa (Figure 5).



Figure 4

An overview of flexural test layout

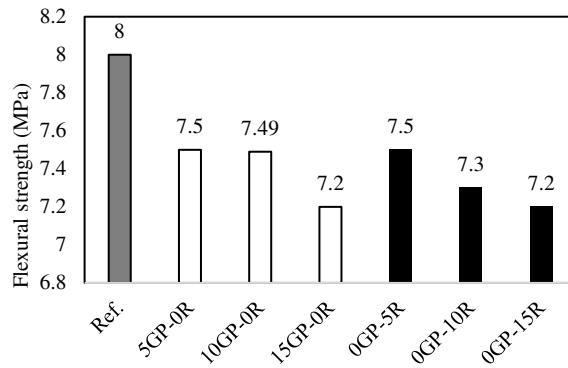


Figure 5

Flexural strength test results of concrete specimens

2.4 Splitting Tensile Strength

The splitting tensile strength of the different admixtures with glass powder and rubber are shown in Figure 6. Concrete has weakness in tension, therefore, splitting tensile strength test is one of the necessary tests to determine the concrete specimens in which load level may crack. The results indicate that the presence of fibers in admixture improves the concrete splitting tensile strength. The highest value of splitting tensile strength test is obtained by 5GP-0R as 5.82 followed by 0GP-5R and Ref. Presence of glass powder and rubber improve tensile strength of concrete. 10% and 15% glass powder and rubber have 10%, 14% and 8%, 10%, respectively, lower strengths than Ref. as shown in Figure 7.



Figure 6

Splitting tensile test layout of concrete specimens

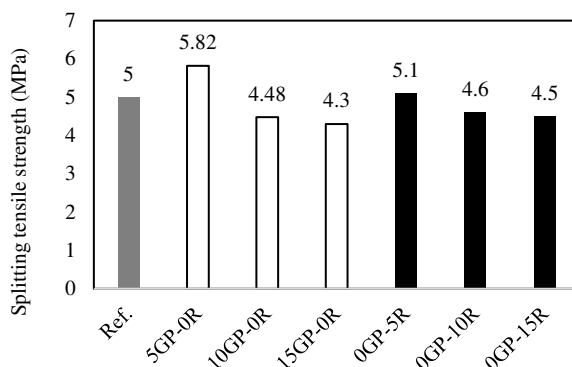


Figure 7
Splitting tensile strength of concrete specimens

3 Results and Discussion

This study aims to use environmentally troublesome waste materials in railway engineering projects. Therefore, three different percentages as 5%, 10% and 15% of glass powder by cement weight and rubber by fine aggregate volume are studied in comparison with a Ref. mix of concrete railway sleeper. Generally, the presence of waste materials reduces concrete strength, but considering cost and environmental issues, they still can be used in concrete railway sleepers production. Thus, concrete mixtures have been manufactured by adding glass powder and rubber as 5GP-0R, 10GP-0R, 15GP-0R, 0GP-5R, 0GP-10R and 0GP-15R. Mechanical properties of all mixtures were measured and compared with compressive, tensile and flexural strengths of concrete railway sleeper to determine the performance of railway concrete mix design as presented in Table 3. The test results show that the mechanical performance of admixture of 5GP-0R is the best among all other admixtures. However, splitting tensile strength of 5% glass powder shows better results than Ref., but generally, the mechanical behavior of concrete decreases. Considering the cost for 1 m³ concrete manufactured, using recycled materials, it can be seen that a 5%GP, has an almost 10% cheaper price, followed by 10% and 15% of GP, with 18% and 27% less cost than the Ref. concrete, respectively. Rubber particles are even cheaper than GP as 5%R, has an 11% cheaper price. The percentages for 10% and 15% of rubber (R) are 20% and 29% cheaper than the Ref., respectively.

Table 3
Steel fibers properties

| Notation | Compressive strength | Flexural strength | Splitting tensile strength | Cost |
|----------|----------------------|-------------------|----------------------------|------|
| | MPa | | | RMB |
| Ref. | 60.5 | 8 | 5 | 6766 |
| 5GP-0R | 45.4 | 7.5 | 5.82 | 6100 |
| 10GP-0R | 42.3 | 7.49 | 4.48 | 5500 |
| 15GP-0R | 34.3 | 7.2 | 4.3 | 4900 |
| 0GP-5R | 43.5 | 7.5 | 5.1 | 6050 |
| 0GP-10R | 43 | 7.3 | 4.6 | 5350 |
| 0GP-15R | 40 | 7.2 | 4.5 | 4820 |

Conclusions

In this study, 7 admixtures are prepared to investigate the performance of waste materials, including waste glass and rubber, and their influence on concrete railway sleeper mix design mechanical properties. To study waste materials and compare their behavior, different glass powder and rubber, ratios are considered as (5%GP-0%R), (10%GP-0%R), (15%GP-0%R) and (0%GP-5%R), (0%GP-10%R), (0%GP-15%R). The following results are concluded from this study:

- 1) The 5%, 10% and 15% glass powder by weight of cement specimens have 25%, 30% and 40% lower compressive strengths than Ref., respectively. While, 5%, 10% and 15% rubber by volume of fine aggregate have 28%, 29% and 34% lower compressive strengths than Ref. with 60.5 MPa strength, respectively.
- 2) The Ref. specimen has 8 MPa strength almost 6%, 6% and 10% higher than 5GP-0R, 10GP-0R and 15GP-0R specimen's strengths, respectively. These difference percentages for rubber concrete specimens, including 0GP-5R, 0GP-10R and 0GP-15R are 6%, 8% and 10%, respectively.
- 3) 10% and 15% glass powder and rubber have 10%, 14% and 8%, 10%, respectively, lower strengths than Ref., while 5% GP and R have higher splitting tensile strengths by 16% and 2% than Ref., respectively.
- 4) A 5G-0R mix design shows the best performance in case of mechanical properties among other specimens contain waste materials and can be used for manufacturing a concrete railway sleeper.
- 5) Considering that sand is an expensive materials, in concrete sleeper manufacturing, using GP and R can reduce the finished concrete sleeper price by 10%, 18% and 27% for a 5%, 10% and 15% of glass powder, respectively, and 11%, 20% and 29% cheaper than the Ref. cost for rubber concrete, respectively.

Acknowledgement

This paper has been supported by China Academy of Railway Science foundation (Grant No. 2020YJ081).

References

- [1] A. S. Hameed and A. P. Shashikala, "Suitability of rubber concrete for railway sleepers," *Perspectives in Science*, Vol. 8, No. Supplement C, pp. 32-35, 2016/09/01/ 2016
- [2] B. Li, H. Li, M. Siahkouhi, and G. Jing, "Study on coupling of glass powder and steel fiber as silica fume replacement in ultra-high performance concrete: Concrete sleeper admixture case study," *KSCE Journal of Civil Engineering*, pp. 1-12, 2020
- [3] P. Qiao, J. F. Davalos, and M. G. Zipfel, "Modeling and optimal design of composite-reinforced wood railroad crosstie," *Composite structures*, Vol. 41, No. 1, pp. 87-96, 1998
- [4] W. Ferdous, A. Manalo, G. Van Erp, T. Aravinthan, S. Kaewunruen, and A. Remennikov, "Composite railway sleepers—Recent developments, challenges and future prospects," *Composite Structures*, Vol. 134, pp. 158-168, 2015
- [5] J.-A. Zakeri and R. Talebi, "Experimental investigation into the effect of steel sleeper vertical stiffeners on railway track lateral resistance," *Proceedings of the Institution of Mechanical Engineers, Part F: Journal of Rail and Rapid Transit*, Vol. 231, No. 1, pp. 104-110, 2017
- [6] G. Jing, D. Yunchang, R. You, and M. Siahkouhi, "Comparison study of crack propagation in rubberized and conventional prestressed concrete sleepers using digital image correlation," *Proceedings of the Institution of Mechanical Engineers, Part F: Journal of Rail and Rapid Transit*, p. 09544097211020595, 2021
- [7] G. Jing, M. Siahkouhi, J. R. Edwards, M. S. Dersch, and N. Hoult, "Smart railway sleepers—a review of recent developments, challenges, and future prospects," *Construction and Building Materials*, p. 121533, 2020
- [8] R. Kohoutek, "Dynamic and static performance of interspersed railway track," in *Conference on Railway Engineering 1991: Demand Management of Assets; Preprints of Papers*, 1991, p. 153; Institution of Engineers, Australia
- [9] H. Siad, M. Lachemi, M. Sahmaran, and K. M. A. Hossain, "Mechanical, physical, and self-healing behaviors of engineered cementitious composites with glass powder," *Journal of Materials in Civil Engineering*, Vol. 29, No. 6, p. 04017016, 2017
- [10] S. Ramdani, A. Guettala, M. Benmalek, and J. B. Aguiar, "Physical and mechanical performance of concrete made with waste rubber aggregate,

- glass powder and silica sand powder," *Journal of Building Engineering*, Vol. 21, pp. 302-311, 2019
- [11] A. Omran and A. Tagnit-Hamou, "Performance of glass-powder concrete in field applications," *Construction and Building Materials*, Vol. 109, pp. 84-95, 2016
- [12] G. Vijayakumar, H. Vishaliny, and D. Govindarajulu, "Studies on glass powder as partial replacement of cement in concrete production," *International Journal of Emerging Technology and Advanced Engineering*, Vol. 3, No. 2, pp. 153-157, 2013
- [13] H. Du and K. H. Tan, "Properties of high volume glass powder concrete," *Cement and Concrete Composites*, Vol. 75, pp. 22-29, 2017
- [14] N. Soliman and A. Tagnit-Hamou, "Partial substitution of silica fume with fine glass powder in UHPC: Filling the micro gap," *Construction and Building Materials*, Vol. 139, pp. 374-383, 2017.
- [15] V. Vaitkevičius, E. Šerelis, and H. Hilbig, "The effect of glass powder on the microstructure of ultra high performance concrete," *Construction and Building Materials*, Vol. 68, pp. 102-109, 2014
- [16] N. A. Soliman and A. Tagnit-Hamou, "Using glass sand as an alternative for quartz sand in UHPC," *Construction and Building Materials*, Vol. 145, pp. 243-252, 2017
- [17] A. Shayan and A. Xu, "Performance of glass powder as a pozzolanic material in concrete: A field trial on concrete slabs," *Cement and concrete research*, Vol. 36, No. 3, pp. 457-468, 2006
- [18] S. C. Kou and F. Xing, "The effect of recycled glass powder and reject fly ash on the mechanical properties of fibre-reinforced ultrahigh performance concrete," *Advances in materials science and engineering*, Vol. 2012, 2012
- [19] A. Shashikala, P. Anilkumar, G. Joseph, J. John, and K. Lijith, "Experimental Investigations on Use of Rubber Concrete in Railway Sleepers"
- [20] A. S. Hameed and A. Shashikala, "Suitability of rubber concrete for railway sleepers," *Perspectives in Science*, Vol. 8, pp. 32-35, 2016
- [21] A. Shashikala, P. Anilkumar, G. Joseph, J. John, and K. Lijith, "Experimental Investigations on Use of Rubber Concrete in Railway Sleepers," in *2nd RN Raikar memorial international conference & Bathia-Basheer international symposium on ADVANCES IN SCIENCE & TECHNOLOGY OF CONCRETE-2015*
- [22] D. Bompa and A. Elghazouli, "Creep properties of recycled tyre rubber concrete," *Construction and Building Materials*, Vol. 209, pp. 126-134, 2019
- [23] B. S. Mohammed, K. M. A. Hossain, J. T. E. Swee, G. Wong, and M. Abdullahi, "Properties of crumb rubber hollow concrete block," *Journal of Cleaner Production*, Vol. 23, No. 1, pp. 57-67, 2012

- [24] M. Ramesh, "Flax (*Linum usitatissimum* L.) fibre reinforced polymer composite materials: A review on preparation, properties and prospects," *Progress in Materials Science*, Vol. 102, pp. 109-166, 2019
- [25] X. Shu and B. Huang, "Recycling of waste tire rubber in asphalt and portland cement concrete: An overview," *Construction and Building Materials*, Vol. 67, pp. 217-224, 2014
- [26] B. Huang, G. Li, S.-S. Pang, and J. Eggers, "Investigation into waste tire rubber-filled concrete," *Journal of Materials in Civil Engineering*, Vol. 16, No. 3, pp. 187-194, 2004
- [27] O. Onuaguluchi and D. K. Panesar, "Hardened properties of concrete mixtures containing pre-coated crumb rubber and silica fume," *Journal of Cleaner Production*, Vol. 82, pp. 125-131, 2014
- [28] T. Gonen, "Freezing-thawing and impact resistance of concretes containing waste crumb rubbers," *Construction and Building Materials*, Vol. 177, pp. 436-442, 2018
- [29] A. O. Atahan and A. Ö. Yücel, "Crumb rubber in concrete: static and dynamic evaluation," *Construction and Building Materials*, Vol. 36, pp. 617-622, 2012
- [30] S. Sgobba, M. Borsa, M. Molfetta, and G. C. Marano, "Mechanical performance and medium-term degradation of rubberised concrete," *Construction and Building Materials*, Vol. 98, pp. 820-831, 2015
- [31] M. K. Ismail and A. A. Hassan, "Performance of full-scale self-consolidating rubberized concrete beams in flexure," *ACI Materials Journal*, Vol. 113, No. 2, pp. 207-218, 2016
- [32] A. R. Khaloo, M. Dehestani, and P. Rahmatabadi, "Mechanical properties of concrete containing a high volume of tire-rubber particles," *Waste management*, Vol. 28, No. 12, pp. 2472-2482, 2008
- [33] F. Hernandez-Olivares, G. Barluenga, M. Bollati, and B. Witoszek, "Static and dynamic behaviour of recycled tyre rubber-filled concrete," *Cement and concrete research*, Vol. 32, No. 10, pp. 1587-1596, 2002
- [34] L. Zheng, X. S. Huo, and Y. Yuan, "Strength, modulus of elasticity, and brittleness index of rubberized concrete," *Journal of Materials in Civil Engineering*, Vol. 20, No. 11, pp. 692-699, 2008
- [35] A. Moustafa and M. A. ElGawady, "Dynamic properties of high strength rubberized concrete," *ACI Spec. Publ*, Vol. 314, pp. 1-22, 2017
- [36] M. K. Ismail and A. A. Hassan, "Shear behaviour of large-scale rubberized concrete beams reinforced with steel fibres," *Construction and Building Materials*, Vol. 140, pp. 43-57, 2017